

NUMERICAL MODELING OF A DIRECT CONTACT EVAPORATOR FOR
HUMIDIFICATION-DEHUMIDIFICATION DESALINATION SYSTEMS

By

Clément Roy

A DISSERTATION

Submitted to
Michigan State University
in partial fulfillment of the requirements
for the degree of

Mechanical Engineering – Doctor of Philosophy

2020

ABSTRACT

NUMERICAL MODELING OF A DIRECT CONTACT EVAPORATOR FOR HUMIDIFICATION-DEHUMIDIFICATION DESALINATION SYSTEMS

By

Clément Roy

Fresh water scarcity is one of the key challenge for this century. Although the planet is 70% covered by water, the access to fresh water suitable for life is highly unequal. The challenge of water desalination using renewable energy requires lower cost solution than is currently available. In the context of solar energy powered desalination, thermal processes offer a promising way to provide fresh water at various scales. The use of a direct contact evaporator and condenser in place of traditional shell and tube heat exchangers greatly enhances the efficiency of heat transfer. Thus the understanding of the thermal and hydrodynamic features of the flow in such heat exchangers plays a fundamental role in their design. The current experimental techniques are still inadequate to obtain a full picture of small scale transport phenomena taking place locally at liquid-vapor interfaces, while the emergence and improvement of multiphase CFD techniques provides powerful tools to investigate two-phase flows at small length scale. The goal of this work is to develop a robust CFD framework to study diffusion driven evaporation as it typically occurs in the evaporator, and implement it in a commercial CFD code, ANSYS Fluent. The completion of this framework allows a better understanding of the hydrodynamic as well as the heat and mass transfer for various operating and system conditions. The use of the single fluid approach, Volume Of Fluid method, that describes each phase by the means of a scalar function that is advected using a transport equation allows an efficient means to solve the two-phase flow problem. Nonetheless, the implementation of an in-house algorithm to model diffusion driven evaporation as well as accurately computing the interfacial area is necessary since this not available on the default solver. The developed algorithm is validated using multiple benchmarks. The framework developed is applied toward the modeling of a direct contact evaporator for a counter-current Humidification-Dehumidification desalination system. The computational results show adequate agreement with

multiple benchmarks. The study uses several boundary conditions, and shows a strong dependence between the packed column performance and the water distribution while the gas distribution has little effect for the conditions studied. Finally, the study takes interest into understanding the blockage or local flooding phenomenon observed both experimentally and numerically. The numerical calculations applied to a Representative Elementary Unit (REU) consider flow pattern, geometry, and wettability as parameters. The results show the geometry and wettability to be the key factors responsible of the blockage instability for the conditions studied.

Copyright by
CLÉMENT ROY
2020

Without challenges there are no changes

ACKNOWLEDGEMENTS

This manuscript marks for me the end of my long journey through the multiple universities that I attended along the way. Those various experiences made me the person that I am today both as a scientist and as a person. As a consequence I would like to thank the persons I has the opportunity to meet and work with.

First and foremost I want to thank my committee members for evaluating my work and particularly my advisor, Pr. James Klausner, for the unconditional trust and freedom along with the support that I received during my time as a doctoral student.

The accomplishment of this manuscript got me thinking about my entire academic curriculum and person that made a difference in their own way. This is the reason why I would like to mention my first year math teacher, Alain Fumey, for the inception he may have accomplished when mentioning the idea of pursuing a doctoral degree to the entire class. This idea stayed in a corner of my head until my final year at ECAM Lyon where the research project among the Energy department. I would like to thank Alexandre Vaudrey, Vincent Caillé, and Yann Marchesse for the help I received when I was on the other side of the world (in China) preparing my application at Centrale Lyon.

This led me to the formidable experience I had in Laboratory of Fluid Mechanic and Acoustics. I would like to thank Stéphane Aubert and Pascal Ferrand for welcoming me in the Turbomachinery group and all the people I had the opportunity to work with: Quentin, Annabelle, Leon. A special thought for Franck with whom I shared my office for our discussions (or debates) about mesh morphing and heat exchangers among others (no, my point of view on heat exchangers has not changed).

Finally, my last experience at Michigan State University from which this manuscript is resulting. I would like thank all my collaborators. Jared for its tireless work on the 3D printed parts. Joseph for is relentlessness at figuring out bureaucratic procedures (I'm still thinking about the ERC copier) and for enlivening the office during the terrible and famous Michigan winter. I also thank

my office mates Atacan and Suhas. Thanks to Amey for helping me in the last couple months with the high speed camera. Thanks to Keith King for sharing the same vision about our lab and for his incredible ability to briefly communicate complex ideas. I would also like to thank Craig Gunn for its positive energy and his patience reviewing my articles and this manuscript.

Ultimately, thanks to my family for their unconditional support in this adventure but also along my entire academic journey. My friends for the incredible times during my short breaks in France but also for the numerous adventures we had together during our studies.

TABLE OF CONTENTS

LIST OF TABLES	xii
LIST OF FIGURES	xiii
KEY TO ABBREVIATIONS	xvii
CHAPTER 1 INTRODUCTION	1
1.1 Context	1
1.2 Objectives	3
1.3 Manuscript Organization	3
CHAPTER 2 SOLAR DESALINATION TECHNOLOGIES	5
2.1 General	5
2.2 Indirect Solar Desalination Technologies	5
2.2.1 General	5
2.2.2 Membrane Processes	6
2.2.2.1 Reverse Osmosis	6
2.2.2.2 Electrodialysis	8
2.2.3 Non-Membrane Processes	9
2.2.3.1 Multi Effect Distillation	9
2.2.3.2 Solar Pond	10
2.2.3.3 Vapor Compression	12
2.2.3.4 Multi-Stage Flash	13
2.2.3.5 Natural Vacuum Desalination	14
2.2.3.6 Freeze Desalination	15
2.2.3.7 Adsorption Desalination	16
2.3 Direct Solar Desalination Technologies	18
2.3.1 General	18
2.3.1.1 Solar Still	18
2.3.1.2 Humidification - Dehumidification	19
CHAPTER 3 EVAPORATOR & PACKED COLUMNS	23
3.1 General	23
3.1.1 Evaporator & Desalination	23
3.1.2 Packed Columns & Desalination	23
3.2 Design of Structured Packed Bed	24
3.2.1 Flow Patterns	24
3.2.2 Hydrodynamic Parameters	26
3.2.2.1 Liquid Holdup	26
3.2.2.2 Pressure Drop	26
3.2.3 Heat & Mass Transfer Parameters	27
3.2.3.1 Interfacial Area	27

3.2.3.2	Heat & Mass Transfer Coefficients	28
3.3	Numerical Modeling of Two-Phase Flows in Structured Packing	28
3.3.1	Porous Media Approach	28
3.3.2	Pore Resolved Simulations	30
CHAPTER 4	MATHEMATICAL FORMULATION OF TWO-PHASE FLOWS	32
4.1	General	32
4.2	Two-Fluid Formulation	33
4.3	Single Fluid Formulation	35
4.4	Front Tracking Algorithm	37
4.5	Level-Set Method	39
4.6	Volume-of-Fluid Method	42
4.7	Hybrid Methods	46
4.8	Surface Tension and Wall Adhesion Modeling	47
4.8.1	Surface Tension	47
4.8.2	Wall Adhesion Modeling	49
4.9	Interface Reconstruction Algorithms	50
CHAPTER 5	MASS TRANSFER MODELING	52
5.1	Mass Transfer Model in Multiphase Flows	52
5.2	Mass Transfer Model & Interfacial Area	54
5.2.1	Mass Transfer Model for Desalination	54
5.2.1.1	Modeling & Assumptions	54
5.2.1.2	Discretization of Fick's Law	55
5.2.2	Volume Enforcement Algorithm	56
5.2.2.1	Initial Bracketing	57
5.2.2.2	Volume Calculation & Interfacial Area	59
5.3	ANSYS Fluent Solver and Implementation of User-Defined-Functions	61
5.3.1	Governing Equations & Source Terms	61
5.3.2	Fluent Discretization Method	62
5.3.3	Reconstruction of Cell Gradient	64
5.3.4	Temporal Discretization	64
5.3.5	Spatial Discretization	65
5.3.6	Pressure-Velocity Coupling	66
5.3.7	Implementation of User Defined Functions	67
CHAPTER 6	VALIDATION OF THE NUMERICAL FRAMEWORK	69
6.1	Accuracy of Interfacial Area Computation: Single Static Droplet	69
6.2	Validation of Mass Transfer Modeling	71
6.2.1	Flow Over a Stationary Body of Fluid	72
6.2.1.1	CFD Domain Generation	72
6.2.1.2	Analytical Domain	73
6.2.1.3	CFD-Analytical Linkage	75
6.2.1.4	Results & Discussion	75
6.3	Conclusion on Mesh Topologies	77

CHAPTER 7	APPLICATION TO A COUNTER-CURRENT PACKED BED	79
7.1	Computational Domain Generation	79
7.1.1	Geometry	79
7.1.2	Domain Setup	80
7.1.3	Mesh Generation	82
7.1.4	Mesh Convergence	84
7.1.5	Boundary & Operating Conditions	86
	7.1.5.1 Boundary Conditions	86
	7.1.5.2 Operating Conditions	87
7.2	Water Inlet Boundary Conditions	89
7.2.1	Results & Discussion	92
	7.2.1.1 Pressure Drop & Liquid Hold-Up	92
	7.2.1.2 Heat & Mass Transfer	97
7.3	Air Inlet Boundary Conditions	104
7.3.1	Results & Discussion	106
	7.3.1.1 Pressure Drop & Liquid Hold-Up	106
	7.3.1.2 Heat & Mass Transfer	106
7.4	Packing Geometry Design Improvements	109
CHAPTER 8	MODELING OF THE BLOCKAGE PHENOMENON	111
8.1	General	111
8.2	Governing Equations	112
8.3	Problem Setup & Boundary Conditions	113
8.4	Mesh Generation & Independence Study	116
8.5	Study in the Column Regime	118
	8.5.1 Validation of Numerical Results	118
	8.5.2 Influence of the Contact Angle & Geometry	119
	8.5.3 Summary of Column Regime	123
8.6	Study in Droplet Regime for Packed Columns	123
	8.6.1 Validation of Numerical Results	125
	8.6.1.1 Experimental Setup	125
	8.6.1.2 Procedure & Results	127
	8.6.2 Result & Discussion	128
	8.6.2.1 Influence of d_l	129
	8.6.2.2 Influence of $u_{l,in}$	132
	8.6.2.3 Influence of Re_δ	133
	8.6.3 Conclusion on Drop Regime	135
8.7	Conclusion on the Blockage Phenomenon	135
CHAPTER 9	PACKED COLUMN GEOMETRY IMPROVEMENTS	137
9.1	General Introduction	137
9.2	Geometry Iterations	139
9.3	Conclusion of Corrugation Geometry Design	142
CHAPTER 10	CONCLUSION AND PERSPECTIVES	144

APPENDICES	148
APPENDIX A WATER SATURATION PRESSURE	149
APPENDIX B SOLUTION OF EQUATION (6.5)	150
APPENDIX C DESCRIPTION OF PARABOLIC CYLINDER FUNCTIONS $U(a, \eta)$ AND $V(a, \eta)$	153
BIBLIOGRAPHY	154

LIST OF TABLES

Table 5.1: Ordained list of vertexes by signed distance from the interface	58
Table 6.1: Mesh metrics and results	71
Table 6.2: Boundary conditions applied in the cartesian numerical model	73
Table 6.3: Domain dimensions and fluid properties	75
Table 6.4: Averaged quantitative values for PLIC-1 and PLIC-2	78
Table 7.1: Domain dimensions	82
Table 7.2: Sphere test results with $\Delta x = 0.3 \text{ mm}$	85
Table 7.3: Linear dry pressure drop for the different mesh cell size and various gas mass flux	85
Table 7.4: Type and values of boundary conditions	87
Table 7.5: Water properties	88
Table 7.6: Individual properties of humid air components	88
Table 7.7: Water inlet boundary properties	92
Table 7.8: Water velocity	97
Table 7.9: Air inlet flow conditions	105
Table 8.1: Blockage domain dimensions	114
Table 8.2: Refinements level for each block	116
Table 8.3: Flow conditions for validation in the column regime	119
Table 8.4: Flow conditions for the drop regime	129

LIST OF FIGURES

Figure 2.1: Reverse Osmosis Principle (Qasim et al. (2019))	7
Figure 2.2: Electrodialysis Principle (Kalogirou (2005))	8
Figure 2.3: Schematic of a conventional MED plant with 6 effects from Christ et al. (2014) .	9
Figure 2.4: Example of Solar Pond Facility (Saleh et al. (2011))	11
Figure 2.5: Schematic of VC desalination unit (Al-Karaghoulis & Kazmerski (2013))	12
Figure 2.6: Schematic of solar powered MSF plant (Sharon & Reddy (2015))	13
Figure 2.7: Schematic of Natural Vacuum Desalination Unit (Maroo & Goswami (2009)) . .	14
Figure 2.8: Diagram of freezing desalination principle (Rahman et al. (2006))	15
Figure 2.9: Schematic of an adsorption desalination unit (Wu et al. (2010))	17
Figure 2.10: Single stage solar still schematic (Sharon & Reddy (2015))	19
Figure 2.11: Working principle of HDH desalination unit (Al-Hallaj et al. (1998))	20
Figure 3.1: Flow regimes in packed columns (Gunjal et al. (2005))	25
Figure 4.1: Front and background grids for the computation of multiphase flows (Tryg- gvason et al. (2001))	38
Figure 4.2: Representation in 2D of the level-set function $\phi(\mathbf{x}, t)$ (Lakehal et al. (2002)) . . .	40
Figure 4.3: Smoothed Heaviside Function	41
Figure 4.4: Volume fraction field: (a) ideal sharp interface (b) smeared interface	44
Figure 4.5: Interface Shape with different reconstruction schemes: (a) original fluid dis- tribution (b) SLIC (x-sweep) (Noh & Woodward (1976)) (c) SLIC (y-sweep) (Noh & Woodward (1976)) (d) Donor-Acceptor (Hirt & Nichols (1981)) (e) PLIC (Youngs (1982)) (f) FLAIR (Ashgriz & Poo (1991))	45
Figure 4.6: Wetting phenomenon	49
Figure 5.1: Interfacial cell	56

Figure 5.2: Interfacial cells after initial calculation for bracketing	58
Figure 5.3: Truncated polyhedron with intersection points	60
Figure 5.4: Spatial discretization with QUICK scheme	65
Figure 6.1: Mesh with different cell topologies	70
Figure 6.2: Contour of the initial liquid volume fraction for the various mesh topologies . . .	70
Figure 6.3: 3-D cartesian numerical domain	72
Figure 6.4: 2-D projection of the 3-D cartesian numerical domain	74
Figure 6.5: Test case results	76
Figure 7.1: Lantec HD-PAC geometry used in the CFD study	80
Figure 7.2: Domain surfaces definition	81
Figure 7.3: Domain fluids inlets	82
Figure 7.4: Meshing process (OpenFOAM Foundation (2020))	83
Figure 7.5: Partial enhanced view of the resulting mesh	83
Figure 7.6: Detail view of the two meshes employed around an individual packing geometrical feature	85
Figure 7.7: Contour of liquid volume fraction at water inlet for different spray densities . . .	90
Figure 7.8: Water inlet time modulation	91
Figure 7.9: Spatially and temporally averaged gas static pressure as function of the vertical position	93
Figure 7.10: Water volume fraction contours at $t = 3.5s$	94
Figure 7.11: Liquid hold-up in the test section	95
Figure 7.12: Liquid volume fraction along the z -axis	96
Figure 7.13: Time and spatial average contour of liquid volume fraction	96
Figure 7.14: Water velocity	97

Figure 7.15: Phase temperature profiles	98
Figure 7.16: Contour of liquid volume fraction in the bottom section at t=3.5s. The horizontal and vertical axes are x and z	99
Figure 7.17: Transient response of water vapor mass fraction and interfacial area	100
Figure 7.18: Mass fraction, Mass transfer rate, and concentration gradient profiles	101
Figure 7.19: Normalized water vapor mass fraction contour at t=4s	102
Figure 7.20: Time and spatial average contour of water vapor mass fraction	103
Figure 7.21: Schematic of modification to obtain homogeneous air inlet	105
Figure 7.22: Static pressure profile and transient response of liquid hold-up	106
Figure 7.23: Transient response of water vapor mass fraction and interfacial area	107
Figure 7.24: Transient response of water vapor mass fraction and interfacial area	108
Figure 7.25: Mass fraction, mass transfer rate, and concentration gradient profiles	108
Figure 7.26: Liquid volume fraction contour showing the blockage phenomenon	110
Figure 7.27: Normalized contour of velocity at t=3.5s	110
Figure 8.1: 2D schematic of the setup	114
Figure 8.2: 3D schematic of the numerical domain with associated surfaces	115
Figure 8.3: Mesh block definition	117
Figure 8.4: Mesh convergence study with $u_{l_{in}} = 0.6$ m/s and $u_{g_{in}} = 0.408$ m/s	118
Figure 8.5: Spanwise averaged film thickness for various angular position in comparison with analytical solution and experimental correlation from Ji et al. (2017)	119
Figure 8.6: Specific water coverage for the three geometries studied as function of the contact angle	121
Figure 8.7: 3D contour of the free surface for the different contact angle at various flow time	122
Figure 8.8: Droplet generated by adjusting the injection time	124

Figure 8.9: Schematic of high speed camera experiment for droplet validation	125
Figure 8.10: Assembly zoom of drop experiment	126
Figure 8.11: Illumination setup	126
Figure 8.12: CFD and high-speed camera comparison	128
Figure 8.13: 3D contour of the free surface for the different drop diameters at various flow time	130
Figure 8.14: Transient specific coverage for each geometry as a function of the drop diameter	131
Figure 8.15: 3D contour of the free surface for the different $u_{l_{in}}$ at various flow time	132
Figure 8.16: Transient specific coverage for each geometry as a function of $u_{l_{in}}$	133
Figure 8.17: 3D contour of the free surface for different Re_{δ} at various flow time	134
Figure 8.18: Transient specific coverage for each geometry as a function of Re_{δ}	134
Figure 9.1: Numerical and experimental visualization of the free surface on diamond geometry	138
Figure 9.2: First iteration results	139
Figure 9.3: Second iteration results	140
Figure 9.4: Third iteration results	141
Figure 9.5: Fourth iteration results	141

KEY TO ABBREVIATIONS

AD Adsorption Desalination

AMR Adaptive Mesh Refinement

BWRO Brackish Water Reverso Osmosis

CAOW Closed Air Open Water

CFD Computational Fluid Dynamic

CLSVOF Couple Level Set Volume Of Fluid

CSF Continuum Surface Force

CSS Continuum Surface Stress

CST Continuum Surface Tension

CWOA Closed Water Open Air

DNS Direct Numerical Simulation

DPM Discrete Particle Model

ED Electro-Dialysis

EDR Energy Recovery Device

ELVIRA Efficient Least squares Volume of fluid Interface Reconstruction

ENO Essentially Non Oscillatory

FD Freeze Desalination

FDM Fusion Deposition Method

FLAIR Flux Line segment model for Advection and Interface Reconstruction.

FT Front Tracking

FVM Finite Volume Method

GFM Ghost Fluid Method

GOR Gained Output Ratio

HDH Humidification-Dehumidification

HF Height Function

HPC High Performance Computer
LCZ Lower Convective Zone
LES Large Eddy Simulation
LS Level-Set
LVIRA Least squares Volume of fluid Interface Reconstruction
MAC Marker And Cell
MD Membrane Distillation
MED Multi Effect Distillation
MRI Magnetic Resonance Imaging
MSF Multi Stage Flash
MSSP Membrane Stratified Solar Pond
MVC Mechanical Vapor Compression
NCZ Non-Convective Zone
NVD Natural Vacuum Desalination
PBR Packed Bed Reactor
PLIC Piecewise Linear Interface Construction
PRESTO PREssure STaggering Option
PROST Parabolic Reconstruction Of Surface Tension
PSP Partitioned Solar Pond
QUICK Quadratic Upstream Interpolation with Convective Kinematics
REU Representative Elementary Unit
RO Reverse Osmosis
SGSP Salt Gradient Solar Pond
SIMPLE Semi-Implicit Method for Pressure Linked Equation
SIMPLEC Semi-Implicit Method for Pressure Linked Equation Consistent
SLIC Simple Line Interface Calculation
SSP Stratified Solar Pond

STL STereoLitography
STSP Saturated Solar Pond
SWRO Sea Water Reverse Osmosis
TVC Thermal Vapor Compression
UCZ Upper Convective Zone
UDF User Defined Function
VC Vapor Compression
VOF Volume Of Fluid
VSSP Viscosity Stabilized Solar Pond
WENO Weighted Essentially Non Oscillatory

CHAPTER 1

INTRODUCTION

1.1 Context

Fresh water is an essential resource to most of living organisms on Earth. 70% of the planet is covered by water, and the vast majority of this water is contained in oceans and is saline. Only 2.5% is fresh water and is suitable for human consumption and crop growth. In addition, the discrepancies in the repartition across the globe makes the access to potable water one of the most challenging problem of the century. A technology solution to this issue is desalination of saline water that is readily available in the oceans and seas. The depletion of fossil fuel resources coupled with the climatic change creates a need to perform water desalination in an environmentally benign and sustainable fashion.

With that in mind, desalination plants across the world use a wide range of technologies depending the local resources, the population density, as well as the infrastructures already in place. The opportunity to drive those systems using solar energy or waste heat from already existing power plants is of great interest. The cost of those resources pushes both towards an efficient design as well as an optimal control for efficient operation.

The performances of solar desalination plants are a combinations of multiple factors. Each technology having its own strengths and weaknesses, and a variety of elements have to be taken into account to recommend one technology over another. The efficiency is without a doubt, a key factor. The economic viability is of first importance. Both capital, operating and maintenance costs have to be taken into account in the decision making. Nonetheless, all the systems are aiming at producing fresh water out of saline or brackish water and performance at the system scale can be measured by comparing the energy input with the fresh water production rate for the given environment.

In this context, two approaches can be taken with both their advantages and inconveniences. On

the one hand, large scale plants with a fresh water production greater than ten thousand meter cube per day with a low water specific energy consumption is one approach, these are usually expensive to build and maintain along with complex operation. On the other hand, small scale production systems are cheaper, easy to operate, and require little maintenance but can only produce few meters cubed per day, usually with a higher specific energy consumption. Though their simplicity allows them to be suitable for decentralized water production, which removes the need to safely distribute the fresh water to a large population.

In this context, the humidification-dehumidification (HDH) desalination systems is a promising technology that is suitable for decentralized production using locally available water. The humidification-dehumidification process is based on the ability of a non-condensable gas to carry a substantial amount of water vapor, which increases with temperature. Currently available macro scale modeling is able to predict the performances at the scale of the system, but it lacks information on the physics that is taking place at the local small scale such as evaporation, condensation, momentum exchange among others. These phenomena find their origin at the liquid-vapor interface and makes experimental studies particularly challenging if not impossible and limits our understanding and improvements in performances.

Over the past 20 years, computational fluid dynamics (CFD) as become a very powerful tool to improve our understanding of fluid based system. The constantly increasing computing power available has allowed scientists to solve more and more complex problems in all domains involving fluid mechanics in both single phase and multiphase flows. This latter application is computationally expensive; it is only over the last decade that the interest in multiphase computational fluid dynamics for system modeling has really captured a growing interest.

A typical solar HDH system involves numerous components such as solar collectors, heat exchangers, pumps and air blower. The focus of this work is to investigate using CFD the critical component that is the evaporator for which the current knowledge is extremely limited. Developing and utilizing the necessary CFD framework will allow a much deeper understanding of the phases interaction taking place in the evaporator and the way to enhance their performances.

1.2 Objectives

This work aims at studying the momentum, heat and mass transport phenomena occurring in the evaporator using computational fluid dynamics to understand and enhance their performances. Using CFD, the accomplishment of this goal is divided into three main objectives. First, it is necessary to develop the computational framework that enables the study of inter-phase mass transfer in a numerical environment. Secondly, the validation of this framework against reliable data is key before applying the model to a larger system such as an evaporator. Finally, the application of the framework to a typical HDH evaporator configuration under various conditions to observe the impact on the performances while observing and understanding the complex interaction of phenomena taking place.

1.3 Manuscript Organization

This manuscript is divided in three identifiable sections. The first three sections present the state of the art and literature reviews on both desalination technologies, packed columns as well as the numerical methods for multiphase flows. The second section details the development and validation of the framework accomplished in this work. Finally, the third part is dedicated to the application and study on a real evaporator.

- Chapter 2 reviews the state of the art in solar desalination technologies.
- Chapter 3 introduces a literature review of packed column modeling using both experimental and numerical tools.
- Chapter 4 is a review of the tools available to model multiphase flows using computational fluid dynamic and sets the mathematical framework necessary.
- Chapter 5 is a brief review of the available mass transfer model available in the literature and then details the method introduced in this work to model the diffusive mass transfer taking

place in the evaporator. Fluent solver settings are also exposed and the implementation of the added source terms is discussed.

- Chapter 6 is assessing the accuracy of the model and the algorithm implemented by comparing the results from CFD against developed analytical solutions.
- Chapter 7 is applying the previously developed method to a counter-current evaporator with a particular emphasize on the domain and mesh generation. The sensitivity to operating conditions and boundary conditions is studied and discussed.
- Chapter 8 is taking on the modeling of the blockage phenomenon to understand the parameters triggering this instability.
- Chapter 9 is giving guidelines in the design of structured packing to enhance performances and scalability along with a first attempt in designing an optimal geometry.

CHAPTER 2

SOLAR DESALINATION TECHNOLOGIES

2.1 General

If this work focuses on solar desalination, which by essence is renewable, the early stages of desalination used fossil fuel in oil rich countries of the Middle East (Kalogirou (2005)). Gude et al. (2010) estimated that driving desalination plants using a conventional fossil fuel such as oil would require 1.42 million tons of oil per day. Aside from the evident costs, the emissions of greenhouse gases (156 tons/d of CO_2) resulting from the oil combustion are unsustainable in the long term. In 2020, ten years later, the increased world population brings that value to 1.63 million tons of oil per day. The need of driving the desalination process using renewable energies has been extensively and regularly treated since the early 2000s for a wide variety of systems (Kalogirou (2005), Sharon & Reddy (2015), Gude (2016), M. & Yadav (2017)). At this period in time, the worldwide desalination capacity was 23 millions m^3 /day. In 2019, Jones et al. (2019) reports a worldwide desalination capacity of 95 millions m^3 /day across 15906 operational plants with multiple technologies employed. This section offers an overview of the technologies currently available and installed across the world.

2.2 Indirect Solar Desalination Technologies

2.2.1 General

The first type of solar desalination process are the so called *indirect processes* in which two sub-categories coexist. The membrane processes, and the non-membrane processes. Indirect systems represent the majority of large plants distribution and consist in the coupling of two sub-systems, solar collectors and a desalination unit. The denomination *indirect* comes from the use of the solar collectors utilized to harvest the solar energy. They can be concentrated or non-concentrated

thermal solar collectors such as flat plates, evacuated tube among others, or simply photo-voltaic panels generating electricity to power the plant. An extensive review of these solar collectors is provided by Kalogirou (2004).

2.2.2 Membrane Processes

2.2.2.1 Reverse Osmosis

The most common desalination technology is the Reverse Osmosis (RO) process who represents more than 50% of the plants installed and 69% of the worldwide production capacity (Ali et al. (2011), Jones et al. (2019)). Among the RO systems, two sub-categories coexist depending upon the water salinity they aim at treating. Brackish water RO plants (BWRO), handle salinity ranging from 500 ppm to 10000 ppm and sea water RO plants (SWRO) handle salinity up 30000 ppm. The working principle of an RO system is based on the natural osmosis process in which the water molecules from a low salinity solution moves toward a high salinity solution across a semi-permeable membrane as shown in Fig. 2.1a. The process naturally stops when the system reaches a chemical equilibrium as shown by Fig. 2.1b. Applying a larger pressure than the osmotic pressure on the high concentration side reverses the natural osmosis, and the water molecules flows toward the low concentration side, thus reducing the salinity of the already low concentration side, as depicted by Fig. 2.1c. The main interest of the RO technology is the ease of adaption to the local environment and the plant size adjustment to meet long term requirements, that are likely to arise from a growing population (Alkaisi et al. (2017)). According to Gude et al. (2010), RO plants specific energy consumption ranges between 5-9 kWh/m³ mainly depending if the plant is equipped with Energy Recovery Device (EDR) for the brine feed. As a result, RO plants specific cost is among the lowest ranging between 0.2 and 1.2 USD per meters cubed depending the plant type (Ghaffour et al. (2013)).

Even if the RO technology is economically viable as shown by its worldwide implementation, it also counts numerous weaknesses. The most critical is the failure of the semi-permeable

membranes used in the plants. Over time, due to the water impurities, the permeation flux decays, which increases the pressure necessary to reverse the flow, and ultimately, leads to the fouling phenomenon. As described by Jiang et al. (2017), the fouling phenomenon can be of multiple origins: biofouling, organic, inorganic or colloidal. Unfortunately, it is impossible to completely suppress this phenomenon but it can be monitored and controlled to avoid the cascade of issues following; such as increased feed pressure, or lower mass fluxes, that inevitably lead to system downtime.

The main challenge in the modeling of RO systems is the membrane modeling which is key into predict and improve the plants efficiency and reliability (Jain & Gupta (2004)). The literature is divided into two model categories. First, the phenomenological models, that are based on the principle of irreversible thermodynamic and assume a quasi-equilibrium of the membrane (Kedem & Katchalsky (1958), Spiegler & Kedem (1966)). On the one hand, they have the advantage of being able to predict the membrane performances at macro-scale as a function of experimentally measurable quantities such as; water mass flow rate, salinity content and temperature. On the other hand, the membrane treatment as a *black box* limits the performances enhancement since the transport phenomena remain unknown. The other type of membrane models, the mechanistic models, correlates the performances with the solutions properties as well as both physical and chemical properties of the membrane. An extensive review of the membrane models available in the literature is proposed by Wang et al. (2014).

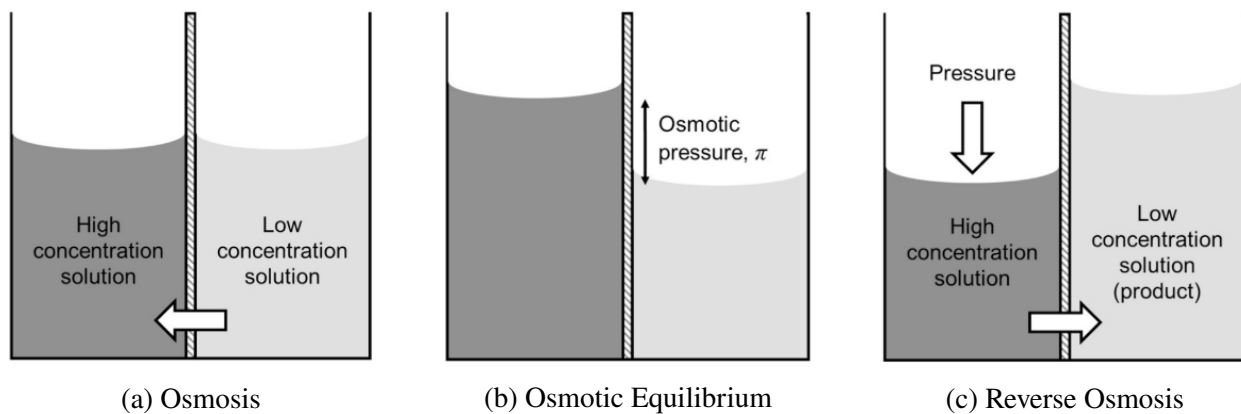


Figure 2.1: Reverse Osmosis Principle (Qasim et al. (2019))

2.2.2.2 Electrodialysis

Originally presented by Maigrot and Sabates in 1890, the industrial exploitation of Electrodialysis (ED) only started in 1970 and represents today 4% of the total worldwide desalination capacity (Al-Amshawee et al. (2020)). The principle, as shown in Fig. 2.2, consists in an ion transfer through membranes from the saline feed water compartment to the fresh water compartment. The system is driven by applying a DC current between the anode and cathode, which forces the positive sodium ions (Na^+) toward the cathode and the negative chlorine ions (Cl^-) toward the anode. Therefore, with the use of anions and cations permeable membranes, the water in the central compartment loses its salinity. This technology scales by stacking multiple cells in parallel (AlMadani (2003)).

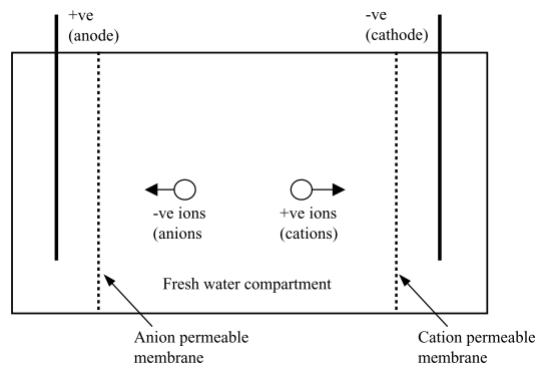


Figure 2.2: Electrodialysis Principle (Kalogirou (2005))

The main advantage of ED is a specific energy consumption between 0.6 and 1 kWh/m^3 , which is lower than the equivalent RO system (Ali et al. (2011)). Nonetheless, the ED process comes with major weaknesses. First, ED only allows a water salinity up to 12000 ppm , which is three times inferior to the average seawater salinity (35000 ppm). Secondly, ED does not remove bacterial contaminants from the feed water, which does not make the water potable. Thirdly, similarly to RO systems, a periodic maintenance of the membranes is necessary. Finally, the capital cost of an ED system is usually superior to its RO equivalent, which can be absorbed overtime due the lower specific energy consumption and membranes longer lifetime (7 to 10 years depending water quality). The techno-economic analysis comparing RO and ED systems accomplished by Abraham & Luthra (2011) showed the ED technology to be more suitable for local water production from

brackish water rather than seawater purification.

2.2.3 Non-Membrane Processes

Non-membrane desalination systems rely on the thermal processes of evaporation and condensation to produce fresh water. Generally, a warm water feed is distilled in an evaporator and further condensed in a condenser. Their main advantage over membrane processes is the high quality of the water obtained (Roberts et al. (2010)). These systems are also less sensitive to the water quality, which make them suitable for high salinity seawater.

2.2.3.1 Multi Effect Distillation

Multi Effect Distillation (MED) plants are in principle constituted of one or multiple vessels usually called effects. These effects are maintained at a gradually decreasing level of pressure, thus increasing the water saturation pressure driving the evaporation process. In the first effect, the feed saline water is sprayed from the top onto a bundle of tubes in which by means of solar collectors, heated water circulates. The vapor generated in the first effect is further injected into the second effect tube bundle where it condenses and the process repeats until the last effect where the cold sea water condenses the remaining water vapor as shown by Fig. 2.3. MED plants represent 6% of the worldwide production distributed among 900 plants (Jones et al. (2019)).

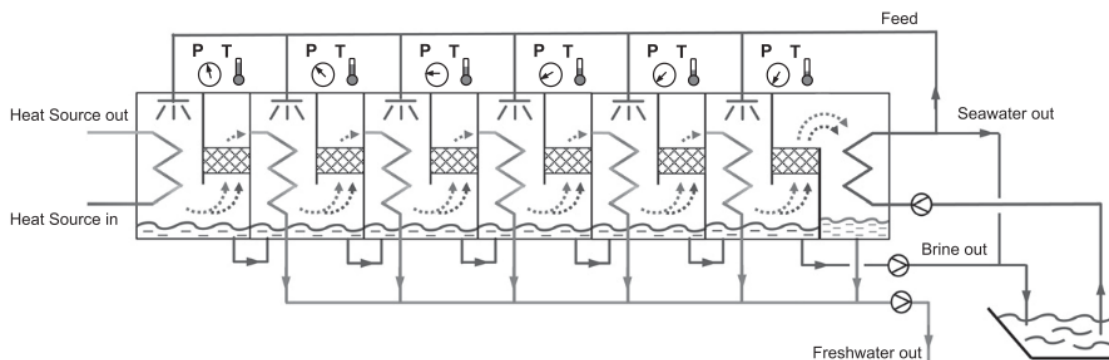


Figure 2.3: Schematic of a conventional MED plant with 6 effects from Christ et al. (2014)

Similarly to most of the non-membrane indirect processes, MED offers an excellent flexibility

regarding the quantity of energy required to operate the system. Therefore, MED systems are suitable for operation using renewable energy supply (Wang et al. (2011)). Christ et al. (2014) shown that with a proper optimization and design, MED plants can efficiently operates using low-grade heat available in a large amount of industrial plants. The downside of using low-grade heat is the that efficiency decays with temperature (Zhao et al. (2011)). The gain output ratio (GOR) reported by various authors is highly dependent on the addition of other components such as thermo-vapor compressor or a recuperative feed heater. Using a conventional MED laboratory scale facility, Joo & Kwak (2013) obtained a GOR of 2.0, Alasfour et al. (2005) obtained a GOR ranging between 8.0 and 10.5 using an MED-TVC configuration with feed heaters. As a result, the specific energy consumption is also extremely variable. Alkaisi et al. (2017) reports a specific energy consumption ranging between 6.5 and 11 kWh/m³ for a conventional MED and ranging between 11 and 28 kWh/m³ for MED-TVC plants. A typical MED industrial plant usually employs a TVC to limit the initial steam requirements (hua Qi et al. (2014)).

As an MED plants usually involves a large quantity of individual components, evaporator, condenser, pumps, heat exchangers among others, the modeling is usually based on an energy balance of the entire system (Alarcón-Padilla & García-Rodríguez (2007), Zhao et al. (2011), Wang et al. (2011), de la Calle et al. (2015)). Similarly to phenomenological models for membranes, the shortcoming of all those studies is the use of empirical correlations to calculate the heat and mass transfer coefficients in the evaporator and condenser. de la Calle et al. (2015) improved by calculating the heat and mass transfer using knowledge acquired from falling film theory on tube bundles. Mabrouk et al. (2015) added the influence of the tube bundle arrangement and outlined the influence of the spray pattern on the performances of the system.

2.2.3.2 Solar Pond

Solar pond is the simplest desalination system and relies on the principle of water stratification with heat supplied by solar radiation to obtain fresh water. Several variations of that technology exist; salt gradient solar pond (SGSP), partitioned solar pond (PSP), viscosity stabilized solar pond

(VSSP), membrane stratified solar pond (MSSP) (Hull (1980)), saturated solar pond (STSP), and shallow solar pond (SSP).

As shown in Fig. 2.4, a solar pond is divided into three sections: the upper convective zone (UCZ), the non-convective zone (NCZ), and the lower convective zone (LCZ) at the bottom. The working principle between each technology remains similar and consist in having warmer water in the LCZ than the UCZ that is compensated by the salinity. The main differences between each technology is the way to prevent the arising convective currents created by the density difference as described by El-Sebaili et al. (2011). Even if the solar pond is rarely used as a standalone desalination system, it is often used as a thermal energy storage for other processes such as Multi-Stage Flash (MSF) to obtain a warmer saline feed water (Lu et al. (2001), Saleh et al. (2011)). When coupled with an MSF plant the reported production ranges from 2.35 to 7.2 m^3/d depending the season (Ali et al. (2011)).

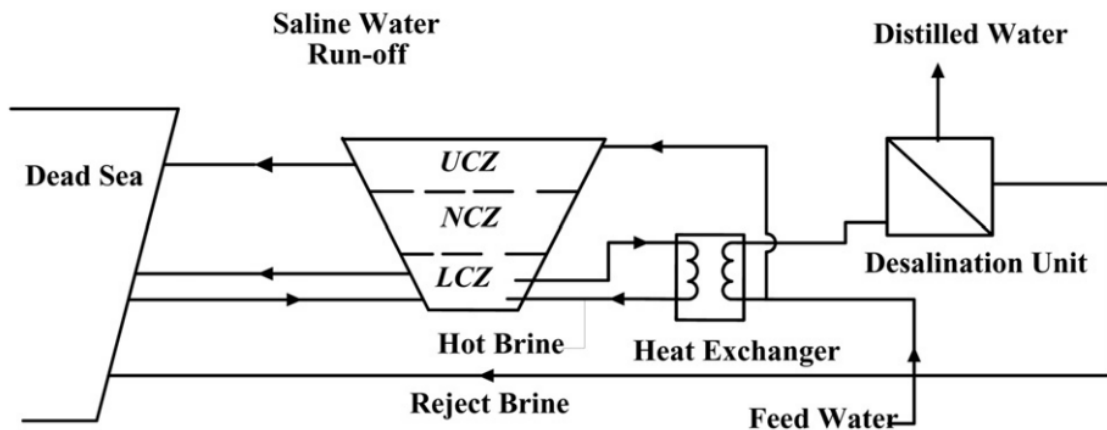


Figure 2.4: Example of Solar Pond Facility (Saleh et al. (2011))

The modeling of solar pond usually consist in a direct application of the conservation equations in one dimension (Ouni et al. (1998)), two dimensions (Liu et al. (2015)) or three dimensions (Karakilcik et al. (2013)). Suárez et al. (2010) published a computational fluid dynamic (CFD) study modeling a trapezoidal solar pond, which took into account the secondary flows created by the natural convection occurring in the pond and showed the convective mixing to significantly affects the pond temperatures.

2.2.3.3 Vapor Compression

Vapor compression (VC) was first described by Aly (1984) as a promising technology for desalination. Two distinct sub-categories of VC plants coexist depending the type of compressor: mechanical vapor compression (MVC) or thermal vapor compression (TVC). In both cases, it consists in heating the saline water feed to produce vapor. The produced vapor is then thermally or mechanically compressed resulting in a pressure and temperature increase that is further used as a heat source. Figure 2.5 presents a single stage VC plant diagram. MVC plants are usually designed for a small to medium water production up to $3000\text{ m}^3/\text{day}$ and TVC plants capacity ranges from $10000\text{ m}^3/\text{day}$ to $30000\text{ m}^3/\text{day}$ (Al-Karaghoul & Kazmerski (2013)). The specific energy consumption reported in the literature are highly variable depending the plants. Sharaf et al. (2011) reported a specific consumption as low as $1.58\text{ kWh}/\text{m}^3$ in an hybrid MED-VC plant. Conventional MVC plants have specific energy consumption reported to be ranging between $6.1\text{ kWh}/\text{m}^3$ and $11.5\text{ kWh}/\text{m}^3$ (Alkhulaifi et al. (2019), Veza (1995), Zimmerman (1994), Matz & Zimmerman (1985)).

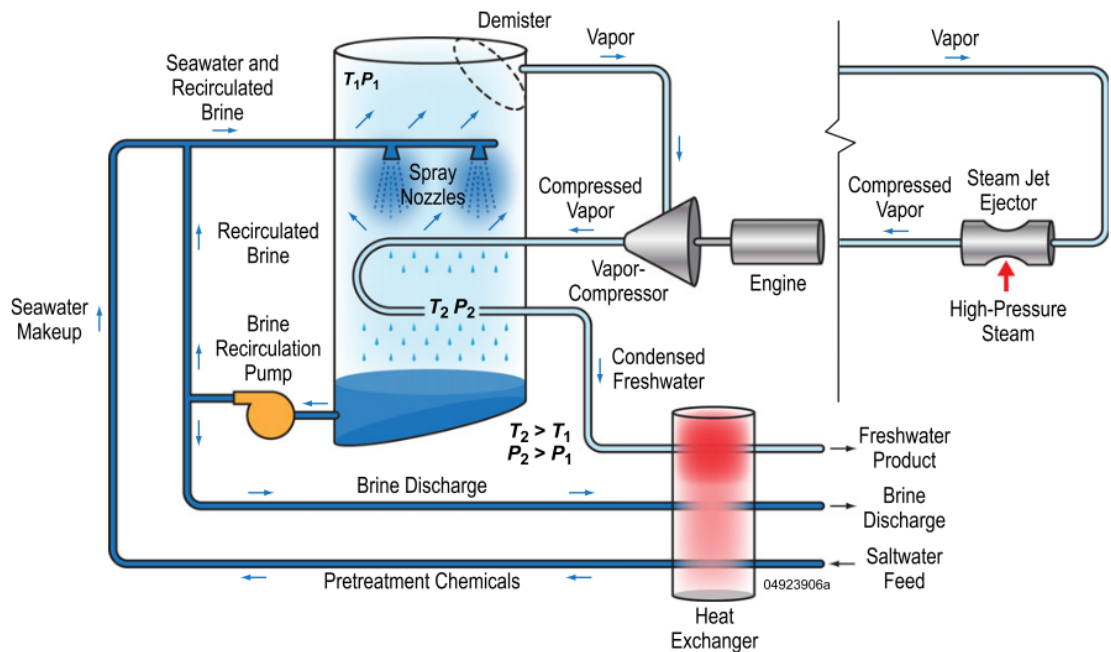


Figure 2.5: Schematic of VC desalination unit (Al-Karaghoul & Kazmerski (2013))

The high specific energy consumption of the VC technology is its main drawback, and is mainly due to the power input required for the compression. Nonetheless, the integration of the latter has

already proven to be successful to enhance other desalination process, such as MED and multi-stage flash plants (Sharaf et al. (2011)). With the additional use of batteries for energy storage, Zejli et al. (2011) successfully demonstrated the viability of an wind/PV powered MVC plant for up to 40 households depending the location.

2.2.3.4 Multi-Stage Flash

Multi-stage flash (MSF) represents 18% of the worldwide desalination capacity and 13% of the indirect solar plants (Ali et al. (2011), Jones et al. (2019)). The MSF working principle consists in heating the saline feed water using the hot brine and solar collectors passed the saturation temperature. The water feed is further flashed in multiple chambers, where using vacuum pumps, a low pressure is maintained as shown in Fig. 2.6. One of the first plant was implemented in the 80's in Mexico with a production capacity of $10 \text{ m}^3/d$ with an estimated specific consumption of 144 kWh/m^3 (Sharon & Reddy (2015), Manjarez & Galvan (1979)). Nowadays, modern MSF plants as proposed by Alsehli et al. (2017) can produce up to $2678 \text{ m}^3/d$ at 5 kWh/m^3 proving the high suitability of MSF for large production plants similarly to RO.

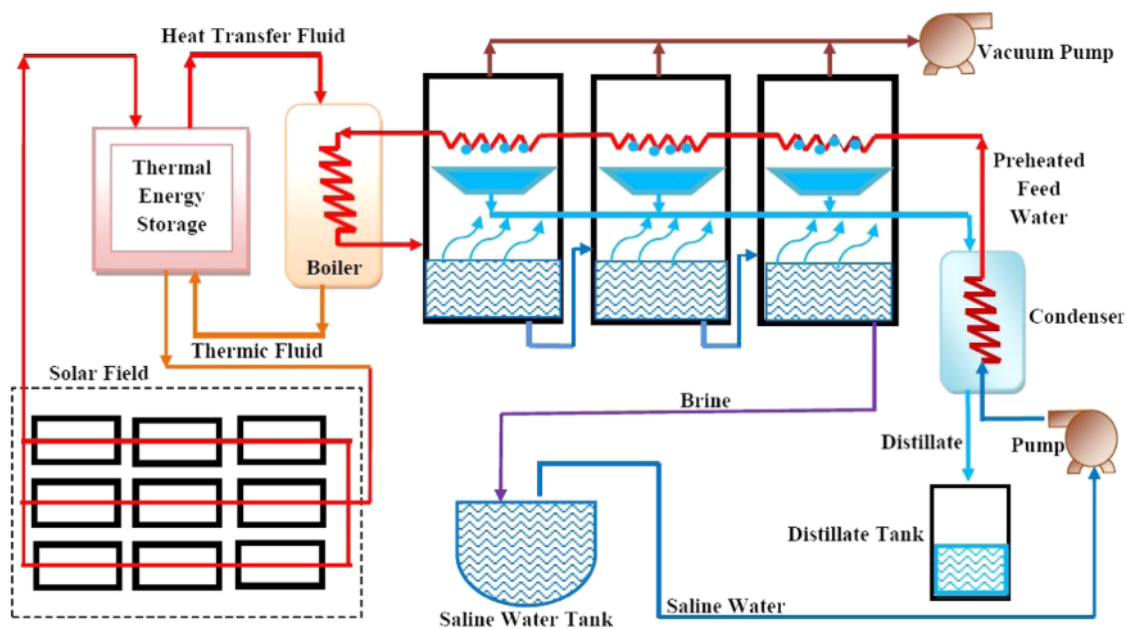


Figure 2.6: Schematic of solar powered MSF plant (Sharon & Reddy (2015))

The main advantage of the MSF process is its suitability for very high salinity contents (up to 70000 ppm) while yielding a potable water containing less than 10 ppm. MSF also has major drawbacks, such as the amount of thermal energy required in addition to the high capital cost. The complexity of the plants also increases maintenance costs. As a result, MSF desalination is not suitable for a small scale decentralized water production.

2.2.3.5 Natural Vacuum Desalination

Thermal desalination usually involves the production of water vapor by increasing the temperature of the saline feed water. Reducing the ambient pressure diminishes the water saturation temperature, thus diminishing the thermal energy requirement to generate water vapor. Using this principle, Tay et al. (1996), first used vacuum pumps to lower the system's pressure and low grade wasted heat to increase the saline water temperature. In a similar fashion, natural vacuum desalination (NVD), is to replace the vacuum pumps by a waterfall, which under gravity, naturally creates a vacuum in the chamber maintained above, as shown in Fig. 2.7. Al-Kharabsheh & Goswami (2003) managed to produce up to 6.5 kg/d.m^2 of evaporator. Maroo & Goswami (2009) coupled a similar facility to 1 m^2 of solar collectors and achieved a production rate of 85 kg/d.m^2 .

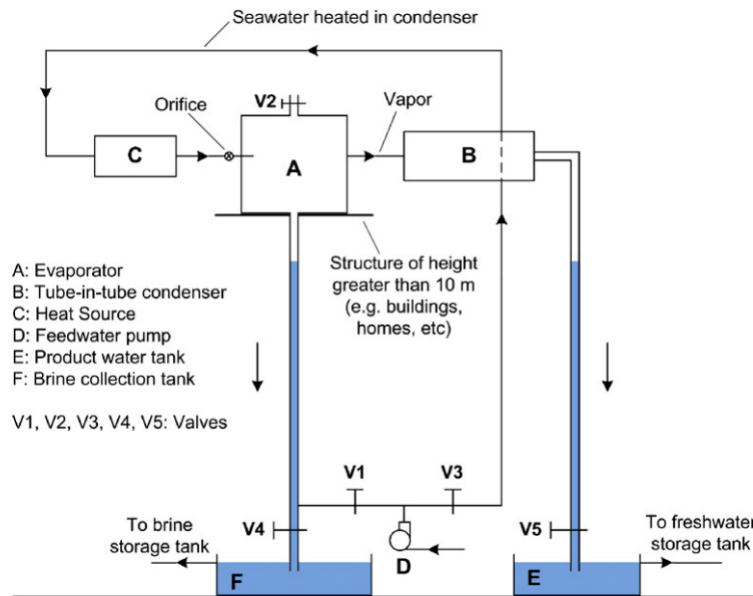


Figure 2.7: Schematic of Natural Vacuum Desalination Unit (Maroo & Goswami (2009))

Similar setup employed by Gude et al. (2012b) achieved 100 L/d using 15 m² of solar collectors and 1 m³ of thermal energy storage. In any case, the production rates yielded by vacuum desalination made it oriented toward decentralized production with small plants. Gude et al. (2012a) proved the viability of such small plants with a two stages system coupled with solar collectors. The specific energy consumption reported is as low as 1.42 kWh/m³ divided in 1500 MJ/m³ of thermal and 3.6 MJ/m³ of mechanical energy respectively. Such a low specific energy consumption resulted in a specific cost of 3 US\$/m³ using wasted heat. Lately, Abbaspour et al. (2019), using evacuated tube collectors, managed to reach 8.065 kg/d.m² with a capital cost of only US\$ 243 proving the suitability for an household production in remote areas. The modeling is very well known and relies on direct solution of governing equations with minimal empiricism (Midilli & Ayhan (2004)).

2.2.3.6 Freeze Desalination

Freeze desalination (FD), was first considered in the late 60s and the first facility driven with solar energy only arrived in the 90s in Saudi Arabia with a production capacity of 200 m³/d (Nebbia & Menozzi (1968), Zahed & Bashir (1990)). The process consists in freezing the saline water, which naturally separates water and ice crystals yielding iced fresh water at the surface as described by Fig 2.8.

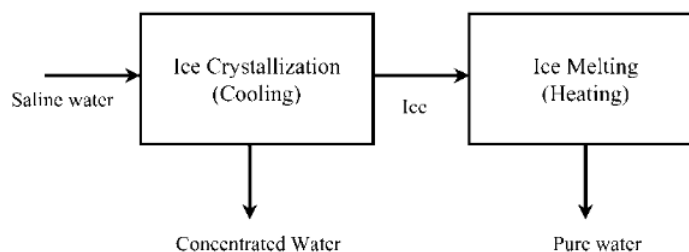


Figure 2.8: Diagram of freezing desalination principle (Rahman et al. (2006))

According to Ali et al. (2011), freezing desalination only represents 1% of the worldwide desalination capacity. It is sub-divided in three main technologies: direct contact, indirect contact, and vacuum method (Rane & Padiya (2011)). Direct contact freezing describes systems where the saline feed water is directly mixed with an immiscible refrigerant (Curran (1970)). With this

method, using n-butane as a refrigerant, Madani (1992) obtained a specific energy consumption of 13.78 kWh/m^3 . The main advantage of the direct contact method is the high interfacial area and low heat transfer resistance between water and refrigerant, but the brine separation necessary thereafter is challenging.

The indirect contact freezing desalination method uses a heat exchanger. Therefore, the saline water and refrigerant are not in contact with each other. The evident gain is the suppression of the water/refrigerant separation process, which is replaced by the need to scrape the ice formation on the heat exchanger (Habib & Farid (2006)). Nonetheless, coupling an indirect freezing process with a membrane distillation (MD) process, Wang & Chung (2012) obtained specific energy consumption of 4.633 kWh/m^3 . Finally, vacuum driven freeze desalination consists in lowering both temperature and pressure of the saline water past the triple point to have the coexistence of solid and gas phase that are then separated using various processes (Rahman et al. (2006)). The advantages of the FD process is that it can handle salinity content up to 40000 ppm while yielding an average fresh water quality with concentrations inferior to a 100 ppm (Youssef et al. (2014)). The specific cost reported by Qiblawey & Banat (2008) is as low as $0.34 \text{ US\$/m}^3$.

2.2.3.7 Adsorption Desalination

Adsorption desalination (AD) is an emerging technology resulting from the efforts to develop a purification method that is inherently designed for the low temperatures provided by wasted heat. In comparison with traditional thermal systems, AD provides two beneficial effects. In addition to yield high quality fresh water with a distillate containing less than 10 ppm, it also provide a cooling effect (Ng et al. (2013)).

The working cycle of a two bed adsorption desalination is divided into two processes. Initially, the evaporation - adsorption where at low temperatures and pressure, the water evaporates and is adsorbed by the silica gel packed bed in bed one as shown in Fig. 2.9. During that process, the heat released by the adsorption is transported by the cold water circulating in the bed. Once the bed reaches saturation, the desorption - condensation process starts. Valve number one closes and

valve number two opens while the water circulating in bed 1 is now hot water, thus triggering the silica gel bed regeneration (desorption) and releasing the water vapor into the condenser. The interest of having two beds lies with the ability to run the system continuously with each bed being alternatively driven. In other words one bed is adsorbing while the other is desorpting.

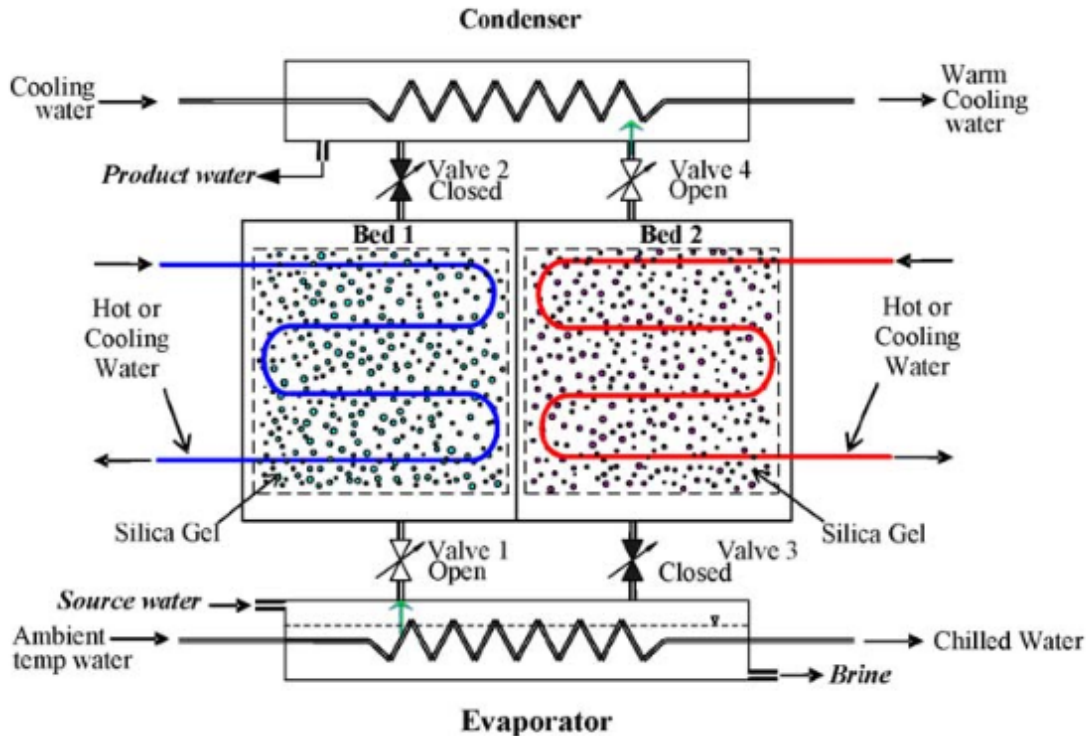


Figure 2.9: Schematic of an adsorption desalination unit (Wu et al. (2010))

In addition of having two beneficial effects and accepting water feed salinity up to 67000 ppm (Youssef et al. (2014)), another advantage of the adsorption process is the low maintenance costs because it does not include moving mechanical part. As the system operates at low temperatures and pressures, fouling is maintained to a minimum. Finally it is environmentally safe since the cleaning of the beds does not require any chemicals (Alsaman et al. (2016)). The specific energy consumption is extremely competitive in comparison with traditional plant using RO , MSF or MED technologies with values reported by various authors ranging between 1.38 and 1.5 kWh/m³ (Ng et al. (2008), Ng et al. (2013), Youssef et al. (2014)). As a consequence, the specific cost is as low as 0.2 US\$/m³. The early stages of adsorption desalination system modeling focused on the

thermodynamic cycles of the units (Zejli et al. (2004), Wang & Ng (2005), Wu et al. (2012)). The research transitioned to macro-scale analysis similarly to other technologies where the whole plant is taken under consideration (Thu et al. (2013)). In the recent years, the research interests moved toward the understanding of the adsorption process as well as the study of multiple adsorbent in order to improve the performances of the systems (Saha et al. (2016), Ali et al. (2018), Elsayed et al. (2020)).

2.3 Direct Solar Desalination Technologies

2.3.1 General

As opposed to indirect solar desalination, with direct systems, the energy coming from solar radiation is directly harvested by the desalination unit. These systems aim at a decentralized production using local brackish water. The production is three to four orders of magnitude smaller than industrial plants with only a few m^3/d . Those systems are usually simpler than indirect units and remove the need of highly trained workers for maintenance in addition to offer a low capital cost.

2.3.1.1 Solar Still

Desalination systems in their simplest and ancient form take the shape of solar still collectors, which is a small scale mimic of the natural hydrology cycle. As shown in Fig. 2.10, the saline water is injected at the bottom of the basin, where it evaporates using the heat radiated by the sun through a magnifying glass. The water vapor naturally rises in the chamber and condenses on the inclined glass. The droplets formed on the glass surface gravitate downward and drip into the collector.

The main energy input being solar, the design efforts to improve the performances of solar still desalination systems aim at maximizing radiation absorption. Hence, the bottom of the basin is usually covered with a black liner and authors use internal or external reflectors to augment the surface area and improve efficiency. Kabeel et al. (2015) and Omara et al. (2017) offer extensive reviews of the various techniques employed to improve the performances of solar still systems.

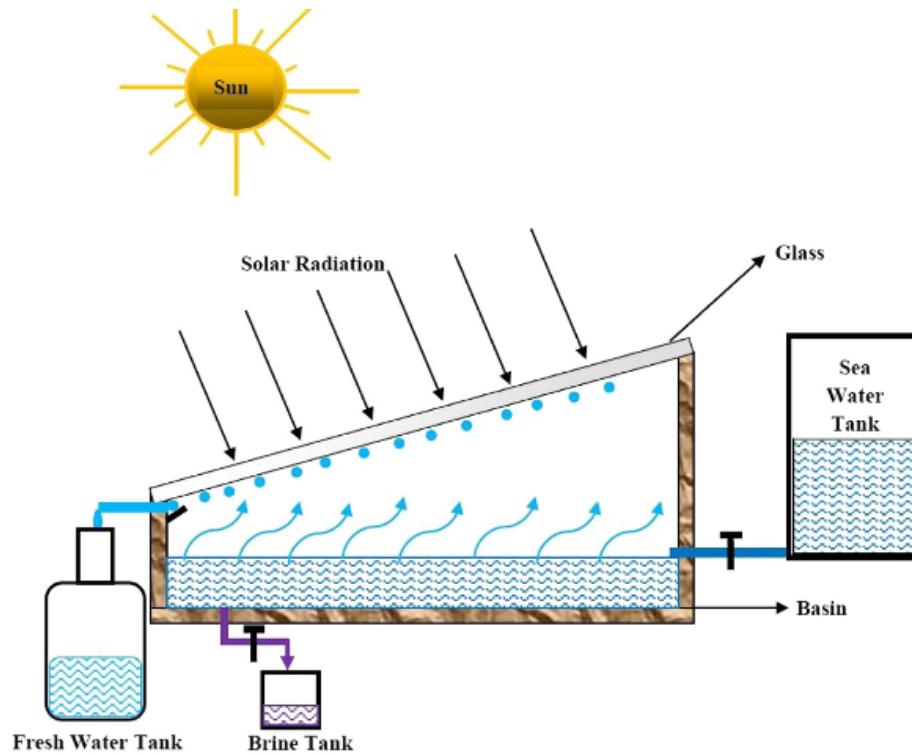


Figure 2.10: Single stage solar still schematic (Sharon & Reddy (2015))

Because of the low productivity, solar still technology is not employed in large scale plants, but is suitable for a small, decentralized, water production. Using external solar collectors, Srivastava & Agrawal (2013) and Tanaka & Nakatake (2005) reported a production between 80 and 40 $kg/m^2/day$ respectively, while conventional solar still systems yield daily fresh water production between 1.2 and 8 $kg/m^2/day$ (Omara et al. (2017)). The modeling of solar system is well covered in the literature and consists in a direct solution of the governing equations as a function of the main parameters; such as water height, materials emissivities, tilt angle among others (Manikandan et al. (2013)). The empiricism of these models is often in the correlations employed to calculate the convection coefficients needed to close the problem (Ahsan et al. (2013); Setoodeh et al. (2011)).

2.3.1.2 Humidification - Dehumidification

The working principle of Humidification-Dehumidification (HDH) is based on the ability of a carrier gas, usually air, to transport a certain amount of water vapor that exponentially increases

with temperature. Therefore, as shown in Fig. 2.11, the system consists in spraying warm saline water at the top of an evaporator while cool dry air is supplied at the bottom. At the contact of the warm saline water, the cool dry air heats up and pure water vapor is extracted, this is the humidification process. On the other side, in the condenser, the dehumidification process takes place where the cold fresh water is used to condense the hot humid air coming out the evaporator yielding pure fresh water and cold dry air at the bottom. Two main configurations of HDH desalination systems are available depending the fluid cycles (Narayan et al. (2010)).

- Closed Air Open Water (CAOW)
- Closed Water Open Air (CWOA)

In both cases, the systems can be air-heated or water-heated with natural or forced circulation. According to Müller-Holst et al. (1998), the most efficient configurations are water heated CAOW systems with a specific consumption ranging between 3 to 7 US\$/m³. The main features of HDH systems is their simplicity. Similarly to other thermal systems, they can handle brackish water with very high salinity with a very low maintenance requirements.

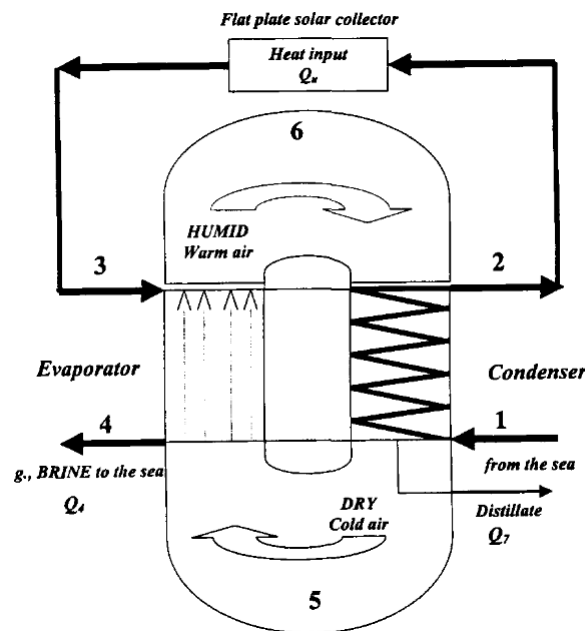


Figure 2.11: Working principle of HDH desalination unit (Al-Hallaj et al. (1998))

Alnaimat et al. (2021) offers an extensive review of the recent advances of HDH systems using solar energy. Nonetheless, an extensive amount of studies are available in the literature that aim at finding the optimal design and operating parameters for HDH desalination systems. Such studies usually observe the influence of mass flow rates and temperatures of the fluids in order to optimize water production and minimize the energy requirements. Other works include the coupling of HDH with other desalination technologies such as solar still or flash evaporation (Srithar & Rajaseenivasan (2018)). Focusing on conventional HDH systems, several innovations have been studied in the literature. Chafik (2003) and more recently Kang et al. (2014) used a multi-stage heating humidification cycle in order to improve the absolute humidity output, the latter achieved a production rate up to 72.6 kg/h and a GOR of 2.44.

Different design approaches consist in having a common heat transfer wall between the evaporator and condenser to enhance the energy recovery efficiency (Govindan et al. (2011)). Other solutions that globally improves the performances of HDH consist in employing a carrier gas with a higher water vapor saturation pressure than air. Abu Arabi & Reddy (2003) used different gases in their HDH facility and concluded carbon dioxide to be the best carrier. The main issue with having a carrier gas different than air is the significant increase of the system's complexity both in terms of operation and maintenance, which impacts the cost of the unit. Finally the last design features that broadly improved the performances of HDH process is the use of direct contact evaporator and condenser in the process. The use of these type of humidifier and dehumidifier removes the resistance induced by the conventional shell and tubes evaporators and condensers usually employed and therefore results in a significant increase of fresh water production (Giwa et al. (2016)).

Modeling of HDH system is usually based on solving an energy balance for each component of the facility: humidifier, dehumidifier and heat exchangers. Each analysis being plant specific, the modeling assumptions are validated with the results from an experimental apparatus. To compare each facility, authors usually calculate the Gained Output Ratio (GOR):

$$GOR = \frac{\dot{m}_{lg}h}{\dot{Q}_{heat}} \quad (2.1)$$

where \dot{m}_{lg} is the production rate of fresh water and \dot{Q}_{heat} is the thermal energy supplied to the

system. In all cases, the difficulty is the calculation of the heat and mass transfer coefficients. They are calculated using the temperatures and humidity ratio at the inlet and outlet of the humidifier and dehumidifier or by using an empirical correlation based on the mass fluxes (Mehrgoo & Amidpour (2012)).

Improvements by taking into account the humidifier and dehumidifier geometries was accomplished by Li et al. (2006). A modified version of Onda's correlation (Onda et al. (1968)) is employed to calculate the interfacial area, heat, and mass transfer coefficients as a function of the packing material properties, geometry, fluid properties, mass flow rates, and temperatures. The proposed 1D model showed a good agreement with experimental data for both steady-state and transient operations (Alnaimat et al. (2011)). Using 16 m^2 of solar collectors, the system is able to produce up to 100 L/d with 0.36 m^2 of evaporator (Alnaimat et al. (2013)). Nonetheless, as concluded by Nawayseh et al. (1999) an accurate evaluation of the heat and mass transfer coefficients is necessary and requires computer simulation.

CHAPTER 3

EVAPORATOR & PACKED COLUMNS

3.1 General

3.1.1 Evaporator & Desalination

As developed in Chapter 2, the coupled use of an evaporator and condenser is essential in all thermal desalination processes. In a wide majority of studies, the authors interest lie in the macro-scale performances, thus evaporator and condenser components are often treated as *black box*.

Nonetheless, it is evident that overlooking the transport phenomena occurring in those components is a critical and limiting factor in globally enhancing the desalination performances of any facility along with the reduction of the capital and operating costs. Currently, the majority of evaporators and condensers are designed using tube bundles (vertical or horizontal) on which water is sprayed creating a downward gravitating film. The heavy usage of those designs made the literature very rich in both experimental and numerical studies regarding flow patterns, pressure drop, heat transfer, and mass transfer. Therefore, some desalination studies are employing the knowledge acquired on tube bundles to model their desalination facility (Bourouni & Chaibi (2004), de la Calle et al. (2015), Mabrouk et al. (2015)). The use of low-grade heat to drive desalination systems pushed researchers toward direct contact evaporation and condensation, which requires the use of packed columns to increase the interfacial area between liquid and gas in replacement of the classic shell and tubes heat exchangers.

3.1.2 Packed Columns & Desalination

A packed column or packed bed, is in general a vessel in which a packing material is setup. These vessels are usually employed to perform chemical processes such as adsorption, distillation or stripping. They are of capital importance in critical industries such as pharmaceutical or food

processing industry. They are filled with a large variety of objects depending the application. On the one hand they can be filled with inert small objects such as Raschig rings, Pall rings or simply spheres. On the other hand they can be filled with catalysts that react with the fluids flowing through and are therefore called packed bed reactor (PBR).

In both cases, the main distinction between packed columns is the nature of the packing material. When the packed column is just filled with objects that are dumped they are called *random packing*. On the opposite, structured packing, consist of numerous small and organized channel. The presence of the material aims at enhancing the surface area between the two or more phases involved in the process. In a similar way as tube bundles, their extensive use in the industry pushed the literature to extensively study hydrodynamics, heat transfer, and mass transfer both numerically and experimentally.

Even if packed columns are a commonly employed device in the industry, their usage in desalination remains limited and almost entirely restricted to HDH systems. Only a few studies are available toward desalination using packed columns. Khedr (1993) used ceramic Raschig rings, Al-Hallaj et al. (1998) used a wooden packing, Klausner et al. (2004) used a polypropylene packing Lantec HD-QPAC, and He et al. (2018) used a Sulzer Mellapak 250Y. In all studies the use of general packed columns was applied towards the need of modeling evaporation or condensation for desalination. The following sections aim at describing the important parameters and considerations in the design of packed columns as well as a literature review of the various studies and models available for structured packed beds.

3.2 Design of Structured Packed Bed

3.2.1 Flow Patterns

As previously mentioned, the use of packed columns for desalination naturally involves the presence of multiphase flows that are inherently complicated to model and study. Depending the configuration of the system, the fluids involved may operate in co-current, counter-current or cross-flow thus leading to different flow patterns depending the operating and design parameters as shown in Fig.

3.1.

At low gas and liquid flow rate, Fig. 3.1a, the liquid flows around the bed surface and is described as the film flow regime. Increasing the gas flow rate leads to the regime shown in Fig. 3.1b where part of the liquid is stripped from the film creating droplets. This regime is known as the trickle regime. Increasing again the gas flow rate leads to the spray regime, where the film no longer covers the bed, and only suspended droplets are existing as described by Fig. 3.1c. Finally increasing the liquid flow rate leads to flooding the packed bed where the continuous phase is no longer the liquid but the gas instead. It is the bubbly regime and is depicted by Fig. 3.1d.

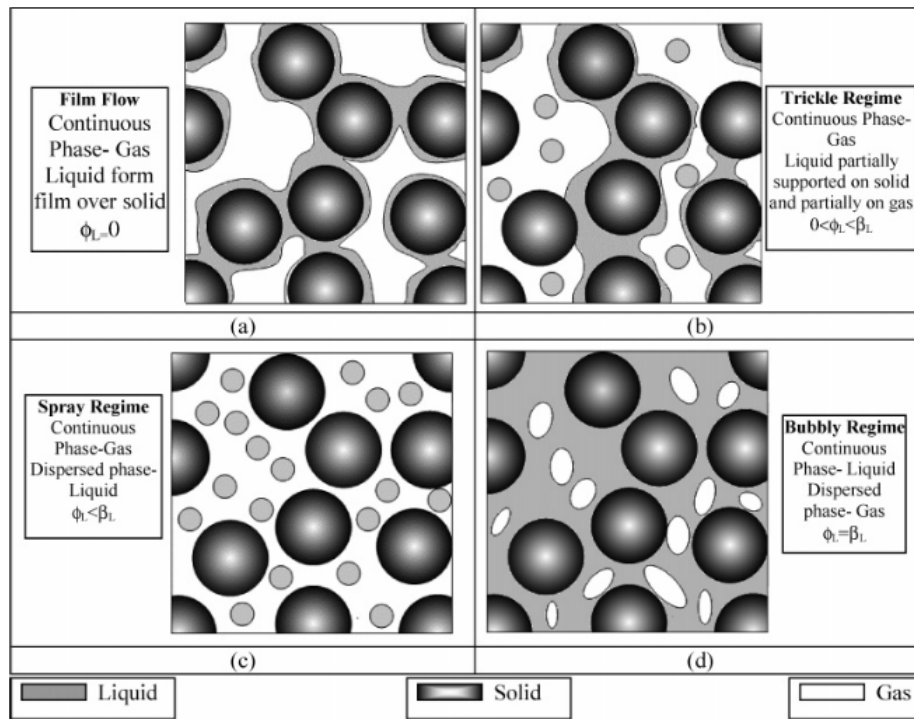


Figure 3.1: Flow regimes in packed columns (Gunjal et al. (2005))

Naturally, multiple flow patterns lead to very different liquid distributions since the interaction between liquid and gas changes. As a consequence, the packed columns literature uses different design and performance parameters to describe and broadly characterize the geometry.

3.2.2 Hydrodynamic Parameters

3.2.2.1 Liquid Holdup

At the scale of the column, the liquid holdup is the total volume or mass of liquid retained in the packing. It depends on the flow parameters, fluid properties and the packing geometry. Billet & Schultes (1999) developed a complete model for random and structured columns and showed the liquid holdup to be strongly affected by the gas capacity factor which characterizes the drag from the gas phase on the liquid phase. Increasing the gas flow rate for the same liquid rate eventually leads to the liquid being entirely retained in the packing, this is described as the flooding point. Many authors proposed correlations for liquid holdup depending on packing geometry, gas and liquid load as well as fluid properties (Suess & Spiegel (1992); Sidi-Boumedine & Raynal (2005); Alix & Raynal (2008)).

The inherent difficulty in the study of packed columns is the extreme complexity of instrumentation, especially when the information to acquire is the presence or not of liquid at a given location in space and time which requires local observation over the entire column. Sato et al. (1973) mounted the packed bed of his experimental apparatus on a scale to determine the liquid holdup. Since then, measurement techniques greatly improved and recent studies use magnetic resonance imaging (MRI) or electrical capacitance tomography imaging with accuracy greatly improving over the years (Mantle et al. (2001); Bolton et al. (2004); Robbins et al. (2012); Aferka et al. (2011); Wu et al. (2018)).

3.2.2.2 Pressure Drop

The operating costs are mainly related to the pumping power required to have the liquid and gas circulating in the column at the desired regime. Therefore, the pressure drop of a packed bed is a key factor in the overall design of a facility. Depending on the operating conditions and the packing geometry, majority of the pressure drop is due to the dry pressure drop or the irrigated pressure drop. This is especially true near and past the flooding point. Similarly to the liquid holdup,

many correlations for pressure drop are available in the literature based on superficial velocity, void fraction, and specific area (Ergun (1952); Stichlmair et al. (1989); Hanley et al. (1994); Stockfleth & Brunner (2001)).

3.2.3 Heat & Mass Transfer Parameters

The use of packed columns is essentially driven by the need to increase the surface area between the phase involved for a chemical or thermal process. In most cases, the mass transfer is highly dependent of the heat transfer since temperature is a catalyst. In the context of desalination, the interest is the amount of fresh water produced which is directly linked to the packed column ability to transfer heat and mass efficiently between liquid and gas. The ability to predict those quantities accurately determines the dimensions of the column, height and cross section, to meet the required output.

3.2.3.1 Interfacial Area

The rate of heat and mass through an interface is proportional to the surface area available for these transfers to occur. As a result, knowledge of the interfacial area between liquid and gas in the packed column is of critical importance. Ideally, the liquid covers entirely and homogeneously with an infinitely thin film the packing surface thus maximizing the surface area available and minimizing pressure-drop. Unfortunately, because of the gas-liquid interaction, surface roughness, packing non-homogeneity, turbulence etc., the apparition of *dry zones* is often observed both experimentally and numerically (Haroun et al. (2014); Ataki & Bart (2006)). The literature provides a reasonable amount of empirical correlations to calculate the interfacial area which, unfortunately, is impossible to measure experimentally. In all studies, authors used an experimental apparatus to infer phenomenologically the interfacial area (Onda et al. (1968); Xu et al. (2000)). Even if these methods allow to back calculate the interfacial area at the scale of the column, they fail at providing a local value and a spatial distribution. The only way to obtain an accurate value of the interfacial

area is through the use Computational Fluid Dynamic (CFD) at multiple scales as developed in section 3.3.

3.2.3.2 Heat & Mass Transfer Coefficients

At the interface between liquid and gas, the heat and mass transfer are usually not symmetric. The consequences of this phenomenon is represented by having different heat and mass transfer coefficients for the liquid side and gas side. These latter assess from the resistance to heat and mass transfer on the gas and liquid side. The heat transfer coefficients, U_l and U_g , are highly function of the fluid properties, operating temperature as well as the flow regime, often expressed as a function of the Reynolds (Re) and Prandtl (Pr) using non-dimensional groups. Mass transfer coefficients, k_L and k_G , mainly depends on the hydrodynamics, the interaction between liquid and gas, and the heat transfer coefficients. In both cases the packing geometry plays a fundamental role in the heat and mass transfer performances of a packed column. Wang et al. (2005) proposed a detailed review of the mass transfer correlations for structured packed columns and concluded that the rigorousness of CFD allows for a detailed picture of the heat and mass transfer in correlation with the fluid flow associated.

3.3 Numerical Modeling of Two-Phase Flows in Structured Packing

3.3.1 Porous Media Approach

The modeling of packed columns started on at a global scale with the prediction of pressure drop. The use of Darcy-Forchheimer's law for single phase flows was further extended to two-phase flows by Muskat & Meres (1936). More recent models for pressure drop are based on the summation of a dry pressure drop and an additional source term that takes into account gas-liquid-packing interaction when irrigated. These interactions were characterized by a wet friction factor function of the liquid loading. The irrigated pressure drop is then accounted for by finding the constants in a modified Ergun equation (Stichlmair et al. (1989); Billet & Schultes (1999); Stockfleth & Brunner (2001)). Finding these constants is achieved by fitting the experimentally measured pressure losses

to the equation. The constants are therefore a representation of the packing geometry as well as the geometry induced fluid interactions. Therefore, each group of constants only characterize one geometry and one material and a pair of fluid. The packing geometry are characterized using their void fraction ε and specific area a_s . Similar assumptions are employed regarding liquid holdup. The retrieval of heat and mass transfer coefficients can also be achieved by inferring the interfacial area as previously mentioned in section 3.2.3.1. Those empirical laws were then employed for the prediction and dimensions calculation of packed bed.

The emergence of CFD offers a powerful alternative to long and expensive experimental campaigns. The early stage used a porous media approach in 2D to solve hydrodynamic at the scale of the columns. Jiang et al. (2002) used an Eulerian k-th fluid to obtain velocity, liquid distribution and pressure drop. Empirical closure correlations were used for inter-phase momentum transfer. The early stage of such approach had interest in liquid distribution and pressure losses, the increase in computing power allows for the simulation of energy and mass transport. Mahr & Mewes (2007) used an Eulerian approach to simulate momentum and mass transport in structured packing at the scale of the column in a 3D environment. Khosravi Nikou & Ehsani (2008) proposed a study on a structured packing Flexipac 1Y accounting for turbulent momentum, heat and mass transfer using various turbulence models. The outcome showed the resistance to mass transfer is mainly in the liquid phase which remains laminar hence the use of turbulent model were not improving the agreement with experimental data. The porous media approach is slowly disappearing for packed bed modeling because of the emergence of Direct Numerical Simulation (DNS) of two phase flows with interface tracking. Nonetheless, Horgue et al. (2015) developed an open source toolbox for general multiphase flows through porous media for the OpenFOAM environment. The model was able to simulate 1010s of flow time in only 26s with only 256 cores allowing the study of phenomena taking place on a longer time scale.

3.3.2 Pore Resolved Simulations

In parallel to simulations done at the scale of the column, with the porous media approach, the DNS studies started at the scale of the corrugation. Petre et al. (2003) introduced the notion of *Representative Elementary Unit* (REU), to predict the dry pressure drop at the scale of the column. This was achieved by adding each individual pressure losses calculated at the scale of the elementary unit or corrugation. Using Large Eddy Simulation (LES), Kuwahara et al. (2006) studied the dry pressure drop at the scale of the REU to obtain the friction factor. The study concluded the Ergun equation to very well describe the pressure drop relationship for turbulent flows in porous media for single phase.

The extension to two phase flows simulations in order to obtain the wet pressure drop, liquid distribution and interfacial area is necessary. Raynal et al. (2008) first started using the Volume-Of-Fluid (VOF) multiphase formulation in 2D at the scale of the column in a co-current configuration to observe liquid holdup and wet pressure drop. The film thicknesses obtained by CFD were within 20% of the experimentally observed using tomography. Similar approach as Petre et al. (2003) in a 2D VOF environment was accomplished by Raynal & Royon-Lebeaud (2007), with the simulation of the wet corrugation that is further extended to the entire column. Even if these simulations yielded a significant quantity of informations on wetting and wet pressure drop, they lacked critical considerations. Firstly, the limitation to a 2D environment is a major shortcoming as improving packing geometries is inherently a 3D problem. Secondly the studies only focused on the hydrodynamics, hence no insights on heat and mass transfer could be extracted. Haroun et al. (2010) developed the framework to accurately study mass transfer in reactive flows with a VOF method. The method was successfully applied at the scale of the corrugation and showed the mass transfer to be very dependent of the advection at the interface (Haroun et al. (2012)). The extension to study mass transfer in 3D was done by Sebastia-Saez et al. (2013) at small scale and showed a strong relation between the packing geometry and the interfacial area. Since, constant increase of the computing powers allowed researcher to include turbulence and the application of DNS at the scale of the column.

Yang et al. (2018) applied LES at the scale of the column in a counter-flow configuration. Results showed the importance of the surface tension forces in the wetting through the use of the Weber (We) number. High We numbers lead to a better wetting but is usually obtained at high liquid mass flux which may lead to flooding. Lee et al. (2019b) studied the flow around an elliptic tube accounting for the complete physics by solving continuity, momentum, temperature and mass transfer in a 3D configuration and showed a decrease in heat transfer depending the angle of distribution of liquid. A similar study was accomplished in a counter current flow configuration (Lee et al. (2019a)). The reader is directed to Wen et al. (2020a) for an extensive review of DNS applications to heat and mass transfer.

Although the improvements over the last 5 years have been tremendous in terms of physics modeled through CFD, several limitations are identifiable and have not been studied to the author knowledge. First, all the configuration studied are either applied to the corrugated plates, tube banks or spheres which are to be considered simple geometries. Second, the liquid distribution is often considered continuous hence limiting the study to the falling film flow regime as described by Fig. 3.1a. In reality, a wide majority of experimental apparatus employed for CFD validation uses sprayer or distributors for which the description is often overlooked. The packed column coverage as well as droplets size distribution is overlooked but it evidently affects the packed column hydrodynamic behavior, and as consequences, the heat and mass transfer. Third, in counter-current flow studies, the splitting of the boundary conditions at the bottom to let gas in and liquid out is not accounted for even though it naturally creates an uneven distribution of the gas phase (Xie et al. (2019)). Hence the work taken in this study is to first develop the numerical framework necessary toward an accurate modeling of diffusion driven evaporation. Study the influence of gas and liquid distribution on the overall performances of a structured packed columns. Ultimately, develop geometries to improve the performances of packed columns for the application to direct contact evaporation in HDH systems.

CHAPTER 4

MATHEMATICAL FORMULATION OF TWO-PHASE FLOWS

4.1 General

The definition of *multiphase flows* covers a very broad amount of physical phenomena that can be studied with each and every one of them being driven differently. As examples the modeling of a dam breaking where body forces are the main source of momentum or the study of droplets in a capillary channel where surface tension forces are predominant. The differences in scale along with the quantities of interest makes the existence of a single mathematical formulation to describe all type of multiphase flows impossible. As consequences, modeling multiphase flows is not achievable without previously identifying the physics one aims to focus on. With this first step accomplished, the development of a rigorous mathematical model relevant to the physics of interest can be developed. Currently, those mathematical models differ by the presence or not, of a surface tracking algorithm. Currently, the two approaches without surface tracking are available, the Eulerian-Eulerian where the phases are treated as interpenetrating continuum developed by Ishii & Hibiki (2011), and the Eulerian-Lagrangian approach.

The Eulerian-Lagrangian formulation is usually employed when the secondary phase is highly dispersed (less than 10% of the domain volume), hence with a low interaction. The most common formulation is the *Discrete Particle Model* (DPM). It consists in modeling the continuous or primary phase with a classic Eulerian formulation while the second phase is tracked in the Lagrangian frame using a lumped mass model. Empirical closure correlations are needed to model the interaction with the continuous phase depending the quantity of interest such as drag, heating, cooling, evaporation, etc. The main limitation of the Eulerian-Lagrangian approach are the computation expenses when a large amount of particles need to be tracked or the inaccuracy engendered by the secondary phase interaction when this latter represent more than 10%. When this occurs the Eulerian-Eulerian formulation is preferable. In both cases both Eulerian-Eulerian and Eulerian-Lagrangian do not

provide informations on the transport phenomena at the interface since this latter is not modeled. This issue is overcome by surface tracking methods.

The main advantage of surface tracking methods are their ability to provide a close understanding of the phenomena occurring at the interface that is not available for non surface tracking models and almost impossible to measure with experimental techniques. The main drawback is the necessity of very fine mesh to track the interface motion accurately which can also be computationally expensive. This is particularly true when the interface position is not predictable. Multiple formulations are available in the literature. They all have in common to assume a zero thickness interface which represent the transition between the fluids involved. The main difference between models is the technique employed to track the interface motion. Two distinct categories exist, *interface capturing* and *interface tracking* method. The following sections presents the various mathematical approaches available for modeling multiphase flows with surface tracking.

4.2 Two-Fluid Formulation

The two-fluid formulation is the most complete mathematical formulation when it comes to model multiphase flows with the interface being explicitly defined. The flow domain is divided into two sub-domains filled with each individual phase. Therefore, each sub-domain is treated as a single phase domain in which the classic single-phase Navier-Stokes equations are valid. Hence each phase posses its own set of conservation equations for mass, momentum and energy principally.

Conservation of mass for k -th phase:

$$\frac{\partial}{\partial t} (\rho_k) + \nabla \cdot (\rho_k \mathbf{u}_k) = 0 \quad (4.1)$$

Conservation of momentum for k -th phase:

$$\frac{\partial}{\partial t} (\rho_k \mathbf{u}_k) + \nabla \cdot (\rho_k \mathbf{u}_k \mathbf{u}_k) = -\nabla p + \nabla \cdot (\boldsymbol{\tau}_k) + \rho_k \mathbf{g} + \mathbf{F} \quad (4.2)$$

where $\boldsymbol{\tau}_k = \mu_k \left[\nabla \mathbf{u}_k + (\nabla \mathbf{u}_k)^T \right]$ is the shear stress tensor when the fluids considered are Newtonian. \mathbf{F} is a general body force such as a magnetic field.

Energy of k -th phase:

$$\frac{\partial}{\partial t} (\rho_k \mathbf{u}_k E_k) + \nabla \cdot (\rho_k E_k \mathbf{u}_k) = -\nabla \cdot (\lambda_k \nabla T_k) + \boldsymbol{\tau}_k : \nabla \mathbf{u}_k + Q_k \quad (4.3)$$

where $E_k = C_{p,k} T_k$ and Q_k accounts for energy source terms within the phase. Along with this set of conservation equation the necessary interfacial jump equations which serve as boundary conditions for each sub-domains. First derived by Ishii & Hibiki (2011), those conditions were simplified by Juric & Tryggvason (1998) using the assumption of, infinitely thin, and massless interface with constant surface tension. The jump conditions for mass, momentum and energy across an interface separating the fluids l and k are as follows:

$$\dot{m}_{kl} = \dot{m}_{lk} = \dot{m} = \rho_k (\mathbf{u}_k - \mathbf{u}_i) \cdot \mathbf{n} = \rho_l (\mathbf{u}_l - \mathbf{u}_i) \cdot \mathbf{n} \quad (4.4)$$

$$p_k - p_l = -\dot{m}^2 \left(\frac{1}{\rho_k} - \frac{1}{\rho_l} \right) + (\boldsymbol{\tau}_k \cdot \mathbf{n}) \cdot \mathbf{n} - (\boldsymbol{\tau}_l \cdot \mathbf{n}) \cdot \mathbf{n} + \sigma \kappa \quad (4.5)$$

$$(\boldsymbol{\tau}_k \cdot \mathbf{n}) \cdot \mathbf{t} = (\boldsymbol{\tau}_l \cdot \mathbf{n}) \cdot \mathbf{t} \quad (4.6)$$

$$\begin{aligned} (\mathbf{q}_k - \mathbf{q}_l) \cdot \mathbf{n} = \dot{m} \left(\frac{(\boldsymbol{\tau}_k \cdot \mathbf{n}) \cdot \mathbf{n}}{\rho_k} - \frac{(\boldsymbol{\tau}_l \cdot \mathbf{n}) \cdot \mathbf{n}}{\rho_l} \right) - \frac{\dot{m}^3}{2} \left(\frac{1}{\rho_k^2} - \frac{1}{\rho_l^2} \right) \\ - \dot{m} \left[h_{lk} + (C_{p,k} - C_{p,l}) (T_i - T_{sat}) \right] \end{aligned} \quad (4.7)$$

where \mathbf{u}_i is the velocity of the interface, \mathbf{n} and \mathbf{t} are the unit normal and tangential vectors to the interface, \dot{m} is the mass flux across the interface, h_{lk} is latent heat, T_i the interface temperature and T_{sat} the saturation temperature. Note that an additional closure correlation is necessary for the interface temperature T_i . In general the two-fluids formulation is employed when particularly high gradients are present in the vicinity of the interface others than the density gradient. This occurs in numerous amount of problems, such has gas-liquid flows where the viscosity ratio is high at the interface, or in cases with a high relative velocity between phases. In those cases, the two-fluid formulation performs really well and the phenomena occurring at the interface are accurately computed.

4.3 Single Fluid Formulation

The single fluid formulation for multiphase flows consists in describing the entire domain with a single set of conservation equations. As a consequence, the numerical domain is considered to be filled with a single fluid whose properties abruptly changes at the interface. Source terms are added to the conservation equations model interfacial effects. Therefore, the jump conditions in the single fluid formulation, are replaced by a Dirac function commonly called δ function and only the domain boundary conditions are needed. The conservation equations are defined as follows:

Conservation of mass:

$$\frac{\partial \rho}{\partial t} + \nabla \cdot (\rho \mathbf{u}) = \int_{\Gamma(t)} \dot{m} \delta(\mathbf{x} - \mathbf{x}_s) ds \quad (4.8)$$

Conservation of momentum:

$$\frac{\partial}{\partial t} (\rho \mathbf{u}) + \nabla \cdot (\rho \mathbf{u} \mathbf{u}) = -\nabla p + \nabla \cdot (\boldsymbol{\tau}) + \rho \mathbf{g} + \int_{\Gamma(t)} \sigma \kappa \mathbf{n} \delta(\mathbf{x} - \mathbf{x}_s) ds \quad (4.9)$$

Conservation of energy:

$$\frac{\partial}{\partial t} (\rho E) + \nabla \cdot (\rho \mathbf{u} E) = -\nabla \cdot (\lambda \nabla T) + \boldsymbol{\tau} : \nabla \mathbf{u} - \int_{\Gamma(t)} \dot{q} \delta(\mathbf{x} - \mathbf{x}_s) ds \quad (4.10)$$

where \dot{m} and \dot{q} are the interphase heat and mass fluxes. $\Gamma(t)$ represents the interface position in the domain and $\delta(\mathbf{x} - \mathbf{x}_s)$ is the a delta function that has the value of unity at $\mathbf{x} = \mathbf{x}_s$ and zero everywhere else. One can immediately notice that equations (4.8), (4.9), and (4.10) are the same as the single phase Navier-Stokes equations except for the source terms due to the interface jump. Numerically, this leads to solve those equations with similar algorithms as the single phase set.

However, in addition to the classic single phase Navier-Stokes equations, an additional marker function is required to compute the position of each phase as well as calculate fluid properties. Along with the marker function, a method to update the latter as the interface topology evolves over time is also necessary. Then, an approximation of the delta function for computational grid is required for modeling interfacial effects. Finally, a reconstruction of the interface topology to calculate normal vector and interface curvature in order to compute surface tension effects is also essential.

Arbitrarily chosen, the marker function, $I(\mathbf{x}, t)$ is equal to unity in the primary phase and nil in the secondary phase. Using the δ function, the marker function is:

$$I(\mathbf{x}, t) = \int_{\Omega(t)} \delta(\mathbf{x} - \mathbf{x}_s) dv \quad (4.11)$$

where $\Omega(t)$ is the control volume. The use of the marker function allows for the calculation of fluid properties at the interface which for a general property b in between phase k and phase l yields:

$$b(\mathbf{x}, t) = I(\mathbf{x}, t)b_l + b_k (1 - I(\mathbf{x}, t)) \quad (4.12)$$

Finally, the gradient of the marker function is employed to retrieve the interface normal vector:

$$\nabla I(\mathbf{x}, t) = \int_{\Gamma(t)} \mathbf{n} \delta(\mathbf{x} - \mathbf{x}_s) ds \quad (4.13)$$

By essence, the definition of the marker function creates abrupt changes of fluid properties which, in a numerical environment, is always problematic. In this case, the numerical instabilities that may arise from this definition are often traded in accuracy with the interface smearing across a few cells. The main difference in between single-fluid formulations is in the expression of the marker function. Those can be classified into two categories:

- interface tracking (surface methods)
- interface capturing (volume methods)

With interface tracking methods, the interface is marked using massless particles (marker) that are explicitly advected in the Lagrangian frame using the local velocity field from the background fixed grid. Therefore, with a sufficient amount of marker, the interface can be reconstructed at every time step by knowing the position of each marker. This technique, called Marker And Cell (MAC), was first developed by Harlow & Welch (1965) and was further improved numerous authors McKee et al. (2008).

The other interface tracking method, is the surface-fitted method, where the interface is attached to the grid which is then forced to move with the interface. The advantages of this method is the

reduction of the storage needed since it does not need to keep track the markers position. A perfectly sharp interface is also ensured since partially filled cells do not exist. The evident drawbacks are the necessity to generate a mesh at each time step along with the impossibility to model breaking or coalescing interface Yeoh & Tu (2010). A common interface tracking method is the Front Tracking algorithm (FT) and is described in the following section.

With interface capturing methods, each fluids is defined on either side of the interface using an indicator function. The interface is further advected by solving a conservation equation derived from the continuity equation. Substituting equation (4.12) into equation (4.8) as shown by Lakehal et al. (2002) yields an equation for the conservation of mass and the marker function:

$$\nabla \cdot \mathbf{u} = 0 \quad (4.14)$$

$$\frac{\partial I}{\partial t} + \mathbf{u} \cdot \nabla I = (\mathbf{u} - \mathbf{u}_i) \cdot \nabla I \quad (4.15)$$

Two main interface capturing methods currently exist, the Level-Set (LS) method developed by Sussman (1994) and the Volume-of-Fluid (VOF) proposed by Hirt & Nichols (1981). Both methods are introduced in the following sections with their strength and weaknesses. Emphasized is made on the VOF since it is the method employed in this work.

4.4 Front Tracking Algorithm

Several versions of the Front Tracking algorithm are available in the literature and have been successfully implemented for various multiphase flow problems. Lately, Hua & Mortensen (2019) successfully implemented the method on the commercial software ANSYS Fluent. Nonetheless, all the front tracking algorithms are derived from the works of Unverdi & Tryggvason (1992). As shown in Fig. 4.1, the conservation equations are solved on the background fixed grid while the interfacial source terms and the interface advection are computed using the front grid. Each markers is tracked in a Lagrangian fashion using a numerical integration from its initial position:

$$\mathbf{x}_m = \mathbf{x}_m^0 + \int_0^t \mathbf{u}_m dt \quad (4.16)$$

where \mathbf{x}_m is the marker position, \mathbf{x}_m^0 is the initial position and \mathbf{u}_m is the local velocity field computed on the fixed Eulerian grid.

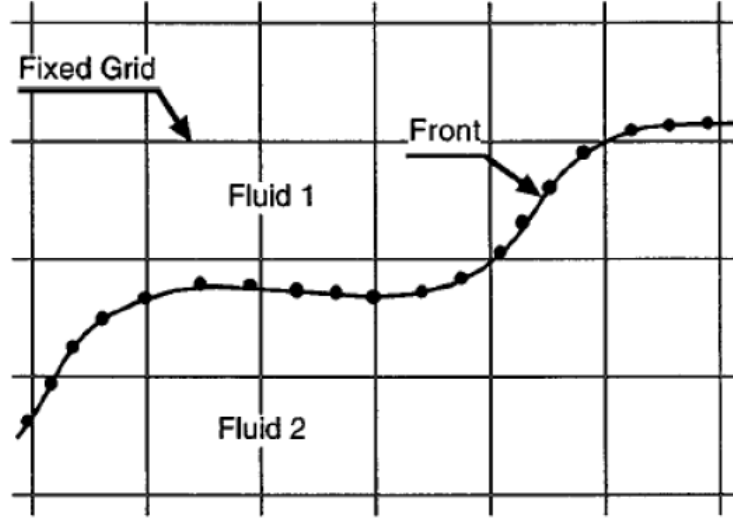


Figure 4.1: Front and background grids for the computation of multiphase flows (Tryggvason et al. (2001))

To reconstruct the indicator function, $I(\mathbf{x}, t)$, the strategy employed is to calculate the divergence of equation (4.13) which leads to a Poisson equation that is further solved.

$$\nabla \cdot \nabla I = \nabla^2 I = \nabla \cdot \int_{\Gamma(t)} \mathbf{n} \delta(\mathbf{x} - \mathbf{x}_s) dS \quad (4.17)$$

The difficulty of this method lies in the transfer of informations between the background grid and the front grid once the indicator function is reconstructed using equation (4.17). To achieve that transfer, a distribution function is employed to estimate the delta function in equation (4.13). This is further used to calculate the smoothly varying fluid properties occurring across the artificially distributed interface. Therefore the sharp jump of the indicator function $I(\mathbf{x}, t)$ is spread across the neighboring cells. The discretized form of equation (4.13) according to Unverdi & Tryggvason (1992) is given by equation (4.18).

$$\nabla I = \sum_f D(\mathbf{x} - \mathbf{x}_f) \mathbf{n}_f \Delta s_f \quad (4.18)$$

where \mathbf{n}_f is the unit normal vector at an interface element of area Δs_f whose centroid is \mathbf{x}_f . The distribution function, $D(\mathbf{x} - \mathbf{x}_f)$, proposed by Peskin (1977), is employed and defined as follows:

$$D(\mathbf{x} - \mathbf{x}_f) = \begin{cases} 4\Delta^{-\alpha} \prod_{i=1}^{\alpha} \left(1 + \cos\left(\frac{\pi}{2\Delta}|\mathbf{x} - \mathbf{x}_f|\right)\right), & \text{if } |\mathbf{x} - \mathbf{x}_f| < 2\Delta \\ 0, & \text{otherwise} \end{cases} \quad (4.19)$$

where Δ is the fixed grid spacing and α represents the number of dimensions. Equation (4.19) is also used in the reverse direction from the calculation of ∇I in equation (4.18) to interpolate the velocity from the background fixed mesh to the front mesh:

$$\mathbf{u}_f = \sum D(\mathbf{x} - \mathbf{x}_f) \mathbf{u} \quad (4.20)$$

Hence, the front position is retrieved using equation (4.16). Other field variables such as energy or momentum are also interpolated and integrated in the same fashion. The front tracking method offers the major advantage of its explicit tracking of the interface on the fixed grid which remove the necessity of computing the interface curvature. Unfortunately, the usage of marker points to define the interface by geometrical reconstruction is its sensitivity to the marker spacing, which, in time, may evolve further apart depending the flow physics. Avoiding that effect requires the computational effort of redistributing the markers across the interface at each time step which becomes extremely complicated in three dimensional calculations. Similar issues occurs when break-up or coalescence of the interface is involved.

4.5 Level-Set Method

The Level-Set (LS) method, first developed by Sussman (1994), is an interface capturing method. It relies on the transport of a function, the level set function, that is only meaningful at the interface. The level set function, $\phi(\mathbf{x}, t)$ is tracked using equation (4.21). Physically, as shown in Fig. 4.2, $\phi(\mathbf{x}, t)$ represents the signed minimum distance from the interface and is equal to zero at this latter. In other words, arbitrarily, $\phi(\mathbf{x}, t) < 0$ within the primary phase and $\phi(\mathbf{x}, t) > 0$ within the secondary phase.

$$\frac{\partial \phi}{\partial t} + \mathbf{u} \cdot \nabla \phi = \frac{\dot{m}}{\rho} |\nabla \phi| \quad (4.21)$$

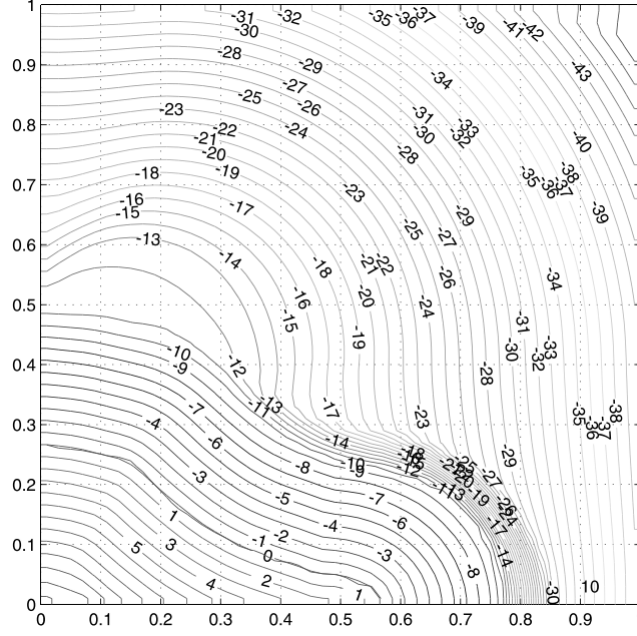


Figure 4.2: Representation in 2D of the level-set function $\phi(\mathbf{x}, t)$ (Lakehal et al. (2002))

Solving the convective term of equation (4.21) is usually complicated and requires high order discretization schemes to avoid the oscillation of the interface. Harten et al. (1987) developed a third order accuracy scheme, Essentially Non Oscillatory (ENO), successfully implemented by Luo et al. (2005) to model bubble rising with phase change. A fifth order scheme, Weighted-ENO (WENO), proposed by Jiang & Peng (2000) is also commonly employed in the literature Gibou et al. (2007); Tanguy et al. (2007). Once the level-set function is known, the normal vector and the curvature are retrieved:

$$\mathbf{n} = \frac{\nabla\phi}{|\nabla\phi|} \quad (4.22)$$

$$\kappa = -\nabla \cdot \mathbf{n} = -\nabla \cdot \frac{\nabla\phi}{|\nabla\phi|} \quad (4.23)$$

The next step in the calculation, similarly to the FT algorithm, is the interpolation of the fluid properties across the interface accomplished with an Heavyside function $H_\varepsilon(\phi)$. The definition given by Sussman (1994) is:

$$H_\varepsilon(\phi) = \begin{cases} 0 & \text{if } \phi < -\varepsilon \\ \frac{1}{2} + \frac{\phi}{2\varepsilon} + \frac{1}{2\pi} \sin\left(\frac{\pi\phi}{\varepsilon}\right) & \text{if } |\phi| \leq \varepsilon \\ 1 & \text{if } \phi > \varepsilon \end{cases} \quad (4.24)$$

where ε is the interface thickness parameter function of the grid spacing Δ . A typical value is to take $\varepsilon = 1.5\Delta$. An example of the smoothed Heaviside function is shown in Fig. 4.3. The main advantage of this method is that it naturally bounds the interface thickness limiting the numerical diffusion usually involved with the interface smearing.

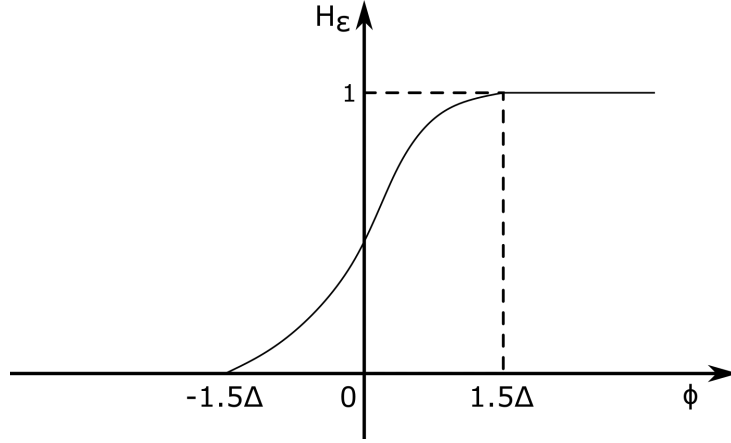


Figure 4.3: Smoothed Heaviside Function

One of the issues of the level-set method is the need to reinitialize the level-set function as it no longer represent the signed distance from the interface when solving equation (4.21) as the interface stretches or smears. Maintaining $\phi(x, t)$ being the signed distance is crucial for the fluid properties computation but also to avoid critical numerical diffusion usually leading to mass loss or gain. Hence $\phi(x, t)$ is reinitialized in the vicinity of $\phi(x, t) = 0$ to enforce:

$$|\nabla\phi| = 1 \quad (4.25)$$

This condition is ensured by solving for the steady-state solution of the following equation:

$$\frac{\partial\phi}{\partial\tau} = S(\phi_0) (1 - |\nabla\phi|) \quad (4.26)$$

where τ is here a pseudo time different from the real time. ϕ_0 is the initial distribution before being reinitialized and $S(\phi_0)$ represent a smoothed signed distance defined equation (4.27).

$$S(\phi_0) = \frac{\phi_0}{\sqrt{\phi_0^2 + \Delta^2}} \quad (4.27)$$

When equation (4.26) reaches steady-state, the condition defined by equation (4.25) is satisfied. Therefore the approximation of the δ function in equations (4.8), (4.9) and (4.10) is realized by taking the derivative of the smoothed Heaviside function:

$$\delta(\phi) = \frac{\partial H_\varepsilon(\phi)}{\partial \phi} \quad (4.28)$$

The main flaw of the level-set method is the non respect of mass conservation. Several numerical procedures are available in the literature to minimize this effect. Russo & Smereka (2000) or Du Ch  n   et al. (2008) computed the fluxes with a second and fourth order accuracy in cells containing an interface. Other solution consist in solving the level-set equation on high resolution grid using Adaptive Mesh Refinement (AMR). The consequence of this issue is the partial loss of the level-set method simplicity that normally only requires to solve one additional equation in comparison with single-phase Navier-Stokes equations. Though this method is still present in the literature, Gibou et al. (2018) recently reviewed the level-set method and its applications.

4.6 Volume-of-Fluid Method

The Volume-Of-Fluid method (VOF), introduced by Hirt & Nichols (1981), relies on a scalar indicator function, the volume fraction, to make the distinction between the fluids in the domain. The volume fraction is bounded between zero and one. Arbitrarily, one corresponds to a cell full of the primary phase and zero correspond to a cell full of the secondary phase. When the values of the volume fraction lies between zero and one, it indicates the presence of an interface. In a similar fashion as the level-set function, the marker function is advected using the following equation derived from (4.15).

$$\frac{\partial I}{\partial t} + \mathbf{u} \cdot \nabla I = \frac{\dot{m}}{\rho} \delta(x) \quad (4.29)$$

where the volume fraction, α , results from a spatial integration within the volume of a computational cell Ω .

$$\alpha = \frac{1}{\Omega} \int_{\Omega} I(\mathbf{x}, t) d\Omega \quad (4.30)$$

$$\sum_{k=1}^N \alpha_k = 1 \quad (4.31)$$

Note that only N-1 volume fraction equations are solved for a system of N phases as defined by equation (4.31) which is a consequence of the mass conservation equation. The fluids properties are then retrieved using a volume fraction averaging which, for a two-phase system yields:

$$b(\mathbf{x}, t) = \alpha b_1 + (1 - \alpha) b_2 \quad (4.32)$$

The interface unit normal vector and curvature are then retrieved using the same equations as the level-set method.

$$\mathbf{n} = \frac{\nabla\alpha}{|\nabla\alpha|} \quad (4.33)$$

$$\kappa = -\nabla \cdot \mathbf{n} = -\nabla \cdot \frac{\nabla\alpha}{|\nabla\alpha|} \quad (4.34)$$

As a consequence, the δ function is also expressed with the same formalism:

$$\delta(\alpha) = |\nabla\alpha| \quad (4.35)$$

The combination of equations (4.30), (4.29) and (4.35) with the use of Green's theorem yields:

$$\frac{\partial\alpha}{\partial t} + \frac{1}{\Omega} \int_S (\mathbf{u} \cdot \mathbf{n}) I(\mathbf{x}, t) dS = \frac{\dot{m}}{\rho} |\nabla\alpha| \quad (4.36)$$

where the S is the external surface of the cell Ω . The use of a transport equation to solve the volume fraction field makes it particularly sensitive to numerical diffusion. Accurate algorithms are necessary to ensure the conservation of mass when the volume fraction is transported. This is especially true for the convective term which usually leads the volume fraction to be smeared across a few cells to ensure the volume fraction remains bounded between zero and one. An example of this phenomenon is described in Fig. 4.4 where instead of a perfectly sharp interface, the volume fraction field gradually transition across a few cells.

Numerous techniques are available in the literature to limit this phenomenon and reconstruct a sharp interface. Two main categories currently exist: donor-acceptor formulation or the so called ,line techniques, that are based on a geometric reconstruction of the interface within the cell. The original version of those geometrical reconstructions is the Simple Line Interface Calculation (SLIC) developed by Noh & Woodward (1976). With this method, the interface is represented by



Figure 4.4: Volume fraction field: (a) ideal sharp interface (b) smeared interface

segments aligned with the grid. The algorithm uses a direction split for which only the neighboring cells in the swept direction are considered. Figures 4.5b and 4.5c show the consequences of the direction split with interface being reconstructed differently as function of the sweeping direction. The full part of the cells is identified using $\nabla\alpha$.

Another type of interface reconstruction is the donor-acceptor formulation, originally employed by Hirt & Nichols (1981). In the donor-acceptor approach, when a cell contains an interface, one cell is marked as donor of a defined amount of fluid from one phase and the other as acceptor of that same amount of fluid. The amount of fluid available in the donor cell and the free volume available in the acceptor cell are bounding the amount of fluid that can be convected across a cell face. In two dimensions the interface orientation is either horizontal or vertical. Depending the interface orientation as well as its motion, the flux values are obtained by upwinding, downwinding or a combination of both. The resulting interface reconstruction is described by Fig. 4.5d.

An interesting improvement on the SLIC method, conducted by Youngs (1982), consist in using oblique lines to describe the interface. This method is called Piecewise Linear Interface Construction (PLIC). The orientation of the interface is determined by unit normal vector as given by equation (4.33). The interface is then reconstructed using geometrical considerations. The major flaw of that algorithm is that it does not enforce the continuity of the interface in between neighboring cells as shown in Fig. 4.5e. This is the algorithm implemented in ANSYS Fluent.

Finally the Flux Line-Segment Model for Advection and Interface Reconstruction (FLAIR) developed by Ashgriz & Poo (1991) solves this issue by enforcing a line at each cell face instead of

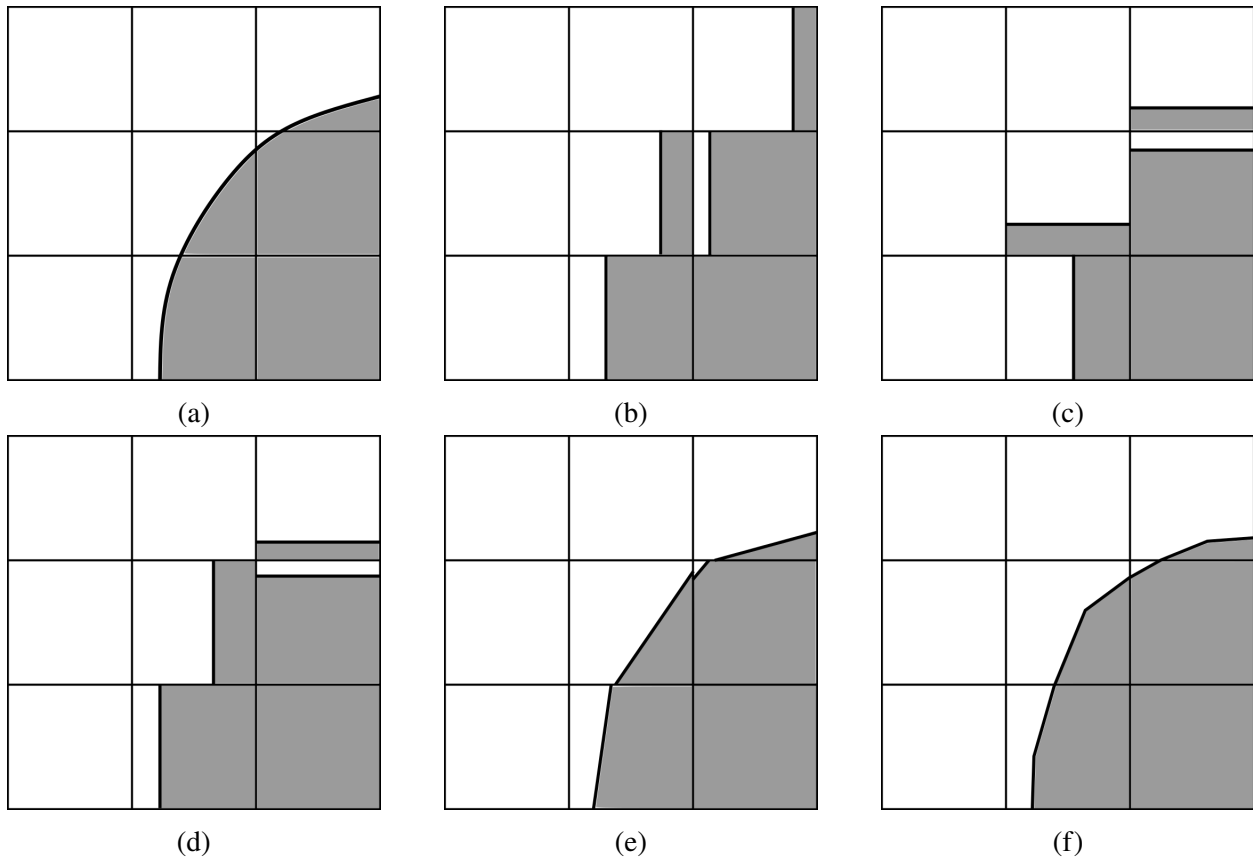


Figure 4.5: Interface Shape with different reconstruction schemes: (a) original fluid distribution (b) SLIC (x-sweep) (Noh & Woodward (1976)) (c) SLIC (y-sweep) (Noh & Woodward (1976)) (d) Donor-Acceptor (Hirt & Nichols (1981)) (e) PLIC (Youngs (1982)) (f) FLAIR (Ashgriz & Poo (1991))

a line per cell as shown in Fig. 4.5f. Even if the FLAIR method yields a really accurate description of the interface, its implementation in three dimensions environment with high order cells is fairly complicated and casts a shadow on the simplicity of the VOF method.

The strength of the VOF approach being its simplicity, because, similarly to the level-set method, only one additional equation is required in comparison to single phase Navier-Stokes equations. Nonetheless, the discretization of the convective term in the volume fraction equation (4.36) requires accurate algorithm to avoid smearing or oscillations of the interface. Although such algorithms are ensuring a very good accuracy in regard of mass conservation, the representation of the interface curvature using equation (4.34) is poor. This phenomenon is due to the derivation schemes employed that are poorly performing with non continuous functions such as the volume

fraction. The consequences are an inaccurate computation of the surface tension force which may leads to numerical instabilities in some cases. Remedying to curvature computation inaccuracies as well as interface smearing is widely covered in the literature and is developed in section 4.9.

4.7 Hybrid Methods

On the one hand, the LS method, with the use of a continuous level function offers an accurate computation of the interface curvature but the re-distancing that needs to be applied to recover the signed distance after the interface advection leads to mass loss or gain. On the other hand, the VOF method, offers an excellent mass conservation but even sophisticated interface reconstruction algorithms such as PLIC or FLAIR fail to accurately represent the interface curvature. Therefore, the solution is naturally to combine VOF and LS methods to take advantage of each approach strengths.

This was accomplished by Sussman & Puckett (2000) with the Coupled Level-Set Volume of Fluid (CLSVOF) algorithm. In the CLSVOF method, both level-set and VOF functions equations are solved in parallel. The level-set function is used to compute the normal vector and curvature as well as the fluid properties while the interface advection is handled by the PLIC scheme from the VOF framework. Hence, the correction of the level-set function to retrieve the signed distance is accomplished using the information from the volume fraction advected field. This method was successfully implemented to model various problems such as dam breaking, droplet break-up among others Zhao & Chen (2017); Chakraborty et al. (2016); Ménard et al. (2007).

Other hybrid methods consist in the coupling of a FT algorithm with LS or VOF approaches. The combination of FT and LS was accomplished by Enright et al. (2002) and consists in placing markers on the zero value of the level-set function. After the advection step is performed, the marker are used for the re-initialization of the level-set function to retrieve the signed distance. The coupling of FT and VOF was proposed by Aulisa et al. (2003). The markers are used to reconstruct and advect the interface while the volume fraction enforce mass conservation. As a result, the interface topology is described by segments connecting two types of markers: intersection markers

and volume conservation markers. The intersection markers remove the need of re-meshing while the volume conservation markers are added to the interface inside each cell to enforce mass conservation through the use of the volume fraction. By enforcing the conservation of the area within a cell instead the volume fraction, Aulisa et al. (2004) improved on the original FT-VOF method. The improved method shown to be computationally more efficient and accurate.

4.8 Surface Tension and Wall Adhesion Modeling

4.8.1 Surface Tension

Surface tension is a phenomenon that occurs at the interface between fluids because of the different molecular forces of attraction in this region. The surface tension force prevents the interface area increase. Therefore a defined amount of work is required for the interface to move. This amount of work is characterized by σ , the surface tension coefficient, which depends on the pair of fluids involved and can be positive or negative. When negative, the fluids are defined as miscible and immiscible when positive. At the macroscale, surface tension forces are expressed as a body force in $N.m^{-3}$ concentrated at the interface and defined by:

$$\mathbf{F}_\sigma = \sigma \kappa \mathbf{n} \quad (4.37)$$

Knowing that, several approaches exist to model surface tension forces. The most common model is the Continuum Surface Force (CSF) proposed by Brackbill et al. (1992). The basic principle of that model is to consider the interface as a transition region of finite thickness on which the forces are continuously distributed. As a result, using a general marker function, the surface tension can be expressed as:

$$\mathbf{F}_\sigma(\mathbf{x}) = \frac{\rho(\mathbf{x})}{\langle \rho \rangle} \sigma \kappa(\mathbf{x}) \frac{\nabla \tilde{I}(\mathbf{x})}{[I]} \quad (4.38)$$

where $\tilde{I}(\mathbf{x})$ is the smoothed expression of the marker function according to the method employed and $[I]$ is the jump in that function across the interface. As an example, in the case of the VOF formulation, $\tilde{I}(\mathbf{x})$ is the volume fraction α , and $[I] = [\alpha] = 1$ since the volume fraction varies from 1 to 0 across an interface. $\rho(\mathbf{x})$ is the local density within the interfacial region calculated using

the necessary interpolation and $\langle \rho \rangle = \frac{1}{2} (\rho_l + \rho_k)$. From the definition of $\langle \rho \rangle$ it is evident that surface tension forces are not evenly distributed across the interface when equation (4.38) is employed. The forces are shifted towards the heavier fluid but the total resulting force is conserved. The drawback of this method comes when the fluids density ratio is important. When this occurs, the sharp jump in surface tension force may leads to numerical difficulties as described further.

Other well-known formulations are the Continuum Surface Tension (CST) and Continuum Surface Stress (CSS) proposed by Jacqmin (1996) and Lafaurie et al. (1994) respectively. The CST model is analytically equivalent to the original CSF model but removes the need of explicitly computing the curvature. The CSS model introduces the use of a pressure tensor \mathbf{T} , which, in the case of the VOF method is expressed as follows:

$$\mathbf{T} = \sigma \left(|\nabla\alpha| \bar{\mathbf{I}} - \frac{\nabla\alpha \otimes \nabla\alpha}{|\nabla\alpha|} \right) \quad (4.39)$$

where $\bar{\mathbf{I}}$ is the identity matrix. Finally the Ghost Fluid Method (GFM) developed by Liu et al. (2000) narrows the region where the surface tension forces are applied in comparison with the CSF model. This leads to a more realistic jump for the pressure field but is computationally more expensive.

Modeling the surface tension with the CSF model leads to the well-known issues of *spurious velocities* or *parasitic currents* as rigorously analyzed by Harvie et al. (2006). These nonphysical velocity fields arise at the interface vicinity and often lead to numerical instabilities responsible for simulation failure or, at least, a strong alteration of the results. The spurious velocities arise from two issues when using the CSF model. First, it is a consequence of the discretization mismatch between the pressure gradient and the surface tension terms in the momentum equation Renardy & Renardy (2002). The solution to minimize that mismatch is to add the pressure jump from the surface tension force during the computation of the velocity field at the pressure correction stage Popinet (2009). Secondly, as shown by Meier et al. (2002), it results from the poor curvature calculation done by the CSF model. The curvature estimation can be greatly improved by the use of high accuracy algorithms to reconstruct the interface as discussed by Guo et al. (2014). Such

algorithms are developed in section 4.9. An extensive review of the surface tension models for the VOF method is proposed by Baltussen et al. (2014).

4.8.2 Wall Adhesion Modeling

The wall adhesion phenomenon also known as wettability is the consequence of the interaction between the molecules of a solid and a liquid, which, provides an adhesive force between them. The force magnitude depends on the liquid and solid properties as well as the roughness of the surface considered. In the CSF model framework, the wetting phenomenon is simply expressed through the definition of θ_{eq} , the static contact angle, which is experimentally measured. Figure 4.6 shows the definition of θ_{eq} . The limiting cases are $\theta_{eq} = 0^\circ$ resulting in the liquid perfectly spreading on the surface as opposed to $\theta_{eq} = 180^\circ$ where the liquid does not wet the surface. A surface will be called hydrophilic if $\theta_{eq} < 90^\circ$ or hydrophobic if $\theta_{eq} > 90^\circ$.

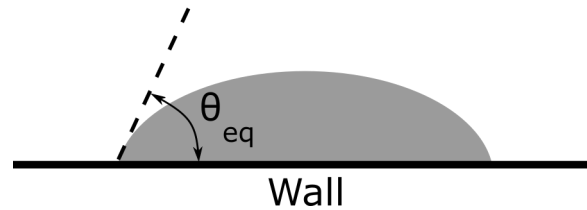


Figure 4.6: Wetting phenomenon

The knowledge of θ_{eq} in the work of Brackbill et al. (1992) is employed to calculate the normal vector to the interface at the wall using:

$$\mathbf{n} = \mathbf{n}_w \cos \theta_{eq} + \mathbf{t}_w \sin \theta_{eq} \quad (4.40)$$

where \mathbf{n}_w is the unit normal vector pointing towards the wall and \mathbf{t}_w is the unit vector that belongs to the wall and is normal to the contact line between the wall and the interface. The combination of this contact angle with the usually computed interface normal vector one cell away from the wall determines the local curvature of the surface. This curvature is further employed to adjust the surface tension body force term in the momentum equation.

4.9 Interface Reconstruction Algorithms

When studying multiphase flows, the key and the challenge to obtain an accurate modeling is a proper computation of the interface topology. This task is accomplished by the interface reconstruction algorithm that computes the interface normal vector and curvature. In the VOF framework, the interface reconstruction algorithm estimate the unit normal vector and curvature from the volume fraction gradient using equations (4.33) and (4.34). The variation between each interface reconstruction algorithm lies in the method employed to make this estimation. Several expectations can be set for an interface reconstruction algorithm.

- Precision on coarse grid
- Convergence as the grid refines
- Adaptable to any grid topology
- Simplicity of implementation

Algorithms that satisfy all the mentioned expectations are not yet available in the literature to the authors knowledge. The literature is rich and many approaches are available depending the accuracy required, the number of dimensions, and the mesh topology. This section offers a brief overview of the methods available.

The first method to geometrically reconstruct the interface was the PLIC algorithm developed by Youngs (1982). The interface is approximated to be a line in 2D or a plane in 3D. With knowledge of the volume fraction in the cell, the normal vector defined by equation 4.33, the interface position is retrieved. It is the only scheme available in ANSYS Fluent that uses a geometrical reconstruction. Unfortunately this method is poorly accurate and its major problem being the non convergence of the curvature when refining the mesh as shown by Magnini et al. (2013). Improving on Youngs algorithm was proposed by Williams et al. (2002) by simply using a smoothed version of the volume fraction field. The resulting normal vector and interface curvature converges with a first order accuracy.

Significant improvement came with the method called Parabolic Reconstruction Of Surface Tension (PROST) introduced by Renardy & Renardy (2002). This method approximates the interface as a parabolic curve in a 3-by-3 stencil. The coefficient of the parabola were obtained using a least-square fitting. A similar method, the Least squares Volume-of-fluid Interface Reconstruction Algorithm (LVIRA) further refined in Efficient LVIRA (ELVIRA) proposed by Pilliod & Puckett (2004) shows a second order accuracy in space. The main drawbacks of those methods are their computational costs along with implementation complexity in 3D unstructured mesh.

The last method category is called Height Function (HF) algorithm. Based on the work of Malik et al. (2007) in 2D, the interface curvature is locally calculated by finite difference in a 7-by-3 or 3-by-7 stencil depending the interface orientation by the means of an height function. The method was extended to 3D by Hernández et al. (2008) and showed a second order curvature accuracy while maintaining an acceptable computation efficiency.

Finally, aside from errors in the computation of the interface normal vector and curvature, the smearing of the interface due to numerical diffusion can also be problematic. To treat this problem, the solution is to artificially sharpen the interface. Following the works of Olsson & Kreiss (2005), it usually consist in adding an artificial viscosity to the marker function in order to maintain the interface thickness. The drawback of these sharpening schemes is the non respect of mass conservation as discussed by numerous authors (So et al. (2012); Sato & Ničeno (2012); Malgarinos et al. (2015)). In ANSYS Fluent, the unique sharpening scheme available is a so called γ model as described by Gupta et al. (2016).

CHAPTER 5

MASS TRANSFER MODELING

5.1 Mass Transfer Model in Multiphase Flows

The mass transfer phenomenon is important in a majority of process involving multiphase flows such as boiling/condensation, CO_2 capture or, in this case, desalination. In thermal desalination application, the heat and mass transfer problem cannot be decoupled as temperature is a catalyst for mass transfer and this latter represents a significant amount of energy transfer when phase change is involved. Therefore solving the heat transfer problem in parallel with the mass transfer is inevitable.

To predict mass transfer, several models have been developed and implemented in CFD solvers for different type of applications. Higbie (1935) developed the penetration model based on film theory. The model assumed a non equilibrium at the interface and mass transfer coefficient are calculated as follows:

$$k_l = 2\sqrt{\frac{D_l}{\pi t_c}} \quad (5.1)$$

$$k_g = 2\sqrt{\frac{D_g}{\pi t_c}} \quad (5.2)$$

where D_l and D_g are the liquid and gas diffusion coefficients respectively and t_c is the exposure time. The interphase mass flux is then retrieved by application of Fick's first law. The main drawback of the Higbie model is it assumes an infinitely developing boundary layer, which in most applications, is false as saturation is reached. Nonetheless it is successfully employed in various studies when the conditions are appropriate. Wen et al. (2020b) used this formulation to model condensation in falling films, van Baten & Krishna (2004) used it to simulate the mass transfer in Taylor bubbles and observed the CFD results deviating from the experimental for given conditions. Because of its ease of implementation, the penetration model is still employed in recent studies. Wen et al. (2020b) used a modified version of the Hibgie model in order to enhance the condensation process for falling film on flat plates.

Based on the Hertz-Knudsen equation, Schrage (1953) developed another model for mass transfer assuming a temperature and pressure jump at the interface.

$$\dot{m} = \frac{2\gamma}{2-\gamma} \left(\frac{M}{2\pi R} \right)^{1/2} \left(\frac{p_v}{\sqrt{T_v}} - \frac{p_l}{\sqrt{T_l}} \right) \quad (5.3)$$

where M is the molecular weight, R the universal gas constant, p_v and T_v , p_l and T_l , are the vapor and liquid pressures and temperatures at the interface. γ is a coefficient of accommodation depending on the fluid properties. It is difficult to measure experimentally with reasonable uncertainty as shown by Marek & Straub (2001). Therefore, the resulting mass transfer is highly dependent of that latter. Nonetheless, this formulation remains highly used for modeling boiling and condensation taking γ as unity for water systems Magnini & Thome (2016); Georgoulas et al. (2017).

A simplification of the Schrage model is the Lee model Lee (1980). It assumes a constant pressure and saturation temperature at the interface. The mass transfer rate is driven by the temperature gradient from saturation and defined as:

$$\dot{m} = \begin{cases} f_{Lee} \alpha_g \rho_g \frac{T - T_{sat}}{T_{sat}} & \text{if } T < T_{sat} \text{ (condensation)} \\ f_{Lee} \alpha_l \rho_l \frac{T - T_{sat}}{T_{sat}} & \text{if } T > T_{sat} \text{ (evaporation)} \end{cases} \quad (5.4)$$

where f_{Lee} is an accommodation coefficient that is fitted to experimental data. This make numerical results obtained using the Lee model as uncertain as the experimentally measured data which is a major flaw. This lack of physical meaning is essentially traded by the ease of implementation in numerical solvers.

Removing the empiricism of the Schrage and Lee models is achieved by the sharp interface model based on the Rankine-Hugoniot jump condition at the interface. Using energy conservation, the mass flux is expressed as

$$\dot{m} = \left(\frac{\lambda_l \nabla T_l - \lambda_g \nabla T_g}{h_{lg}} \right) \cdot \mathbf{n} \quad (5.5)$$

where λ_l and λ_g are the liquid and gas thermal conductivities, h_{lg} is the latent heat and \mathbf{n} the unit normal vector to the interface. This formulation is usually employed in CFD studies using

commercial software because of its simplicity and the accuracy provided Nichita & Thome (2010); Ganapathy et al. (2013).

Even if all these mass transfer models have proven their accuracy in capturing the physics in a wide variety of fundamental problems, they generally show one or multiple flaws. On the one hand, the Schrage, Lee and Sharp Interface model are only suitable when a non-condensable is not involved hence restricting them to boiling and condensation problem. In addition, the Schrage model require a suitable value for γ that is challenging to obtain. Similarly, the Lee model requires f_{Lee} , the accommodation coefficient which depends entirely on experimental data. On the other hand, the Higbie model relies on the value of exposure time, t_c , to calculate the mass transfer coefficients. The calculation of the exposure time is extremely dependent of flow conditions van Baten & Krishna (2004).

As a result, in this study, a model based on theoretical analysis is employed in order to remove the empiricism or the limit to a narrow range of flow conditions. The model employed, based on a direct application Fick's first law, is compatible with the presence of a non-condensable gas as it is the case in the evaporator or condenser of an HDH system. Finally, regardless of the model employed, an accurate computation of the interfacial area is necessary to accurately compute the mass transfer flux. The following section develops the mass transfer model implemented and the in algorithm employed.

5.2 Mass Transfer Model & Interfacial Area

5.2.1 Mass Transfer Model for Desalination

5.2.1.1 Modeling & Assumptions

Within an HDH system, the evaporation process is taking place at low temperatures through diffusion and convection in the presence of a non-condensable gas that is, by principle, used as a carrier for the water vapor. For economical purposes the carrier gas is usually air but other carrier could be employed as previously mentioned. In this study, the computation of the interfacial mass

transfer consist in a direct local application of Fick's first law of diffusion. Therefore, the need of empiricism for closure as well as the limitation to certain flow conditions are removed. In its most general form Fick's first law is written as follows:

$$\mathbf{J}_i = -\rho D_{ij} \nabla Y_i \quad (5.6)$$

where \mathbf{J}_i is the flux vector of species i into j , ρ is the mixture density, D_{ij} is the molecular diffusion coefficient and Y_i is the mass fraction of species i . Note that with this form of Fick's first law, \mathbf{J}_i as the dimension of a mass flux ($kg.m^{-2}.s^{-1}$). Assuming the diffusion of air in liquid water to be negligible, only the diffusion of water vapor in the gas remains. Therefore, the application of Fick's first law as described by equation (5.6) at an air-water interface with air assumed to be a single component gas yields:

$$\mathbf{J}_{H_2O/air} = -\rho D_{H_2O/air} \nabla Y_{H_2O} \quad (5.7)$$

5.2.1.2 Discretization of Fick's Law

The application of equation (5.7) onto a computational grid requires the discretization at the local scale. To model the diffusive mass flux, the assumption taken here is to treat the interface between air and water as a moving, internal, boundary condition. As a consequence, the air at the interface is assumed to be saturated with water vapor. In the numerical environment, this translate as treating the liquid to be an internal Dirichlet boundary condition for the species conservation equation. As a result, the mass fraction gradient in equation (5.7) to be along the interface normal vector \mathbf{n} :

$$\nabla Y_{H_2O} = \frac{\partial Y_{H_2O}}{\partial \mathbf{n}} = \nabla Y_{H_2O} \cdot \mathbf{n} \quad (5.8)$$

which is then discretized at the scale of a computational cell by applying a first order approximation:

$$\nabla Y_{H_2O} \cdot \mathbf{n} \approx \frac{Y^* - Y_\infty}{\Delta x} \quad (5.9)$$

$$\Delta x = (\mathbf{x}_G - \mathbf{x}_I) \cdot \mathbf{n} \quad (5.10)$$

where Y^* is the mass fraction corresponding to saturation that is assigned at the interface, Y_∞ is the current mass fraction of water vapor in the air, and Δx the characteristic length. In this work,

the normal distance Δx is taken as defined by equation (5.10) where \mathbf{x}_G is the position vector of the gravity center of the truncated cell and \mathbf{x}_I is the position vector of a point belonging to the interface. The interface is assumed to be flat locally, as depicted by Fig. 5.1. Combining equations (5.9) and (5.7) the mass flux is approximated as follows:

$$J^* = \rho D_{H_2O/air} \frac{Y^* - Y_\infty}{\Delta x} \quad (5.11)$$

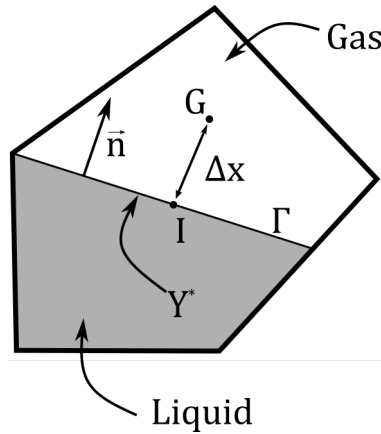


Figure 5.1: Interfacial cell

The calculation of Δx , the characteristic length, requires knowledge of the coordinates of G (see Fig. 5.1) which can only be determined by knowing the exact position of the interface. By default, even if computed, the position of the interface is not available to the user in ANSYS Fluent. Hence, an in-house geometric reconstruction is necessary to retrieve the interface position.

5.2.2 Volume Enforcement Algorithm

Retrieving the interface position knowing the interface orientation and the volume of fluid in a cell is a classic volume enforcement problem which can be solved using different scheme. The assumption of a flat interface, line in 2D or plane in 3D naturally leads to employing a PLIC scheme. Several algorithms are available in the literature, Rider & Kothe (1998), López & Hernández (2008), Soh et al. (2016) to reconstruct the interface using a geometrical interpretations. In this study, the algorithm implemented to retrieve the interface position is based on the work of López et al. (2016)

and is detailed here. The example taken here is for a general cell with a J amount of faces, N number of vertices, and an I_j number of vertices per face.

5.2.2.1 Initial Bracketing

At the beginning of the calculation the only known cell variable are the volume fraction, the interface normal unit vector, and the coordinates of the cell vertices in the domain. In the case of the VOF method it yields:

$$\mathbf{n} = \frac{\nabla\alpha}{|\nabla\alpha|} \quad (5.12)$$

$$V_T = \alpha V_{cell} \quad (5.13)$$

As the volume enforcement is solved iteratively, providing an adequate initial guess is very important in order to obtain an computationally efficient algorithm. In this case, the initial values takes the form of guessing the upper and lower bound position of the interface position along the normal vector direction. The initial bracketing starts by calculating d_n , the signed normal distance from the interface for each cell vertices.

$$d_n = \mathbf{x}_n \cdot \mathbf{n} \quad (5.14)$$

where \mathbf{x}_n is the position vertex position vector in the domain. Using equation (5.14), the position of each vertex relatively to the interface can be determined. The vertices at a minimum and maximum distance from the interface immediately yield the nodes corresponding to an empty and a full cell. As shown in the example depicted by Fig. 5.2 the vertices corresponding to an empty and full cell are $n = 1$ and $n = 3$.

The vertexes are then sorted in growing d_n order. In the example shown the ordained list is given in Table 5.1. Note that the distances d_n given here are arbitrary and only used as example. An index k is assigned to each vertex once ordained.

$$d_{ib} = \frac{V_T - V_{min}}{V_{max} - V_{min}} (d_{max} - d_{min}) + d_{min} \quad (5.15)$$

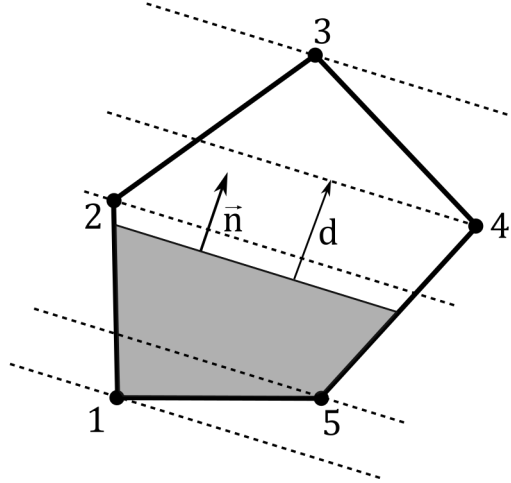


Figure 5.2: Interfacial cells after initial calculation for bracketing

Table 5.1: Ordained list of vertexes by signed distance from the interface

<i>Vertex number</i>	1	5	2	4	3
d_n	-2	-1	1	2	4
k	1	2	3	4	5

The next step in the calculation consist in using equation (5.15) with d_{min} corresponding to the signed distance of an empty cell and d_{max} the signed distance of a full cell. In the example depicted by Fig. 5.2, assuming $\alpha = 0.45$ the initial linear interpolation is done between the vertex number 1 and number 3 yielding:

$$d_{ib}^0 = 0.45 (d_3 - d_1) + d_1 = 0.7 \quad (5.16)$$

Based on that value of d_{ib}^0 the closest plane passing through one of the cell vertex is selected and an exact calculation of the truncated volume is obtained using the algorithm developed in section 5.2.2.2. The resulting volume, V_{ib} is compared to the targeted volume V_T .

On the one hand, if $V_{ib} > V_T$, then the selected vertex is assigned the upper bound (k_{max}) and a new truncation is done using the next cell vertex in descending sequence until $V_{ib} < V_T$. After each truncation the upper bound is updated.

On the other hand, if $V_{ib} < V_T$, the selected vertex is assigned the lower bound and a new truncation is done using the next cell vertex in ascending sequence until $V_{ib} > V_T$. At the end of

this routine, two cell vertices are defined as k_{min} and k_{max} respecting the conditions:

$$\begin{cases} V_{k_{min}} < V_T < V_{k_{max}} \\ k_{max} - k_{min} = 1 \end{cases} \quad (5.17)$$

Applying this procedure to the picture shown in Fig. 5.2 yields $V_{ib} = V_2$ which is superior to V_T . Hence, the value $k_{max} = 3$ (corresponding to vertex number 2, see Table 5.1) for the upper bound is selected and a new volume calculation is done using vertex number 5 that yields $V_5 < V_T$. Thus yielding the lower bound of the bracketing since the condition $k_{max} - k_{min} = 1$ is respected.

Finally with the initial bracketing obtained, a new linear interpolation is accomplished using equation (5.15) with $V_{min} = V_{k_{min}}$, $V_{max} = V_{k_{max}}$ and $d_{min} = d_{k_{min}}$, $d_{max} = d_{k_{max}}$. The new volume calculated, V_{i+1} , is used to update the value of V_{min} or V_{max} and d_{min} or d_{max} following:

$$\begin{cases} V_{min} = V_{i+1} & \text{if } V_T > V_{i+1} \\ V_{max} = V_{i+1} & \text{if } V_T < V_{i+1} \end{cases} \quad (5.18)$$

This process is repeated until the calculated volume is within 1% of the cell total volume.

5.2.2.2 Volume Calculation & Interfacial Area

The first step in the volume calculation of the truncated polyhedron is to determine the coordinates of the intersection points between the plane and the edges of the cell. For example, using the case depicted by Fig. 5.3 it consists in obtaining the position vectors of the vertices 8, 9, 10 and 11.

Knowing the normal distance from each cell vertex (d_n) to the truncation plane, a linear interpolation yields the intersection position vector \mathbf{x}_{inter} as follows:

$$\mathbf{x}_{inter} = \mathbf{x}_+ - \frac{d_+}{d_- - d_+} (\mathbf{x}_- - \mathbf{x}_+) \quad (5.19)$$

where \mathbf{x}_+ and \mathbf{x}_- denotes the vertexes above and below the truncation plane with respect of the normal vector orientation. d_+ and d_- are calculated using equation (5.14). As example, the intersection point calculation between vertex 6 and 1 is obtained as $\mathbf{x}_{10} = \mathbf{x}_6 - \frac{d_6}{d_1 - d_6} (\mathbf{x}_1 - \mathbf{x}_6)$.

When all the intersection points are known, the volume of the truncated polyhedron is calculated

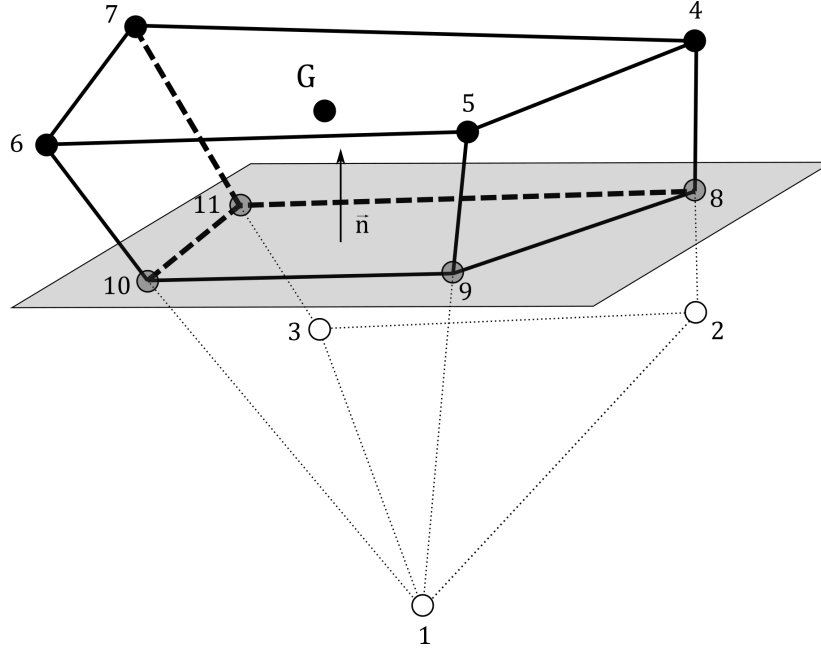


Figure 5.3: Truncated polyhedron with intersection points

using the formula given by Schneider & Eberly (2003):

$$V = \frac{1}{3} \sum_{j=1}^J \left[(\mathbf{n}_j \cdot \mathbf{x}_{j,1}) \mathbf{n}_j \cdot \mathbf{A}_j \right] \quad (5.20)$$

where \mathbf{A}_j is the area vector of face j with an I_j number of vertices within a polyhedron with J faces. \mathbf{n}_j is the unit normal vector to face number j pointing outward of the polyhedron. The area vector is obtained as follow:

$$\mathbf{A}_j = \frac{1}{2} \sum_{i=1}^{I_j} (\mathbf{x}_{j,i} \times \mathbf{x}_{j,i+1}) \quad (5.21)$$

where $\mathbf{x}_{j,i}$ is the position vector of the i -th vertex of the j -th face, ordered counterclockwise from an outside point of view of the polyhedron. Note that $\mathbf{x}_{j,I_j} = \mathbf{x}_{j,1}$.

It is now evident that the computation of the truncated polyhedron volume implies the calculation of the area vector which, in Fig. 5.3, corresponds to the area of the polygon defined by the vertices $\{8; 9; 10; 11\}$. Per definition, the effective area, A_{int} , is simply calculated by taking the norm of the area vector. When the volume calculation is converged, the position vector of the gravity center is

extracted using equation (5.22) and Δx is retrieved using equation (5.10).

$$\mathbf{x}_G = \frac{1}{N_{trunc}} \sum_{i=1}^{N_{trunc}} \mathbf{x}_i \quad (5.22)$$

where N_{trunc} is the amount of vertices of the truncated polyhedron.

5.3 ANSYS Fluent Solver and Implementation of User-Defined-Functions

ANSYS Fluent is a commercial solver for computational fluid dynamic that is widely employed in the industry and in academic research. The version employed in this work is the 19.2 with double precision to limit the truncation error. The parallel version of the solver is employed since all calculations are accomplished in an High Performance Computing (HPC) environment. Even if the solver has made a lot of improvements in its last release, it remains critically lacking for complex flow problems which is the case here. To overcome this issue, the software allows partial modification of the solver through the so called User-Defined Functions (UDF) that are written in C or C++. These UDFs are further compiled and added to the solver to orient the code toward the seek usage. Therefore, the modeling developed in section 5.2 is implemented in the solver using UDFs. The goal of this section is to introduce the reader to the setup employed in this work to solve the partial differential equations governing the physics we are aiming to model as well as an introduction of the UDFs employed to achieve that goal.

5.3.1 Governing Equations & Source Terms

In this work, the flow solver requires the solution of 7, non-linear, partial differential equations: continuity equation (4.8), volume fraction equation (4.36), momentum equation (4.9) in the three space coordinates, the energy equation (4.10), and the species conservation to track the water vapor concentration in the non-condensable gas. Within the VOF framework of ANSYS Fluent, the two Newtonian and incompressible phases with mass transfer assuming laminar flow results in the following equations. Note that the viscous heating terms are neglected in the energy equation and α , by choice, represents the gas volume fraction. The liquid mass fraction is simply retrieved using

equation (4.31).

$$\nabla \cdot \mathbf{u} = \left(\frac{1}{\rho_g} - \frac{1}{\rho_l} \right) S_\alpha \quad (5.23)$$

$$\frac{\partial \alpha}{\partial t} + \nabla \cdot (\alpha \mathbf{u}) = \frac{S_\alpha}{\rho_g} \quad (5.24)$$

$$\frac{\partial}{\partial t} (\rho \mathbf{u}) + \nabla \cdot (\rho \mathbf{u} \mathbf{u}) = -\nabla p + \nabla \cdot \mu \left[(\nabla \mathbf{u}) + (\nabla \mathbf{u})^T \right] + \rho \mathbf{g} + \mathbf{F}_\sigma + \mathbf{F}_{buoy} \quad (5.25)$$

$$\frac{\partial}{\partial t} (\rho E) + \nabla \cdot (\rho \mathbf{u} E) = \nabla \cdot (\lambda \nabla T) + S_E \quad (5.26)$$

$$\frac{\partial}{\partial t} (\rho_g Y_{H_2O}) + \nabla \cdot (\rho_g \mathbf{u} Y_{H_2O}) = \nabla \cdot (\rho_g D_{H_2O/air} \nabla Y_{H_2O}) + S_{Y_{H_2O}} \quad (5.27)$$

In the above equations the source terms S_α , S_E , and S_{Y_i} are the source terms due to the evaporative mass transfer and are defined as follows:

$$S_\alpha = J^* \frac{A_{int}}{V_{cell}} \quad (5.28)$$

$$S_E = -S_\alpha h_{lg} \quad (5.29)$$

$$S_{Y_{H_2O}} = S_\alpha \quad (5.30)$$

where A_{int} is the interfacial area calculated by the volume enforcement algorithm and h_{lg} is the latent heat of vaporization. This normalization per unit volume of the source terms using V_{cell} is necessary as Fluent employs a finite-volume method to solve the governing equations. The fluid properties are calculated using equation (4.12) which, in the case of the VOF framework leads to:

$$\begin{cases} \rho = \alpha \rho_g + (1 - \alpha) \rho_l \\ \mu = \alpha \mu_g + (1 - \alpha) \mu_l \\ \lambda = \alpha \lambda_g + (1 - \alpha) \lambda_l \end{cases} \quad (5.31)$$

Note that each individual phase properties remains defined by the user.

5.3.2 Fluent Discretization Method

Similarly to any numerical approach, the set of governing equation needs to be discretized. As Fluent employs a finite volume method (FVM), the transport equations are integrated over a control

volume that, once discretized, transforms the set of non-linear equations into a discrete system of linear equations further solved numerically. For a generic variable ϕ , the transport equation is:

$$\frac{\partial}{\partial t} (\rho\phi) + \nabla \cdot (\rho\mathbf{u}\phi) = \nabla \cdot (D\nabla\phi) + S_\phi \quad (5.32)$$

where D is a generic diffusion coefficient. Applying to a control volume Ω with a surface area Γ , the above equation becomes:

$$\underbrace{\int_{\Omega} \frac{\partial}{\partial t} (\rho\phi) d\Omega}_{\text{unsteady term}} + \underbrace{\int_{\Omega} \nabla \cdot (\rho\mathbf{u}\phi) d\Omega}_{\text{convective term}} = \underbrace{\int_{\Omega} \nabla \cdot (D\nabla\phi) d\Omega}_{\text{diffusion term}} + \underbrace{\int_{\Omega} S_\phi d\Omega}_{\text{source term}} \quad (5.33)$$

Using the divergence theorem, the convective and diffusion terms in equation (5.33) become:

$$\int_{\Omega} \nabla \cdot (\rho\mathbf{u}\phi) d\Omega = \int_{\Gamma} (\rho\mathbf{u}\phi) \cdot \mathbf{n} d\Gamma \quad (5.34)$$

$$\int_{\Omega} \nabla \cdot (D\nabla\phi) d\Omega = \int_{\Gamma} (D\nabla\phi) \cdot \mathbf{n} d\Gamma \quad (5.35)$$

where \mathbf{n} is the unit normal vector pointing outside of the control volume. Within FVM the control volume is the cell volume.

Assuming the value at the center of the cell is equal to the average of the function in the cell, the unsteady and source terms are estimated by multiplying the average value by the cell volume. Using a similar assumption, and assuming the value of the term at the cell center is the average of the function over all the cell faces and the value at each face is equal to the average of the function over that face multiplied by the surface area, the surface integrals in equations (5.34) and (5.35) are estimated for a cell with N_f faces as follows:

$$\int_{\Gamma} (\rho\mathbf{u}\phi) \cdot \mathbf{n} d\Gamma = \sum_1^{N_f} (\rho_f \mathbf{u}_f \phi_f) \cdot \mathbf{n}_f A_f \quad (5.36)$$

$$\int_{\Gamma} (D\nabla\phi) \cdot \mathbf{n} d\Gamma = \sum_1^{N_f} (D_f (\nabla\phi)_f) \cdot \mathbf{n}_f A_f \quad (5.37)$$

where the subscript f designate the face centered value of the variable. Hence the discretized version of equation (5.33) is:

$$\frac{\partial}{\partial t} (\rho_c \phi_c) \Omega + \sum_1^{N_f} (\rho_f \mathbf{u}_f \phi_f) \cdot \mathbf{n}_f A_f = \sum_1^{N_f} (D_f (\nabla\phi)_f) \cdot \mathbf{n}_f A_f + S_\phi \Omega \quad (5.38)$$

where the subscript c designate the cell centered value of the variable. Note that the source term S_ϕ is always applied at the cell center.

5.3.3 Reconstruction of Cell Gradient

Within Fluent, the governing equations are solved using variables at the cell center. As a result, knowledge of the gradients involved in these equations at that location is required. Using Green-Gauss theorem, the gradient at the cell center is expressed as follows:

$$(\nabla\phi)_c = \frac{1}{\Omega} \sum_1^{N_f} \phi_f \mathbf{n}_f A_f \quad (5.39)$$

As a consequence, calculating the value of the cell centered gradients requires knowledge of the face centered value (ϕ_f) for all faces within a cell. Within Fluent, several interpolation schemes are available, Green-Gauss Cell Based, Green-Gauss Node Based and Least-Square Cell Based ANSYS Inc. (2018). In this work the Least-Square Cell Based formulation is employed unless stated otherwise because it yields a similar accuracy on unstructured mesh as the Green-Gauss Node Based but with a far inferior computational cost.

5.3.4 Temporal Discretization

Solving numerically partial differential equations for unsteady flows, all the terms are summed in order to obtain the temporal derivative and then update the solution to the next time step. Two types of temporal discretization exist: explicit and implicit. Depending the types of partial differential equations, hyperbolic, parabolic or elliptic, one or the other should be employed Anderson (1995). Using a first order scheme, the unsteady term is expressed as follows:

$$\frac{\phi^{n+1} - \phi^n}{\Delta t} = F(\phi^n) \quad (5.40)$$

while the implicit formulation takes the following form:

$$\frac{\phi^{n+1} - \phi^n}{\Delta t} = F(\phi^{n+1}) \quad (5.41)$$

where $F(\phi^n)$ represent all the convective, diffusive and source terms in equation (5.38) at time step n and Δt is the time step size. The explicit formulation is consistent but usually requires a small time step to be stable. On the opposite the implicit formulation is unconditionally stable but requires an iterative process at each time-step to solve the transport equations. For Fluent incompressible solver, only the implicit time-stepping method is available to solve all the conservation equations except the VOF equation. This latter is solved explicitly using a sub time-stepping method to maintain stability. In this work, the first order implicit formulation is employed for the time discretization for two reasons. Firstly it is the only time stepping method available when using the geometric reconstruction algorithm. Secondly, the second-order temporal discretization method is necessary when important temporal gradients are expected in the simulation and are of interest to the user which is not the case here as a pseudo-transient solution is targeted.

5.3.5 Spatial Discretization

The spatial discretization scheme is in charge of interpolating the face centered variable (ϕ_f) with the cell centered value (ϕ_c) for the convective term of each conservation equation. Note that the diffusion term is always discretized using a central differencing which is a second order accuracy scheme. Fluent possesses multiple schemes to interpolate the face centered value that can be adjusted for each equation individually. In this study all the convective term are spatially discretized using Quadratic Upstream Interpolation for Convective Kinematics (QUICK) introduced by Leonard (1979).

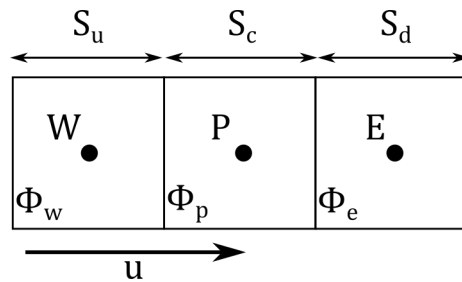


Figure 5.4: Spatial discretization with QUICK scheme

For face e the face centered variable is expressed as follows:

$$\phi_e = \theta \left[\frac{S_d}{S_c + S_d} \phi_P + \frac{S_c}{S_c + S_d} \phi_E \right] + (1 - \theta) \left[\frac{S_u + 2S_c}{S_u + S_c} \phi_P - \frac{S_c}{S_u + S_c} \phi_W \right] \quad (5.42)$$

Immediately, if $\theta = 1$ equation (5.42) yields a central second order interpolation and $\theta = 0$ yields second order upwind interpolation. The original formulation of the QUICK scheme used $\theta = 1/8$ but in Fluent this value is adjusted depending the flow conditions and the cells topology. On hybrid meshes, Fluent will use the second order upwind scheme at non hexahedral cells and at partition cell boundaries when the parallel solver is employed which is the case here. Hence the use of the QUICK scheme is ensuring a stable second order accuracy.

5.3.6 Pressure-Velocity Coupling

Numerically solving the Navier-Stokes equation requires a minimum of knowledge about the flow pattern in order to determine the approach one should take. At low Mach number ($Ma \ll 1$), the fluids are considered incompressible. Therefore, the coupling between density and pressure is weak and the former is not considered as a variable that needs to be calculated. In that case, the pressure is considered an independent variable and solving the continuity equation is reduced into solving the pressure equation (Poisson equation). On the opposite, for high Mach number, compressibility effects are not negligible anymore and a density field must be obtained by solving the continuity equation and pressure is retrieved with a state equation. Within Fluent, these two distinguishable approach are called *pressure-based* and *density based*. In this work, since $Ma \ll 1$, only the *pressure-based* approach is used and the continuity and momentum equations are solved using a segregated algorithm.

Originally, the continuity and momentum are 4 equations (3D environment) that are coupled and non-linear. The segregated approach allows to solve them sequentially with an iterative process until convergence for momentum is reached and continuity is respected. Segregated approach consist in a predictor-corrector fashion to predict the velocity and pressure field. Using the momentum equation and an initial guess on the pressure field, a velocity field is calculated (predictor). Then,

with that previously calculated velocity field a pressure correction equation is solved to obtain a new pressure field used to correct the initial velocity field that respects continuity.

Fluent offers several options to accomplish that prediction-correction such as Semi Implicit Method for Pressure Linked Equation (SIMPLE) or SIMPLE Consistent (SIMPLEC) that are often employed in the literature. Here because it is the most robust and computationally efficient on hybrid meshes, the Pressure Implicit Splitting of Operator PISO algorithm is employed Issa (1986). As shown by Magnini et al. (2013), the PISO algorithm reaches convergence faster than others pressure-velocity coupling methods.

Finally, the use of the FVM requires knowledge of the pressure at the face centroid that is not available since a staggered grid is employed to respect continuity. As a result, the pressure is known at the cell center and the velocity at the face center thus requiring an interpolation for the pressure from the cell centroid to the face centroid. Different schemes are available in Fluent to accomplish this interpolation. Here, because of the surface tension modeling, the spurious velocities must be maintained to a minimum in order to maintain accuracy and stability. Therefore, the PREssure STaggering Option (PRESTO) scheme is used. It solves the pressure correction equation on a staggered volume which directly evaluate the pressure at the face center. Hence, the need of interpolation is removed. As a consequence, the part of the spurious currents arising from the interpolation error is also non-existent.

5.3.7 Implementation of User Defined Functions

The implementation of the algorithm presented in section 5.2.2 is accomplished using multiple User Defined Functions. Multiple type of UDF are available in Fluent depending the task the user aim to achieve and the model employed. Here is a list of the type of UDF employed in this work and their purpose.

- *Define Profile*: Defining a field profile such as velocity profile at an inlet for the validation case.

- *Define Adjust*: Function executed at the beginning of each iteration to modify or extract variable. In this work, it is employed to extract the volume fraction gradient and to correct the mass fraction value in the interfacial cells.
- *Define Source*: Adding source terms to conservation equations.
- *Define Mass Transfer*: Implementation of interphase mass transfer. The mass transfer model in this work is implemented using this framework.
- *Define Execute at End*: Called at the end of each time step, this type of UDF can be used for multiple purposes: compute variables, modify variables, write text files. In this work it was use to write monitoring and controls text files.
- *Define Properties*: Custom laws or values for fluid properties such as density, viscosity among others. Here it is used to implement a temperature dependent molecular diffusivity or enforce a constant density in multicomponents phase.

CHAPTER 6

VALIDATION OF THE NUMERICAL FRAMEWORK

As rigorous as the mathematics involved in numerical modeling may be, the need for validation benchmark is always critical to justify the assumptions taken. For this study, two validation cases are employed. The first benchmark, is a classic static droplet which, is often employed in the literature as a benchmark for surface tension models as well as measuring the accuracy of the curvature and interface normal vector computation. Here, this latter is employed to assess the accuracy of the interfacial area computation. The second test, consists in simulating a gas flowing above a body of fluid to test the validity of Fick's law first order approximation at the interface.

6.1 Accuracy of Interfacial Area Computation: Single Static Droplet

The static droplet in equilibrium is a classic test case in numerical multiphase flows studies to assess the accuracy of CFD solvers in computing curvature and normal vector as well as their stability and convergence (Soh et al. (2016); Magnini et al. (2013)). Here, it is employed to validate the interfacial area calculation on various type of meshes. As a consequence, various meshes are generated using Fluent Meshing software with three different cell topologies as shown by Fig. 6.1. Fig. 6.1a is an hexahedral core mesh, Fig. 6.1b is a tetrahedral mesh, and Fig. 6.1c is a polyhedral mesh.

The domain consist of a cube with a 100 mm edge length that is meshed using tetrahedral, hexahedral and polyhedral cells with similar targeted metric. The resulting metrics are summed up in Table 6.1. The calculation consist in initializing a static 10 mm radius sphere of water at the center of the domain with all the domain boundaries set as walls.

Usually authors in the literature use this technique to compute magnitude of the velocity field arising (spurious currents) due to the numerical errors. In the absence of gravity and a nil initial velocity, only the surface tension forces and pressure gradient remain non nil in the momentum equation. Therefore, these two terms should be in perfect equilibrium and no velocity field should

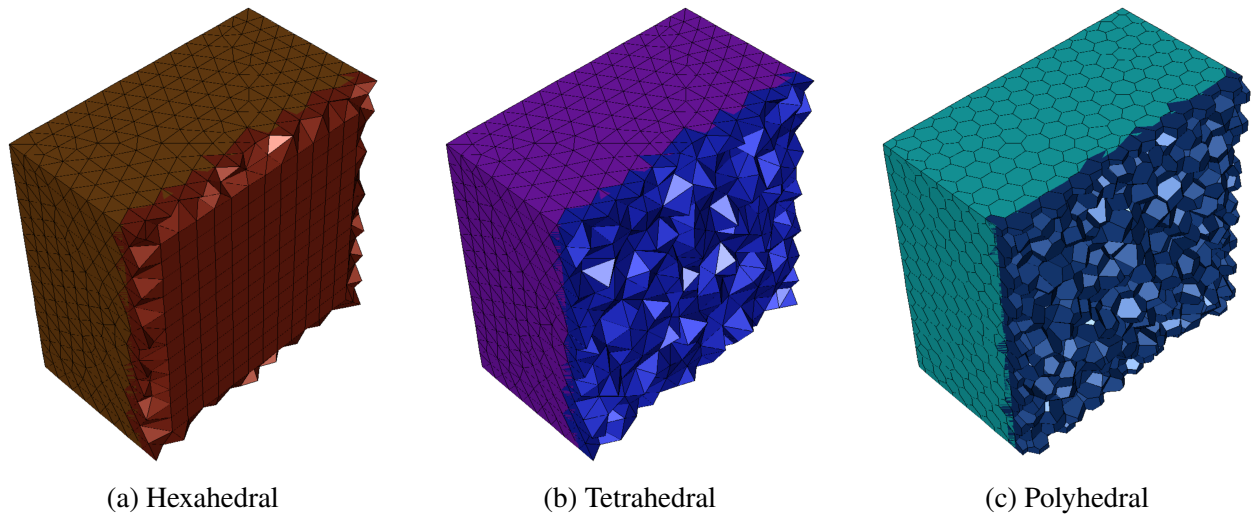


Figure 6.1: Mesh with different cell topologies

arise. Here, this benchmark is employed to compute the interfacial area yielded by the in-house volume enforcement algorithm and compare with the $|\nabla\alpha|$ commonly employed in the literature. In order to initialize a sphere at the domain center, the user inputs the sphere radius and centroid coordinates. Then, the solver sets the volume fraction to unity at any cell centroid that is contained in this defined sphere. As a result, the initialized sphere is not exactly as defined by the user.

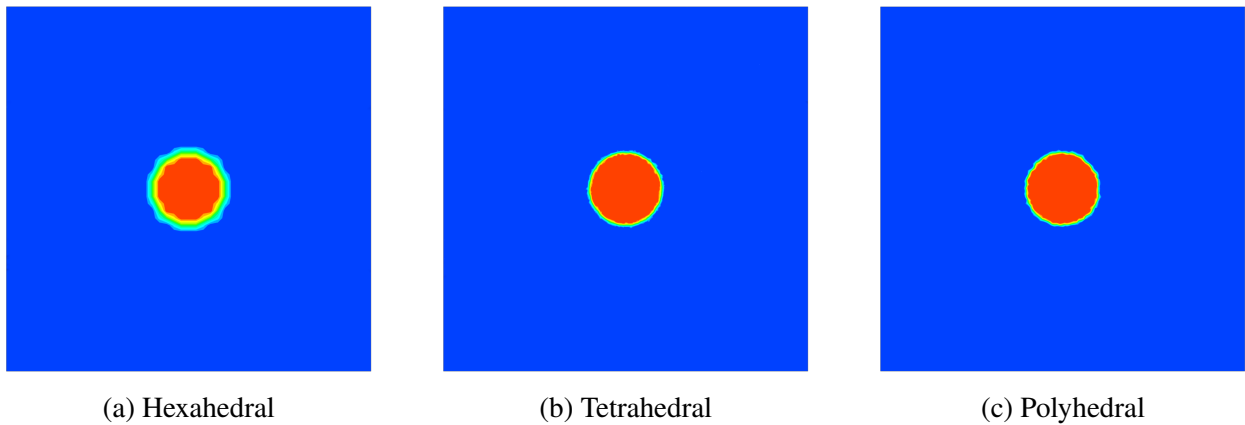


Figure 6.2: Contour of the initial liquid volume fraction for the various mesh topologies

In order to suppress this error, the calculation of an equivalent diameter based on the mass of liquid in the domain at initialization is employed. The radius, r_{eq} , is then used to calculate the

theoretical area A_{eq}

$$r_{eq} = \sqrt[3]{\frac{3}{4} \frac{m_l}{\rho_l \pi}} \quad (6.1)$$

$$A_{eq} = 4\pi r_{eq}^2 \quad (6.2)$$

where m_l is the mass of liquid computed by the solver after initialization and ρ_l is the liquid density. Because of the natural instability of Young's algorithm, the interface reconstruction algorithm, and its non convergence as the mesh refines the reported areas are time averaged. The procedure consist in averaging the computed area over a 100 time steps where $\Delta t = 5 \cdot 10^{-5} s$. The results are compiled in Table 6.1.

Table 6.1: Mesh metrics and results

<i>Topology</i>	Tetrahedral	Hexahedral	Polyhedral
<i>Cell count</i>	9,332,973	681,869	1,619,210
$A_{min} \text{ (m}^2\text{)}$	6.805×10^{-8}	9.16×10^{-8}	1.15×10^{-9}
$A_{max} \text{ (m}^2\text{)}$	9.63×10^{-7}	4.00×10^{-6}	1.23×10^{-6}
$V_{min} \text{ (m}^3\text{)}$	6.80×10^{-12}	1.96×10^{-11}	7.28×10^{-11}
$V_{max} \text{ (m}^3\text{)}$	2.92×10^{-10}	8.00×10^{-9}	9.86×10^{-10}
$A_{eq} \text{ (m}^2\text{)}$	1.257×10^{-3}	1.302×10^{-3}	1.256×10^{-3}
$A_{PLIC} \text{ (m}^2\text{)}$	1.188×10^{-3}	1.285×10^{-3}	1.477×10^{-3}
$A_{ \nabla\alpha } \text{ (m}^2\text{)}$	7.290×10^{-4}	6.209×10^{-4}	5.684×10^{-4}
$\varepsilon \text{ (\%)} $	5.49	1.30	17.5

As shown by the results in Table 6.1, the in-house algorithm is far more accurate than the usual $|\nabla\alpha|$ formulation of the interfacial area that shows an error above 40% on all topologies. The results also show low order cells (tetrahedral and hexahedral) to be preferable in regard of area computation than polyhedral due to a smaller interpolation error between the face and cell center.

6.2 Validation of Mass Transfer Modeling

The previous section showed the accuracy of the interfacial area computation for any type of convex grid. Nonetheless, it is necessary to verify if the first order approximation of Fick's first law

and the assumption taken on the characteristic length (Δx) defined by equations (5.9) and (5.10), are valid. The following section consist in a test case that allows a direct comparison of numerical results with a newly developed analytical solution.

6.2.1 Flow Over a Stationary Body of Fluid

6.2.1.1 CFD Domain Generation

Flow of gas over a stationary body of liquid is a classic test case for mass advection-diffusion and is used here to validate the mass transfer model. Figure 6.3 depicts the numerical domain and the associated surfaces. The bottom part of the domain is filled with a liquid. The gas enters at the inlet with a fully-developed parabolic velocity profile (laminar flow) and flows over the body of liquid. The mass transfer model assumes a constant concentration at the interface between liquid and gas (Y^*), and the liquid naturally evaporates into the gas phase creating a species concentration boundary layer. Table 6.2 specifies the type of boundary conditions applied to each surface of the computational domain.

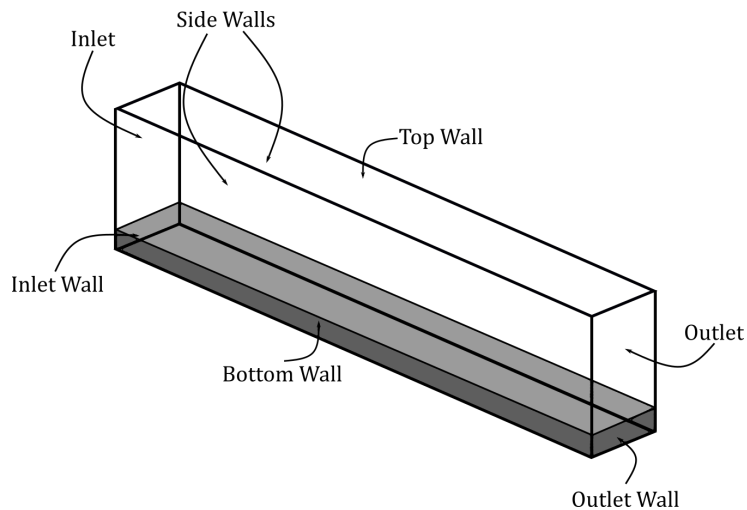


Figure 6.3: 3-D cartesian numerical domain

The slip boundary condition applied on the side walls allows this three-dimensional problem to be reduced to a two-dimensional problem for all the governing equations. As a consequence, if only the gas phase is considered, this allows the comparison of the CFD results with a solution

Table 6.2: Boundary conditions applied in the cartesian numerical model

<i>Boundary</i>	<i>Hydrodynamic</i>	<i>Species</i>
Inlet	Velocity Inlet ($V_x(y)$)	$C_0 = 0$
Outlet	Pressure Outlet	Zero flux
Top Wall	No Slip	$C_0 = 0$
Bottom Wall	No Slip	Zero flux
Outlet Wall	No Slip	Zero flux
Inlet Wall	No Slip	Zero flux
Side Walls	Slip	Zero flux

of the species equation that can be solved analytically. Hence, for this test case, two models are employed to compute the characteristic length Δx . The first, PLIC-1, correspond to the value given by equation (5.10). The second, PLIC-2, is defined as:

$$\Delta x = \sqrt[3]{\alpha V_{cell}} \quad (6.3)$$

The formulation of Δx using equation (6.3) is simpler and computationally very efficient since, the costly calculation of the volume enforcement problem is removed. The downside of this method is the non computation of the interfacial area. Therefore, the calculation of this latter relies on the $|\nabla\alpha|$ formulation. In order to obtain a consistent comparison between PLIC-1 and PLIC-2, this formulation of the interfacial area is employed for both methods. In both cases, similarly to Soh et al. (2016), a volume fraction cut-off $0 < \alpha < 0.95$ is employed to take into account interface smearing as well as properly identify interfacial cells. It also prevent the concentration gradient to go to infinity when α goes to unity.

6.2.1.2 Analytical Domain

The analytical solution consists in solving the species conservation equation in the gas phase as shown in Fig. 6.4. In cartesian coordinates the species conservation equation without source term is:

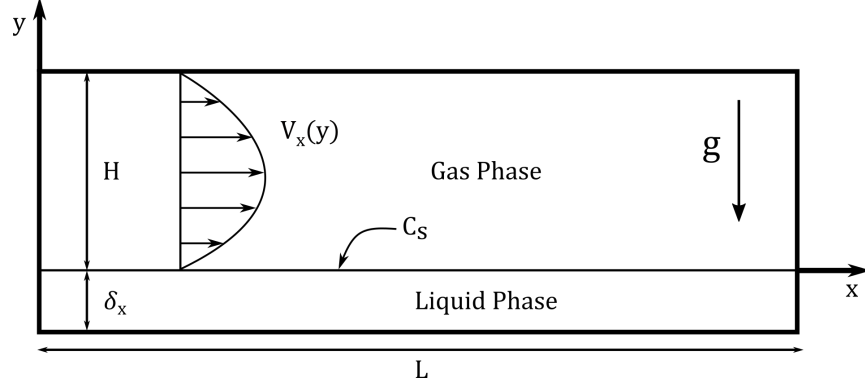


Figure 6.4: 2-D projection of the 3-D cartesian numerical domain

$$\frac{\partial C}{\partial t} + \frac{\partial(V_x C)}{\partial x} + \frac{\partial(V_y C)}{\partial y} + \frac{\partial(V_z C)}{\partial z} = \frac{\partial}{\partial x} \left(D_x \frac{\partial C}{\partial x} \right) + \frac{\partial}{\partial y} \left(D_y \frac{\partial C}{\partial y} \right) + \frac{\partial}{\partial z} \left(D_z \frac{\partial C}{\partial z} \right) \quad (6.4)$$

where C is the concentration, \mathbf{V} is the velocity vector, and D the molecular diffusion. For a two-dimensional steady-state problem considering a fully developed laminar flow with an isotropic and constant molecular diffusion, the equation simplifies to:

$$\frac{\partial^2 C}{\partial x^2} + \frac{\partial^2 C}{\partial y^2} - \frac{V_x(y)}{D} \frac{\partial C}{\partial x} = 0 \quad (6.5)$$

$$V_x(y) = -a_0 y^2 + b_0 y + c_0 \quad (6.6)$$

where the velocity profile, $V_x(y)$, is the solution of the Navier-Stokes equations for laminar flow.

The exact solution of equation (6.5) is developed in Appendix B and is given as follows:

$$C(x, y) = C_s \left(1 - \frac{y}{H} \right) + \sum_{n=0}^{\infty} A_n C_n(y) e^{-\alpha_n^2 x} \quad (6.7a)$$

$$C_n(y) = C_1 U \left(a, \varepsilon_n \left(y - \frac{B}{2A} \right) \right) + C_2 V \left(a, \varepsilon_n \left(y - \frac{B}{2A} \right) \right) \quad (6.7b)$$

$$A_n = \frac{\int_0^H (C_0(y) - \phi(y)) C_n(y) w(y) dy}{\int_0^H w(y) C_n^2(y) dy} \quad (6.7c)$$

$$w(y) = \frac{V_x(y)}{D} \quad (6.7d)$$

6.2.1.3 CFD-Analytical Linkage

Since the liquid-gas interface is not a rigid wall, the shear continuity existing between gas and liquid creates a residual inter-facial velocity which, may lead to local Kelvin-Helmholtz instabilities in the CFD simulation. This phenomenon being dependent on the fluid viscosity ratios, the fluid viscosities are increased compared to an air/water system. As such, the fluid and mass problem can be decoupled, which only requires solution of equation (6.5), while treating the liquid as a Dirichlet boundary condition for the species equation. Figure 6.4 is a 2D projection of the three dimensional numerical domain. The parameters used for the numerical solution are shown in Table 6.3.

Table 6.3: Domain dimensions and fluid properties

(a) Domain dimensions			(b) Fluids Properties		
<i>Parameter</i>	<i>Value</i>	<i>Unit</i>	<i>Parameter</i>	<i>Value</i>	<i>Unit</i>
a_0	4.9383×10^4	$m^{-1}.s^{-1}$	D	2.88×10^{-5}	$m^2.s^{-1}$
b_0	444.44	s^{-1}	C_s	0.013986	$mol.L^{-1}$
c_0	0	$m.s^{-1}$	ρ_l	998.2	$kg.m^{-3}$
H	0.009	m	μ_l	0.5	$kg.m^{-1}.s^{-1}$
L	0.1	m	ρ_g	1.225	$kg.m^{-3}$
δ	0.001	m	μ_g	0.001	$kg.m^{-1}.s^{-1}$

6.2.1.4 Results & Discussion

In order to validate the computational approach, grid independence is first established. This is accomplished using the overall mass transfer rate in the domain at steady-state. Therefore, the mesh employed in this section consist of 575,000 hexahedral cells. The resulting profiles are shown in Fig. 6.5.

Figure 6.5a shows the computed and analytical velocity profiles in the domain at $x = 80 \text{ mm}$ downstream of the inlet at steady-state. The analytical profile corresponds to a perfect parabolic velocity profile with a zero velocity at the upper wall and the interface. It is also the velocity profile set at the inlet as boundary condition ($V_x(y)$). As shown in Fig. 6.5a, the computational velocity profile downstream slightly deviates from the analytical profile at the interface. This phenomena

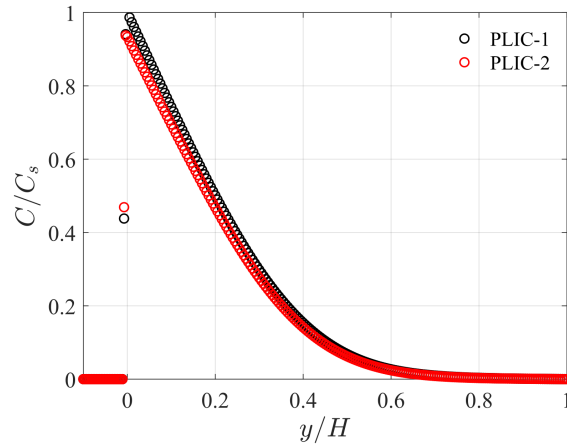
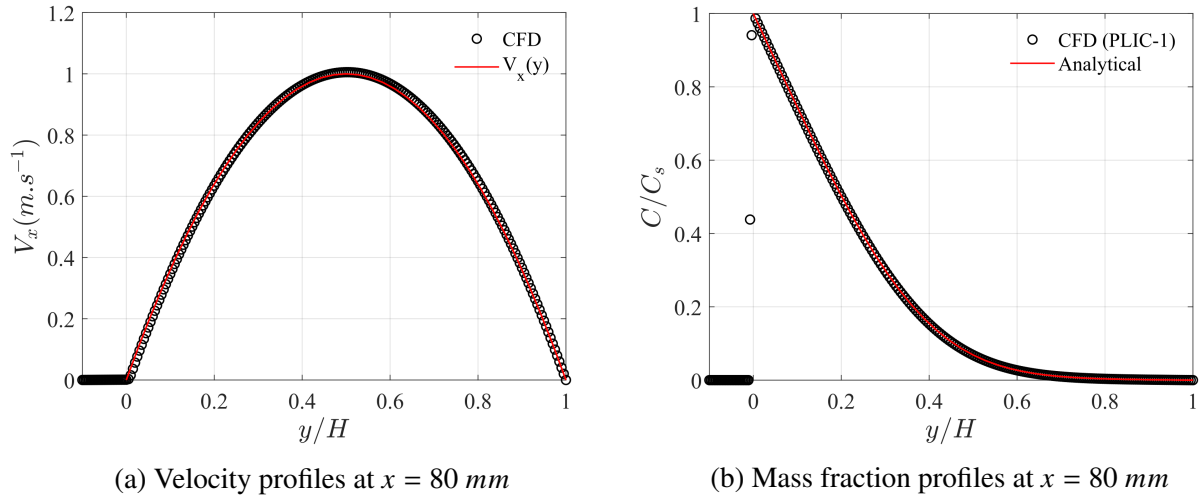


Figure 6.5: Test case results

exists for two reasons. Firstly, as mentioned before, the interface is not a perfect wall and a residual interfacial velocity is created because of the shear continuity between liquid and gas. Secondly, this phenomenon is exacerbated by the VOF one fluid formulation. Within the interfacial cells, the velocity field is the one of the mixture, which is calculated using volume fraction averaged properties (density and viscosity) of the phases involved. Finally, because of the volume fraction equation stiffness and the algorithm employed, the interface diffuses across a few cells (interface smearing) increasing the amount of cells where the fluid hydrodynamics is affected. Although, the velocity profile is slightly modified, the concentration profile shown in Fig. 6.5b is in excellent

agreement with the analytical solution thus validating the mass transfer modeling on a cartesian grid.

Finally the last result of this section involves comparing the results between the PLIC-1 and PLIC-2 methods. As shown in Fig. 6.5c, the second method (PLIC-2) for the characteristic length calculation is not able to reproduce the concentration profile obtained with the first method (PLIC-1). The concentration is significantly lower near the interface because underestimating of the mass flux.

$$\overline{\Delta x} = \frac{1}{V} \int_V \Delta x \, dV \quad (6.8)$$

$$\overline{C(x)/C_s} = \int_0^1 \frac{C(x, y)}{C_s} d\left(\frac{y}{H}\right) \quad (6.9)$$

$$\varepsilon = \frac{\left| \left(\overline{C(x)/C_s} \right)_{CFD} - \left(\overline{C(x)/C_s} \right)_{analytical} \right|}{\left(\overline{C(x)/C_s} \right)_{analytical}} \times 100 \quad (6.10)$$

Various quantities can be used to evaluate the accuracy of the two schemes considered. Table 6.4 groups the quantities calculated using equations (6.8), (6.9), and (6.10). The concentration gradient drives the mass transfer, which is itself largely driven by Δx ; and its overestimation shown in Table 6.4 leads to a smaller gradient and a lower evaporative flux. Although $\overline{\Delta x}$, is ten times higher using PLIC-2, the average normalized concentration shows an error that is less than 10%. The mass flux calculated is supposedly the one necessary to obtain saturation at the interface. When a saturation state is reached in a cell containing an interface, the mass flux becomes nil. With PLIC-1, the mass flux is accurately computed to reach saturation within the interfacial cells. Hence, the mass flux becomes nil in these cells, whereas with the PLIC-2 method, a saturation state is not reached due to the lower mass flux. Therefore, these cells remain active for mass transfer thus resulting in a smaller concentration error than in $\overline{\Delta x}$.

6.3 Conclusion on Mesh Topologies

In this chapter, the in-house algorithm developed to calculate the interfacial area was applied to various cell topologies and obtained satisfactory results. The author emphasize here the difficulty

Table 6.4: Averaged quantitative values for PLIC-1 and PLIC-2

Quantity	$\overline{\Delta x}$ (m)	$\overline{C/C_s}$ ($x = 80mm$)	ε
PLIC-1	2.811×10^{-7}	0.2297	2.92
PLIC-2	2.439×10^{-6}	0.2139	9.59
Analytical	-	0.2366	-

of the static drop test case for the VOF single fluid formulation with CSF model for surface tension.

Then the first order approximation of the gradient at the scale of the cell was tested and yielded excellent results in comparison with the analytical solution. Knowing that, several other factor should be taken into account for achieving calculations on the packed bed complex geometries. First, the cell counts of the meshes used in the static drop case are separated by more than one order of magnitude which should be accounted for. The computational cost of a mesh containing 9 millions tetrahedral cells is far superior than a 0.7 million hexahedral cells. In addition, the convergence rate of tetrahedral cells is far slower than the one of hexahedrals. In other words, with the same amount of cells, the cost of using tetrahedral cells is already higher. The advantage of tetrahedral cells is their ability to mesh complex geometries rapidly in comparison with the time and efforts required to obtain a perfectly structured hexahedral mesh. As a consequence, the solution is naturally to use hybrid meshes that employ hexahedral elements in parallel with tetrahedral or polyhedral when the geometry cannot be properly described with conventional hexahedral cells. This is the strategy employed here where hybrid meshes are employed to discretized the complex geometries studied.

CHAPTER 7

APPLICATION TO A COUNTER-CURRENT PACKED BED

The previous chapters of this work were written for the reader to understand the context, the stakes, as well as the difficulties encountered in the modeling an evaporator using a packed column with direct numerical simulations. This chapter provides the insights necessary to build a proper domain in order to study the response of a packed column under multiple flow conditions. An in depth analysis of the evaporator behavior as function of the boundary conditions is provided.

7.1 Computational Domain Generation

7.1.1 Geometry

Originally accomplished by Klausner et al. (2006) and further improved by Alnaimat et al. (2011), the studies that lead to this work all employed the packing material HQ Q-PAC manufactured by Lantec. For validation of the CFD results and because of the availability of data, this is the geometry employed here.

First, to obtain a CAD model, a sample of the packing geometry was measured and drawn in Solidworks. Experimental apparatuses employed in former studies are considered large scale from a CFD point a view. Li et al. (2006) used a 200mm height column and Alnaimat & Klausner (2013) system had a 254mm cross section diameter with one meter high column. Using CFD in a three dimensional environment to simulate domains of that size is computationally expensive and here only part of the problem is simulated by assuming symmetry and periodicity in transverse directions. Here, as the column is counter-currently driven; reducing the problem in the vertical direction is not possible since the boundary conditions are only known at the top and bottom of the column. The geometry is similar in both transverse directions allowing for a reduction of the domain along those axes. The resulting geometry is shown in Fig. 7.1. The final dimensions are $50.89 \times 25.52 \times 25.52$ mm corresponding to 6.5 elementary corrugations in the vertical direction

and 4 in the transverse directions.

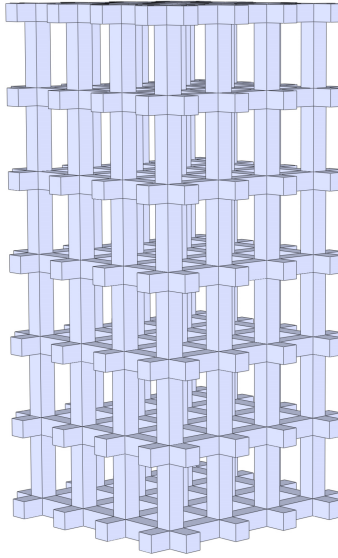


Figure 7.1: Lantec HD-PAC geometry used in the CFD study

7.1.2 Domain Setup

Building the numerical domain consist in setting the packing geometry in an environment as close as possible to the experimental conditions. Here, the goal is to reproduce the conditions in former experiments to the best extent possible as described by Li et al. (2006).

Therefore, the numerical domain is divided in five sections as depicted by Fig. 7.2a corresponding to different vertical position. From bottom to top the description is as follow:

- $z < -\delta_g$ is the bottom section where the water crossing the domain gets stored. It is ensured that the volume of this section is sufficient to *store* all the water injected during the total duration of the simulation.
- $-\delta_g < z < 0$ is the gas developing section that allows the gas to develop and homogeneously cover the packing material.
- $0 < z < H$ is the packing section also called *test section*. This section is highlighted by a red dashed line in Fig. 7.2a.

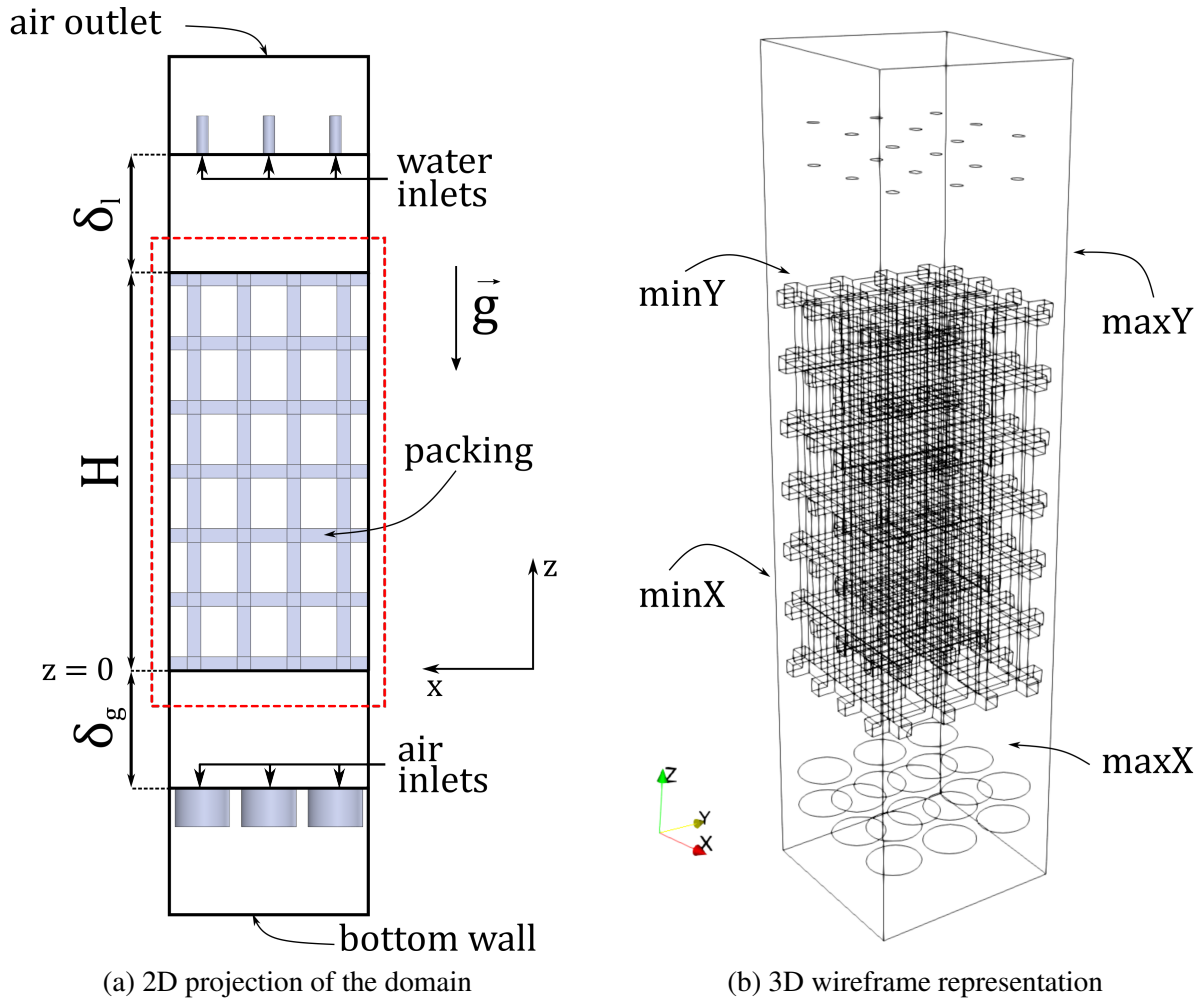


Figure 7.2: Domain surfaces definition

- $H < z < H + \delta_l$ is the water flow developing section.
- $z > H + \delta_l$ is the exhaust section where the humidified air is evacuated.

The total domain height measures 108 millimeters. Figures 7.3a and 7.3b show a cross-sectional view of the domain from the top and bottom respectively. The water and air inlets in the domain are depicted. The domain dimensions are given in Table 7.1. The positions of each water and air injectors is calculated in order to homogeneously cover the whole cross section of the packing.

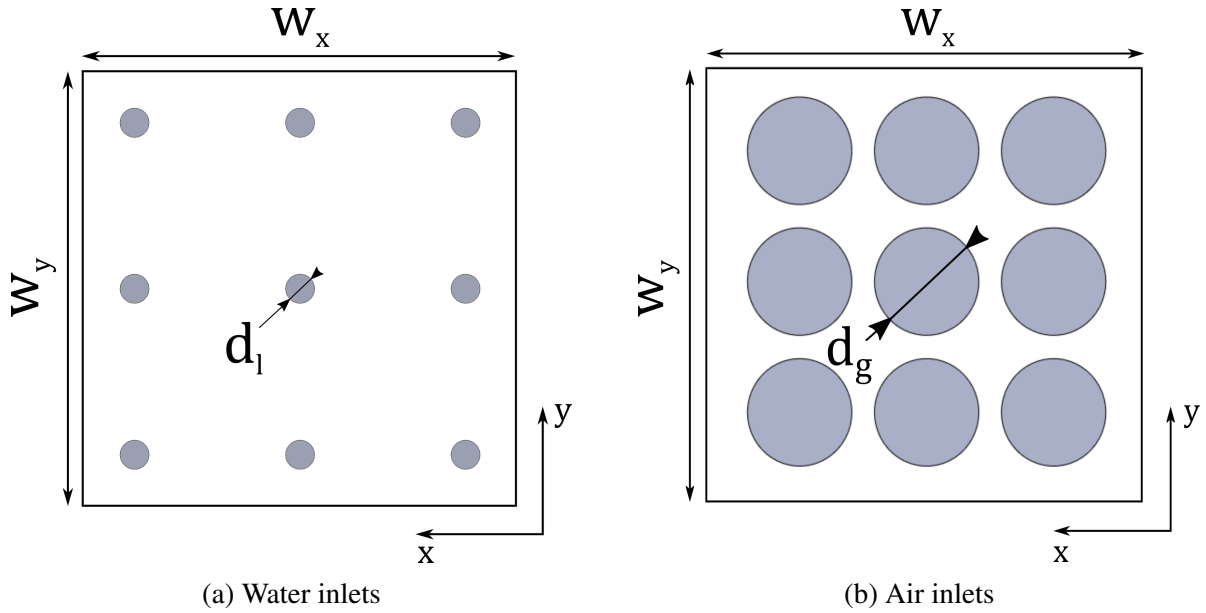


Figure 7.3: Domain fluids inlets

Table 7.1: Domain dimensions

Parameter	Value (mm)
H	50.89
δ_g	15
δ_l	15
d_l	1.5
d_g	7
w_x	25.52
w_y	25.52

7.1.3 Mesh Generation

As mentioned in section 6.3 the meshing strategy taken in this work is to employ hybrid meshes to ensure the creation of hexahedral cells that are computationally efficient and accurate while allowing the creation of polyhedral elements to perfectly acquire the small features of the geometries studied. For that purpose, the meshing tools employed here are BlockMesh and SnappyHexMesh, the meshing tools of the well known open source CFD package OpenFOAM. The use of this package allows the creation a highly configurable routines providing a fast mesh generation while maintaining high quality meshes. The geometry is exported from Solidworks using an stereo-

lithography (STL) format and meshed by successively using BlockMesh and SnappyHexMesh.

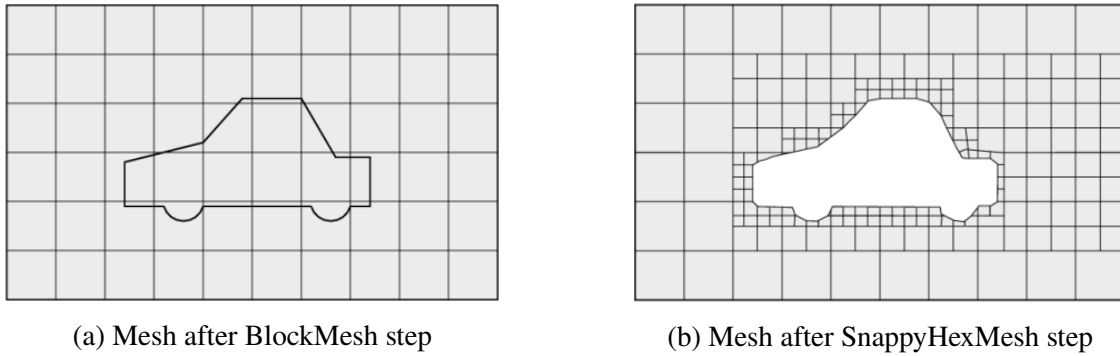


Figure 7.4: Meshing process (OpenFOAM Foundation (2020))

Firstly, as shown in Fig. 7.4a, BlockMesh generates a background structured hexahedral mesh with a user defined cell size. In this case, to mesh the domain shown in Fig. 7.2a, three blocks were used in order to make the packing section independent from the top and bottom of the domain so has to apply different cell size depending the needs.

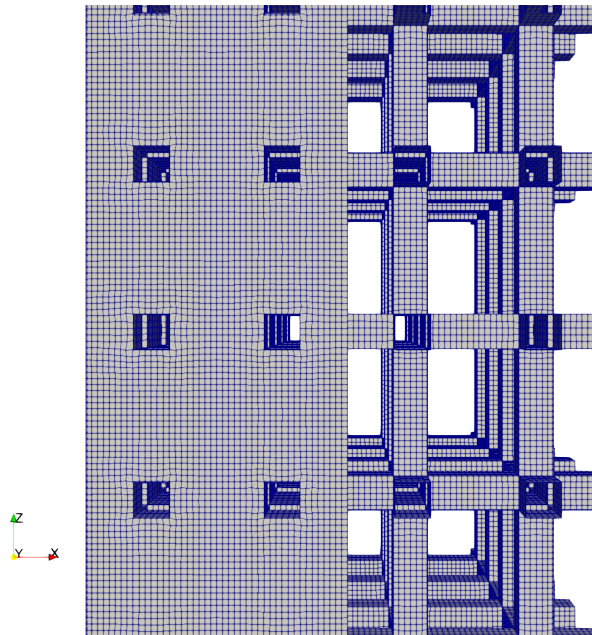


Figure 7.5: Partial enhanced view of the resulting mesh

Secondly, SnappyHexMesh crops the previously generated hexahedral mesh to the surface of the geometry using the STL file provided. Figure 7.5 shows a zoomed partial cut view of the obtained

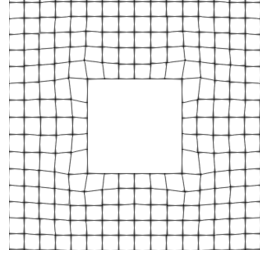
mesh. For this geometry the resulting mesh possesses 2.4 millions cells at 99.39% hexahedral. The water and air inlets being circular, they were meshed using polyhedral elements by SnappyHexMesh.

Several other features are accomplished during the meshing steps such as the surface definition which is further used for assigning boundary conditions in Fluent as well as the conversion of the mesh in the format employed by Fluent. This is accomplished by successively calling the functions *topoSet*, *createPatch*, and *foamMeshToFluent* that are included with OpenFOAM. The resulting mesh file is then ready for use with Fluent solver.

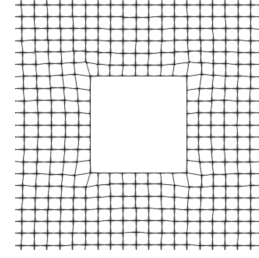
7.1.4 Mesh Convergence

Mesh convergence is typically achieved by tracking several quantities relevant to the phenomena studied. Those values are usually obtained by running the entire numerical problem for various grid sizes until the solution becomes independent of the mesh. Here, because of the high computational cost to compute even one solution, mesh convergence is a two step process. The first step consist in measuring the computed interfacial area as a function of the curvature to cell size ratio, which is accomplished by placing a static droplet in a cuboid domain, similar to Soh et al. (2016). This is achieved by reusing the test case of the static droplet. Through this benchmark, as shown by the results compiled in Table 7.2, it was determined that to maintain a satisfactory accuracy, based on the water inlet diameter d_l , the cell size should not exceed $d_l/5$. The assumption taken here is that no secondary break-up of the droplets is occurring in the packed bed which is justified using the break-up criteria from Kitscha & Kocamustafaogullari (1989). As a consequence, for the second benchmark, two meshes are generated. The first mesh uses 0.3mm cell size resulting in 2.4 million cells and a finer mesh using 0.23mm cell size resulting in 4.4 million cells as shown by Fig. 7.6

The second benchmark consists in running the model without the presence of water to control the accuracy of the mesh in modeling the gas flow behavior in the packing. This case is solved with both meshes for three different gas fluxes, and the pressure drop is extracted. The resulting linear pressure drops are compiled in Table 7.3 in Pa/m for each mesh for the gas mass fluxes studied. The results are compared with the experimental correlation given by equation (7.9) reported by



(a) Coarse mesh (2.4M)



(b) Fine mesh (4.4M)

Figure 7.6: Detail view of the two meshes employed around an individual packing geometrical feature

Table 7.2: Sphere test results with $\Delta x = 0.3 \text{ mm}$

d_l/l_{cell}	$A_{PLIC} (m^2)$	$A_{ \nabla\alpha } (m^2)$	$Theory (m^2)$	ε
20	1.101×10^{-4}	5.396×10^{-5}	1.131×10^{-4}	2.65%
15	6.079×10^{-5}	3.040×10^{-5}	6.362×10^{-4}	4.71%
10	2.897×10^{-5}	1.300×10^{-5}	2.827×10^{-5}	10.6%
3.3	2.717×10^{-6}	4.166×10^{-7}	3.141×10^{-6}	13.5%

Alnaimat et al. (2011). As the resulting linear pressure drop does not vary by more than 5% for all operating conditions with almost doubling the amount of cells, the coarser mesh (2.4 millions) is employed for the rest of the study.

Table 7.3: Linear dry pressure drop for the different mesh cell size and various gas mass flux

$G (kg.m^{-2}.s^{-1})$	0.25		0.5		1	
Gas Velocity ($m.s^{-1}$)	0.3835		0.767		1.534	
$l_{cell} (mm)$	0.3	0.23	0.3	0.23	0.3	0.23
HD Q-PAC Pa/m	6.631	6.710	15.372	15.744	37.931	39.446
Eq.(7.9) Pa/m	6.3		16.7		44.1	
$\varepsilon (\%)$	5.3	6.5	5.7	3.4	14.0	10.5

7.1.5 Boundary & Operating Conditions

7.1.5.1 Boundary Conditions

In this case, the boundary conditions are straightforward in regard of the numeric. Both water and air inlets are set as *velocity inlets* where a fluid inflow is imposed. As a consequence, the pressure at the boundary face is calculated from the pressure correction equation. This type of boundary condition, in Fluent, imposes the user to set velocity, temperature and volume fraction of each fluids. Within the VOF framework, only a single temperature and velocity is set since it is a single-fluid formulation. In addition, the water vapor mass fraction is also set since it is necessary to solve equation (5.27), the species concentration equation.

The *packing* is numerically considered a wall where the velocity is nil (no slip). Within the FVM, this translate to an imposed nil velocity value at the boundary face centroid. This information is then interpolated to the cell center using the chosen discretization scheme for the momentum and pressure correction equation. In addition to its geometry, the packing material also plays a role in the water distribution because of the contact angle between water and the packing surface. Numerically this translate to the wall adhesion as described in section 4.8.2. The contact angle, θ_{eq} , is set constant and equal to 60 degrees in all simulations, no moving contact lines are considered. Thermally, the packing is considered adiabatic.

The *air outlet* is defined as a *pressure outlet* which is Dirichlet type boundary condition for pressure. The relative nature of pressure in the Navier-Stokes equations makes the user input to be the static gauge pressure. Other quantities such as volume fraction, velocity, temperature, and mass fraction are calculated from the interior cells assuming a zero gradient at the boundary faces. In this case, the gauge pressure is equal to zero.

Finally, the side boundaries of the domain are divided in two categories. The first type, applied to the surfaces $minY$ and $maxY$ as shown in Fig. 7.2b, are *symmetry* type boundary conditions which, numerically, impose a zero gradient for all variables in the normal direction to the surface. The second type, applied to $minX$ and $maxX$, is a *periodic* type boundary conditions. Numerically, the

face value at one of the plane is calculated using the value of the cell center adjacent to the opposing plane. In this case the values at the surface $maxX$ are accomplished using the values of the cell center adjacent to the surface $minX$. Values applied to each boundary conditions are compiled in Table 7.4.

Table 7.4: Type and values of boundary conditions

<i>Boundary</i>	<i>Hydrodynamic</i>	<i>Thermal</i>	<i>Species</i>
Water Inlet	Velocity Inlet	333K	$Y_{H_2O} = 0$
Air Inlet	Velocity Inlet	296K	$Y_{H_2O} = 0$
Bottom Wall	Wall	Adiabatic	Zero Gradient
Air Outlet	Pressure Outlet	296K	$Y_{H_2O} = 0$
Packing	No Slip	Adiabatic	Zero Gradient

7.1.5.2 Operating Conditions

As previously mentioned, the pressure only appears as the form of a gradient in the Navier-Stokes equations. Therefore, knowledge of the absolute pressure is not necessary a priori. In the pressure based approach, the solver uses a relative pressure calculation and then add the operating pressure set by the user at the end of the calculation. Nonetheless, the operating pressure may play an important role to calculate fluid properties with a state equation as it is done in compressible computations. In this study the operating pressure is set to 1 atm.

When body forces terms are involved in the computation, which is the case in single phase buoyancy driven flows as well as in a wide majority of multiphase flows problems (bubble riser, falling films, etc...), the operating density plays a fundamental roles. The operating density is necessary to calculate the buoyancy force, F_{buoy} , appearing in the momentum equation (5.25). In Fluent, the computation of this term is accomplished by combining the buoyancy force term with the gravity term as follows:

$$\mathbf{F}_{body} = (\rho - \rho_0) \mathbf{g} \quad (7.1)$$

where ρ_0 is the operating density. In multiphase flows, as the fluids densities are usually separated by several order of magnitude, the contribution from the buoyancy forces to the body forces is extremely high (bubble riser) or extremely low (droplet flow). In the absence of a user defined value, Fluent calculates the operating density as the volume average density in the computational domain which, in this case, would lead to an overestimation of the buoyancy forces. Therefore, $\rho_0 = 1.225 \text{ kg.m}^{-3}$ which corresponds to the density of dry air at 25°C.

As previously mentioned, in the VOF formulation, the fluid properties in a cell are a volume fraction average of both phase, as defined by equation (5.31). Nonetheless, the properties of each individual phase remain a user input. In this study, the two phases involved are water and humid air. Water being a single component phase, its properties are defined by Table 7.5.

Table 7.5: Water properties

Property	Value	Unit
ρ_l	998.2	kg.m^{-3}
C_{pL}	4182	$\text{J.kg}^{-1}.\text{K}^{-1}$
λ_l	0.6	$\text{W.m}^{-1}.\text{K}^{-1}$
μ_l	1.003×10^{-3}	$\text{kg.m}^{-1}.\text{s}^{-1}$
M_w	18.0152	g.mol^{-1}

Table 7.6: Individual properties of humid air components

(a) Water vapor properties			(b) Air properties		
Property	Value	Unit	Property	Value	Unit
ρ_v	0.5542	kg.m^{-3}	ρ_a	1.225	kg.m^{-3}
C_{pv}	polynomial	$\text{J.kg}^{-1}.\text{K}^{-1}$	C_{pa}	1006.43	$\text{J.kg}^{-1}.\text{K}^{-1}$
M_v	18.0152	g.mol^{-1}	M_a	28.966	g.mol^{-1}

The second phase, humid air, is a two components phase composed of air and water vapor. Note that air is treated as a single component. As a consequence, the properties of the gas phase are not necessarily constant but defined as a function of the mass fractions of each component within the phase. The thermal conductivity and viscosity, λ_g and μ_g , of humid air are taken as constants while the density and specific heat are function of the mass fraction and are given by the following

equations:

$$\lambda_g = 0.0454 \text{ W.m}^{-1}.\text{K}^{-1} \quad (7.2)$$

$$\mu_g = 1.72 \times 10^{-5} \text{ kg.m}^{-1}.\text{s}^{-1} \quad (7.3)$$

$$\rho_g = \frac{\rho_v \rho_a}{Y_{H_2O} (\rho_a - \rho_v) + \rho_v} \quad (7.4)$$

$$C_{p_g} = Y_{H_2O} C_{p_v} + (1 - Y_{H_2O}) C_{p_a} \quad (7.5)$$

The individual properties of water vapor and air are given in Table 7.6. The molecular diffusivity of water vapor into air, $D_{H_2O/air}$, that appears in equations (5.27) and (5.11) is set as a function of temperature using equation (7.6) from Massman (1998). Note that (7.6) returns the molecular diffusivity in the dimensions of cm^2/s with $T_0 = 298\text{K}$.

$$D = 0.2178 \left(\frac{T}{T_0} \right)^{1.81} \quad (7.6)$$

Finally, the water vapor saturation pressure necessary to calculate the mass fraction at the interface, Y^* , is the same as employed by Alnaimat & Klausner (2012) and is given by equation (A.1).

7.2 Water Inlet Boundary Conditions

Early studies on the flow dynamics of packed columns were experimental and consisted in measuring simple quantities such as pressure drop and temperatures. The literature naturally developed its way of expressing mass flow rates as function of what is called the superficial velocity. The well-known Ergun equation and its numerous variations are all function of that velocity formulation. This latter is convenient because it removes the need of characterizing the flow pattern at the bed entrance. The application of the mass conservation equation between the feed mass flow rate and the cross sectional area of the packed column yields the superficial velocity.

$$u_s = \frac{Q}{A_c} \quad (7.7)$$

where Q is the feed volume flow rate and A_c the cross sectional area of the packed column. Note that multiplying the superficial velocity by the fluid density leads to the mass flux which is also a

commonly employed formulation in the literature. As mentioned before, two problems arise from this formulation. First it assumes an homogeneous distribution of the feed over the column which is, in reality, unachievable. Second it does not account for the flow pattern at the entrance that could take the form of droplets, sheets or columns among others.

The aim of this study is to observe how the water distribution can have a significant impact on the performances of the packed column. For that purpose, three different cases are set with the same water mass flux but are generated using three different inlet configurations. Figure 7.7 shows the water distribution employed in all three cases view from the top of the domain.

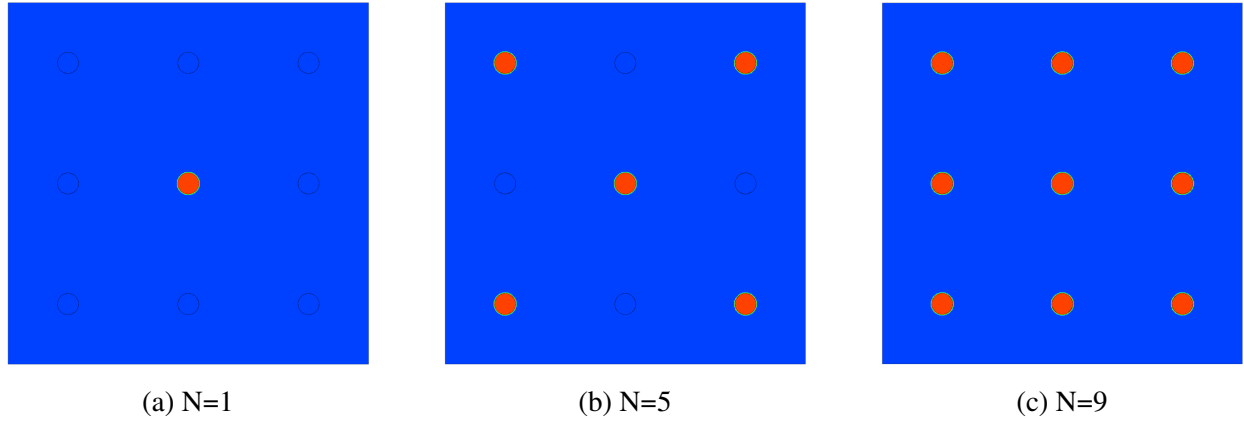


Figure 7.7: Contour of liquid volume fraction at water inlet for different spray densities

The water mass flux is fixed for all three cases at $0.97 \text{ kg.m}^{-2}.\text{s}^{-1}$ and the diameter of each individual inlet is $d_l = 1.5 \text{ mm}$. To match the targeted mass flux, the strategy taken here is to modulate the water entrance so that the time average value of the mass flux remains the same. Hence the time average mass flux is now calculated as follows:

$$L = \frac{\rho_l u_l t_{on}}{A_c t_{tot}} N \frac{\pi d_l^2}{4} \quad (7.8)$$

where u_l is the inlet absolute velocity, t_{on} is the time during water is injected in the domain and t_{tot} is the total time of an injection cycle. Figure 7.8 shows an example of the injection cycles for the three studied cases. With this model, the mass flux, L is now function of the number of inlets, the diameter of each individual inlets d_l , t_{on} , t_{tot} , and the inlet velocity. Therefore an infinite

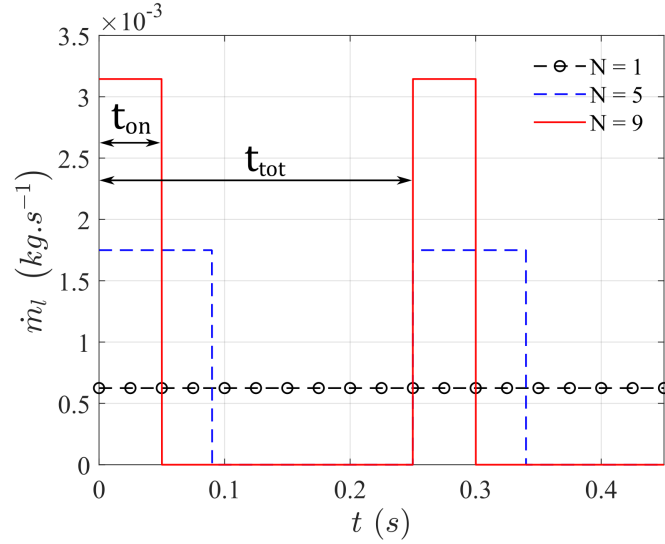


Figure 7.8: Water inlet time modulation

amount of configurations are possible and the choice of adjusting the modulation ratio was dictated by multiple physical or numerical issues.

The first natural choice in adjusting the mass flux would be to adjust the inlet velocity $u_{l_{in}}$. This leads to three problems. Firstly, with the targeted mass flux ($0.97 \text{ kg}\cdot\text{m}^{-2}\cdot\text{s}^{-1}$), if $t_{on}/t_{tot} = 1$ and $d_l = 1.5 \text{ mm}$ with 9 inlets employed, the inlet velocity is on the order of 40 mm/s thus leading to an extremely long computational time to reach a pseudo steady-state. Secondly, using the same conditions with 1 inlet leads to an inlet velocity of $u_{l_{in}} = 0.36 \text{ m/s}$ changing the inertia forces by an order of magnitude which is expected to affect the flow behavior. Finally, on a computational point of view, it affects the Courant number which could lead to numerical instabilities. The second logical choice is to modify the inlet diameter, d_l , which immediately changes the surface tension forces as defined by the Young-Laplace equation. As a consequence, the only remaining choice is to adjust the modulation ratio.

The flow conditions employed in each case summed up in Table 7.7. For the cases N equal to 9 and 5, each individual injector is the exact same from a physical standpoint (inertia and surface tension forces). The velocity for N=1 case has to be increased in order to reach the targeted mass flux. Though the calculated We_l and Re_l based on the inlet diameter stay within the same range. For this study the gas flow rate was fixed at $0.5 \text{ kg}\cdot\text{m}^{-2}\cdot\text{s}^{-1}$ corresponding to $u_{g_{in}} = 0.767 \text{ m/s}$.

Table 7.7: Water inlet boundary properties

N	$u_{l_{in}} \left(m \cdot s^{-1} \right)$	$t_{on} \text{ (s)}$	$t_{tot} \text{ (s)}$	Re_l	We_l
9	0.20	0.05	0.25	298	0.83
5	0.20	0.09	0.25	298	0.83
1	0.36	0.25	0.25	529	2.62

Finally, for each case, the system runs until 4s with a fixed time-step of $5 \cdot 10^{-5} s$ which corresponds to the time necessary to reach a pseudo steady-state. Each case represents 10 days of computational time on 4 nodes with a total of 160 cores.

7.2.1 Results & Discussion

7.2.1.1 Pressure Drop & Liquid Hold-Up

In a similar fashion to the first experimental campaigns in the study of packed columns, the first quantity of interest is the pressure drop across the column. Similarly to experimental measurements, the acquisition of the pressure drop is accomplished on the gas side and is time averaged since the presence of water affects the instantaneous pressure values. To compute the gas pressure drop, in pre-processing, planes are initialized at various vertical positions within the packed column. Every 5 milliseconds, the static pressure and volume fraction are recorded at every cell crossed by each individual plane. In post-processing, the data recorded are temporally and spatially averaged over the last second of the run when pseudo steady-state is reached.

$$\frac{\Delta p}{H} = \frac{G^{1.4}}{\rho_g} \left[0.054 + 654.48 \left(\frac{L}{\rho_l} \right)^2 + 1.176 \times 10^7 \left(\frac{L}{\rho_l} \right)^4 \frac{G^4}{\rho_g^2} \right] \quad (7.9)$$

Figure 7.9 shows the resulting static pressure profiles in the packing section with the linear regression accomplished in each case. The slope of each regression gives the pressure drop in Pa/m. The results show a 30 % difference in the linear pressure drop depending the configuration which shows the importance of the distribution on the packing performance. All cases are on the same order as 16.9 Pa/m obtained using equation (7.9) from Alnaimat & Klausner (2013).

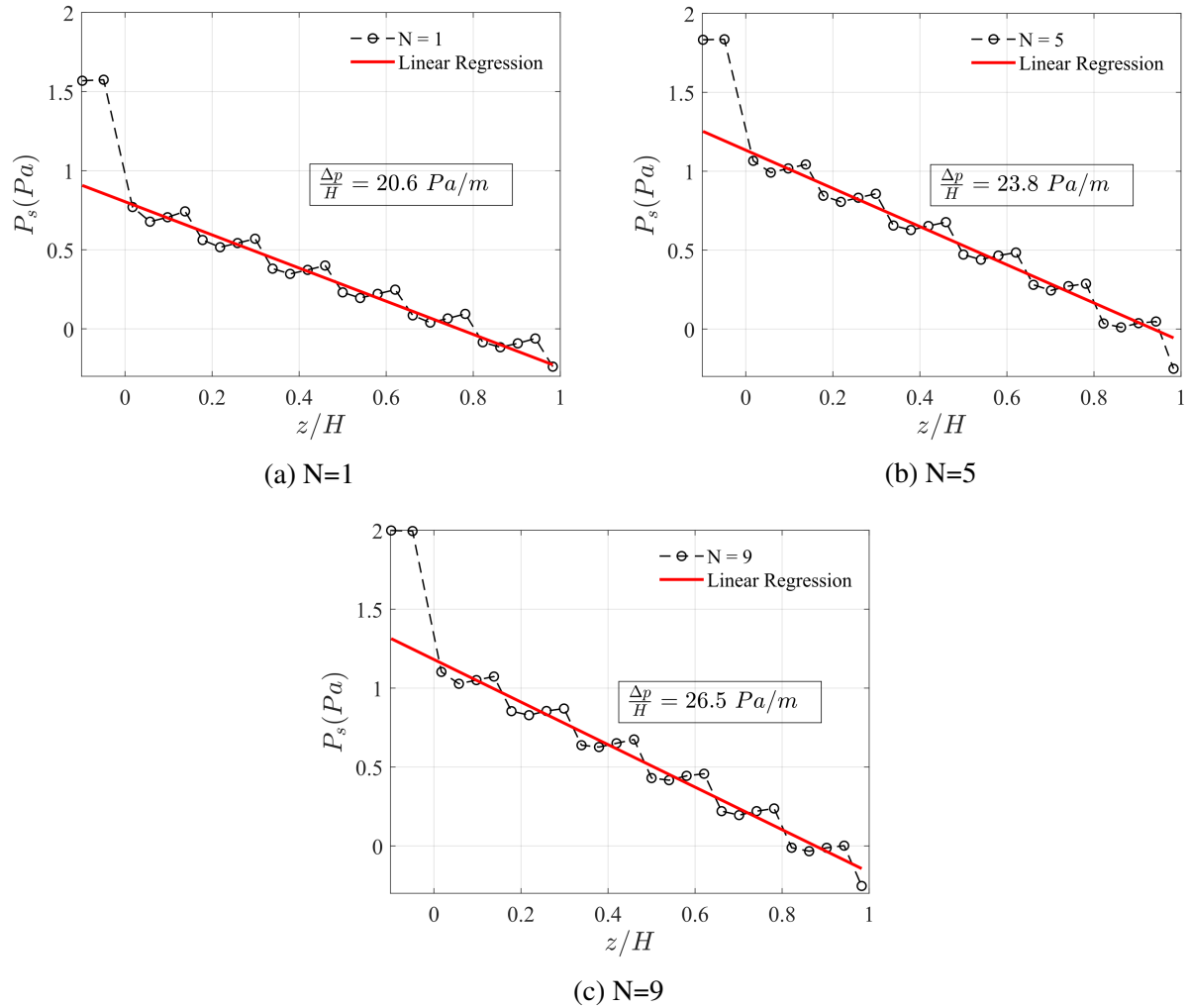


Figure 7.9: Spatially and temporally averaged gas static pressure as function of the vertical position

The increase in pressure drop with the number of inlets is explained by the enhanced interaction between the packing and the water, which leads to an increase in the liquid hold-up thus globally reducing the cross-sectional area available for the gas to flow through the packing as well as the increased shear between water and liquid. Nonetheless, in comparison with the dry linear pressure drop obtained, this latter represents at least 60% of the wet values, hence showing the need for low drag column designs.

Figure 7.10 pictures contours of the volume fraction of water in the three cases. The water is mainly maintained in the column through the wall adhesion forces due to surface tension. With a low spray density ($N = 1$) the water has a limited interaction with the packing resulting in a

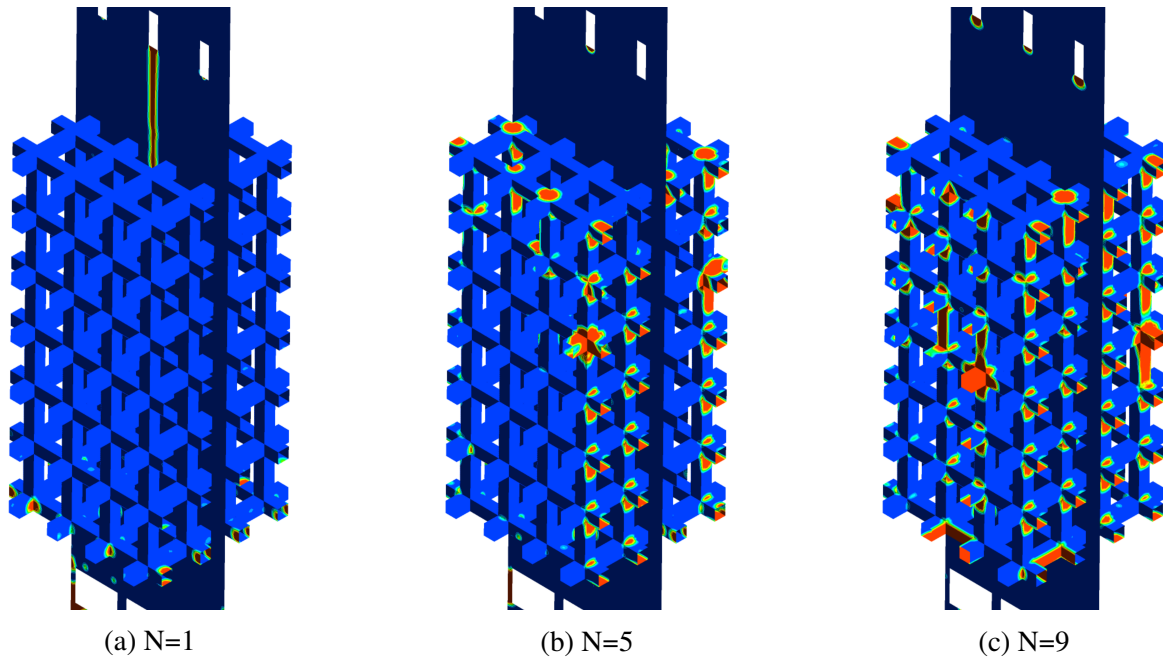


Figure 7.10: Water volume fraction contours at $t = 3.5s$

low liquid-hold up. The surface interaction between the liquid and the packing geometry naturally increases with the spray density and results in a larger liquid hold-up. Though, increasing the spray density from $N = 1$ to $N = 5$ increases the liquid hold-up by a factor of 9, the gain diminishes with increasing N . Going from $N = 5$ to $N = 9$, the liquid hold-up only increases by a factor of 45%. With this result, the liquid hold-up is expected to reach a limit with when the number of inlets per unit area corresponds to the amount of corrugations per unit area. Here, the domain possesses 16 corrugations, thus the independence of the liquid hold-up is expected to be reached with the use of 16 inlets, which shows a critical need of conceiving a packed column adapted to the distributor and vice-versa. Figure 7.11b shows an interpolation of the liquid hold-up as a function of N using a least square fit method.

Even if the observation of global values over the whole domain are interesting for validation purposes, the real added value of CFD calculations is the knowledge of every quantity at every point of the domain where reliable experimental measurements or observations are at best limited and in most cases, not possible. This gives the possibility to observe and understand the interactions between liquid, gas and packing. Using the same data and procedure as for the pressure drop

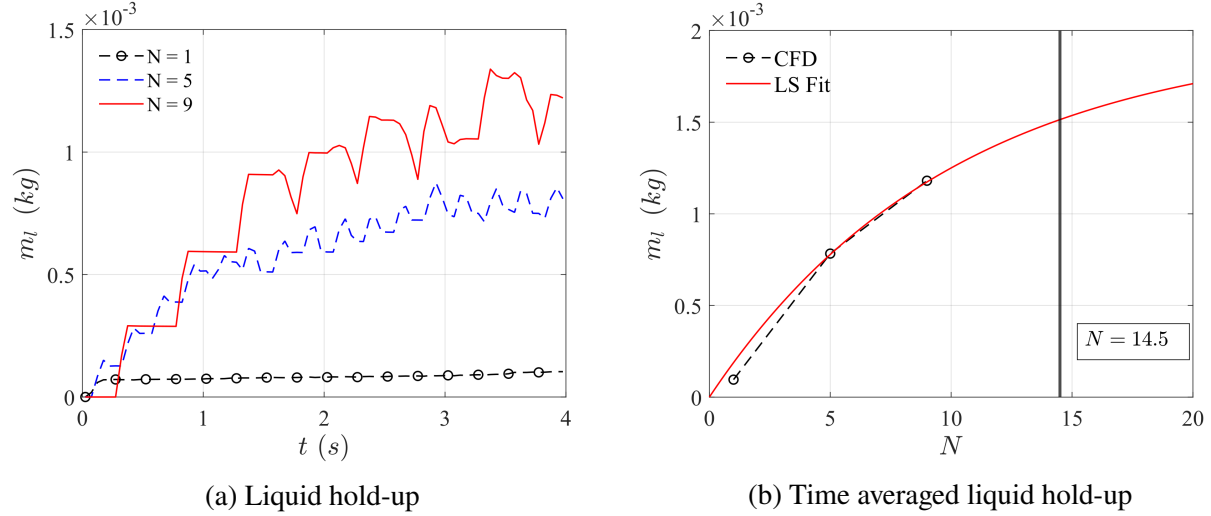


Figure 7.11: Liquid hold-up in the test section

profiles, Fig. 7.12 shows the water volume fraction α_l extracted at different vertical positions.

The resulting profiles confirm the liquid hold-up results as the water volume fraction for the two highest spray density ($N = 5$ and $N = 9$) are close to each other. In both cases, the peak location are situated underneath each packing vertical corrugation. Knowing that, the planes where the peaks are observed are further used to calculate a spatially averaged contour of volume fraction in the transverse directions as depicted by Fig. 7.13.

In both cases, water is less at the center of the column because it is the region where the evaporation is the most important as described in the next section. In Figure 7.13a, this phenomena is exacerbated because of a lesser water coverage in the central region. Nonetheless, the water reside at the same location, underneath each vertical corrugation of the packed column. The spray density only improves the activation of the horizontal corrugation of the geometry. The systematic presence of water in those region is explained by the strong adhesion force due to the presence of both vertical and horizontal features of the packing geometry.

Recording the velocity in the vertical direction and the volume fraction allows the extraction of the water and air velocity. Figure 7.14 shows the water time averaged velocity as function of height for the highest spray densities. It is naturally in phase opposition with the water volume fraction profile. Computing the mean velocity for each case leads to $\bar{u}_l = 0.096$ m/s for $N = 5$ and $\bar{u}_l = 0.065$ m/s

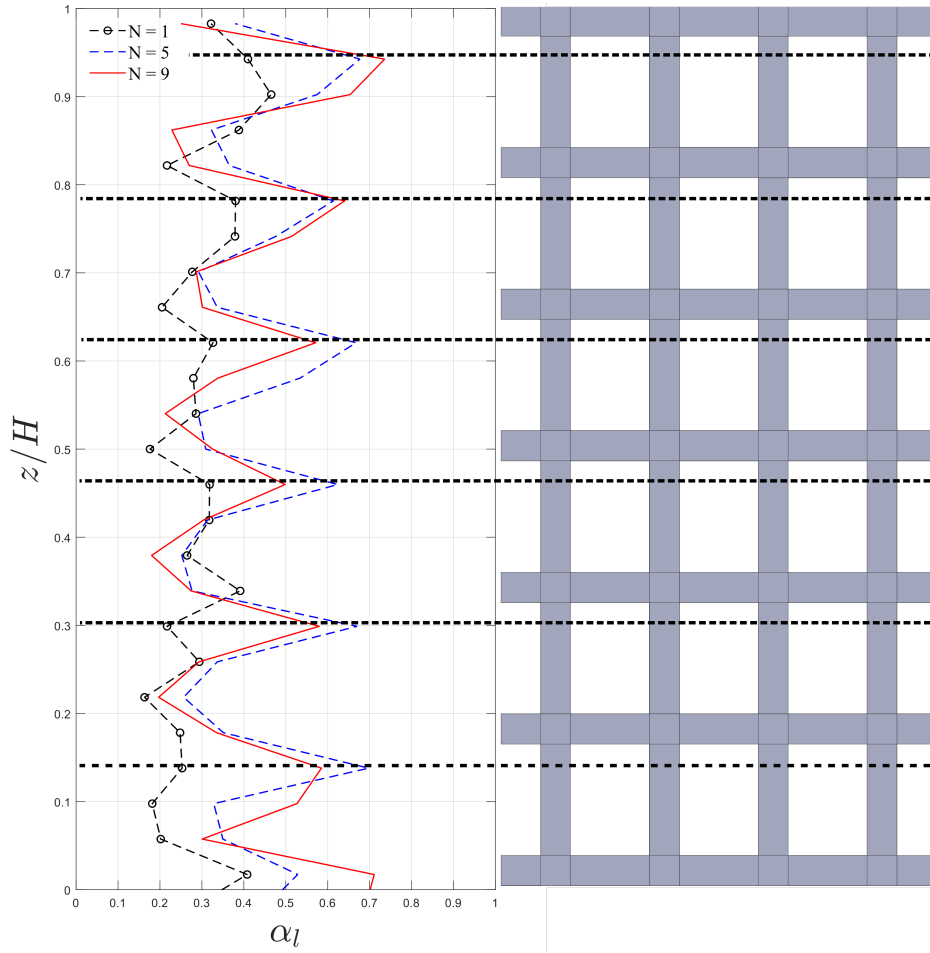


Figure 7.12: Liquid volume fraction along the z-axis

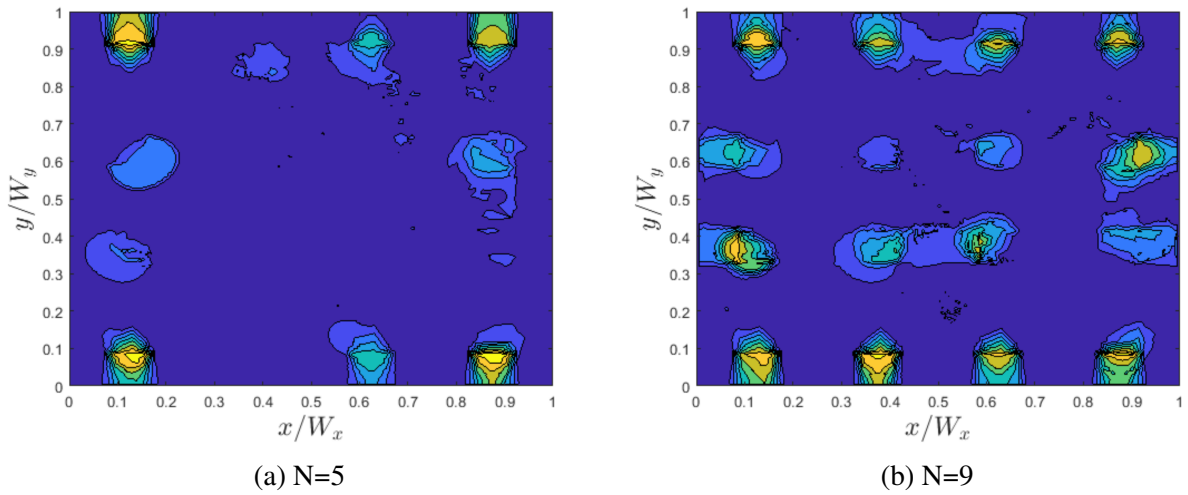


Figure 7.13: Time and spatial average contour of liquid volume fraction

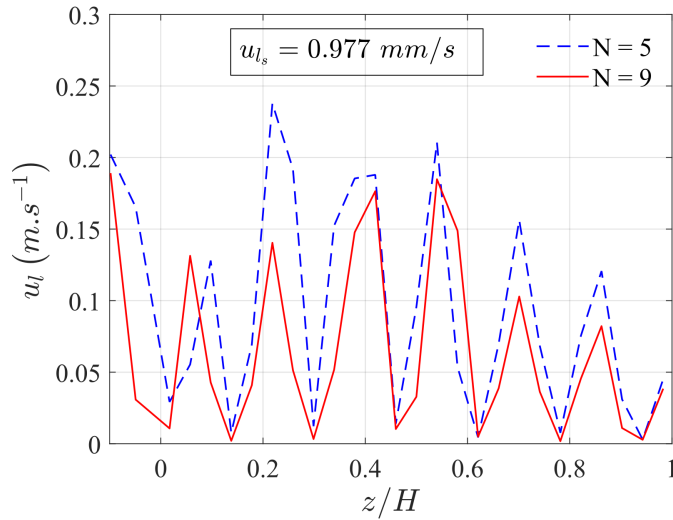


Figure 7.14: Water velocity

Table 7.8: Water velocity

N	$u_{l_{max}}$ ($m.s^{-1}$)	$u_{l_{min}}$ ($m.s^{-1}$)	\bar{u}_l ($m.s^{-1}$)
9	0.19	0.0033	0.065
5	0.24	0.0029	0.096

for $N = 9$. The difference is due to the enhanced shear between water and air for increasing N as well as the increased interaction with the packing.

The superficial velocity u_{l_s} for these conditions is equal to 0.977 mm/s which is 3 to 250 times smaller than values calculated by CFD. Globally the velocity values are much closer to the set inlet value ($u_{l_{in}} = 0.2$ m/s at inlet) than the superficial velocity. Investigating the water velocity dependence to the inlet velocity would be of interest in future studies.

7.2.1.2 Heat & Mass Transfer

The performance of a thermal desalination system depends on the evaporator efficiency and the ability to exchange heat and mass between gas and liquid. This section examines the heat and mass transfer performances of the packed column for the three different cases. In the same fashion as pressure drop and velocity, the time average temperature of each phase can be extracted as shown

in Fig. 7.15.

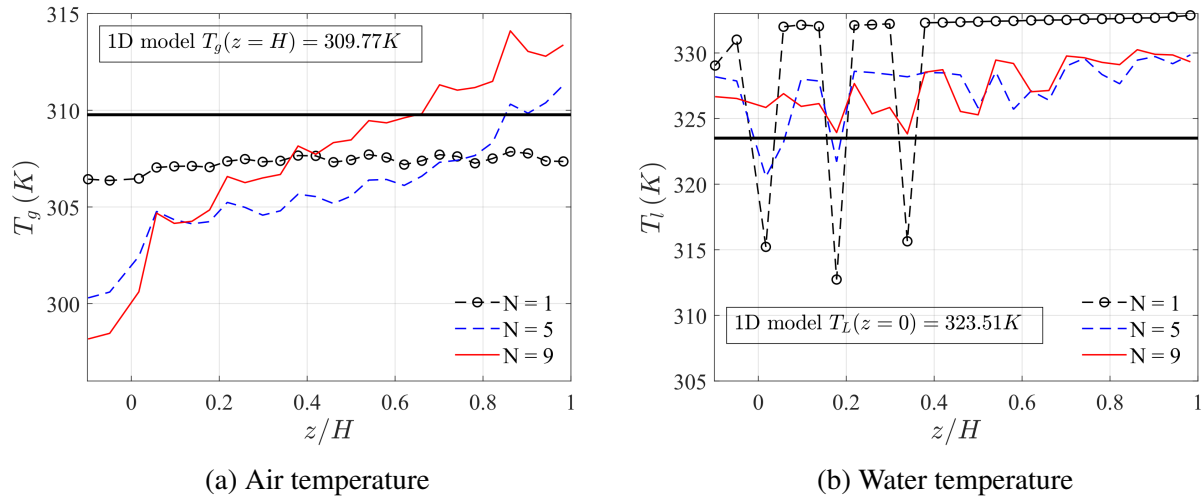


Figure 7.15: Phase temperature profiles

As shown in Fig. 7.15a the gas temperatures at the top of the packed column for $N = 5$ and $N = 9$ are 311.3K and 313.4K respectively which is good agreement with 309.8K predicted by the 1D model. For $N = 1$, the outlet temperature is well underneath because of the limited interfacial area available for heat and mass transfer(see Fig. 7.17b).

In contrast, the temperature at the bottom of the column is higher than $N = 5$ and $N = 9$ cases. This is due to the presence of water at the bottom of the domain as depicted by Fig. 7.16. With $N = 1$, Fig. 7.16a, the liquid hold-up in the column is small leading to a large amount of warmer water in the bottom section that transfers heat and mass to the air entering the test section thus pre-heating the gas entering the column. With a higher liquid hold-up, for cases $N = 5$ and $N = 9$, the amount of water contained in the bottom section of the domain is less important as shown by Fig. 7.16b and Fig. 7.16c; hence there is a diminishing influence of the bottom section on temperature profiles. The discrepancy between $N = 5$ and $N = 9$ profiles is dictated by the single energy equation employed in the VOF method. Since the temperature is shared, the only inter-phase heat transfer mode is through conduction, which in this case is driven by the interfacial area available. Figure 7.15b shows the water temperature profiles. For all spray densities, the temperature value at the bottom is slightly higher than the 323.5K predicted by the 1D model. This

discrepancy is due to minimal convection that would otherwise transport heat from the liquid into the gas phase, thus decreasing the water temperature at the outlet(bottom).

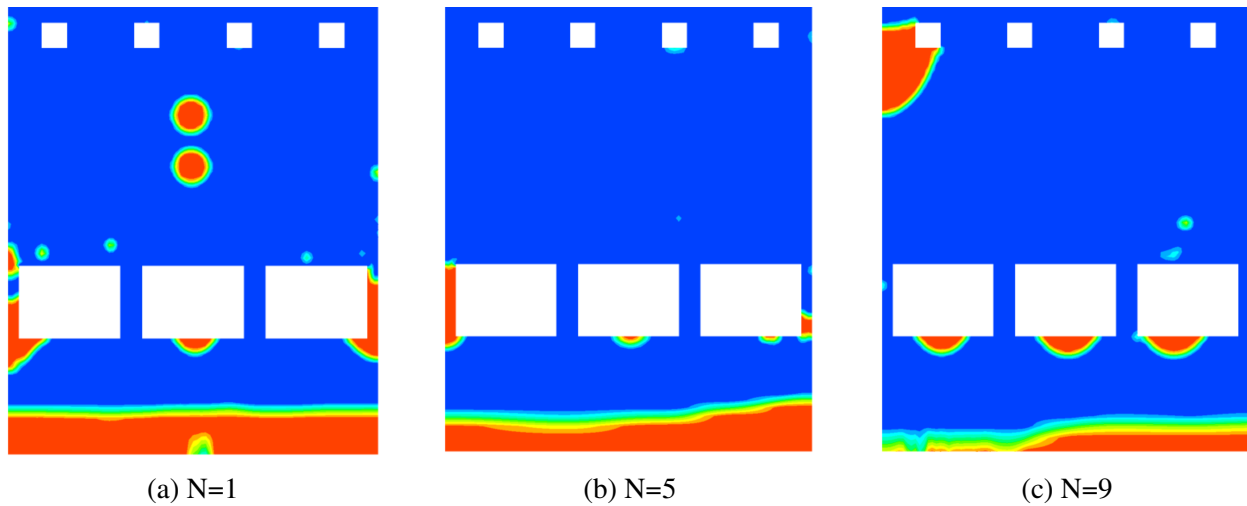


Figure 7.16: Contour of liquid volume fraction in the bottom section at $t=3.5$ s. The horizontal and vertical axes are x and z

In their experimental facility, Klausner et al. (2006), determined the interfacial area by measuring the mass fraction of water vapor at the top of the evaporator. For validation, the same procedure is employed here and consist to record overtime the average mass fraction of vapor at a plane located at $z = 55.89$ mm, which is 5 mm above the top of the packed column. As shown in Fig. 7.17a the mass fraction is strongly dependent on the spray density.

This dependence is explained by the higher interfacial area available for mass transfer when the spray density increases as shown by Fig. 7.17b. Having a higher spray density naturally increases the vapor mass fraction output since more water is held-up in the packing as previously shown. It is interesting to compare mass fraction results, which are in good agreement with the 1D model, and the interfacial area concentration that is in poor agreement in all three cases due to the presence of water in the bottom section. The values reported in Fig. 7.17b only take into account the interfacial area available in the test section, which is highlighted in red in Fig. 7.2a and ranges from $z = -5$ mm to $z = 55.89$ mm. Therefore the reported values do not account for the bottom section where, as shown by Fig. 7.16, water resides and contributes to the overall interfacial area and therefore the mass transfer.

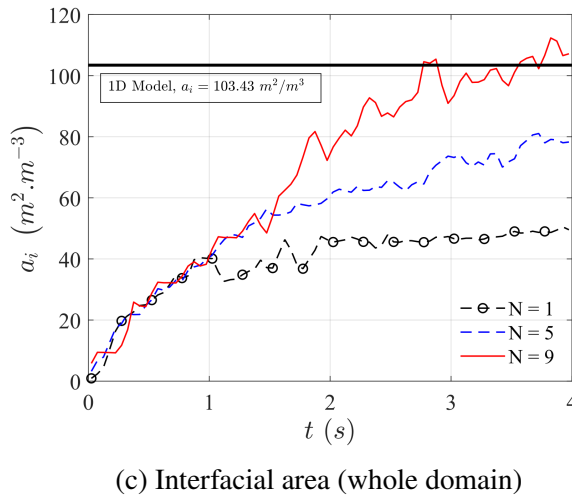
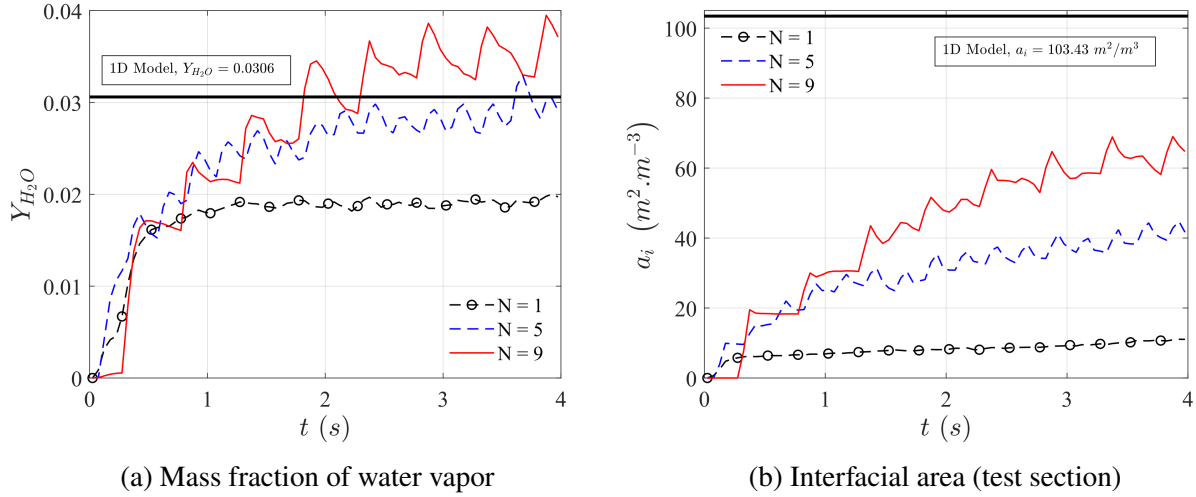


Figure 7.17: Transient response of water vapor mass fraction and interfacial area

In experimental campaigns, the empirical correlation employed to determine the interfacial area is usually fitted to match the data using knowledge of the mass fraction, which, by essence, considers the whole evaporator with the bottom section. As a result the interfacial area concentration effectively present in the packing is overestimated. As shown in Fig. 7.17c, using the same definition as used for experiments, the results are in good agreement with the 1D model.

Figure 7.18 shows mass fraction profiles, evaporation mass flow rate and the discretized vapor concentration gradient at the interface value as function of heights. The mass fractions behaves in a similar way as the gas temperature profile which is reasonable considering heat and mass transfers are coupled phenomena. Similarly the entrance mass fraction for $N = 1$ is higher because the

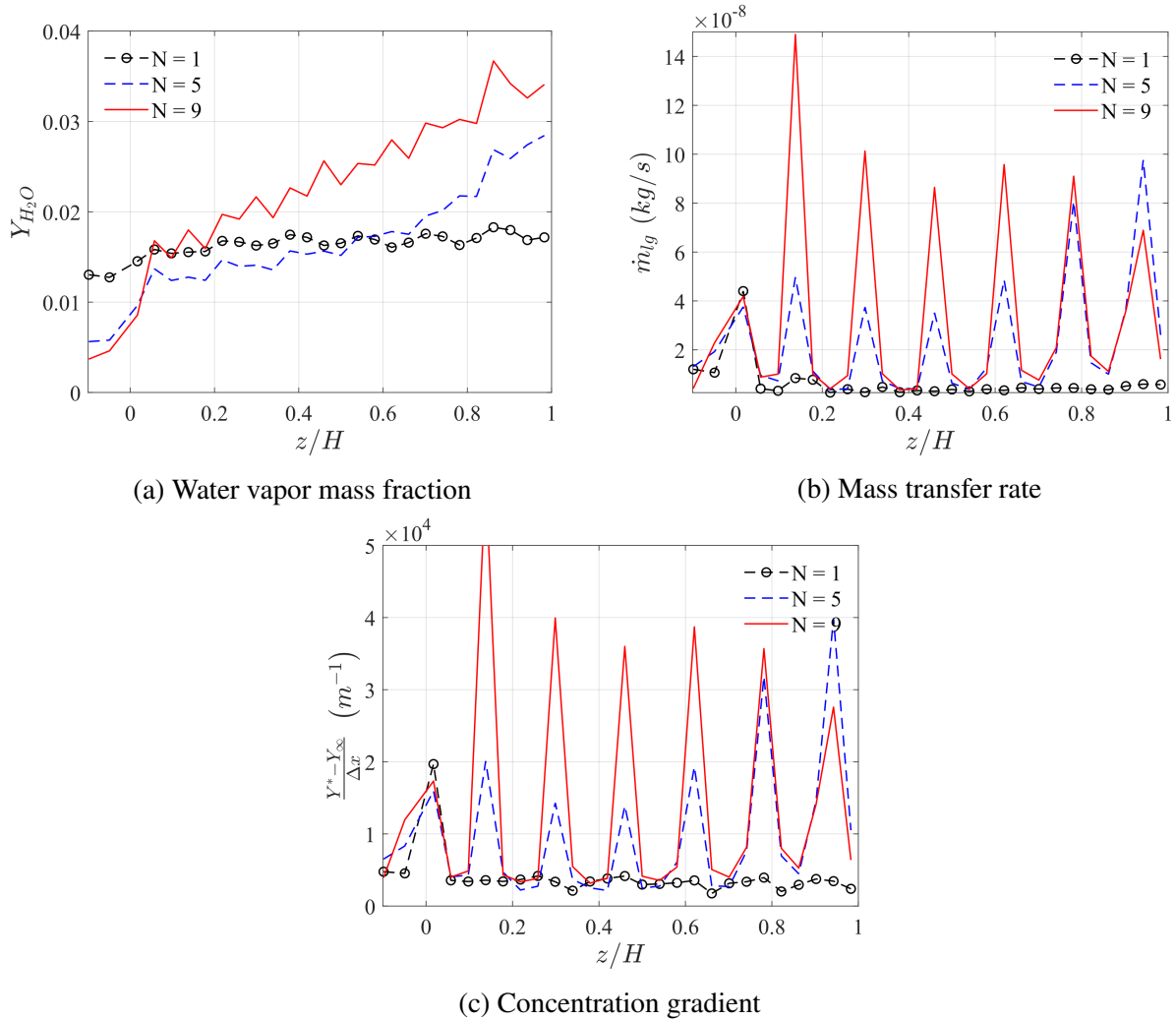


Figure 7.18: Mass fraction, Mass transfer rate, and concentration gradient profiles

bottom section influence.

The mass transfer rate as depicted in Fig. 7.18b shows periodic peaks that are naturally in phase with the volume fraction since the evaporation process can only occur in the presence of water. In all cases, the amplitude of those peaks coincide with the amplitude of the mass fraction gradient as shown in Fig. 7.18c which shows a very different behavior depending the spray density.

For $N = 1$, the mass transfer rate shows only one peak at the bottom of the column even though the presence of water is periodic throughout the packing (see Fig. 7.12). Nonetheless, with a low spray density, the hydrodynamics lead the water droplets to travel in the water vapor boundary layer as depicted by the contour in Fig. 7.19a. Therefore, as shown in Fig. 7.20a the evaporation process

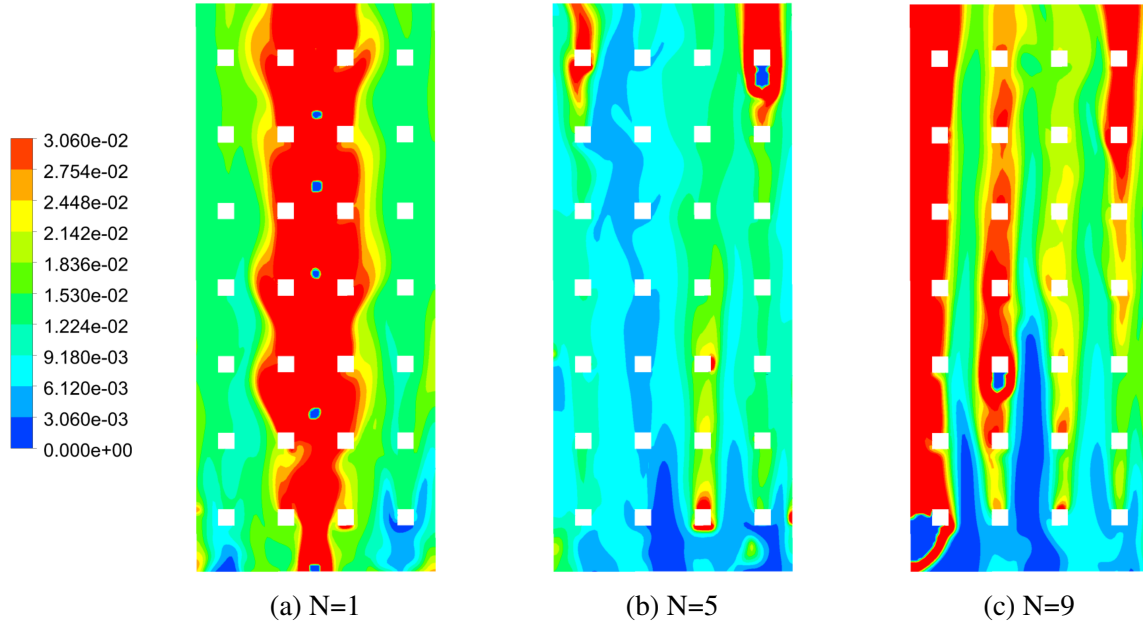


Figure 7.19: Normalized water vapor mass fraction contour at $t=4s$

is concentrated in a small portion of the total available volume. Hence the gas in contact with the water is closer to the thermodynamic equilibrium, yielding a lower gradient value at the interface along the column height.

With the spray density increasing ($N = 5$), the mass transfer rate naturally increases because of the superior interfacial area available, which also results in a better distribution of the water vapor in the gas phase as shown in Fig. 7.19b. Similarly, the mass transfer peak amplitudes are driven by the value of the gradient peaks, which increase along the height. The amplitude of those peaks gradually increases across the height signifying that $(Y^* - Y_\infty)$ increases. This is the result of Y^* exponentially increasing with temperature while Y_∞ remains limited by the interfacial area available for the mass transfer to take place. As shown in Fig. 7.20b the mass fraction remains low in most of the gas stream.

Finally, with the highest spray density, $N = 9$, the mass transfer rate rises again because of the gain in interfacial area. The enhancement of this latter translates to very high amplitudes for the mass transfer peaks, similarly driven by the mass fraction gradient. Though in comparison with $N = 5$ the amplitude of these peaks decays. In this configuration the interfacial area available at

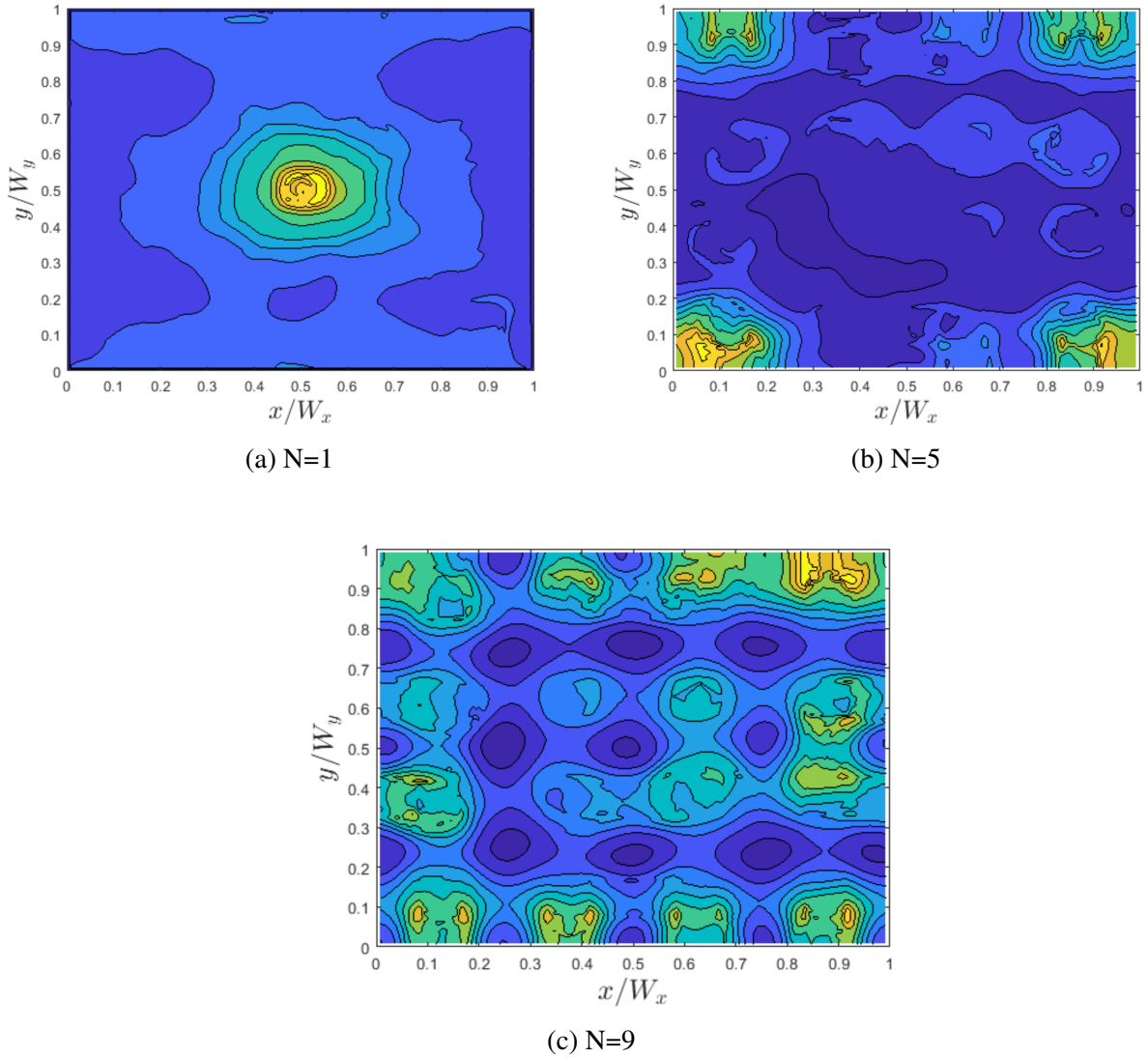


Figure 7.20: Time and spatial average contour of water vapor mass fraction

the bottom is sufficient to increase Y_∞ very close to saturation. As a consequence, the gradient becomes limited by the temperature rise and the the difference $(Y^* - Y_\infty)$ is decreasing. The mass fraction contour, Fig. 7.13b, shows a well distributed mass fraction but at a much higher value than Fig. 7.13a. This trend is confirmed by Fig. 7.20c with high mass fraction values across the section.

The bottom part of the packed column ($z/H < 0.5$) delivers more than 50% of the overall mass transfer. As a result, the top part of the column is relatively inefficient since the linear pressure drop remains but the evaporated mass is much lower due the gas stream getting closer to saturation. This is the reason why the calculation of the packed column height should be coupled with the water

distribution system employed and vice-versa. As an example, when delivering a certain amount of fresh water requires $Y_{H_2O}(z = H) = 0.025$, the highest spray density will only need a 21 mm high column to achieve that target while the lowest won't be able to achieve it. When sizing an evaporator there is always a trade between evaporation rate and pressure drop through the column. There is a need for innovative packing design that delivers high evaporation rate at low pressure drop.

7.3 Air Inlet Boundary Conditions

The previous section emphasized the critical correlation between the water distribution and the packed column response regarding pressure drop, liquid hold-up, heat and mass transfer. The counter-flow configuration also requires the gas distribution at the bottom of the column which may be non uniform because of the water dripping at the bottom but also because of a poorly designed distributor. In the same fashion, this section reproduces a similar study as for the liquid distribution but on the gas side to observe the impact of the gas distribution on the packed column response.

For that purpose the air inlet diameters varies and the velocity is adjusted to match the targeted gas mass flux. Two additional cases were created, one with $d_g = 5$ mm for which the setup is straightforward and another that would correspond to a perfect coverage of the packed column by introducing an artificial boundary conditions at the bottom of the domain. In all cases, the highest water spray density ($N = 9$) is employed and all other conditions remain the same.

As shown in Fig. 7.21, the bottom section of the domain was suppressed and the wall boundary condition defined at the bottom is now the gas inlet. The *removal section* is here to remove the water dripping out the packing. This water removal is accomplished by the addition of the following

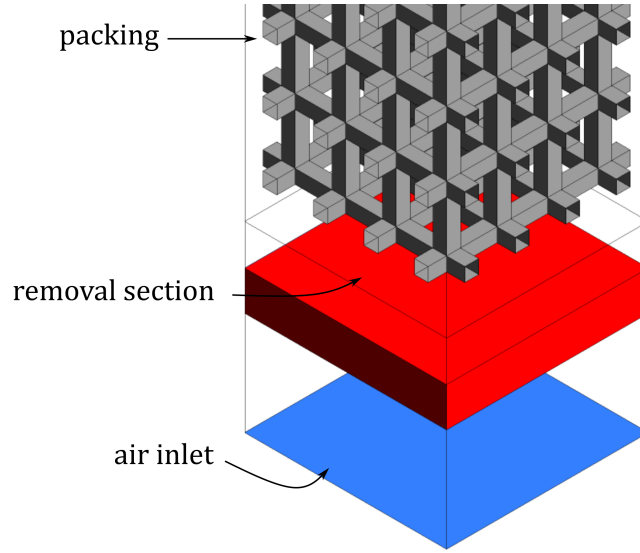


Figure 7.21: Schematic of modification to obtain homogeneous air inlet

source terms in the conservation equations:

$$S_{m_l} = -\frac{\rho_l \alpha_l}{\Delta t} \quad (7.10a)$$

$$S_{F_l} = -\frac{\rho_l \alpha_l \mathbf{u}}{\Delta t} \quad (7.10b)$$

$$S_{E_l} = -\frac{\rho_l \alpha_l E}{\Delta t} \quad (7.10c)$$

where S_{m_L} is the water mass removal added to the continuity equation, S_{F_L} is the momentum source term and S_{E_L} is the enthalpy source terms for the energy equation. The flow conditions for the case studied are given in Table 7.9.

Table 7.9: Air inlet flow conditions

d_g (mm)	ϕ_g ($kg \cdot m^{-2} \cdot s^{-1}$)	u_g ($m \cdot s^{-1}$)	$\Delta P/H$ ($Pa \cdot m^{-1}$)
5	0.25	0.752	10.9
7	0.25	0.3835	11.20
<i>Uniform</i>	0.25	0.204	11.44

7.3.1 Results & Discussion

7.3.1.1 Pressure Drop & Liquid Hold-Up

Using the same post-processing algorithm as in section 7.2.1.1 the linear pressure drop can be computed. As shown in Fig. 7.22a the pressure drop is not significantly affected by the distribution for the cases studied. The geometry employed is a build of very small corrugations which leads the flow to develop in a similar fashion as observed in porous media. Therefore, the gas velocity profile develops extremely quickly and the pressure drop becomes linear after the first corrugation, independent of the air distribution.

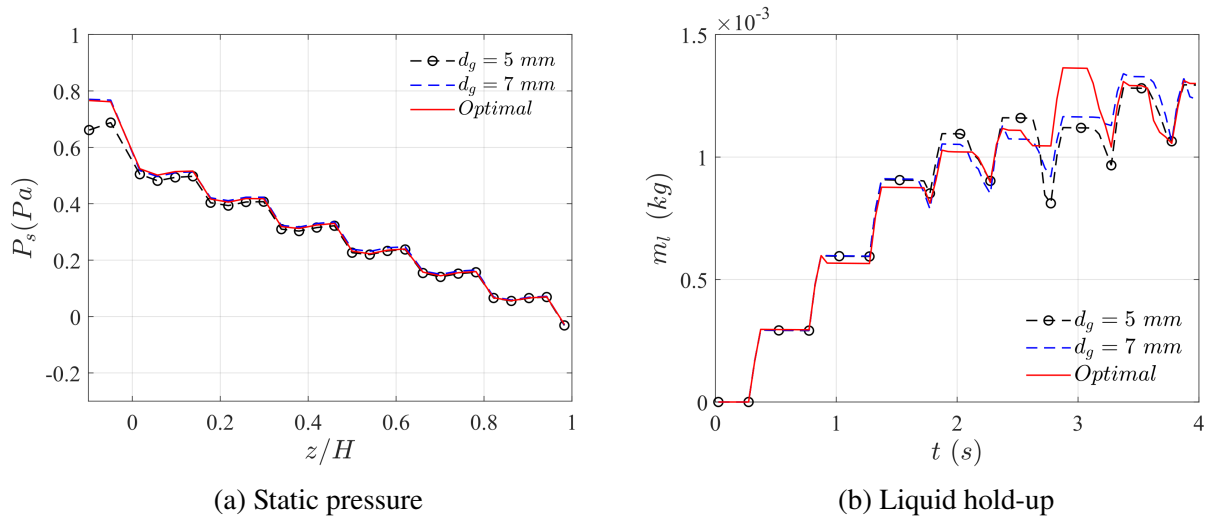


Figure 7.22: Static pressure profile and transient response of liquid hold-up

Similarly, the liquid hold-up in the test section remains unaffected by the gas distribution for the same reasons as the pressure drop. The interaction between the packing and water, is the main driver for variations in liquid hold-up. Since the gas velocity profile develops extremely fast, the gas-liquid interaction remains the same thus leading to a similar liquid hold-up.

7.3.1.2 Heat & Mass Transfer

With similar liquid hold-up and pressure drop, the liquid distribution and gas-liquid interactions remain close; hence the heat and mass transfer are also expected to be similar. As shown in Fig.

7.23 the phase temperature profiles are very close from each other. The water temperature profiles shown in Fig. 7.23b are overlapping one another while a slight difference is observed on the air temperature profiles shown in Fig. 7.23a. The air temperature of the *uniform* configuration shows a lower temperature at the bottom of the column mainly due to the heat and mass sink acting in the removal section. In the other cases, the residual water in the test section slightly pre-heats the gas before entering the column. Past that lower region, the gas temperature gradient has the same slope in all cases.

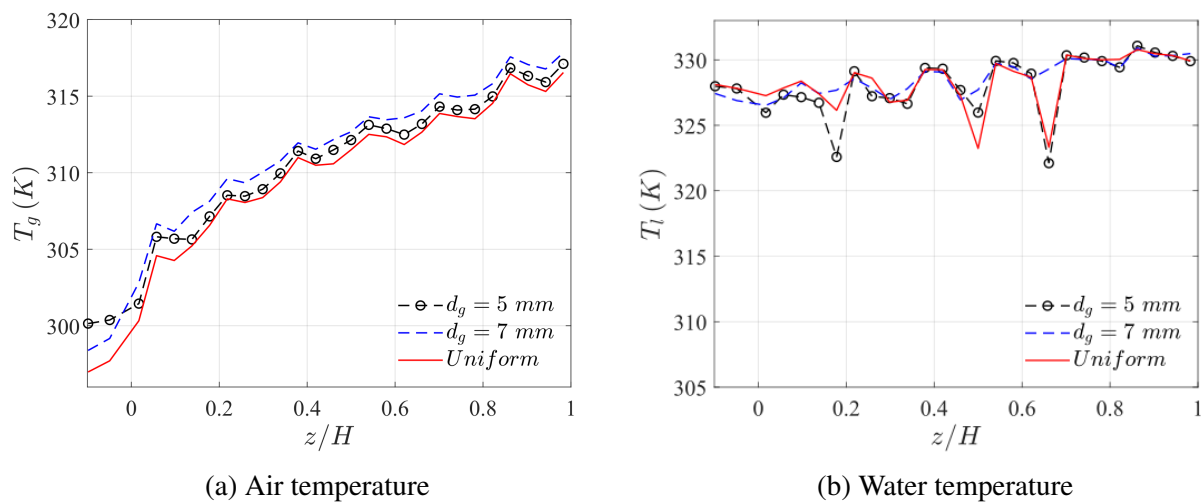


Figure 7.23: Transient response of water vapor mass fraction and interfacial area

Similar results are observed regarding the transient response shown in Fig. 7.24. In all cases, the water vapor mass fraction and interfacial area remain unaffected by the gas distribution at this regime. The mass fraction profiles shown on Fig. 7.25a are also lying on one another. The mass transfer and the gradient shown in Figs.7.25b and 7.25c have the same profile with the peak amplitude.

The results obtained show a clear insensitivity to the air distribution for these conditions. Caution should be exercised to not overgeneralize. The results obtained could be different with vastly different boundary conditions. As an example for $\phi_g = 0.25 \text{ kg}\cdot\text{m}^{-2}\cdot\text{s}^{-1}$, the velocity needed for a single 7 mm inlet is 3.45 m/s. At such velocity, the flow would transition to a turbulent regime, hence strongly affecting the results. The use of a single fluid formulation such as the VOF also

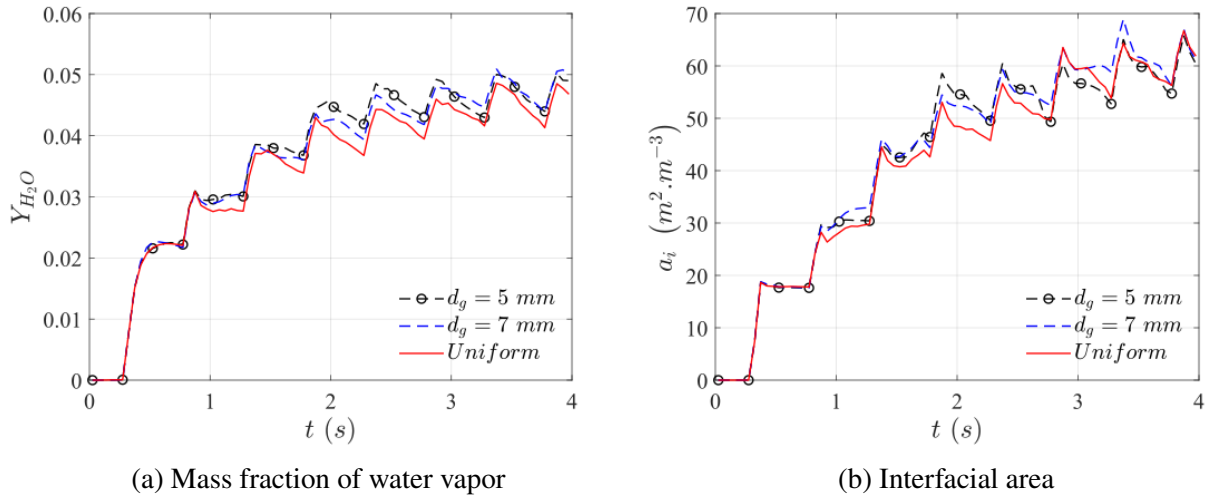


Figure 7.24: Transient response of water vapor mass fraction and interfacial area

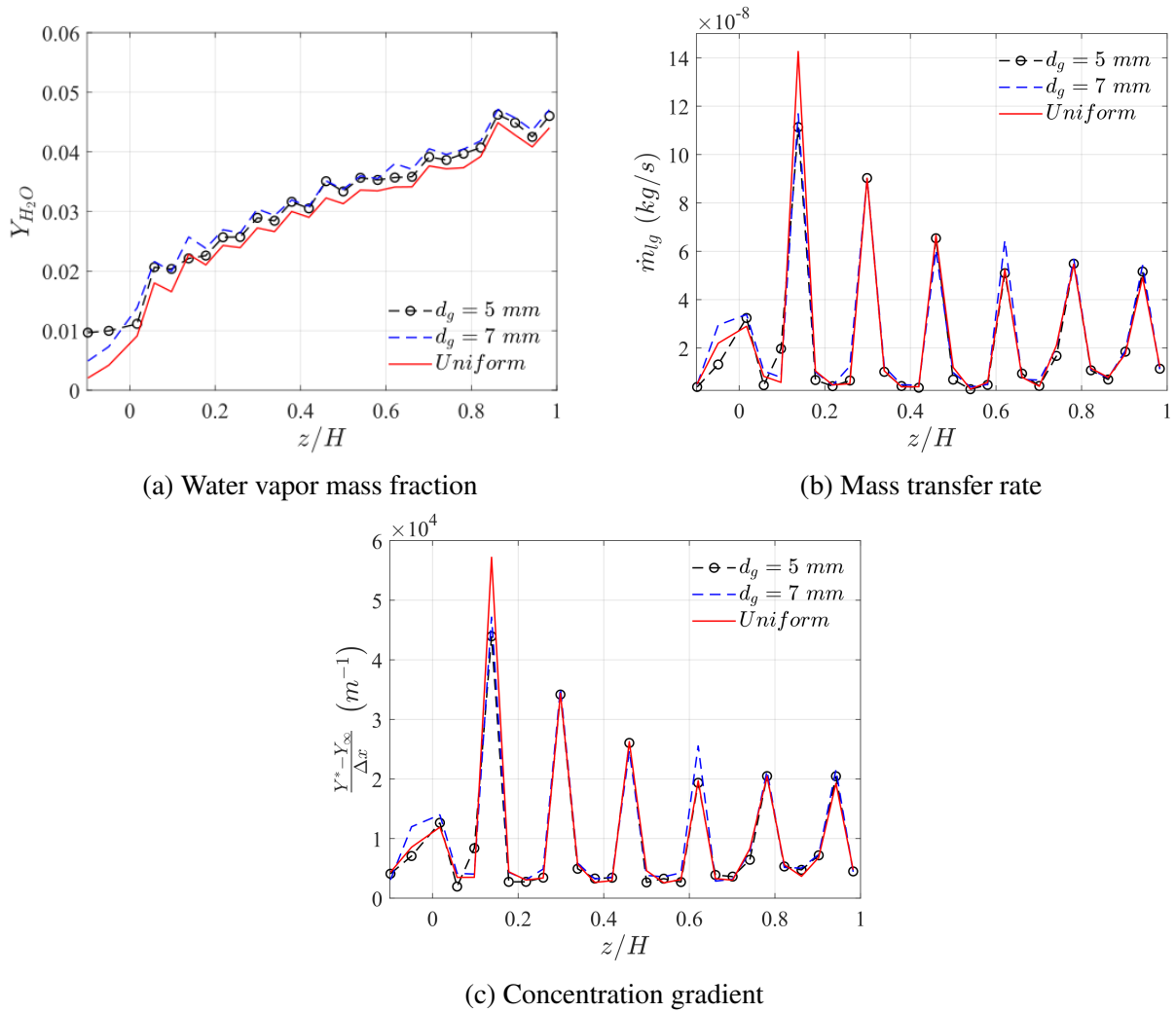


Figure 7.25: Mass fraction, mass transfer rate, and concentration gradient profiles

limits the modeling of inter-phase momentum exchange. With high relative velocities, the drag induced by the gas on the liquid is expected to take a significant role on the hydrodynamic behavior of the column. Accurate modeling of these inter-phase phenomena would require a significantly finer mesh or the introduction of a two-fluid formulation.

7.4 Packing Geometry Design Improvements

After studying the influence of the liquid and gas distribution, the multiple configurations provide guidance on the design of novel geometries for direct contact evaporation. Novel packing geometries should seek to improve aerodynamics, reduce water blockage, and enhance air/vapor mixing.

The calculation of the dry pressure drop during the mesh convergence study shows that, for the geometry studied, this latter represents 60 % of the wet pressure drop. Employing an aerodynamically optimal geometry would considerably decrease the pressure drop and increase the overall efficacy of the evaporator tower. The added pressure drop due to the presence of water can be divided into two contributions. The contribution from the enhanced interfacial area inducing more shear between gas and liquid and the contribution from the non-homogeneous distribution of liquid along the packing that necessarily reduces the cross-sectional area available for the gas to flow through. Ultimately, this non-homogeneity leads to the *blockage* phenomenon as depicted by Fig. 7.26, where 4 corrugations are blocked by water. This phenomenon, first observed experimentally by Li et al. (2006), is due to the surface tension effects and wall adhesion which becomes the primary momentum source when the water velocity is low. As a result, the water accumulates in these regions until a blockage is created.

For the conditions studied, the heat and mass transport is mainly through convection in the vertical direction and diffusion based in the transverse directions as shown by the quasi-nil normalized velocities in Fig. 7.27a.

This unidirectional transport phenomena limits the efficacy of the packing when the interfacial area in the transverse direction is too low. This phenomenon is particularly strong for the lowest

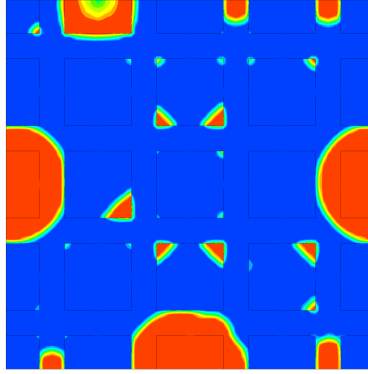


Figure 7.26: Liquid volume fraction contour showing the blockage phenomenon

spray density ($N = 1$) where a significant part of the air stream is not exploited. The natural solution to broadly improve the efficacy is to enhance the mixing in the gas phase to obtain a homogeneous distribution of the mass fraction across the section, leading to a lower mass fraction at the vicinity of the interface, yielding a higher gradient.

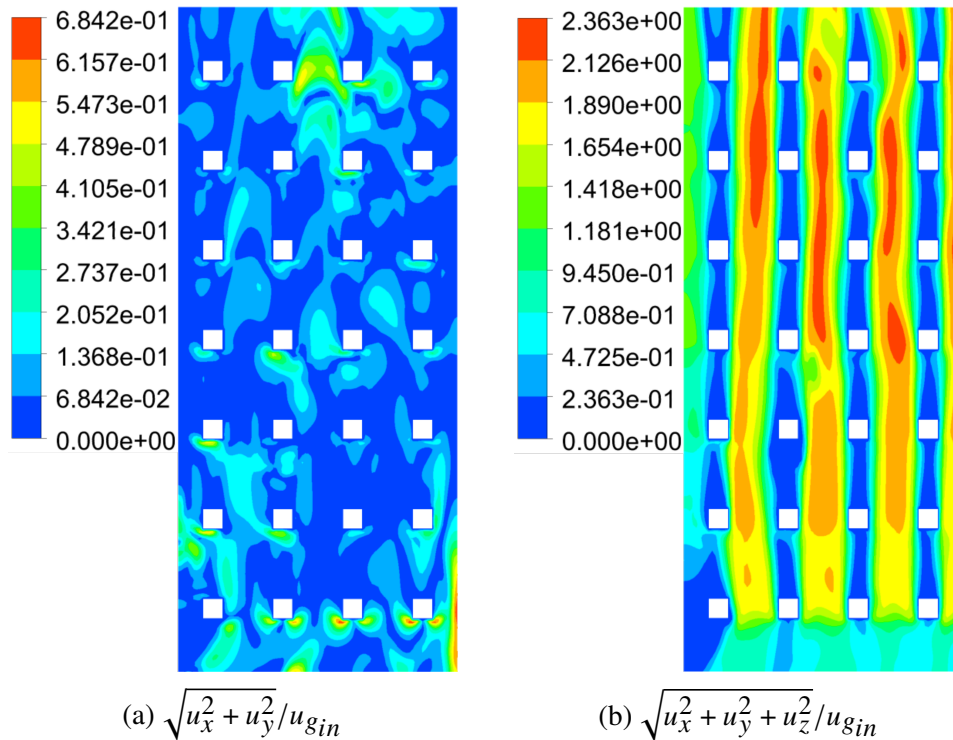


Figure 7.27: Normalized contour of velocity at t=3.5s

CHAPTER 8

MODELING OF THE BLOCKAGE PHENOMENON

8.1 General

Phenomena commonly associated with packed columns are blockage and flooding. On one hand, the latter is known to be associated with a significant increase in liquid hold-up, pressure drop and thus a loss in efficiency which typically occurs at high gas or liquid loading. The flooding phenomenon has been extensively studied in the literature since the late 30s, Sherwood et al. (1938) developed a correlation for Raschig rings to determine the flooding point depending on the mass flow rates and the properties of the fluids involved. In the following decades, multiple studies aimed at developing predictive models of the flooding point. Hutton et al. (1974) obtained a similar correlation for Pall rings. Stichlmair et al. (1989) developed a general model for the flooding point that uses empirically determined constants for each packing type. The resulting model yields good agreement with experimental data. The common ground for all these models is that their aim is predicting the flooding point for various packing materials using an experimental measurement that is further fitted to the model. Wolf-Zöllner et al. (2019) recently reviewed eight flooding point correlations for 32 packings and concluded that the sole use of the specific area and void fraction to describe the packing is a significant limitation. A geometry with the same void fraction and specific area but a different geometrical shape is defined by the same values but yields a very different flow pattern.

On the other hand, blockage or local flooding, in opposition with flooding, can occur at any operating conditions and is defined as when the liquid locally creates a bridge in a corrugation as described by Li et al. (2006) experimentally and is shown numerically in chapter 7. It is a function of the packing geometry, the contact angle, and the flow pattern. The harmful consequences of blockage are multiple as it globally reduces the cross-sectional area available for the gas to flow through. Hence, it increases the pressure drop and locally reduces the active interfacial area

available for mass transfer to take place. To the author's knowledge, in opposition with flooding, no predictive models of blockage are currently available in the literature. Improving packed columns performance necessarily goes through a deeper understanding of the blockage phenomenon.

Blockage being a phenomena taking place locally, the use of experimental techniques is extremely complicated; and isolating individual parameters such as contact angle, surface tension, flow pattern, velocity, and mass flow rate is not yet achievable. On the other hand, the use of multiphase computational fluid dynamic allows a relatively accessible and rigorous solution to control and monitor local variables such as pressure, velocity, and volume fraction. Computational fluid dynamics have been extensively employed over the last decades to solve more and more complicated multiphase problems involving packed columns. At the scale of the corrugation also called Representative Elementary Unit, Sebastia-Saez et al. (2018) studied the impact on mass transfer of the contact angle on an inclined plate and showed a strong correlation between wetting and the interfacial area. Kang et al. (2017) compared the resulting liquid-gas interfacial area from a 2D VOF calculation with well known empirical correlations such as Onda et al. (1968) and Billet & Schultes (1999) in a random packed column made of Raschig rings. Fu et al. (2020) proposed a similar study using a 3D model and derived a novel correlation for calculating the interfacial area for a random packed column of Pall rings. The common ground of these studies is the calculation of the flow hydrodynamic in currently existing geometries: random or structured.

The work developed and completed in this chapter aims at understanding the influence of flow pattern and packing geometric characteristics on the hydrodynamics between liquid and gas with an emphasis on the blockage and flooding phenomena. The results obtained give important insight in order to improve the geometries employed for the design of structured packed columns.

8.2 Governing Equations

To numerically model this phenomenon, simplified equations from section 5.3.1 are employed. The system of equations is simplified because heat and mass transfer are not modeled to save

computational time. Therefore, the remaining equations are given as follows:

$$\nabla \cdot \mathbf{u} = 0 \quad (8.1)$$

$$\frac{\partial \alpha}{\partial t} + \nabla \cdot (\alpha \mathbf{u}) = 0 \quad (8.2)$$

$$\alpha + \alpha_l = 1 \quad (8.3)$$

$$\frac{\partial}{\partial t} (\rho \mathbf{u}) + \nabla \cdot (\rho \mathbf{u} \mathbf{u}) = -\nabla p + \nabla \cdot \mu \left[(\nabla \mathbf{u}) + (\nabla \mathbf{u})^T \right] + \mathbf{F} \quad (8.4)$$

The surface tension forces are still modeled using the CSF model developed by Brackbill et al. (1992)

$$\mathbf{F}_\sigma = \sigma \kappa \nabla \alpha \quad (8.5)$$

where $\nabla \alpha$ is computed by the interface reconstruction algorithm Youngs (1982). At the wall the contact angle is defined to enforce the interface normal vector using the following equation:

$$\mathbf{n} = \mathbf{n}_w \cos \theta_{eq} + \mathbf{t}_w \sin \theta_{eq} \quad (8.6)$$

All calculations for this study employ the same discretization methods as in the previous chapter, and the only difference lies in the use of an adaptive time-stepping method where the time step is calculated in order to maintain the CFL condition that is set to unity.

8.3 Problem Setup & Boundary Conditions

The enhancement in heat and mass transfer for packed columns is highly dependent on increasing the specific area of the packing. Unfortunately, increasing this latter goes through the reduction of the hydraulic diameters the fluids must flow through, which is the main cause of the blockage onset. The goal here is to understand the influence of the flow pattern, packing geometry, and material on the blockage instability. As a consequence, the choice is made to study the problem at the scale of the corrugation assuming the symmetry in the whole column. As shown in Fig. 8.1, the domain consists of one corrugation in both horizontal and vertical directions to limit the computational expense. Water coming from the previous corrugation is modeled by placing an injector at the top

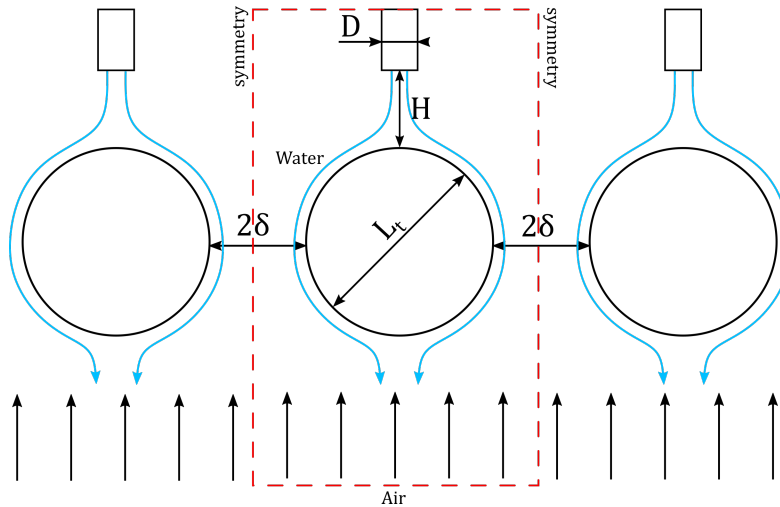


Figure 8.1: 2D schematic of the setup

of the domain. The counter-current gas stream is assumed to be perfectly homogeneous using the *removal section* in a similar fashion to section 7.3.

Figure 8.2 depicts the numerical domain in 3D with the name of the associated surfaces. The side walls are defined as *symmetry* boundary conditions; both fluids' inlets are *velocity inlets*; and the geometry surface is defined as a *wall* where the no slip and contact angle condition is imposed. The domain dimensions are given in Table 8.1. Note that the total height of the domain is equal to 40 mm .

Table 8.1: Blockage domain dimensions

Parameter	Value	Unit
w_x	8	mm
w_y	8	mm
D	1.5	mm
H	5	mm
L_t	5	mm
δ	1.5	mm

In order to obtain a more accurate description of the geometries using broadly non-dimensional numbers, the novel approach taken here is to characterize the Re number using the size of the constriction in place of the traditional void fraction and specific area (Klausner et al. (2006)).

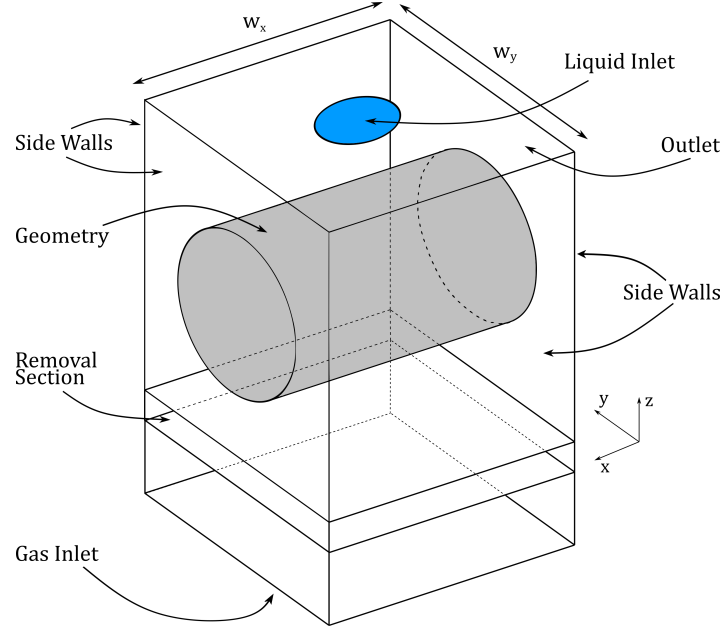


Figure 8.2: 3D schematic of the numerical domain with associated surfaces

This choice is dictated by two needs. First, as recently mentioned by Wolf-Zöllner et al. (2019), those definitions (void fraction, specific area) are limiting in terms of geometry characterization. Secondly, since the case studied here only considers a single corrugation, using the specific area and void fraction that are based on a per unit volume characterization is irrelevant. In other words, it would be easy to match a targeted void fraction and specific area by adjusting the distance in between each corrugation in the vertical direction. As a consequence, the Re number for the gas phase here is defined as Re_δ is given as follows:

$$Re_\delta = \frac{\rho_g u_\delta D_h}{\mu_g} \quad (8.7a)$$

$$D_h = \frac{4A_\delta}{P_\delta} = \frac{4(2\delta w_x)}{2(2\delta + w_x)} \quad (8.7b)$$

$$u_\delta = u_{gin} \frac{A_c}{A_\delta} = u_{gin} \frac{w_y w_x}{2\delta w_x} \quad (8.7c)$$

This definition characterizes the flow pattern at the constriction where the blockage is expected to occur while remaining robust for any type of geometry. Water properties remain identical and are

given in Table 7.5. The gas properties in this case are taken as constants with $\rho_g = 1.225 \text{ kg.m}^{-3}$ and $\mu_g = 1.72 \times 10^{-5} \text{ kg.m}^{-1}.s^{-1}$. The surface tension remains at 0.072 N/m . The gravity vector points in the opposite direction to the z-axis and $g = 9.81 \text{ m.s}^{-2}$.

8.4 Mesh Generation & Independence Study

The difficulty of this study is the application of the same boundary conditions to different geometries. Hence, the mesh generation and convergence consists of converging a meshing method that is further applied to all the geometries studied. As a result, the domain shown in Fig. 8.1 is subdivided into multiple blocks as depicted by Fig. 8.3. The *block 0* is generated using 0.3 mm hexahedral cells in every directions. *Block 1* is defined as a box spanning the whole depth and width of the numerical domain and starts 0.5 mm under the corrugation and finishes 0.5 mm above it. This refinement is here to ensure that there is a high resolution of the gas phase flowing through the constriction where velocity gradients are expected. *Block 2* is a boundary layer type refinement that is normal to the corrugation with a constant thickness equal to δ . Water is expected to form a film at the surface of the corrugation; thus, it is necessary to ensure the proper resolution of the film hydrodynamics at the corrugation surface as well as a smooth interface to obtain a satisfactory accuracy, while maintaining numerical stability. *Block 3* is here to maintain accuracy when water forms a drop or a sheet underneath the corrugation, which has been shown to have a strong influence on the rest of the film as described by Wang et al. (2019). Finally, *Block 4*, is defined in order to have an accurate definition of the jet or drops impinging on the packing surface. The cell size of each block is given in millimeters in Table 8.2 for the three mesh densities tested. Note that when the blocks intersect, the intersections are meshed using the smaller cell size.

Table 8.2: Refinements level for each block

Mesh	<i>Block 0</i>	<i>Block 1</i>	<i>Block 2</i>	<i>Block 2+</i>	<i>Block 3</i>	<i>Block 4</i>	δ_2	δ_{2+}
0.8 M	0.3	0.075	0.075	0.075	0.15	0.075	2	1
3.26 M	0.3	0.075	0.0375	0.0375	0.15	0.075	2	1
5.2 M	0.3	0.0375	0.0375	0.0375	0.15	0.075	2	1

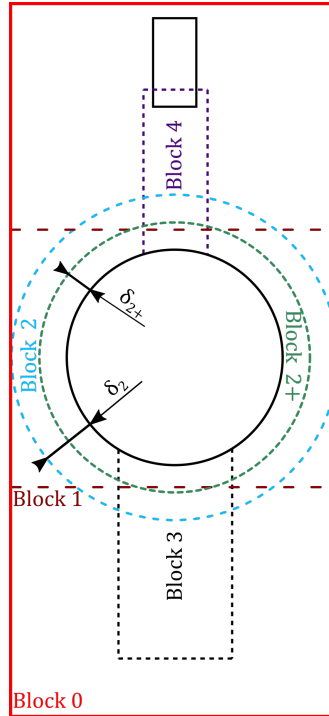
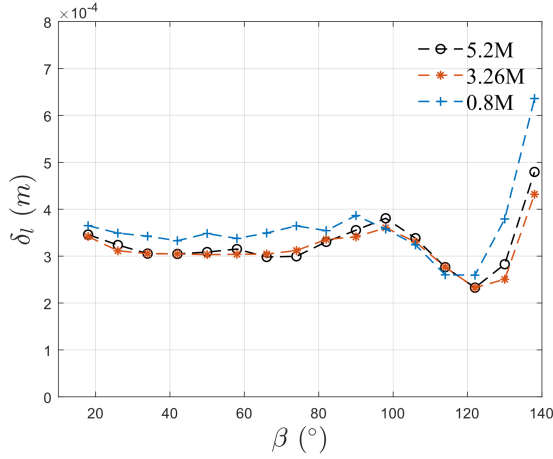


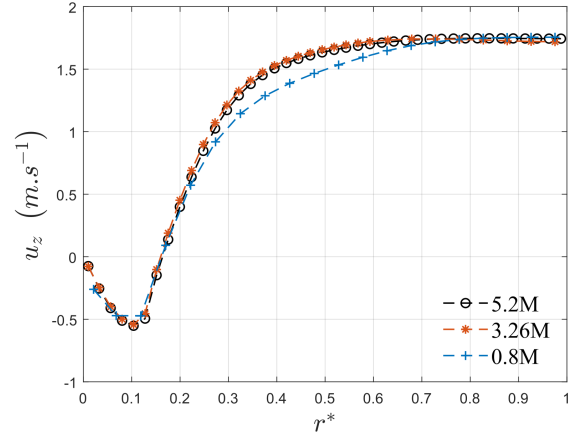
Figure 8.3: Mesh block definition

The meshing method validation is accomplished by measuring the average thickness of the falling film along the x-axis as well as observing the vertical velocity profile in both gas and liquid at the center-line of the constriction. For this convergence test, the contact angle is set to zero, the water velocity at the inlet is set at 0.6 m/s, and the air velocity at the bottom is set at 0.408 m/s corresponding to $Re_\delta = 492$.

As shown by Figs. 8.4a and 8.4b both the film thickness and velocity profile converge when the cell size in the vicinity of the interface refines to 0.0375 mm. Therefore, since the target of this study is to observe the blockage phenomenon where the film thickness would be equal to the constriction, the choice is made to globally refine *Block 1* with the 0.0375 mm cells. As a consequence, this meshing method is applied to the three geometries tested in this study.



(a) Average film thickness along the tube



(b) Vertical component of velocity at the constriction

Figure 8.4: Mesh convergence study with $u_{lin} = 0.6$ m/s and $u_{gin} = 0.408$ m/s

8.5 Study in the Column Regime

8.5.1 Validation of Numerical Results

In the water column regime that usually leads to the well-known flow pattern of falling film around a tube, the analytical solution developed by Nusselt is often used for validation of numerical results (Zhao et al. (2018), Li et al. (2016), Hou et al. (2012)) and is given as follows:

$$\delta_l = \left(\frac{3\mu_l\Gamma}{\rho_l(\rho_l - \rho_g)g\sin(\beta)} \right)^{1/3} \quad (8.8)$$

$$\delta_l = \left(\frac{3\mu_l\Gamma}{\rho_l(\rho_l - \rho_g)g\sin\left(\frac{3\beta}{4}\right)} \right)^{1/3} \quad (8.9)$$

where Γ is the liquid flow rate per unit length on each side of the horizontal tube and β is the circumferential angle measured from the top of the tube. As shown in the literature, several factors besides water flow rate are known to have an impact on the film thickness, such as surface tension, liquid distribution height (H), tube diameter (L), or the pitch between tubes if a tube bank is considered Zhao et al. (2018). Finally the presence of a counter-current flow is also a factor affecting the film thickness. In this study the film thickness is compared with the Nusselt solution and the correlation from Ji et al. (2017) given by equation (8.9). The flow conditions are given in Table 8.3.

Table 8.3: Flow conditions for validation in the column regime

Parameter	Value	Unit
$u_{l_{in}}$	0.6	$m.s^{-1}$
Γ	0.066	$kg.m^{-1}.s^{-1}$
$u_{g_{in}}$	0.408	$m.s^{-1}$

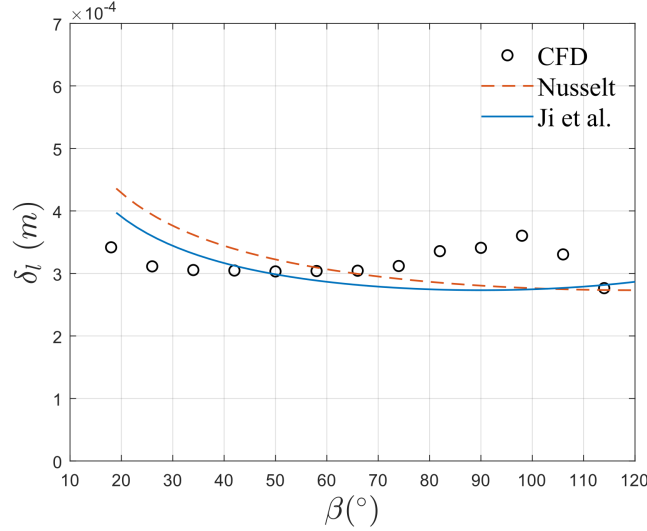


Figure 8.5: Spanwise averaged film thickness for various angular position in comparison with analytical solution and experimental correlation from Ji et al. (2017)

As shown by Fig. 8.5 the spanwise averaged film thickness is in good agreement with both the Nusselt solution and the correlation. The discrepancy between these ideal cases and the results obtained are due to two contributions. Firstly, the numerical calculation yields a highly three-dimensional flow pattern because of the tube to inlet diameter ratio in opposition with both equations (8.8) and (8.9) that were obtained assuming a two-dimensional problem. Secondly, the increased film thickness observed for $80^\circ < \beta < 110^\circ$ is due both to the strong drag generated by the gas flow along with the influence of the removal section (Hou et al. (2012)).

8.5.2 Influence of the Contact Angle & Geometry

The first part of this study consists in studying the influence of the contact angle, θ_{eq} , on the film hydrodynamics for each geometry. The water mass flux remains the same as for the mesh

convergence study, and the gas mass flux is divided by two. Hence, using equation (8.7), $Re_\delta = 246$. Figure 8.6 shows the average specific coverage of the corrugation as a function of the contact angle. When $\theta_{eq} = 0^\circ$, a perfect wetting of each corrugation is obtained as expected. Nonetheless the flow pattern obtained for the three different geometries is widely different as depicted by Fig. 8.7a. For the cylindrical geometry, the flow pattern obtained depicts a falling film over a cylinder as reported both numerically and experimentally in the literature (Qiu et al. (2017), Li et al. (2016), Fernández-Seara & Pardiñas (2014)). The crest observed is due to the water impinging the surface and generating a slight hydraulic shock. On the one hand, the diamond geometry yields a similar flow pattern with a film covering the entire surface and results in a column underneath and a crest at the top of the geometry, where the water impinges the surface. On the other hand, even if the specific water coverage remains equal to unity, the square geometry is presenting a strongly different flow pattern. First, because of the flat surface where the water impinges, this latter first accumulates at the top and it is only when the top surface is covered that the water starts reaching out and flowing on the sides. When the entire surface of the geometry gets covered, the drag generated by the gas stream on the interface present at the bottom plane prevents the water from gravitating further down. As a consequence, on the sides, the film thickness homogeneously increases on the whole span until the constriction is blocked. When the blockage occurs, the pressure increases until the liquid sheet atomizes upward.

With θ_{eq} increasing to 30° , the specific water coverage shows a discrepancy in between the geometries. The cylinder remains perfectly covered, but the adhesion force generated by the surface through the contact angle homogenizes the film thickness across the span. Hence, the flow pattern at the bottom transitions to a sheet mode where these latter are periodically released from the surface. The diamond geometry shows a significant decay in the specific water coverage with only 70% of the surface covered. The water impinges on the sharp edge at the top and spreads on the upper part of the corrugation before forming a rivulet type flow pattern on the down part. Finally, the water leaves the corrugation surface at the centerline of the bottom sharp edge in a steady column flow. This is extremely interesting because, in addition to providing a good coverage, the

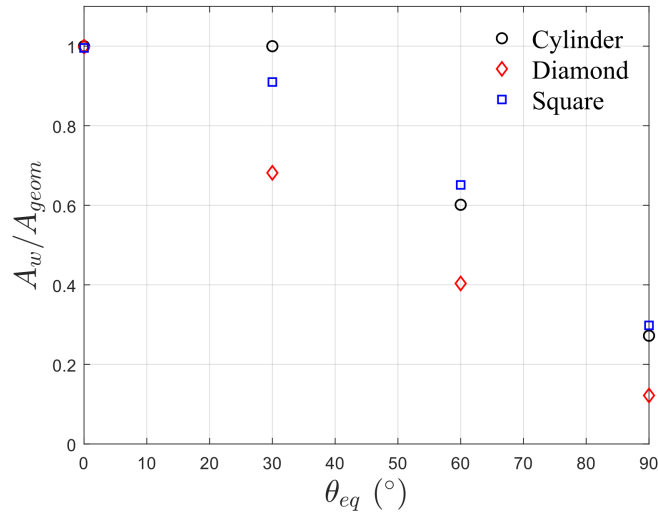


Figure 8.6: Specific water coverage for the three geometries studied as function of the contact angle

water flow stream leaving the corrugation has the same pattern as the incoming water, making the system periodic in the water streamwise direction. This flow characteristic is very important to develop a reliable model to calculate the interfacial area in order to predict mass transfer. The square geometry shows a specific water coverage around 90%, which is really close to the ideal coverage. The flow pattern shows the blockage instability with partial atomization of the liquid film. The higher contact angle prevents the perfect wetting thus, allowing the gas to flow through the constriction; and sheets of liquid are periodically released from the bottom plane.

Increasing θ_{eq} to 60° naturally decreases the specific water coverage, and both the cylinder and diamond transition to a rivulet flow pattern on the top and bottom part of the geometry. The former shows a transitory blockage at the constriction, which naturally disappears once steady-state is reached. Similarly, the column flow pattern exiting the geometry is the same as the one that is impinging, making the water flow periodic. The latter (diamond) also shows an exiting column flow that is slightly off the center line due to the apparition of the *teapot effect* triggered by the contact angle increase in the presence of a sharp edge (Duez et al. (2010), Kistler & Scriven (1994)). The square shaped geometry shows a similar trend with a specific water coverage decaying but less than the other geometries tested. The increased contact angle exacerbates the accumulation of water at the top of the corrugation and no liquid flowing is observed. When the mass of liquid is sufficient to

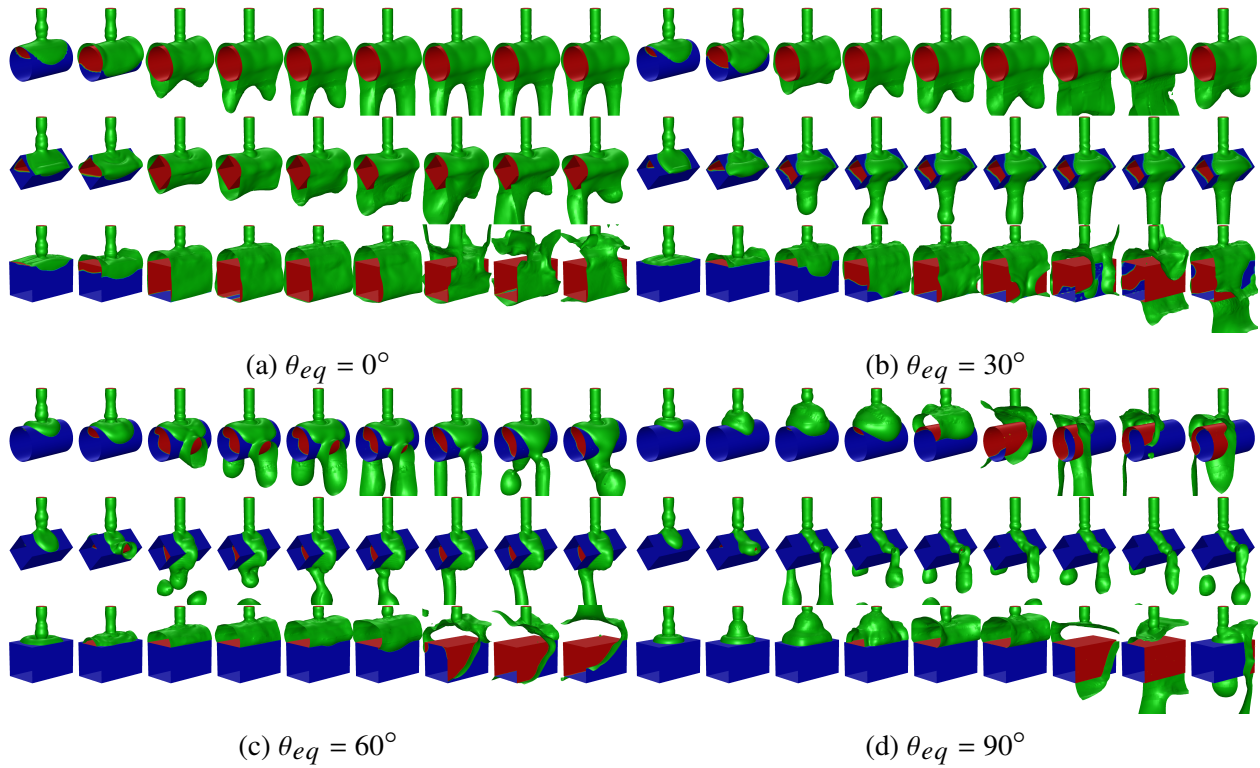


Figure 8.7: 3D contour of the free surface for the different contact angle at various flow time

overcome both surface tension and drag forces, the constriction is instantly overflowed and blockage is observed. Because of the amount of momentum required to cover the entire surface, the blockage is only partial in the spanwise direction and the gas flow can flow through the non-blocked portion of the constriction.

Ultimately, θ_{eq} is set to 90° and the surfaces are now considered hydrophobic. The specific water coverage of all geometries decreases and partial blockage is present in all cases. Only 30% of the cylinder and square shaped geometries are now covered with a similar flow pattern. After accumulating at the top, the water starts flowing down using one side of the span and the gas flows on the other in a quasi-steady fashion. Drops and columns form at the bottom of these geometries that are periodically released. On the other hand, the diamond geometry shows a specific water coverage of 14%, which is the lowest of all three geometries; but the impossibility for water to accumulate on top initiate an instantaneous stream of water that creates a small blockage at the constriction. This further leads to the steady release of droplets at the constriction and, as a result,

the bottom part of the corrugation is dry. The consequence of a non periodic water stream is that, in this case, if another corrugation is positioned aligned underneath, the water will not interact with this latter unless another disruption would cause it to.

8.5.3 Summary of Column Regime

As shown in the previous section the water flow pattern can take widely different shapes depending on both the geometry and the contact angle assigned to the surface. As shown by Fig. 8.6, each geometry possesses a critical value of the contact angle from which the coverage diminishes linearly. It is emphasized here that the linear decay is quasi-independent of the geometries considered for the of contact angles studied. As shown by the free-surface contours in Fig. 8.7, the flow pattern varies widely as a function of geometry and out of the 12 cases studied, only two showed periodicity in the water flow direction. The square geometry showed blockage to different extents depending upon the contact angle and would be a poor packed column design. This is mainly due to the flat surface at the top that prevents water from gravitating downward. The cylinder improves this phenomenon until the surface contact angle reaches $\theta_{eq} = 90^\circ$ and then the same flow pattern is observed. Finally, in this regime, the diamond geometry shows a good compromise across a wide range of contact angle since only a partial blockage at $\theta_{eq} = 90^\circ$ is observed. Nonetheless, one should keep in mind that for low contact angles, the square shaped geometry can be considered if the bottom plane is removed to allow water to gravitate downward.

8.6 Study in Droplet Regime for Packed Columns

The study in the column regime provides useful insights on the flow pattern and the blockage instability depending on both geometry and contact angle. In the study of falling films around cylinders, Γ , which represents the mass flow rate per unit length of liquid on one side of the tube, which is employed as parameter to describe the flow rate of liquid. Depending on the study, Γ ranges between 0.01 kg/s.m^{-1} and $0.284 \text{ kg/s.m}^{-1}$ (Xie et al. (2019), Zhao et al. (2018), Ji et al. (2017)). Unfortunately, for multiple reasons, this formulation is not applicable to packed columns. Firstly,

it assumes a symmetry of the film on each side of the tube, which is a limiting factor. Secondly, it is also a different mass flow rate scale where, in packed columns studies, the superficial velocity or mass flux are usually employed to describe the fluid supplied to the column (Alnaimat et al. (2013), Carbonell (2000), Billet & Schultes (1999)). With $\Gamma = 0.066 \text{ kg/s.m}^{-1}$ the corresponding mass flux is 16.5 kg/s.m^{-2} based on the cross-sectional area of the domain. This value is extremely high for packed columns where the typical mass flux ranges between 0.5 kg/s.m^{-2} and 10 kg/s.m^{-2} (Li et al. (2006), Lopes & Quinta-Ferreira (2009), Alnaimat & Klausner (2013)). Therefore, the strategy taken here is similar to section 7.2 where the water is modulated in order to control the droplet size (d_l), velocity ($u_{l,in}$) along with the mass flux (L). As a consequence, the modulation of the water input is done by applying a simple mass conservation. Figure 8.8a depicts the periodically generated droplets.

$$t_{on} = \frac{16}{3D^2 u_{l,in}} \left(\frac{d_l}{2} \right)^3 \quad (8.10)$$

$$t_{tot} = \frac{\rho_l u_{l,in}}{A_c L} \frac{\pi D^2}{4} t_{on} \quad (8.11)$$

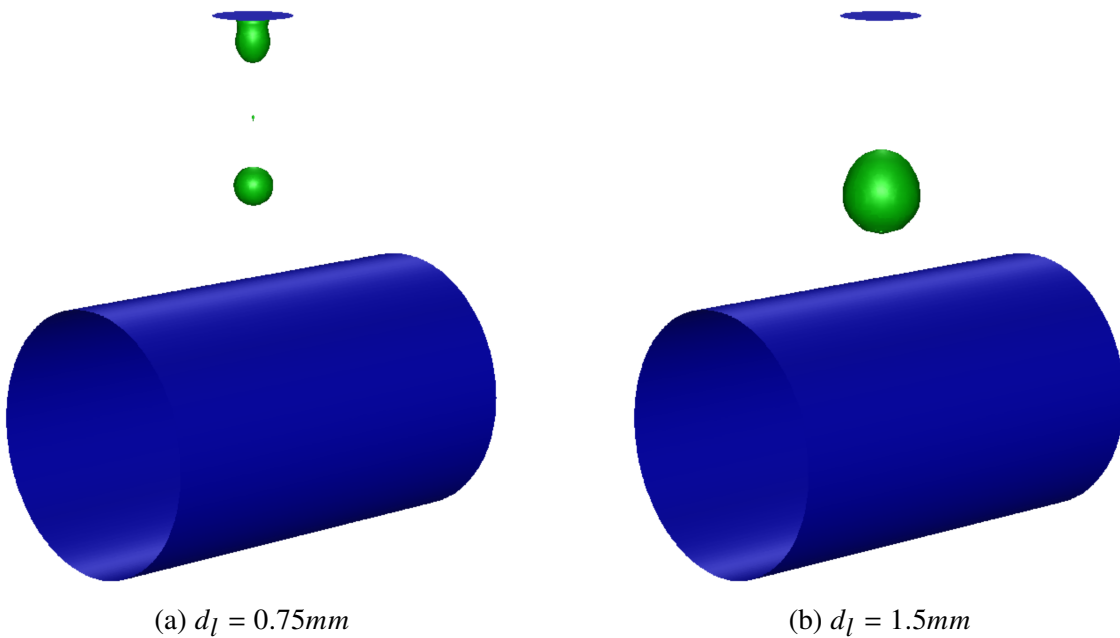


Figure 8.8: Droplet generated by adjusting the injection time

8.6.1 Validation of Numerical Results

8.6.1.1 Experimental Setup

In the column regime, the validation of the numerical results was done using the Nusselt analytically derived solution. Unfortunately, this approach is not valid in the drop regime, as the flow pattern of a falling film is very different from the drop regime. Therefore, the choice is made to validate the numerical results with flow visualization using a high speed camera.

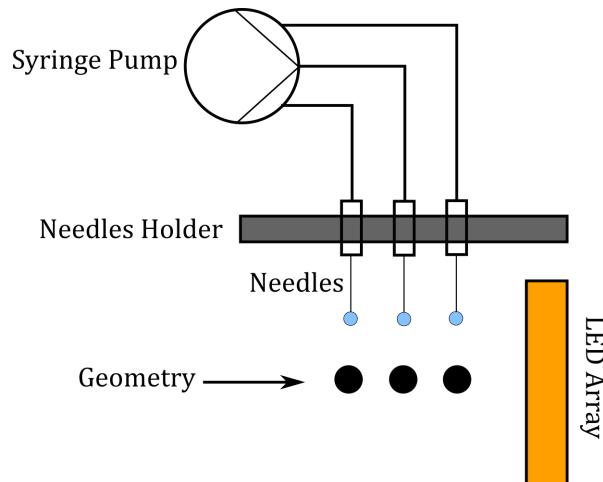
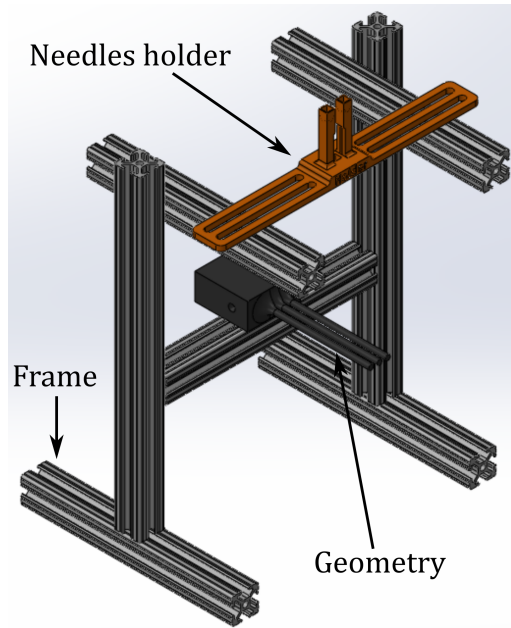


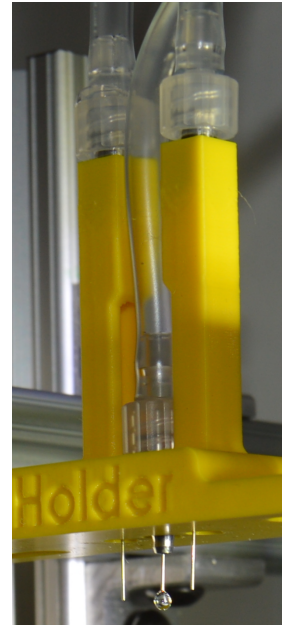
Figure 8.9: Schematic of high speed camera experiment for droplet validation

As depicted in Fig. 8.9, the experiment consist of generating droplets using hypodermic needles that will impinge on the geometry and are then recorded using a high-speed camera. The needles are fed using a programmable syringe pump capable of pushing all 3 syringes in parallel in order to obtain the same mass flow rate at all needles. Figure 8.10a shows the assembly with the frame, needle holder and the geometry. Both the geometry part and the needle holder were created using a 3D printer for the ease and flexibility of the manufacturing as well as the high precision of the parts obtained. In post-processing, the geometry is coated with black paint to limit as much as possible the glare generated by the illumination.

Figure 8.10b depicts an enhanced view of the needle holder assembly. The difficulty of this part was to maintain the space in between needle to 8mm as well as the leveled position of the tips while making the assembly possible since the Luer-Lock fittings radius is greater than 4mm. In



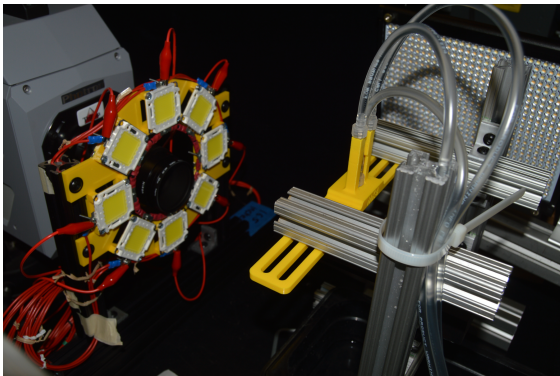
(a) CAD assembly



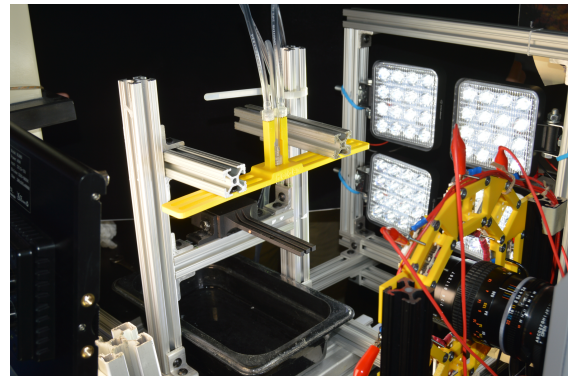
(b) Enhanced view of needles holder

Figure 8.10: Assembly zoom of drop experiment

other words, the fittings cannot be placed inline and have to be staggered as shown in Fig. 8.10b. In combination with needles of different length (6.35mm in the center and 50.8mm on the sides), the tips are aligned so that the drops release height is the same for each needle. For this study, 26 gauge needles are employed, which have a 0.464mm OD and 0.26mm ID.



(a) Front and left illumination



(b) Front and right illumination

Figure 8.11: Illumination setup

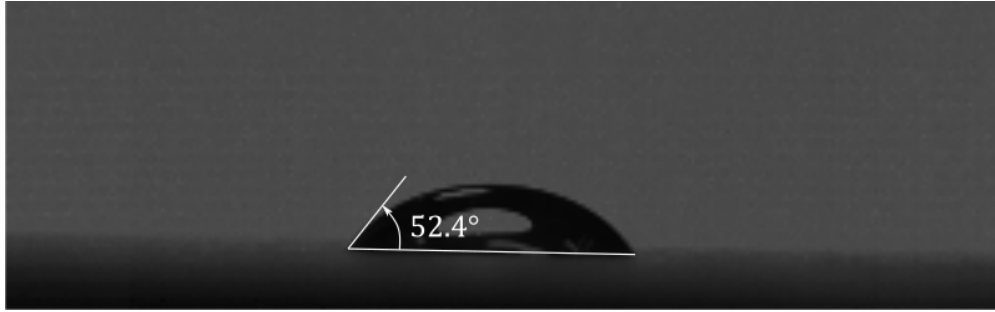
Finally, the main constraint with the use of high-speed cameras is the illumination. Traditional setups usually involve using back illumination, which is impossible here since the frame and the

geometry would be in the shadow. To solve this issue, the strategy taken here is to use a two sided illumination along with a front illumination as shown in Fig. 8.11. As depicted by Fig. 8.11a and 8.11b, the side illumination is accomplished using two LED arrays. The left array produces up to 3600 lumens (lm), while the custom made, right LED array, consists in 4 LED panels with each producing 4000 lm for a total of 16000 lm. The front illumination is handled using another custom made ring LED array that allows the camera objective to get through and therefore an excellent illumination without any obstruction. This latter is composed of 8 squared LEDs that produces up to 8000 lm each. Depending upon the camera framerate, the power supplied to the ring array is modulated to avoid excessive brightness querying the image quality. The high speed camera employed is a Photron SA-Z 2100K with an internal memory of 64GB, which allows the storage of 43,682 frames with a resolution of 1024x1024 pixels.

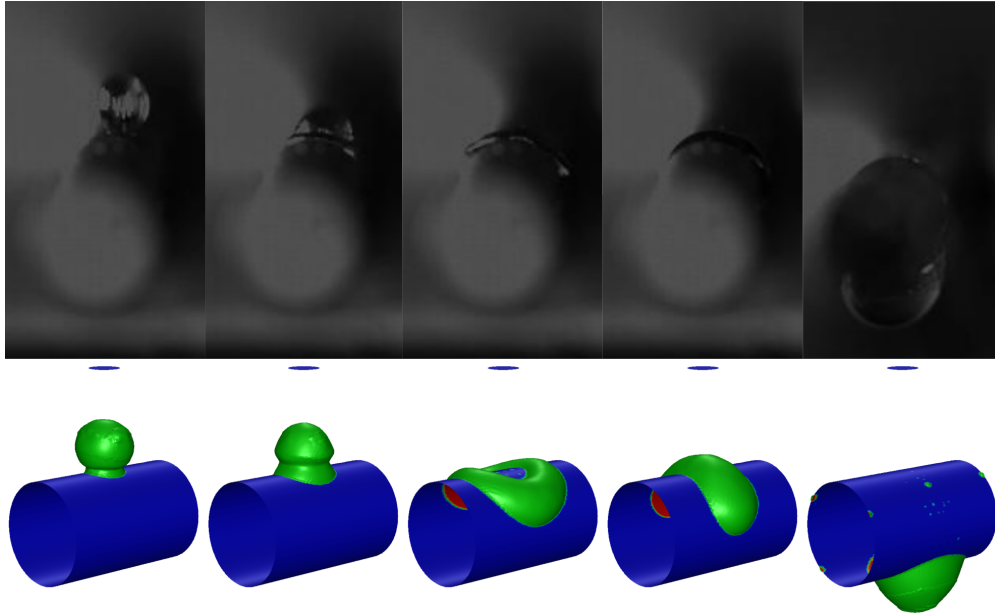
8.6.1.2 Procedure & Results

The experimental procedure consists of measuring the static contact angle of the painted geometry as shown in Fig 8.12a. Then, the high speed camera is employed to measure the droplets diameter. Finally, the velocity of the droplets is then calculated using the standard free fall equation neglecting the air resistance. As shown by Van Der Leeden et al. (1955), air resistance can be neglected when the distance at which velocity is of interest is situated less than half a meter underneath the departure location. The drop size and velocity are then set as input for the CFD; and a visual comparison of the free surface is accomplished as shown in Fig. 8.12b.

As shown in Fig. 8.12b the resulting free surface obtained with the CFD is in good agreement with the images obtained experimentally. The shift observed on the experimental image is due to the slight misalignment between the needles and the geometry as well as the surface roughness of the latter. The use of a 3D printer employing the Fusion Deposition Method (FDM) yields parts with very small ridges, which by nature affect the contact angle value. Nonetheless, the drop dynamic on the surface remains similar. The droplet impinges the surface and spreads homogeneously on each side of the corrugation until the adhesion and viscous forces stops this process. Then the surface



(a) Static drop on painted geometry



(b) Dynamic free-surface comparison

Figure 8.12: CFD and high-speed camera comparison

tension forces pulls the drop back together. When this process is done the drop slides underneath the corrugation and is then in a stable equilibrium. Experimentally 4 drops were observed to be necessary to trigger the departure of the lump created by the accumulation of water underneath.

8.6.2 Result & Discussion

This section discusses the parametric study results. The numerical procedure consists of varying the parameters of interest and running the CFD code using adaptive time-stepping until 0.5s of flow-time in a similar fashion as the column regime. For this study, the contact angle is set at $\theta_{eq} = 30^\circ$.

8.6.2.1 Influence of d_l

The first parameter of interest is the droplet size since, as observed experimentally, the flow pattern departing a corrugation is either a drop of a different diameter from the one impinging or as observed in the column regime study, drops of various size are generated with a column of fluid. The parameters for this study are given as cases 1,2, and 3 in Table 8.4. The input values of t_{on} and t_{tot} are calculated using equations (8.10) and (8.11). As the same meshing method as in the column regime is employed, the smallest diameter d_l that can be accurately computed is determined by the cell sizes in *block 4*, where the drop travels prior to impinge the surface. According to Meier et al. (2002), with the use of the CSF method, the smallest droplet diameter for which the surface tension force is accurately computed is $d_l = 0.75 \text{ mm}$.

Table 8.4: Flow conditions for the drop regime

Case	d_l (mm)	L	$u_{l_{in}}$	t_{on} (s)	t_{tot} (s)	G	$u_{g_{in}}$	Re_δ
1	0.75	1	0.10	0.0013	0.0034	0.25	0.204	246
2	1.5	1	0.10	0.0100	0.0276	0.25	0.204	246
3	3	1	0.10	0.0800	0.2205	0.25	0.204	246
4	1.5	1	0.05	0.0200	0.0276	0.25	0.204	246
5	1.5	1	0.10	0.0100	0.0276	0.25	0.204	246
6	1.5	1	0.30	0.0333	0.0276	0.25	0.204	246
7	1.5	1	0.60	0.0166	0.0276	0.25	0.204	246
8	1.5	1	0.90	0.0111	0.0276	0.25	0.204	246
9	0.75	1	0.10	0.0013	0.0034	0.25	0.204	246
10	0.75	1	0.10	0.0013	0.0034	0.50	0.408	492
11	0.75	1	0.10	0.0013	0.0034	0.75	0.612	739
12	0.75	1	0.10	0.0013	0.0034	1.00	0.816	986

The free surface patterns resulting from the diameter variation on each geometry are shown in Fig. 8.13. Depending upon the geometry, the resulting flow pattern for each drop diameter is relatively different. For the cylinder geometry, three different patterns are observed. When $d_l = 0.75 \text{ mm}$, the high frequency of drops impinging upon the surface and later on the water film, the water starts accumulating and generates a steady source of momentum that is sufficient to overcome the adhesion force from the surface. As a consequence, a steady rivulet type flow is

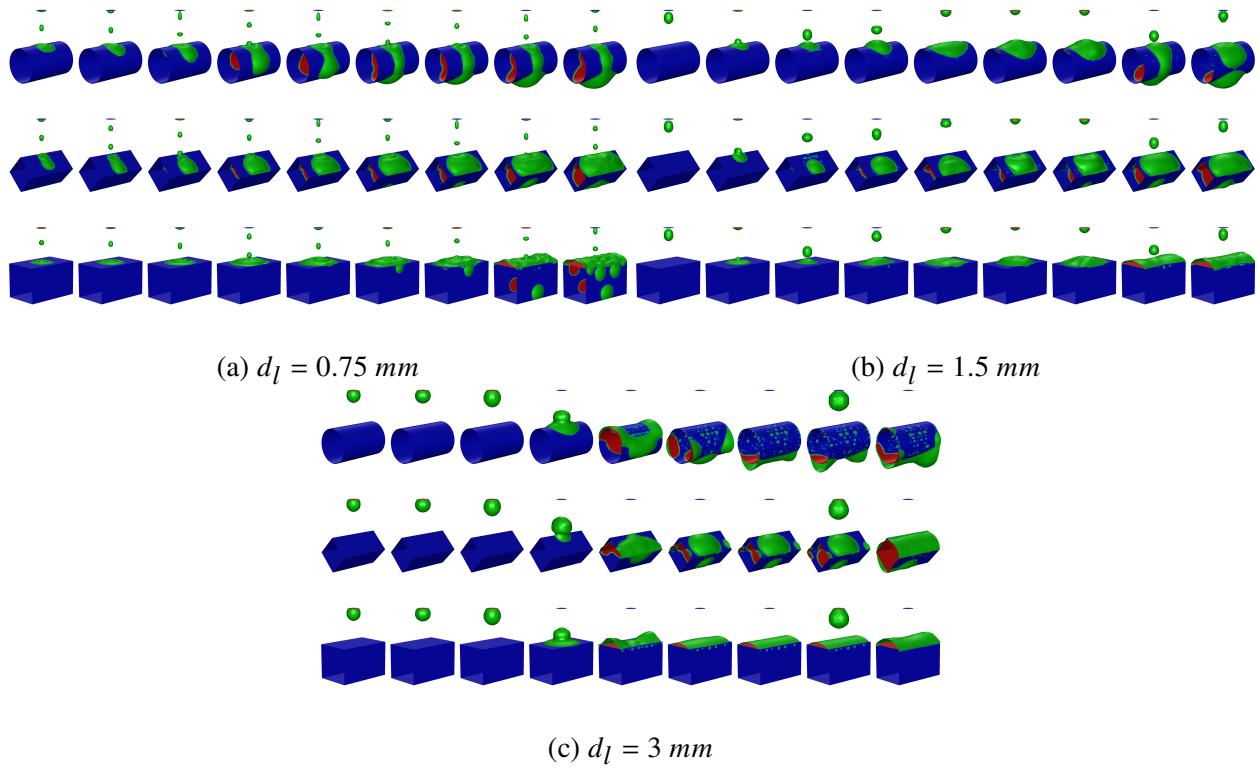


Figure 8.13: 3D contour of the free surface for the different drop diameters at various flow time observed with water accumulating at the bottom. When the drop diameter increases, the frequency at which the drops impinge the film diminishes; and if a rivulet type flow is observed, this film is unstable and the surface tension forces separate the lump of water at the top from the lump accumulating at the top. Nonetheless, this translates to a very similar specific water coverage as shown by Fig. 8.14a. Finally, increasing d_l to 3mm leads to the drop atomization because of the lower surface tension forces. Therefore, no water remains at the top, and water accumulates underneath. Hence, as shown in Fig. 8.14a, the specific water coverage is 15 % lower than the other configurations.

The diamond geometry does not show significant differences depending on the drop diameter because of the sharp edge at the top that systematically breaks the surface tension of the drop and forces the the water to spread on the corrugation surface. This tendency is confirmed by Fig. 8.14b where the coverage is approximately 60% at the final time but with a different trend. This difference is due to the larger mass of water injected at once instead of a smaller and regular feed that lead to

a sharp increase in coverage.

Finally, the square geometry shows interesting features depending upon the droplet diameter. In all cases, the water first accumulates on the top surface as shown by Figs. 8.13a, 8.13b, and 8.13c. The difference appears in a second phase where, because of the regular input of momentum generated by the drop impinging the water film created, small drops start sliding on the side of the corrugation. This phenomenon is confirmed by Fig. 8.14c where the coverage increases significantly with the small drops ($d_l = 0.75\text{mm}$) where the larger drops coverage stagnates. On the other hand, with $d_l = 3\text{mm}$ the water film created at the top has time to be stabilized by the surface tension forces until the next drop comes, which leads to a increased water accumulation. This excessive water accumulation would likely lead to a blockage later in time in a similar fashion observed on Fig. 8.7b.

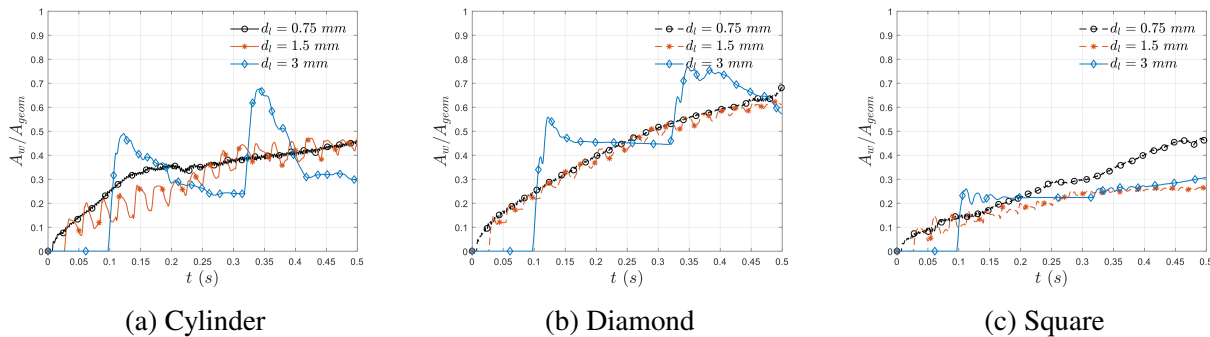


Figure 8.14: Transient specific coverage for each geometry as a function of the drop diameter

The geometry comparison yields a similar conclusion to the film regime. First, it is emphasized here that no blockage is observed for the flow-time computed; though the square geometry shows a large accumulation of water at the top for a large drop diameter, which is likely to produce this instability. The main advantage of the diamond geometry is its versatility with a similar water coverage in all cases along with a high specific water coverage. Finally, the cylinder also offers good coverage when the drops are small, but this is adversely affected for large drops that atomize on the surface.

8.6.2.2 Influence of $u_{l_{in}}$

The second hydrodynamic parameter studied is the velocity at the inlet, $u_{l_{in}}$. This parameter corresponds to cases 4, 5, 6, 7, and 8 in Table 8.4. With a contact angle of $\theta_{eq} = 30^\circ$, the results both in terms of flow pattern and specific coverage are very close. Increasing the drop velocity evidently changes the drop inertia, which for every geometry, increases the initial spread of the drop onto the surface. This phenomenon repeats over time at every drop because of the more important perturbation of the film that is created at the top of the surface. This explains the slightly higher specific water coverage observed for the high velocity as shown in Fig. 8.15.

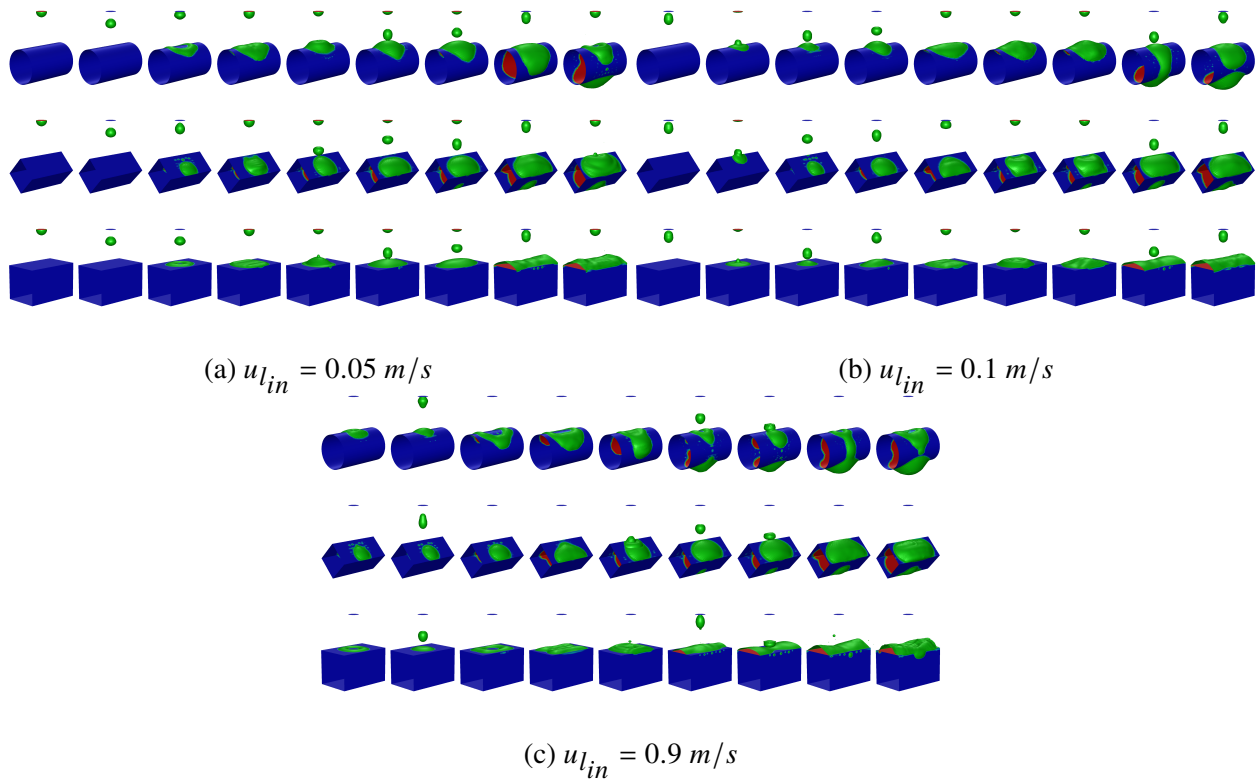


Figure 8.15: 3D contour of the free surface for the different $u_{l_{in}}$ at various flow time

As a result of the increased velocity and, therefore, the perturbation, the differences observed on the flow pattern are similar across geometries where the water starts flowing through the constriction earlier in flow time. This is particularly noticeable on the square geometry in Fig. 8.15c where the water starts flowing on the side explaining the slight increase in coverage starting at 0.35s in Fig. 8.16c. This tendency is also observable on other geometries but is less pronounced.

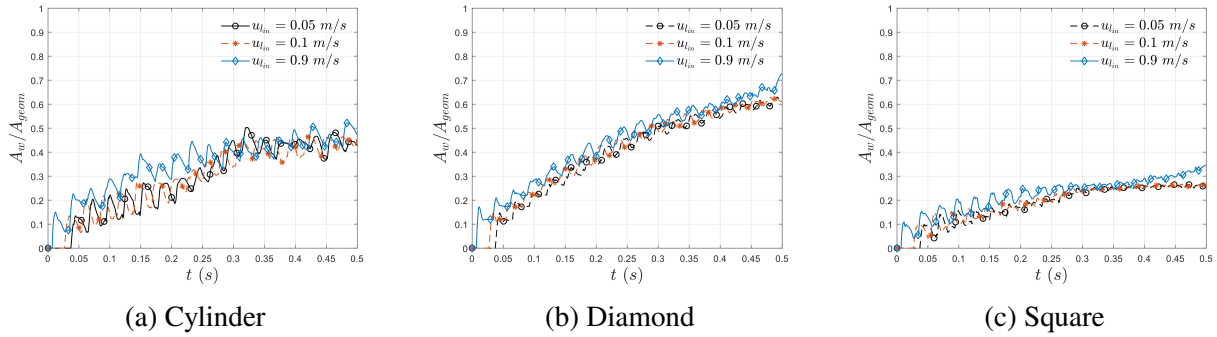


Figure 8.16: Transient specific coverage for each geometry as a function of $u_{l,in}$

In terms of blockage, a similar conclusion to the drop diameter study can be drawn. No blockages were observed for the flow time studied. Similarly, the accumulation of water at the top on the square geometry is likely to trigger blockage since more water is held up before it starts gravitating downward. Nonetheless, increasing the velocity naturally improves the water capability to overcome the surface tension forces, which later on allows water to flow through the constriction earlier in time. Hence, the likeliness for blockage to occur is diminished.

8.6.2.3 Influence of Re_δ

Finally, the last parameter to be studied is the gas Reynolds number at the constriction, Re_δ , which characterizes the amount of gas flowing through the packed column. This parameter study corresponds to cases 9, 10, 11, and 12 in Table 8.4.

As shown in Fig. 8.17, blockage is not observed for all geometries in all cases. It is emphasized here that on a longer time scale, blockage might be observed in the form of flooding because of the increased water accumulation taking place underneath, due to the drag generated by the counter-current gas flow. The cylinder geometry, because of its shape, does not show any major sensitivity in terms of specific water coverage for the range studied. The slightly higher coverage observed in Fig 8.17a is due to the drag increasing the water spread. A similar trend is observed on the diamond geometry where the highest gas flow rate, as depicted by Fig. 8.18c, shows a 5% increase after $t = 0.45s$, which corresponds to the water reaching all the inferior faces of the corrugation

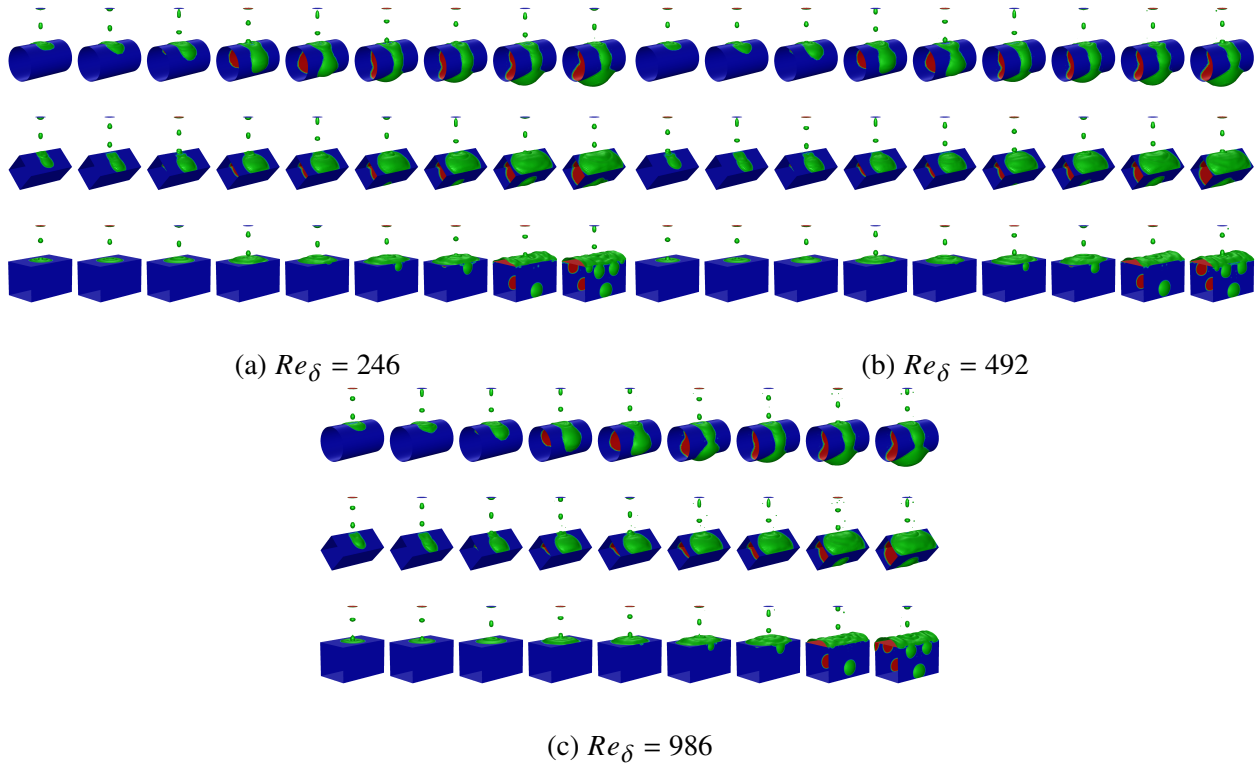


Figure 8.17: 3D contour of the free surface for different Re_δ at various flow time

where the gas stream is favorable for the water to spread. Ultimately, the square geometry shows a similar pattern and specific water coverage for all configuration. Nonetheless, it is expected for the latter to display a comparable trend where the coverage would increase once the water reaches the underneath plane.

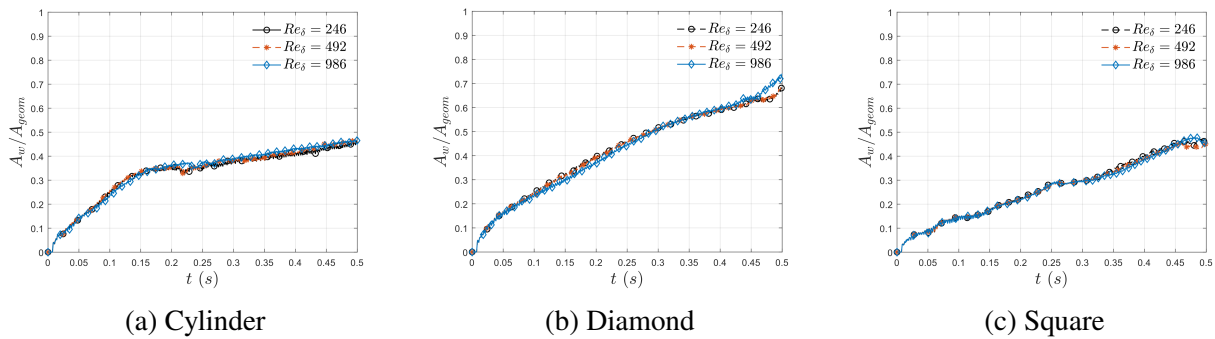


Figure 8.18: Transient specific coverage for each geometry as a function of Re_δ

With these observations, the author emphasizes the importance of the contact angle for the study of this parameter. As shown by Figs. 8.17 and 8.18 the specific water coverage increases

slightly because of the pressure generated by the counter-current gas stream when this latter reaches the bottom part of the corrugations. Therefore with a lower contact angle, the water would already naturally spread more on the surface, thus offering a superior surface area for the gas stream to apply pressure. This enhanced interfacial area for momentum exchanged, coupled to the inferior amount of work necessary to wet the surface, will result in a greater sensitivity to the gas flow rate.

8.6.3 Conclusion on Drop Regime

As shown in the previous sections, the drop characteristic shows a limited influence on the flow pattern observed at the scale of corrugation. For all the configurations tested, no blockages were observed, but caution is exerted here because of the short flow times simulated due to the computing expense that the study of multiple geometries and conditions cost. The square geometry shows incipience of the blockage phenomenon because of the water accumulating on the top plane. Similarly, with d_l increasing, the atomization observed with the cylinder geometry, as shown in Fig. 8.13c, would also lead to a temporary blockage with a slight increase in speed. A similar conclusion can be said for the specific water coverage where the drop pattern does not significantly affect the wetting of the corrugations for all geometry.

8.7 Conclusion on the Blockage Phenomenon

This study on the blockage phenomenon brings a lot of information on the packed bed hydrodynamic behavior. The most prominent information to retain from the observations is the blockage phenomenon is entirely determined by the corrugation geometry and material through the contact angle rather than the flow conditions for both gas and liquid. These parameters (geometry and contact angle) determine the amount of water that needs to accumulate before an actual film forms and starts flowing. They also determine the pattern in which the film gravitates downward as shown by Fig. 8.7. This also explains why the blockage phenomenon is observed independently of the liquid and gas mass fluxes. As a consequence, for future studies the column regime can be considered as a good indicator to determine the hydrodynamic performance of a corrugation

for purpose of coverage and blockage. Knowing that, among the geometries studied, the diamond shape showed interesting results for purposes of blockage at high contact angles, which is traded by a lower specific water coverage. The square showed the highest specific water coverage but a high predisposition to create blockage. Finally the cylinder showed satisfying results for low contact angles but water periodicity in the vertical direction should be improved. This allows one to design packed columns with corrugations very close to one another driving a significant increase of specific area while remaining free of the blockage instability that queries the efficiency of the tower. It should also be mentioned that under certain conditions this geometry also provides a quasi-periodic flow pattern that is important in developing accurate design tools.

CHAPTER 9

PACKED COLUMN GEOMETRY IMPROVEMENTS

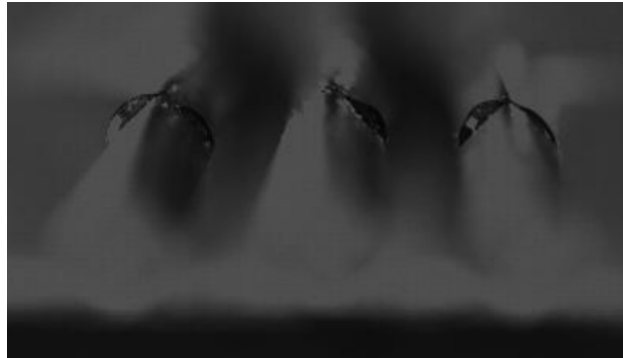
9.1 General Introduction

The initial interrogation that led to this work was the opportunity to improve on almost 90 years of research in the study of packed columns. The studies presented in this work allow general guidelines for the packing design. As mentioned in section 7.4, at the scale of the column, the necessity to analyze the column as a whole with the distributor is necessary in order to drive the efficiency of the evaporator higher. With that in mind the usage of hydrophilic packing material that naturally spreads the water into a film will considerably reduce the costly atomization taking place in the sprayer that is currently employed to ensure homogeneous wetting of the packing surface. Nonetheless, geometry improvements should start at the scale of the corrugation in order to obtain the following:

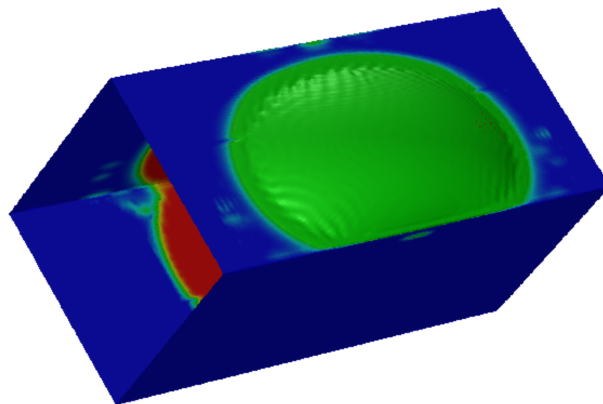
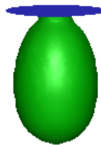
- Blockage free for a wide range of contact angle
- High specific water coverage
- Periodicity in the water flow pattern
- Low gas pressure drop

The blockage free geometry is the first design parameter to consider because it is the main issue encountered when the corrugations are getting closer to one another. As shown in the previous chapter, this phenomenon mainly depends on the geometry itself and the material employed for manufacturing. The results obtained with the diamond shaped geometry clearly drives the design in this direction. The presence of a sharp edge at the top to break the surface tension of the impinging stream is of first importance. Then preventing water accumulation on the upper part of the corrugation has to be addressed. It simply consists in avoiding at any location the geometry

surface normal vector pointing in the upward direction. It is the case with the diamond geometry because the inclined planes present on both sides in the upper region immediately force the water to flow downward.



(a) High speed camera visualization



(b) Free surface contour using CFD

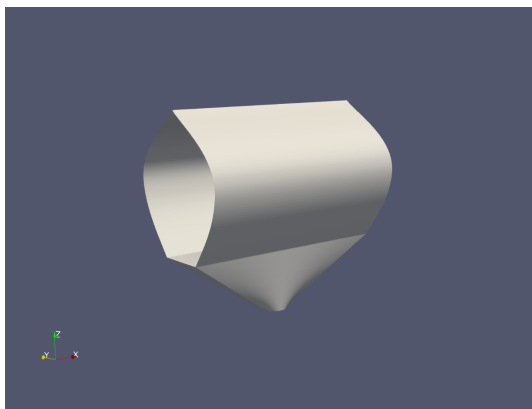
Figure 9.1: Numerical and experimental visualization of the free surface on diamond geometry

The third feature that one should seek is to remove sharp edges at the constriction in order to prevent the water accumulation on the upper faces as depicted both numerically and experimentally in Fig. 9.1. The presence of a sharp edges also causes, as shown in Fig. 8.7d, the film to separate from the surface past the sharp edge, which seriously affects the specific water coverage. Ultimately

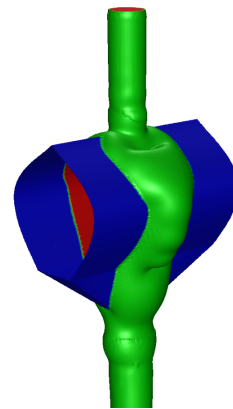
ensuring periodicity of the water stream is also of importance for interfacial area predictability and developing 1D models. Hence, the goal is to obtain a similar flow pattern between corrugation impinging and exiting. Even if the diamond shaped geometry showed interesting results regarding that matter, the presence of the *teapot effect* as shown in Fig. 8.7c requires further analysis. As a consequence, one should avoid having a straight sharp edge at the bottom of a corrugation. A similar statement can be said for the presence of a flat face at the bottom that creates a strong amount of drag on the water film leading to its atomization and blockage. Along with this issue, working on the gas pressure drop, which is a main source of losses, the presence of a flat face significantly increases the gas pressure drop in comparison with aerodynamically optimized shapes.

9.2 Geometry Iterations

With all these observations, the diamond shaped geometry is taken as a baseline and all of its defects are removed. In order to be able to compare the new geometries with the one tested in the previous chapter, two design constraints are imposed. First, the distance between the water inlet and the geometry must remain equal to H . Second, the characteristic length of the geometry, L_t , as shown in Fig. 8.1 is also equal in order to maintain the constriction characterization. The



(a) First iteration geometry



(b) Free surface ($\theta_{eq} = 60^\circ$)

Figure 9.2: First iteration results

first iteration depicted on Fig. 9.2a and only addresses the flaws of the diamond geometry. As a consequence, the sharp edge at the constriction is traded for a round and smooth surface. The main

changes are at the bottom where instead of the sharp edge, a conical surface is added to make water converge toward the center-line to enforce the periodicity along with preventing incipience of the *teapot effect*.

A first calculation is accomplished under the same flow conditions as in section 8.5.2 with $\theta_{eq} = 60^\circ$. In comparison with Fig. 8.7c, the resulting free-surface obtained, as shown in Fig. 9.2, depicts a rivulet type flow that is periodic while remaining free of blockage. The specific water coverage remains similar at 40%. Even if this already constituted satisfying results, this iteration failed to provide a blockage free flow pattern when $\theta_{eq} = 90^\circ$. Therefore, the second iteration, shown in Fig. 9.3a, adds chamfers on the side to enhance the film spreading on the side of the corrugation and diminish its thickness at the constriction to prevent blockage.

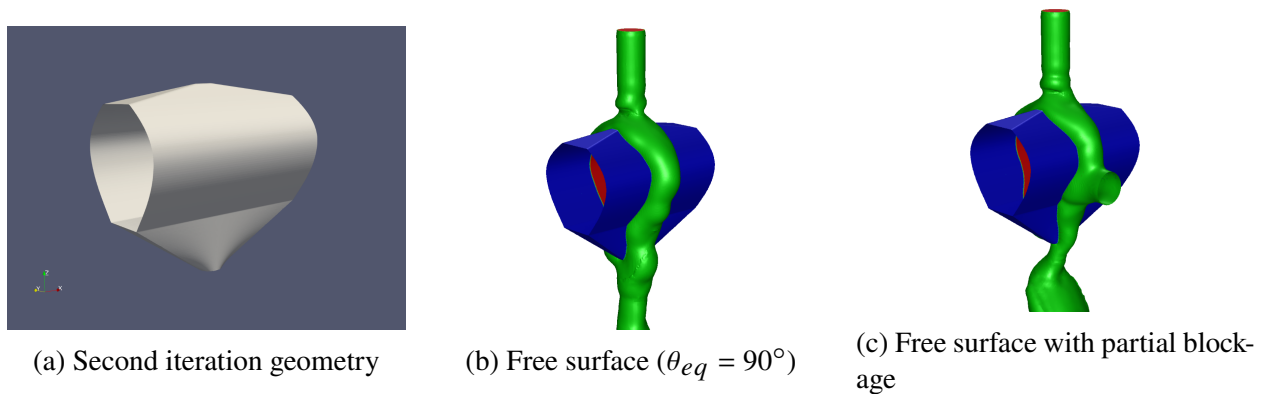
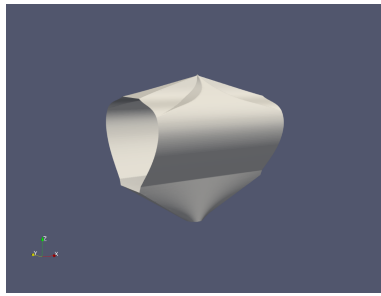


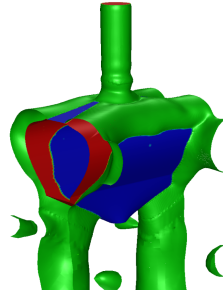
Figure 9.3: Second iteration results

The resulting free-surface shown on Fig. 9.3b does not present a chronic blockage, but the instability of the liquid column at the bottom sometimes triggers a brief clogging of the constriction (see Fig. 9.3c). Nonetheless, the specific water coverage obtained is about 25%, which is twice as high as the diamond geometry for the same conditions. This gain is mainly due to the suppression of the sharp edge at the constriction, preventing the water film separating from the surface.

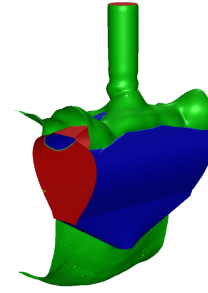
The good results obtained with the second iteration enforces the idea of spreading the water onto the surface further, which resulted in the geometry shown in Fig. 9.4a. As shown in Fig. 9.4b, the carved shape added at the top shows the result expected where the water is directed on the whole surface. Unfortunately, a too important portion of the the water gets directed to the side



(a) Third iteration geometry



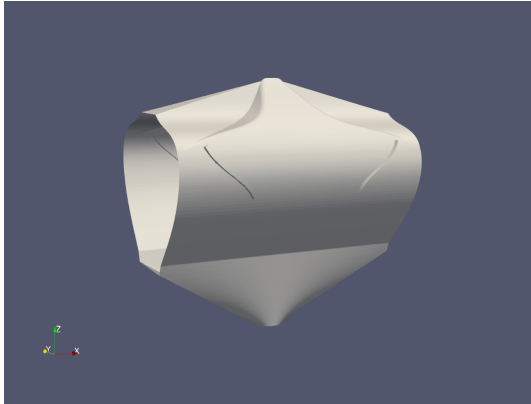
(b) Free surface ($\theta_{eq} = 60^\circ$)



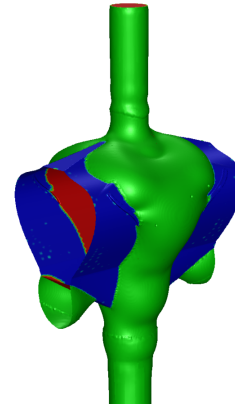
(c) Free surface ($\theta_{eq} = 90^\circ$)

Figure 9.4: Third iteration results

leading the center-line to be dry and a partial blockage of the constriction when $\theta_{eq} = 60^\circ$ and a complete blockage when $\theta_{eq} = 90^\circ$.



(a) Fourth iteration geometry



(b) Free surface ($\theta_{eq} = 60^\circ$)

Figure 9.5: Fourth iteration results

Finally, using these observations, the carving in the upper part is diminished to enlarge the tip and direct an increased amount of the water towards the center-line. Fins pointing toward the center-line are also added to reduce the flow inertia and avoid accumulation on the sides that lead to the partial blockage observed in Fig. 9.4b. As shown in Fig. 9.5b, the resulting free-surface is blockage free, both during the transient phase and at steady-state while yielding a specific water coverage of about 50%. The flow pattern observed is very similar to the one obtained for the cylinder geometry on Fig. 8.7c, where water naturally goes on the side, which shows the water stream periodicity. The common conclusion for both of these situations is that the length of the corrugation could be increased to make the most of the water impinging the surface. Using the

same reasoning, the mass flow rate of water could be reduced so that the water front stops exactly at the side boundary. At the system scale, this will lead to a great reduction of the water needed to obtain the interfacial area required for the targeted mass fraction output.

9.3 Conclusion of Corrugation Geometry Design

As briefly shown in the previous section, improving the corrugation designs is straightforward as long as the fluids' flow rate and patterns are known along with the contact angle, which is determined by the material employed for manufacturing. The contact angle and material cost should be a first concern in the design of an evaporator because the ideal geometry and distributor to be employed in the evaporator are heavily dependent on contact angle. The three elementary geometries studied are necessary stepping stones to give a baseline to anyone who seeks the design of an efficient evaporator. Depending on the contact angle, any geometry can be used and more or less design refinement work will be necessary. As an example, if one uses a super hydrophilic material, the square geometry could be considered as long as some design work is accomplished on the bottom part to avoid the formation of a liquid sheet normal to the gas stream.

Knowing that, one should find a satisfying corrugation geometry that is blockage free both transiently and at steady-state with a high and homogeneous specific water coverage while offering water flow periodicity. The targeted geometry characteristics are necessary in order to develop simpler models at the scale of the column or more precisely at the scale of a row of corrugations and update the design tools currently available.

Though the blockage phenomenon is depicted as harmful when it leads to the entire constriction to be blocked in the packing, it could also be thought as a feature to enhance the interfacial area between liquid-gas beyond the specific area provided by the packed column geometry. In other words, the design of a corrugation could be to naturally bridge with its neighbors for a given design point.

Finally, in the counter-current configuration, and has been shown in chapter 7, requires significant work on the gas side to reduce the pressure drop and, if possible at the corrugation scale, as

well as enhancing the air/vapor mixing. The author emphasizes here that a blockage free geometry intrinsically allows corrugations to be extremely close to each other, hence limiting the need to enhance mixing. The work accomplished here shows very satisfying results with corrugations being 3mm apart from each other. Therefore, two philosophies in the evaporator design should emerge based on the global size of the system. On the one hand, very compact systems with low gas mass fluxes that will have small corrugations very close to each other and where a blockage free geometry has to be targeted but air/vapor mixing would not matter. Because of the small hydraulic diameters, the pressure losses would rapidly increase with the gas mass flux. On the other hand, large systems, characterized by corrugations placed further apart such that the presence of capillary instabilities becomes impossible. Those systems would naturally possess a low linear pressure drop at high mass fluxes due to the large hydraulic diameters. The consequence of that design strategy is the requirement of additional geometrical features to obtain a proper mixing in the gas phase as well as a larger evaporator footprint.

CHAPTER 10

CONCLUSION AND PERSPECTIVES

The study of a direct contact evaporator for Humidification-Dehumidification desalination systems guided the orientation of this thesis. The absence of prior work in the domain of computational fluid dynamic applied to desalination and more broadly low temperature evaporation at the local scale led the author to develop, validate, and finally contribute to the ultimate challenge of water scarcity.

In the second chapter, a global review of solar desalination technologies is covered and showed the great interest of using HDH system in remote areas using local water. The main issue of an HDH system is the poor scalability along with the high specific water consumption when compared to other thermal process such as MSF. In the last decade, several solutions have been proposed to enhance the performances such as the use of a TVC or using different carrier gas, but they all query the simplicity of the system. The use of direct contact evaporation and condensation that consist in using a packed column instead of a traditional tube and shell design has shown to greatly enhance the performances of the system while maintaining its simplicity.

The third chapter covers the state of the art in the modeling of packed columns, either structured or random. The early extensive experimental campaigns offer a good prediction of a given geometry in various conditions but critically lack the understanding at the local scale of the liquid-gas interaction. The use of the porous media approach, if convenient, does not solve this issue as it relies on empirical closure correlations to close the governing equations. The tremendous increase in computing power over the last decade as allowed researchers to move on to direct numerical simulation of multiphase flows at various scale.

Chapter four pursues the current methods available in the modeling of multiphase flow with interface tracking with an emphasis on the VOF method. The reader is introduced to the various techniques to reconstruct and sharpen the interface, model surface tension, and wall adhesion. An understanding of those method limitations is crucial in obtaining a stable and accurate simulation.

The fifth chapter pursues an interest in the current methods employed to model interfacial mass transfer in CFD and their limitations. The model proposed by the author, based on a first order approximation of Fick's first law at the interface, removes the need of empiricism to close the mass transfer problem. In addition, the calculation of the characteristic length necessary to compute the mass fraction gradient at the interface also yields an accurate calculation of the interfacial area on any type of convex grid. This chapter also briefly develops the Finite Volume Method and the discretization schemes, the equations solved in ANSYS Fluent, and the implementation of the UDF used in this work.

Chapter six aims at validating the numerical framework developed in chapter five using a classic static drop test where the accuracy of the interfacial area calculation is assessed on various grid topologies. The results show an excellent accuracy on hexahedral and tetrahedral cells and is acceptable on mixed polyhedral cells. Nonetheless, the calculation of the interfacial area shows an error reduction of up to 30% in comparison with the $|\nabla\alpha|$ formulation usually employed. The second test consisted in testing the assumption taken on the mass fraction gradient discretization at the interface, which assumes the characteristic length to be the normal distance between the interface and the center of gravity of the truncated cell. This is accomplished by comparing the numerical results with a novel analytical solution. The computed error between analytical and numerical is inferior to 2%, mainly due to the approximation of the VOF method on the fluid properties in the interfacial cells.

Chapter seven is a detailed description of the transition between the experimental setup using a direct contact evaporator and the necessary simplification and assumptions taken in order to model the problem using computational fluid dynamic. The chapter covers geometry, domain, and mesh generation and validation along with the complex post-processing. The mesh validation being particularly complicated due to the trade between accurate geometry description, interface curvature computation, and computational expenses. Hence, the latter is accomplished using multiple test cases relevant to the physics being modeled here.

A comparison of the evaporator performances obtained is accomplished under various fluid

distribution conditions. The study shows a strong dependence on the water spray density. The results showed a little sensitivity to the gas distribution for the conditions studied with the Lantec HD-QPAC geometry. It also showed the critical need to couple the distributor and column designs together will significantly increase the efficiency of the systems. The detailed results obtained depicted the importance of an homogeneous mixing in the gas mixture to avoid local vapor saturation limiting the evaporative process. Finally, the numerical model, similarly to experimental observations, also displayed the presence of the blockage phenomenon or local flooding. This phenomenon, appearing when driving down the hydraulic diameters to increase the geometries specific area, is responsible for increases pressure losses and querying heat and mass transfer.

These observations lead to chapter eight where an in-depth study of the parameters responsible for blockage are investigated and applied to three elementary geometric shapes. Two regimes are considered: the column regime, usually associated with falling film on tube banks and the droplet regime usually associated with packed columns where a spray distributor is employed. The study has two important observations. First, the wettability of the surface, which is directly associated to the contact angle value, is the main parameter affecting the flow pattern for each geometry. If a poor wettability clearly shows a higher predisposition for any geometry to generate the blockage instability, their general shape have a significant impact on mitigating this instability. Secondly, the study in the column regime showed little sensitivity to the distribution since, the existence of water flowing only starts after a defined amount of water has been distributed. It should also be mentioned that during the blockage incipience, the cross sectional area available for the gas to flow through becomes small, hence the gas velocity increases. This phenomenon may lead to a brief and local transition to the turbulent regime of the gas stream.

Finally, a few design iterations were accomplished in chapter nine that aimed at making the diamond geometry free of blockage for high contact angle values in the given flow conditions. Result showed, after only four iterations, improvement on the specific water coverage of 10% for $\theta_{eq} = 60^\circ$ and 12.5% for $\theta_{eq} = 90^\circ$ while suppressing blockage and obtaining water flow periodicity.

These encouraging results open several needs both in terms of modeling at the scale of the column and at the scale of the corrugation. The progress accomplished here in modeling the transport phenomenon at the local scale yields significant insight. Nonetheless, more studies on larger models should be accomplished to confirm the tendencies observed here. With the emergence of low drag geometries, the interest in high gas mass fluxes to improve the scalability in the height of HDH will require the modeling of turbulence with its effect on heat and mass transport. At the scale of the corrugation, much needs accomplished on the geometry with, in the first place, a proper parametrisation. One area to explore is the use of similar laws (camber and thickness) as used in turbomachinery that will allow a fine and structured tuning of the geometry. A significant amount of work should be accomplished on the corrugation scalability by determining the relevant non-dimensional groups. This would prove extremely helpful for experimental work by significantly increasing the working scale from the millimeter to the centimeter. With the global shrinking in the corrugation sizes, the influence on the flow pattern when the droplets or column size becomes equal or larger than the characteristic size of the corrugation is yet to be observed. A similar study when the impinging water flow is no longer normal to the geometry but comes at an angle is of interest when a sprayer is employed in the experiments and determining its impact on the hydrodynamic, heat, and mass transfer.

APPENDICES

APPENDIX A

WATER SATURATION PRESSURE

$$P_{sat} = 0.611379e^{(aT - bT^2 + cT^3)}$$

$$a = 0.07236669 \tag{A.1}$$

$$b = 2.78793 \times 10^{-4}$$

$$c = 6.76138 \times 10^{-7}$$

APPENDIX B

SOLUTION OF EQUATION (6.5)

For a steady-state 2D fully developed laminar flow with an isotropic and constant diffusion coefficient the advection-diffusion equation becomes:

$$\frac{\partial^2 C}{\partial x^2} + \frac{\partial^2 C}{\partial y^2} - \frac{u_x(y)}{D} \frac{\partial C}{\partial x} = 0 \quad (\text{B.1})$$

With the following boundary conditions:

$$C(y = 0) = C_s \quad (\text{B.2})$$

$$C(y = H) = 0 \quad (\text{B.3})$$

$$C(x = 0) = C_0(y) \quad (\text{B.4})$$

$$C(x \Rightarrow \infty) = \phi(y) \quad (\text{B.5})$$

$C_0(y)$ is the initial concentration profile in the duct and $\phi(y)$ is the concentration profile when the species boundary is fully developed. The boundary conditions in the vertical axis described by (B.2) and (B.3) makes the problem non-homogeneous which forces the adoption of a split solution.

$$C(x, y) = \psi(x, y) + \phi(y) \quad (\text{B.6})$$

Injecting (B.6) into (6.5) yields the following system of equations:

$$\frac{\partial^2 \psi}{\partial x^2} + \frac{\partial^2 \psi}{\partial y^2} - \frac{u_x(y)}{D} \frac{\partial \psi}{\partial x} = 0 \quad (\text{B.7a})$$

$$\frac{d^2 \phi}{dy^2} = 0 \quad (\text{B.7b})$$

The adoption of the split solution also splits the boundary conditions. Hence the boundary conditions for $\psi(x, y)$ are:

$$\psi(y = 0) = 0 \quad (\text{B.8})$$

$$\psi(y = H) = 0 \quad (\text{B.9})$$

$$\psi(x = 0) = C_0(y) - \phi(y) \quad (\text{B.10})$$

$$\psi(x \Rightarrow \infty) = 0 \quad (\text{B.11})$$

Naturally the in-homogeneity is driven onto the boundary conditions for $\phi(y)$.

$$\phi(y = 0) = C_s \quad (\text{B.12})$$

$$\phi(y = H) = 0 \quad (\text{B.13})$$

Immediately the solution for $\phi(y)$ is found by integrating twice (B.7b). The coupling with the boundary conditions from (B.12) and (B.13) allows the integration constants to be determined.

$$\phi(y) = C_s \left(1 - \frac{y}{H}\right) \quad (\text{B.14})$$

To solve (B.7a) the same approach as Hes & Staňková (1987) is employed, which consists of substituting $\psi(x, y)$ as shown in (B.15) which will automatically respect the boundary conditions defined by (B.10) and (B.11).

$$\psi(x, y) = C_n(y)e^{-\alpha_n^2 x} \quad (\text{B.15})$$

Substituting (B.15) in (B.7a) leads to the following second order ordinary differential equation:

$$\frac{d^2 C_n}{dy^2} + \left(-Ay^2 + By + C\right) C_n = 0 \quad (\text{B.16})$$

Where the constants A , B , and C are defined as follow:

$$A = \alpha_n^2 \frac{a_x}{D} \quad (\text{B.17a})$$

$$B = \alpha_n^2 \frac{b_x}{D} \quad (\text{B.17b})$$

$$C = \alpha_n^4 + \alpha_n^2 \frac{c_x}{D} \quad (\text{B.17c})$$

Equation (B.16) is the parabolic cylinder differential equation. By rewriting (B.16) and replacing the original variable y by $u = y - \frac{B}{2A}$.

$$\frac{d^2 g(u)}{du^2} + \left(-Au^2 + E\right) g(u) = 0 \quad (\text{B.18a})$$

$$E = \alpha_n^4 + \frac{\alpha_n^2}{D} \left(c_x + \frac{1}{4} \frac{b_x^2}{a_x}\right) \quad (\text{B.18b})$$

Furthermore replacing by the variable u by $\eta = u\sqrt{2}\sqrt[4]{A} = \varepsilon_n u$ the following equation is obtained:

$$\frac{d^2 v(\eta)}{d\eta^2} - \left(\frac{1}{4}\eta^2 + a\right)v(\eta) = 0 \quad (\text{B.19a})$$

$$a = \frac{-E}{2\sqrt{A}} = -\frac{1}{2}\sqrt{\frac{D}{a_x}} \left[\alpha_n^3 + \frac{\alpha_n}{D} \left(c_x + \frac{1}{4} \frac{b_x^2}{a_x} \right) \right] \quad (\text{B.19b})$$

The solutions of (B.19a) are the linear combination of an odd and an even function defined by Abramowitz et al. (1965). The descriptions of $U(a, \eta)$ and $V(a, \eta)$ are given in Appendix C.

$$v(\eta) = C_1 U(a, \eta) + C_2 V(a, \eta) \quad (\text{B.20})$$

Hence, the solution of (B.16) is:

$$C_n(y) = C_1 U\left(a, \varepsilon_n \left(y - \frac{B}{2A}\right)\right) + C_2 V\left(a, \varepsilon_n \left(y - \frac{B}{2A}\right)\right) \quad (\text{B.21})$$

The constants C_1 and C_2 are found using the boundary conditions in the spanwise direction and leads to the following transcendental equation:

$$V\left(a, \frac{-\varepsilon_n B}{2A}\right) - \frac{V\left(a, \varepsilon_n \left(H - \frac{B}{2A}\right)\right)}{U\left(a, \varepsilon_n \left(H - \frac{B}{2A}\right)\right)} U\left(a, \frac{-\varepsilon_n B}{2A}\right) = 0 \quad (\text{B.22})$$

Finally the complete solution to (6.5) can be derived where A_n is the normalization factor and $w(y)$ is the weighting function from the Sturm-Liouville theory,

$$C(x, y) = C_s \left(1 - \frac{y}{H}\right) + \sum_{n=0}^{\infty} A_n C_n(y) e^{-\alpha_n^2 x} \quad (\text{B.23a})$$

$$A_n = \frac{\int_0^H (C_0(y) - \phi(y)) C_n(y) w(y) dy}{\int_0^H w(y) C_n^2(y) dy} \quad (\text{B.23b})$$

$$w(y) = \frac{u_x(y)}{D} \quad (\text{B.23c})$$

APPENDIX C

DESCRIPTION OF PARABOLIC CYLINDER FUNCTIONS $U(a, \eta)$ AND $V(a, \eta)$

The two standard linearly independent solutions of (B.19a) defined by Abramowitz et al. (1965) are denoted $U(a, \eta)$ and $V(a, \eta)$.

$$U(a, \eta) = \cos \left[\pi \left(\frac{1}{4} + \frac{1}{2}a \right) \right] Y_1 - \sin \left[\pi \left(\frac{1}{4} + \frac{1}{2}a \right) \right] Y_2 \quad (\text{C.1})$$

$$V(a, \eta) = \frac{\sin \left[\pi \left(\frac{1}{4} - \frac{1}{2}a \right) \right] Y_1 + \cos \left[\pi \left(\frac{1}{4} + \frac{1}{2}a \right) \right] Y_2}{\Gamma \left(\frac{1}{2} - a \right)} \quad (\text{C.2})$$

where

$$Y_1 = \frac{1}{\sqrt{\pi}} \frac{\Gamma \left(\frac{1}{4} - \frac{1}{2}a \right)}{2^{a/2+1/4}} e^{-\frac{\eta^2}{4}} {}_1F_1 \left(\frac{1}{2}a + \frac{1}{4}, \frac{1}{2}, \frac{1}{2}\eta^2 \right) \quad (\text{C.3})$$

$$Y_2 = \frac{\eta}{\sqrt{\pi}} \frac{\Gamma \left(\frac{3}{4} - \frac{1}{2}a \right)}{2^{a/2-1/4}} e^{-\frac{\eta^2}{4}} {}_1F_1 \left(\frac{1}{2}a + \frac{3}{4}, \frac{3}{2}, \frac{1}{2}\eta^2 \right) \quad (\text{C.4})$$

where ${}_1F_1(\alpha, \beta, \gamma)$ is the confluent hypergeometric of the first kind. Various representations are given by Arfken et al. (2013) either as a sum or as an integral.

BIBLIOGRAPHY

BIBLIOGRAPHY

- Abbaspour, Mohammad Javad, Meysam Faegh & Mohammad Behshad Shafii. 2019. Experimental examination of a natural vacuum desalination system integrated with evacuated tube collectors. *Desalination* 467(May). 79–85. doi:10.1016/j.desal.2019.06.004.
- Abraham, Tinu & Amit Luthra. 2011. Socio-economic & technical assessment of photovoltaic powered membrane desalination processes for India. *Desalination* 268(1-3). 238–248. doi: 10.1016/j.desal.2010.10.035.
- Abramowitz, Milton, Irene A. Stegun & David Miller. 1965. Handbook of Mathematical Functions With Formulas, Graphs and Mathematical Tables, 685–700. Washington, DC: National Bureau of Standards.
- Abu Arabi, Mousa K. & Kandi Venkat Reddy. 2003. Performance evaluation of desalination processes based on the humidification/dehumidification cycle with different carrier gases. *Desalination* 156(1-3). 281–293. doi:10.1016/S0011-9164(03)00359-X.
- Aferka, S., A. Viva, E. Brunazzi, P. Marchot, M. Crine & D. Toye. 2011. Tomographic measurement of liquid hold up and effective interfacial area distributions in a column packed with high performance structured packings. *Chemical Engineering Science* 66(14). 3413–3422. doi: 10.1016/j.ces.2011.01.022. <http://dx.doi.org/10.1016/j.ces.2011.01.022>.
- Ahsan, Amimul, Monzur Imteaz, Rahul Dev & Hassan A. Arafat. 2013. Numerical models of solar distillation device: Present and previous. *Desalination* 311. 173–181. doi:10.1016/j.desal.2012.11.023.
- Al-Amshawee, Sajjad, Mohd Yusri Bin Mohd Yunus, Abdul Aziz Mohd Azoddein, David Geraint Hassell, Ihsan Habib Dakhil & Hassimi Abu Hasan. 2020. Electrodialysis desalination for water and wastewater: A review. *Chemical Engineering Journal* 380(July 2019). doi:10.1016/j.ces.2019.122231.
- Al-Hallaj, Said, Mohammed Mehdi Farid & Abdul Rahman Tamimi. 1998. Solar desalination with a humidification - dehumidification cycle: Performance of the unit. *Desalination* 120(3). 273–280. doi:10.1016/S0011-9164(98)00224-0.
- Al-Karaghoul, Ali & Lawrence L. Kazmerski. 2013. Energy consumption and water production cost of conventional and renewable-energy-powered desalination processes. *Renewable and Sustainable Energy Reviews* 24. 343–356. doi:10.1016/j.rser.2012.12.064.
- Al-Kharabsheh, S. & D. Yogi Goswami. 2003. Analysis of an innovative water desalination system using low-grade solar heat. *Desalination* 156(1-3). 323–332. doi:10.1016/S0011-9164(03)00363-1.
- Alarcón-Padilla, Diego César & Lourdes García-Rodríguez. 2007. Application of absorption heat pumps to multi-effect distillation: a case study of solar desalination. *Desalination* 212(1-3). 294–302. doi:10.1016/j.desal.2006.10.014.

- Alasfour, F. N., M. A. Darwish & A. O. Bin Amer. 2005. Thermal analysis of ME-TVC+MEE desalination systems. *Desalination* 174(1). 39–61. doi:10.1016/j.desal.2004.08.039.
- Ali, Ehab S., Ahmed A. Askalany, K. Harby, Mohamed Refaat Diab & Ahmed S. Alsaman. 2018. Adsorption desalination-cooling system employing copper sulfate driven by low grade heat sources. *Applied Thermal Engineering* 136(February). 169–176. doi:10.1016/j.applthermaleng.2018.03.014.
- Ali, Muhammad Tauha, Hassan E.S. Fath & Peter R. Armstrong. 2011. A comprehensive techno-economical review of indirect solar desalination. *Renewable and Sustainable Energy Reviews* 15(8). 4187–4199. doi:10.1016/j.rser.2011.05.012.
- Alix, Pascal & Ludovic Raynal. 2008. Liquid distribution and liquid hold-up in modern high capacity packings. *Chemical Engineering Research and Design* 86(6). 585–591. doi:10.1016/j.cherd.2008.02.021.
- Alkaisi, Ahmed, Ruth Mossad & Ahmad Sharifian-Barforoush. 2017. A Review of the Water Desalination Systems Integrated with Renewable Energy. *Energy Procedia* 110(December 2016). 268–274. doi:10.1016/j.egypro.2017.03.138.
- Alkhulaifi, Yousif, Esmail M.A. Mokheimer & Jihad H. AlSadah. 2019. Performance optimization of mechanical vapor compression desalination system using a water-injected twin-screw compressor. *Journal of Energy Resources Technology, Transactions of the ASME* 141(4). 1–13. doi:10.1115/1.4042087.
- AlMadani, H. M.N. 2003. Water desalination by solar powered electro dialysis process. *Renewable Energy* 28(12). 1915–1924. doi:10.1016/S0960-1481(03)00014-4.
- Alnaimat, Fadi & James F. Klausner. 2012. Solar diffusion driven desalination for decentralized water production. *Desalination* 289. 35–44. doi:10.1016/j.desal.2011.12.028.
- Alnaimat, Fadi & James F. Klausner. 2013. Enhanced performance of solar diffusion driven desalination. *Journal of Thermal Science and Engineering Applications* 5(4). 1–9. doi:10.1115/1.4024020.
- Alnaimat, Fadi, James F. Klausner & Renwei Mei. 2011. Transient analysis of direct contact evaporation and condensation within packed beds. *International Journal of Heat and Mass Transfer* 54(15-16). 3381–3393. doi:10.1016/j.ijheatmasstransfer.2011.03.048.
- Alnaimat, Fadi, James F. Klausner & Renwei Mei. 2013. Transient dynamic response of solar diffusion driven desalination. *Applied Thermal Engineering* 51(1-2). 520–528. doi:10.1016/j.applthermaleng.2012.09.038.
- Alnaimat, Fadi, Mohammed Ziauddin & Bobby Mathew. 2021. A review of recent advances in humidification and dehumidification desalination technologies using solar energy. *Desalination* 499(August 2020). 114860. doi:10.1016/j.desal.2020.114860.
- Alsaman, Ahmed S., Ahmed A. Askalany, K. Harby & Mahmoud S. Ahmed. 2016. A state of the art of hybrid adsorption desalination-cooling systems. *Renewable and Sustainable Energy Reviews* 58. 692–703. doi:10.1016/j.rser.2015.12.266.

- Alsehli, Mishal, Jun Ki Choi & Mohammed Aljuhan. 2017. A novel design for a solar powered multistage flash desalination. *Solar Energy* 153. 348–359. doi:10.1016/j.solener.2017.05.082.
- Aly, S. E. 1984. Energy savings in distillation plants by using vapor thermo-compression. *Desalination* 49(1). 37–56. doi:10.1016/0011-9164(84)80011-9.
- Anderson, Jd. 1995. Computational Fluid Dynamics: The Basics with Applications. 1995. *McGrawhill Inc* doi:10.1017/CBO9780511780066.
- ANSYS Inc. 2018. *ANSYS Fluent Theory Guide Release 19.2*.
- Arfken, George B., Hans J. Weber & Frank E. Harris. 2013. *Mathematical Methods for Physicists*. Elsevier 6th edn. doi:10.1016/C2009-0-30629-7.
- Ashgriz, N. & J. Y. Poo. 1991. FLAIR: Flux line-segment model for advection and interface reconstruction. *Journal of Computational Physics* 93(2). 449–468. doi:10.1016/0021-9991(91)90194-P.
- Ataki, Adel & Hans Jörg Bart. 2006. Experimental and CFD simulation study for the wetting of a structured packing element with liquids. *Chemical Engineering and Technology* 29(3). 336–347. doi:10.1002/ceat.200500302.
- Aulisa, Eugenio, Sandro Manservigi & Ruben Scardovelli. 2003. A mixed markers and volume-of-fluid method for the reconstruction and advection of interfaces in two-phase and free-boundary flows. *Journal of Computational Physics* 188(2). 611–639. doi:10.1016/S0021-9991(03)00196-7.
- Aulisa, Eugenio, Sandro Manservigi & Ruben Scardovelli. 2004. A surface marker algorithm coupled to an area-preserving marker redistribution method for three-dimensional interface tracking. *Journal of Computational Physics* 197(2). 555–584. doi:10.1016/j.jcp.2003.12.009.
- Baltussen, M. W., J. A.M. Kuipers & N. G. Deen. 2014. A critical comparison of surface tension models for the volume of fluid method. *Chemical Engineering Science* 109. 65–74. doi:10.1016/j.ces.2013.12.045.
- van Baten, J. M. & R. Krishna. 2004. CFD simulations of mass transfer from Taylor bubbles rising in circular capillaries. *Chemical Engineering Science* 59(12). 2535–2545. doi:10.1016/j.ces.2004.03.010.
- Billet, R. & M. Schultes. 1999. Prediction of Mass Transfer Columns with Dumped and Arranged Packings. *Chemical Engineering Research and Design* 77(6). 498–504. doi:10.1205/026387699526520.
- Bolton, G. T., C. W. Hooper, R. Mann & E. H. Stitt. 2004. Flow distribution and velocity measurement in a radial flow fixed bed reactor using electrical resistance tomography. *Chemical Engineering Science* 59(10). 1989–1997. doi:10.1016/j.ces.2004.01.049.
- Bourouni, K. & M.T. Chaibi. 2004. Modelling of heat and mass transfer in a horizontal-tube falling-film condenser for brackish water desalination in remote areas. *Desalination* 166. 17–24. doi:10.1016/j.desal.2004.06.055.

- Brackbill, J. U., D. B. Kothe & C. Zemach. 1992. A continuum method for modeling surface tension. *Journal of Computational Physics* 100(2). 335–354. doi:10.1016/0021-9991(92)90240-Y.
- de la Calle, Alberto, Javier Bonilla, Lidia Roca & Patricia Palenzuela. 2015. Dynamic modeling and simulation of a solar-assisted multi-effect distillation plant. *Desalination* 357. 65–76. doi:10.1016/j.desal.2014.11.008.
- Carbonell, R. G. 2000. Multiphase Flow Models in Packed Beds. *Oil and Gas Science and Technology* 55(4). 417–425. doi:10.2516/ogst:2000030.
- Chafik, Efat. 2003. A new type of seawater desalination plants using solar energy. *Desalination* 156(1-3). 333–348. doi:10.1016/S0011-9164(03)00364-3.
- Chakraborty, I., M. Rubio-Rubio, A. Sevilla & J. M. Gordillo. 2016. Numerical simulation of axisymmetric drop formation using a coupled level set and volume of fluid method. *International Journal of Multiphase Flow* 84. 54–65. doi:10.1016/j.ijmultiphaseflow.2016.04.002.
- Christ, Alexander, Klaus Regenauer-Lieb & Hui Tong Chua. 2014. Thermodynamic optimisation of multi effect distillation driven by sensible heat sources. *Desalination* 336(1). 160–167. doi:10.1016/j.desal.2013.12.006.
- Curran, H. M. 1970. Water desalination by indirect freezing. *Desalination* 7(3). 273–284. doi:10.1016/S0011-9164(00)80201-5.
- Du Chéné, Antoine, Chohong Min & Frédéric Gibou. 2008. Second-order accurate computation of curvatures in a level set framework using novel high-order reinitialization schemes. *Journal of Scientific Computing* 35(2-3). 114–131. doi:10.1007/s10915-007-9177-1.
- Duez, Cyril, Christophe Ybert, Christophe Clanet & Lydéric Bocquet. 2010. Wetting controls separation of inertial flows from solid surfaces. *Physical Review Letters* 104(8). 1–4. doi:10.1103/PhysRevLett.104.084503.
- El-Sebaili, A. A., M. R.I. Ramadan, S. Aboul-Enein & A. M. Khallaf. 2011. History of the solar ponds: A review study. *Renewable and Sustainable Energy Reviews* 15(6). 3319–3325. doi:10.1016/j.rser.2011.04.008.
- Elsayed, Eman, Raya AL-Dadah, Saad Mahmoud, Paul Anderson & Ahmed Elsayed. 2020. Experimental testing of aluminium fumarate MOF for adsorption desalination. *Desalination* 475(November 2019). 114170. doi:10.1016/j.desal.2019.114170.
- Enright, Douglas, Ronald Fedkiw, Joel Ferziger & Ian Mitchell. 2002. *A hybrid particle level set method for improved interface capturing*, vol. 183 1. doi:10.1006/jcph.2002.7166.
- Ergun, Sabri. 1952. Fluid Flow Through Packed Columns. *Chemical Engineering Progress* 89–94.
- Fernández-Seara, José & Ángel Á Pardiñas. 2014. Refrigerant falling film evaporation review: Description, fluid dynamics and heat transfer. *Applied Thermal Engineering* 64(1-2). 155–171. doi:10.1016/j.applthermaleng.2013.11.023.

- Fu, Yucheng, Jie Bao, Rajesh Singh, Chao Wang & Zhijie Xu. 2020. Investigation of countercurrent flow profile and liquid holdup in random packed column with local CFD data. *Chemical Engineering Science* 221. 115693. doi:10.1016/j.ces.2020.115693.
- Ganapathy, H., A. Shooshtari, K. Choo, S. Dessiatoun, M. Alshehhi & M. Ohadi. 2013. Volume of fluid-based numerical modeling of condensation heat transfer and fluid flow characteristics in microchannels. *International Journal of Heat and Mass Transfer* 65. 62–72. doi:10.1016/j.ijheatmasstransfer.2013.05.044.
- Georgoulas, Anastasios, Manolia Andredaki & Marco Marengo. 2017. An enhanced VOF method coupled with heat transfer and phase change to characterise bubble detachment in saturated pool boiling. *Energies* 10(3). doi:10.3390/en10030272.
- Ghaffour, Noreddine, Thomas M. Missimer & Gary L. Amy. 2013. Technical review and evaluation of the economics of water desalination: Current and future challenges for better water supply sustainability. *Desalination* 309(2013). 197–207. doi:10.1016/j.desal.2012.10.015.
- Gibou, Frédéric, Ligu Chen, Duc Nguyen & Sanjoy Banerjee. 2007. A level set based sharp interface method for the multiphase incompressible Navier-Stokes equations with phase change. *Journal of Computational Physics* 222(2). 536–555. doi:10.1016/j.jcp.2006.07.035.
- Gibou, Frederic, Ronald Fedkiw & Stanley Osher. 2018. A review of level-set methods and some recent applications. *Journal of Computational Physics* 353. 82–109. doi:10.1016/j.jcp.2017.10.006.
- Giwa, Adewale, Nawshad Akther, Amna Al Housani, Sabeera Haris & Shadi Wajih Hasan. 2016. Recent advances in humidification dehumidification (HDH) desalination processes: Improved designs and productivity. *Renewable and Sustainable Energy Reviews* 57. 929–944. doi:10.1016/j.rser.2015.12.108.
- Govindan, P.N., J.H. Lienhard, Ronan K. McGovern, G. Prakash Narayan, Ronan K. McGovern, Gregory P. Thiel, Jacob A. Miller, John H. Lienhard V, Mostafa H. Sharqawy, Syed M. Zubair & Mohammed A. Antar. 2011. Status of Humidification Dehumidification Desalination. *IDA World Congress on Desalination and Water Reuse* 20.
- Gude, Veera Ganeswar. 2016. Desalination and sustainability - An appraisal and current perspective. *Water Research* 89. 87–106. doi:10.1016/j.watres.2015.11.012.
- Gude, Veera Ganeswar, Nagamany Nirmalakhandan & Shuguang Deng. 2010. Renewable and sustainable approaches for desalination. *Renewable and Sustainable Energy Reviews* 14(9). 2641–2654. doi:10.1016/j.rser.2010.06.008.
- Gude, Veera Ganeswar, Nagamany Nirmalakhandan, Shuguang Deng & Anand Maganti. 2012a. Feasibility study of a new two-stage low temperature desalination process. *Energy Conversion and Management* 56. 192–198. doi:10.1016/j.enconman.2011.11.026.
- Gude, Veera Ganeswar, Nagamany Nirmalakhandan, Shuguang Deng & Anand Maganti. 2012b. Low temperature desalination using solar collectors augmented by thermal energy storage. *Applied Energy* 91(1). 466–474. doi:10.1016/j.apenergy.2011.10.018.

- Gunjal, Prashant R., Madhavanand N. Kashid, Vivek V. Ranade & Raghunath V. Chaudhari. 2005. Hydrodynamics of trickle-bed reactors: Experiments and CFD modeling. *Industrial and Engineering Chemistry Research* 44(16). 6278–6294. doi:10.1021/ie0491037.
- Guo, Z., D.F. Fletcher & B.S. Haynes. 2014. A Review of Computational Modelling of Flow Boiling in Microchannels. *The Journal of Computational Multiphase Flows* 6(2). 79–110. doi:10.1260/1757-482X.6.2.79.
- Gupta, Vinay Kumar, Mohib Khan & Hemant Puneekar. 2016. Development and Application of Interfacial Anti-Diffusion and Poor Mesh Numerics Treatments for Free Surface Flows. *Proceedings - 22nd IEEE International Conference on High Performance Computing Workshops, HiPCW 2015* 12–18. doi:10.1109/HiPCW.2015.12.
- Habib, Boaz & Mohammed Farid. 2006. Heat transfer and operating conditions for freeze concentration in a liquid-solid fluidized bed heat exchanger. *Chemical Engineering and Processing: Process Intensification* 45(8). 698–710. doi:10.1016/j.cep.2006.02.006.
- Hanley, Brian, Brian Dunbobbin & Douglas Bennett. 1994. A Unified Model for Countercurrent Vapor/Liquid Packed Columns. 1. Pressure Drop. *Industrial and Engineering Chemistry Research* 33(5). 1208–1221. doi:10.1021/ie00029a017.
- Harlow, Francis H. & J. Eddie Welch. 1965. Numerical calculation of time-dependent viscous incompressible flow of fluid with free surface. *Physics of Fluids* 8(12). 2182–2189. doi:10.1063/1.1761178.
- Haroun, Y., D. Legendre & L. Raynal. 2010. Volume of fluid method for interfacial reactive mass transfer: Application to stable liquid film. *Chemical Engineering Science* 65(10). 2896–2909. doi:10.1016/j.ces.2010.01.012.
- Haroun, Y., L. Raynal & P. Alix. 2014. Prediction of effective area and liquid hold-up in structured packings by CFD. *Chemical Engineering Research and Design* 92(11). 2247–2254. doi:10.1016/j.cherd.2013.12.029.
- Haroun, Y., L. Raynal & D. Legendre. 2012. Mass transfer and liquid hold-up determination in structured packing by CFD. *Chemical Engineering Science* 75. 342–348. doi:10.1016/j.ces.2012.03.011.
- Harten, Ami, Bjorn Engquist, Stanley Osher & Sukumar R. Chakravarthy. 1987. Uniformly high order accurate essentially non-oscillatory schemes, III. *Journal of Computational Physics* 71(2). 231–303. doi:10.1016/0021-9991(87)90031-3.
- Harvie, D. J.E., M. R. Davidson & M. Rudman. 2006. An analysis of parasitic current generation in Volume of Fluid simulations. *Applied Mathematical Modelling* 30(10). 1056–1066. doi:10.1016/j.apm.2005.08.015.
- He, W. F., D. Han, W. P. Zhu & C. Ji. 2018. Thermo-economic analysis of a water-heated humidification-dehumidification desalination system with waste heat recovery. *Energy Conversion and Management* 160(29). 182–190. doi:10.1016/j.enconman.2018.01.048.

- Hernández, J., J. López, P. Gómez, C. Zanzi & F. Faura. 2008. A new volume of fluid method in three dimensions - Part I: Multidimensional advection method with face-matched flux polyhedra. *International Journal for Numerical Methods in Fluids* doi:10.1002/fld.1776.
- Hes, L. & H. Staňková. 1987. Convection Heat Transfer to the Continuous Cylinder of Finite Thermal Capacity Moving Inside the Heating Pipe. *International Journal of Heat and Mass Transfer* 30(10). 2193–2195. doi:10.1016/0017-9310(87)90097-4.
- Higbie, R. 1935. The Rate of Absorption of a Pure Gas into a Still Liquid during Short Periods of Exposure. *Trans. A.I.ChE* 31. 365–369.
- Hirt, C.W & B.D Nichols. 1981. Volume of fluid (VOF) Method for the Dynamics of Free Boundaries. *Journal of Computational Physics* 39(1). 201–225. doi:10.1016/0021-9991(81)90145-5.
- Horgue, P., C. Soullaine, J. Franc, R. Guibert & G. Debenest. 2015. An open-source toolbox for multiphase flow in porous media. *Computer Physics Communications* 187. 217–226. doi:10.1016/j.cpc.2014.10.005.
- Hou, Hao, Qincheng Bi, Hong Ma & Gang Wu. 2012. Distribution characteristics of falling film thickness around a horizontal tube. *Desalination* 285. 393–398. doi:10.1016/j.desal.2011.10.020.
- Hua, Jinsong & Dag Mortensen. 2019. A front tracking method for simulation of two-phase interfacial flows on adaptive unstructured meshes for complex geometries. *International Journal of Multiphase Flow* 119. 166–179. doi:10.1016/j.ijmultiphaseflow.2019.07.011.
- Hull, John R. 1980. Membrane stratified solar ponds. *Solar Energy* 25(4). 317–325. doi:10.1016/0038-092X(80)90344-8.
- Hutton, B. E.T., L. S. Leung, P. C. Brooks & D. J. Nicklin. 1974. On flooding in packed columns. *Chemical Engineering Science* 29(2). 493–500. doi:10.1016/0009-2509(74)80060-6.
- Ishii, Mamoru & Takashi Hibiki. 2011. *Thermo-Fluid Dynamics of Two-Phase Flow*. New York, NY: Springer New York. doi:10.1007/978-1-4419-7985-8.
- Issa, R. I. 1986. Solution of the implicitly discretised fluid flow equations by operator-splitting. *Journal of Computational Physics* 62(1). 40–65. doi:10.1016/0021-9991(86)90099-9.
- Jacqmin, David. 1996. An energy approach to the continuum surface tension method. In *34th aerospace sciences meeting and exhibit*, doi:10.2514/6.1996-858.
- Jain, Semant & Sharad K. Gupta. 2004. Analysis of modified surface force pore flow model with concentration polarization and comparison with Spiegler-Kedem model in reverse osmosis systems. *Journal of Membrane Science* 232(1-2). 45–62. doi:10.1016/j.memsci.2003.11.021.
- Ji, Ge, Jiafeng Wu, Yaping Chen & Guangju Ji. 2017. Asymmetric distribution of falling film solution flowing on hydrophilic horizontal round tube. *International Journal of Refrigeration* 78. 83–92. doi:10.1016/j.ijrefrig.2017.03.022.

- Jiang, Guang Shan & Danping Peng. 2000. Weighted ENO schemes for Hamilton-Jacobi equations. *SIAM Journal on Scientific Computing* 21(6). 2126–2143. doi:10.1137/S106482759732455X.
- Jiang, Shanxue, Yuening Li & Bradley P. Ladewig. 2017. A review of reverse osmosis membrane fouling and control strategies. *Science of the Total Environment* 595. 567–583. doi:10.1016/j.scitotenv.2017.03.235.
- Jiang, Y., M. R. Khadilkar, M. H. Al-Dahhan & M. P. Dudukovic. 2002. CFD of multiphase flow in packed-bed reactors: II. Results and applications. *AIChE Journal* 48(4). 716–730. doi:10.1002/aic.690480407.
- Jones, Edward, Manzoor Qadir, Michelle T.H. van Vliet, Vladimir Smakhtin & Seong mu Kang. 2019. The state of desalination and brine production: A global outlook. *Science of the Total Environment* 657. 1343–1356. doi:10.1016/j.scitotenv.2018.12.076.
- Joo, Hong Jin & Hee Youl Kwak. 2013. Performance evaluation of multi-effect distiller for optimized solar thermal desalination. *Applied Thermal Engineering* 61(2). 491–499. doi:10.1016/j.applthermaleng.2013.08.006.
- Juric, Damir & Grétar Tryggvason. 1998. Computations of boiling flows. *International Journal of Multiphase Flow* 24(3). 387–410. doi:10.1016/S0301-9322(97)00050-5.
- Kabeel, A. E., Z. M. Omara & M. M. Younes. 2015. Techniques used to improve the performance of the stepped solar still-A review. *Renewable and Sustainable Energy Reviews* 46. 178–188. doi:10.1016/j.rser.2015.02.053.
- Kalogirou, Soteris A. 2004. *Solar thermal collectors and applications*, vol. 30 3. doi:10.1016/j.pecs.2004.02.001.
- Kalogirou, Soteris A. 2005. Seawater desalination using renewable energy sources. *Progress in Energy and Combustion Science* 31(3). 242–281. doi:10.1016/j.pecs.2005.03.001.
- Kang, Huifang, Yingjun Yang, Zehui Chang, Hongfei Zheng & Zhanchun Duan. 2014. Performance of a two-stage multi-effect desalination system based on humidification-dehumidification process. *Desalination* 344. 339–349. doi:10.1016/j.desal.2014.04.004.
- Kang, Jia Lin, Wei Fu Chen, David Shan Hill Wong & Shi Shang Jang. 2017. Evaluation of gas-liquid contact area and liquid holdup of random packing using CFD simulation. *2017 6th International Symposium on Advanced Control of Industrial Processes, AdCONIP 2017* 636–641. doi:10.1109/ADCONIP.2017.7983854.
- Karakilcik, Mehmet, Ibrahim Dincer, Ismail Bozkurt & Ayhan Atiz. 2013. Performance assessment of a solar pond with and without shading effect. *Energy Conversion and Management* 65. 98–107. doi:10.1016/j.enconman.2012.07.001.
- Kedem, O. & A. Katchalsky. 1958. Thermodynamic analysis of the permeability of biological membranes to non-electrolytes. *BBA - Biochimica et Biophysica Acta* 27(C). 229–246. doi:10.1016/0006-3002(58)90330-5.

- Khedr, Maaly. 1993. Techno-Economic investigation of an air humidification-dehumidification desalination process. *Chemical Engineering & Technology* 16(4). 270–274. doi:10.1002/ceat.270160410.
- Khosravi Nikou, M. R. & M. R. Ehsani. 2008. Turbulence models application on CFD simulation of hydrodynamics, heat and mass transfer in a structured packing. *International Communications in Heat and Mass Transfer* 35(9). 1211–1219. doi:10.1016/j.icheatmasstransfer.2008.05.017.
- Kistler, S. F. & L. E. Scriven. 1994. The Teapot Effect: Sheet-Forming Flows With Deflection, Wetting and Hysteresis. *Journal of Fluid Mechanics* 263. 19–62. doi:10.1017/S0022112094004027.
- Kitscha, J. & G. Kocamustafaogullari. 1989. Breakup criteria for fluid particles. *International Journal of Multiphase Flow* 15(4). 573–588. doi:10.1016/0301-9322(89)90054-2.
- Klausner, James F., Yi Li, Mohamed Darwish & Renwei Mei. 2004. Innovative Diffusion Driven Desalination Process. *Journal of Energy Resources Technology* 126(3). 219. doi:10.1115/1.1786927. <http://energyresources.asmedigitalcollection.asme.org/article.aspx?articleid=1414357>.
- Klausner, James F., Yi Li & Renwei Mei. 2006. Evaporative heat and mass transfer for the diffusion driven desalination process. *Heat and Mass Transfer/Waerme- und Stoffuebertragung* 42(6). 528–536. doi:10.1007/s00231-005-0649-2.
- Kuwahara, F., T. Yamane & A. Nakayama. 2006. Large eddy simulation of turbulent flow in porous media. *International Communications in Heat and Mass Transfer* 33(4). 411–418. doi:10.1016/j.icheatmasstransfer.2005.12.011.
- Lafaurie, Bruno, Carlo Nardone, Ruben Scardovelli, Stéphane Zaleski & Gianluigi Zanetti. 1994. Modelling merging and fragmentation in multiphase flows with SURFER. doi:10.1006/jcph.1994.1123.
- Lakehal, D., M. Meier & M. Fulgosi. 2002. Interface tracking towards the direct simulation of heat and mass transfer in multiphase flows. *International Journal of Heat and Fluid Flow* 23(3). 242–257. doi:10.1016/S0142-727X(02)00172-8.
- Lee, W. H. 1980. Pressure iteration scheme for two phase flow modeling. In *Multi-phase transport: Fundamentals, reactor safety, applications*, .
- Lee, Yee Ting, S. Hong, Chaobin Dang, Liang Han Chien & An Shik Yang. 2019a. Effect of counter current airflow on film dispersion and heat transfer of evaporative falling film over a horizontal elliptical tube. *International Journal of Heat and Mass Transfer* 141. 964–973. doi:10.1016/j.ijheatmasstransfer.2019.07.029.
- Lee, Yee Ting, Sihui Hong, Chaobin Dang, Liang Han Chien, Li Wang Chang & An Shik Yang. 2019b. Heat transfer characteristics of obliquely dispensed evaporating falling films on an elliptic tube. *International Journal of Heat and Mass Transfer* 132. 238–248. doi:10.1016/j.ijheatmasstransfer.2018.12.031.

- Leonard, B. P. 1979. A stable and accurate convective modelling procedure based on quadratic upstream interpolation. *Computer Methods in Applied Mechanics and Engineering* 19(1). 59–98. doi:10.1016/0045-7825(79)90034-3.
- Li, Meijun, Yuan Lu, Shijie Zhang & Yunhan Xiao. 2016. A numerical study of effects of counter-current gas flow rate on local hydrodynamic characteristics of falling films over horizontal tubes. *Desalination* 383. 68–80. doi:10.1016/j.desal.2016.01.016.
- Li, Yi, James F. Klausner, Renwei Mei & Jessica Knight. 2006. Direct contact condensation in packed beds. *International Journal of Heat and Mass Transfer* 49(25-26). 4751–4761. doi:10.1016/j.ijheatmasstransfer.2006.06.013.
- Liu, Hongsheng, Linsong Jiang, Dan Wu & Wence Sun. 2015. Experiment and simulation study of a trapezoidal salt gradient solar pond. *Solar Energy* 122. 1225–1234. doi:10.1016/j.solener.2015.09.006.
- Liu, Xu Dong, Ronald P. Fedkiw & Myungjoo Kang. 2000. A Boundary Condition Capturing Method for Poisson's Equation on Irregular Domains. *Journal of Computational Physics* 160(1). 151–178. doi:10.1006/jcph.2000.6444.
- Lopes, Rodrigo J.G. & Rosa M. Quinta-Ferreira. 2009. CFD modelling of multiphase flow distribution in trickle beds. *Chemical Engineering Journal* 147(2-3). 342–355. doi:10.1016/j.cej.2008.11.048.
- López, J. & J. Hernández. 2008. Analytical and geometrical tools for 3D volume of fluid methods in general grids. *Journal of Computational Physics* 227(12). 5939–5948. doi:10.1016/j.jcp.2008.03.010.
- López, J., J. Hernández, P. Gómez & F. Faura. 2016. A new volume conservation enforcement method for PLIC reconstruction in general convex grids. *Journal of Computational Physics* 316. 338–359. doi:10.1016/j.jcp.2016.04.018.
- Lu, Huanmin, John C. Walton & Andrew H.P. Swift. 2001. Desalination coupled with salinity-gradient solar ponds. *Desalination* 136(1-3). 13–23. doi:10.1016/S0011-9164(01)00160-6.
- Luo, Xiao Yong, Ming Jiu Ni, Alice Ying & M. A. Abdou. 2005. Numerical modeling for multiphase incompressible flow with phase change. *Numerical Heat Transfer, Part B: Fundamentals* 48(5). 425–444. doi:10.1080/10407790500274364.
- M., Chandrashekhara & Avadhesh Yadav. 2017. Water desalination system using solar heat: A review. *Renewable and Sustainable Energy Reviews* 67. 1308–1330. doi:10.1016/j.rser.2016.08.058.
- Mabrouk, A. A., K. Bourouni, H. K. Abdulrahim, M. Darwish & A. O. Sharif. 2015. Impacts of tube bundle arrangement and feed flow pattern on the scale formation in large capacity MED desalination plants. *Desalination* 357. 275–285. doi:10.1016/j.desal.2014.11.028.
- Madani, A. A. 1992. Zero-discharge direct-contact freezing/solar evaporator desalination complex. *Desalination* 85(2). 179–195. doi:10.1016/0011-9164(92)80004-S.

- Magnini, M., B. Pulvirenti & J. R. Thome. 2013. Numerical investigation of hydrodynamics and heat transfer of elongated bubbles during flow boiling in a microchannel. *International Journal of Heat and Mass Transfer* 59(1). 451–471. doi:10.1016/j.ijheatmasstransfer.2012.12.010.
- Magnini, M. & J. R. Thome. 2016. A CFD study of the parameters influencing heat transfer in microchannel slug flow boiling. *International Journal of Thermal Sciences* 110. 119–136. doi:10.1016/j.ijthermalsci.2016.06.032.
- Mahr, B. & D. Mewes. 2007. CFD modelling and calculation of dynamic two-phase flow in columns equipped with structured packing. *Chemical Engineering Research and Design* 85(8 A). 1112–1122. doi:10.1205/cherd06117.
- Margarinos, Ilias, Nikolaos Nikolopoulos & Manolis Gavaises. 2015. Coupling a local adaptive grid refinement technique with an interface sharpening scheme for the simulation of two-phase flow and free-surface flows using VOF methodology. *Journal of Computational Physics* 300. 732–753. doi:10.1016/j.jcp.2015.08.004.
- Malik, Mayank, Eric Sheung Chi Fan & Markus Bussmann. 2007. Adaptive VOF with curvature-based refinement. *International Journal for Numerical Methods in Fluids* doi:10.1002/flid.1490.
- Manikandan, V., K. Shanmugasundaram, S. Shanmugan, B. Janarthanan & J. Chandrasekaran. 2013. Wick type solar stills: A review. *Renewable and Sustainable Energy Reviews* 20. 322–335. doi:10.1016/j.rser.2012.11.046.
- Manjarez, R. & M. Galvan. 1979. Solar multistage flash evaporation (smsf) as a solar energy application on desalination processes. *Desalination* 31(1-3). 545–554. doi:10.1016/S0011-9164(00)88437-4.
- Mantle, M. D., A. J. Sederman & L. F. Gladden. 2001. Single-and two-phase flow in fixed-bed reactors: MRI flow visualisation and lattice-Boltzmann simulations. *Chemical Engineering Science* 56(2). 523–529. doi:10.1016/S0009-2509(00)00256-6.
- Marek, R. & J. Straub. 2001. Analysis of the evaporation coefficient and the condensation coefficient of water. *International Journal of Heat and Mass Transfer* 44(1). 39–53. doi:10.1016/S0017-9310(00)00086-7.
- Maroo, Shalabh C. & D. Yogi Goswami. 2009. Theoretical analysis of a single-stage and two-stage solar driven flash desalination system based on passive vacuum generation. *Desalination* 249(2). 635–646. doi:10.1016/j.desal.2008.12.055.
- Massman, W. J. 1998. A review of the molecular diffusivities of H₂O, CO₂, CH₄, CO, O₃, SO₂, NH₃, N₂O, NO, and NO₂ in air, O₂ and N₂ near STP. *Atmospheric Environment* 32(6). 1111–1127. doi:10.1016/S1352-2310(97)00391-9.
- Matz, R. & Z. Zimmerman. 1985. Low-temperature vapour compression and multi-effect distillation of seawater. Effects of design on operation and economics. *Desalination* 52(2). 201–216. doi:10.1016/0011-9164(85)85009-8.

- McKee, S., M. F. Tomé, V. G. Ferreira, J. A. Cuminato, A. Castelo, F. S. Sousa & N. Mangiavacchi. 2008. The MAC method. *Computers and Fluids* 37(8). 907–930. doi:10.1016/j.compfluid.2007.10.006.
- Mehrgoo, Morteza & Majid Amidpour. 2012. Constructal design and optimization of a direct contact humidification-dehumidification desalination unit. *Desalination* 293. 69–77. doi:10.1016/j.desal.2012.02.025.
- Meier, Markus, George Yadigaroglu & Brian L. Smith. 2002. A novel technique for including surface tension in PLIC-VOF methods. *European Journal of Mechanics, B/Fluids* 21(1). 61–73. doi:10.1016/S0997-7546(01)01161-X.
- Ménard, T., S. Tanguy & A. Berlemont. 2007. Coupling level set/VOF/ghost fluid methods: Validation and application to 3D simulation of the primary break-up of a liquid jet. *International Journal of Multiphase Flow* 33(5). 510–524. doi:10.1016/j.ijmultiphaseflow.2006.11.001.
- Midilli, Adnan & Teoman Ayhan. 2004. Natural vacuum distillation technique - Part I: Theory and basics. *International Journal of Energy Research* 28(4). 355–371. doi:10.1002/er.970.
- Müller-Holst, H., M. Engelhardt, M. Herve & W. Schölkopf. 1998. Solarthermal seawater desalination systems for decentralised use. *Renewable Energy* 14(1-4). 311–318. doi:10.1016/S0960-1481(98)00083-4.
- Muskat, Morris & Milan W. Meres. 1936. The flow of heterogeneous fluids through porous media. *Journal of Applied Physics* 7(921). 346–363. doi:10.1063/1.1745403.
- Narayan, G. Prakash, Mostafa H. Sharqawy, Edward K. Summers, John H. Lienhard, Syed M. Zubair & M. A. Antar. 2010. The potential of solar-driven humidification-dehumidification desalination for small-scale decentralized water production. *Renewable and Sustainable Energy Reviews* 14(4). 1187–1201. doi:10.1016/j.rser.2009.11.014.
- Nawayseh, Naser Kh, Mohammed Mehdi Farid, Said Al-Hallaj & Abdul Rahman Al-Timimi. 1999. Solar desalination based on humidification process - I. Evaluating the heat and mass transfer coefficients. *Energy Conversion and Management* 40(13). 1423–1439. doi:10.1016/S0196-8904(99)00018-7.
- Nebbia, Giorgio & Gabriella Nebbia Menozzi. 1968. Early experiments on water desalination by freezing. *Desalination* 5(1). 49–54. doi:10.1016/S0011-9164(00)80191-5.
- Ng, Kim Choon, Bidyut Baran Saha, Anutosh Chakraborty & Shigeru Koyama. 2008. Adsorption desalination quenches global thirst. *Heat Transfer Engineering* 29(10). 845–848. doi:10.1080/01457630802125310.
- Ng, Kim Choon, Kyaw Thu, Youngdeuk Kim, Anutosh Chakraborty & Gary Amy. 2013. Adsorption desalination: An emerging low-cost thermal desalination method. *Desalination* 308. 161–179. doi:10.1016/j.desal.2012.07.030.
- Nichita, Ba & Jr Thome. 2010. A level set method and a heat transfer model implemented into FLUENT for modeling of microscale two phase flows 1–15.

- Noh, W. F. & Paul Woodward. 1976. SLIC (Simple Line Interface Calculation), doi:10.1007/3-540-08004-x_336.
- Olsson, Elin & Gunilla Kreiss. 2005. A conservative level set method for two phase flow. *Journal of Computational Physics* 210(1). 225–246. doi:10.1016/j.jcp.2005.04.007.
- Omara, Z. M., A. E. Kabeel & A. S. Abdullah. 2017. A review of solar still performance with reflectors. *Renewable and Sustainable Energy Reviews* 68(December 2015). 638–649. doi:10.1016/j.rser.2016.10.031.
- Onda, Kakusaburo, Hiroshi Takeuchi & Yoshio Okumoto. 1968. Mass transfer coefficients between gas and liquid phases in packed columns. *Journal of Chemical Engineering of Japan* 1(1). 56–62. doi:10.1252/jcej.1.56.
- OpenFOAM Foundation. 2020. OpenFOAM v8 User Guide <https://cfd.direct/openfoam/user-guide/>.
- Uni, M., A. Guizani & A. Belguith. 1998. Simulation of the Transient Behaviour of Salt Gradient Solar Pond in Tunisia. *Renewable Energy* 14(1-4). 69–76.
- Peskin, Charles S. 1977. Numerical analysis of blood flow in the heart. *Journal of Computational Physics* 25(3). 220–252. doi:10.1016/0021-9991(77)90100-0.
- Petre, C. F., F. Larachi, I. Iliuta & B. P.A. Grandjean. 2003. Pressure drop through structured packings: Breakdown into the contributing mechanisms by CFD modeling. *Chemical Engineering Science* 58(1). 163–177. doi:10.1016/S0009-2509(02)00473-6.
- Pilliod, James Edward & Elbridge Gerry Puckett. 2004. Second-order accurate volume-of-fluid algorithms for tracking material interfaces. *Journal of Computational Physics* 199(2). 465–502. doi:10.1016/j.jcp.2003.12.023.
- Popinet, Stéphane. 2009. An accurate adaptive solver for surface-tension-driven interfacial flows. *Journal of Computational Physics* 228(16). 5838–5866. doi:10.1016/j.jcp.2009.04.042.
- Qasim, Muhammad, Mohamed Badrelzaman, Noora N. Darwish, Naif A. Darwish & Nidal Hilal. 2019. Reverse osmosis desalination: A state-of-the-art review. *Desalination* 459(December 2018). 59–104. doi:10.1016/j.desal.2019.02.008.
- hua Qi, Chun, Hou jun Feng, Qing chun Lv, Yu lei Xing & Nan Li. 2014. Performance study of a pilot-scale low-temperature multi-effect desalination plant. *Applied Energy* 135. 415–422. doi:10.1016/j.apenergy.2014.08.096.
- Qiblawey, Hazim Mohameed & Fawzi Banat. 2008. Solar thermal desalination technologies. *Desalination* 220(1-3). 633–644. doi:10.1016/j.desal.2007.01.059.
- Qiu, Qinggang, Chuiju Meng, Shenglin Quan & Weishu Wang. 2017. 3-D simulation of flow behaviour and film distribution outside a horizontal tube. *International Journal of Heat and Mass Transfer* 107. 1028–1034. doi:10.1016/j.ijheatmasstransfer.2016.11.009.

- Rahman, Mohammad Shafiur, Mushtaque Ahmed & X. Dong Chen. 2006. Freezing-melting process and desalination: I. review of the state-of-the-art. *Separation and Purification Reviews* 35(2). 59–96. doi:10.1080/15422110600671734.
- Rane, M. V. & Y. S. Padiya. 2011. Heat pump operated freeze concentration system with tubular heat exchanger for seawater desalination. *Energy for Sustainable Development* 15(2). 184–191. doi:10.1016/j.esd.2011.03.001.
- Raynal, L. & A. Royon-Lebeaud. 2007. A multi-scale approach for CFD calculations of gas-liquid flow within large size column equipped with structured packing. *Chemical Engineering Science* 62(24). 7196–7204. doi:10.1016/j.ces.2007.08.010.
- Raynal, Ludovic, Christophe Boyer & Jean-Pierre Ballaguet. 2008. Liquid Holdup and Pressure Drop Determination in Structured Packing with CFD Simulations. *The Canadian Journal of Chemical Engineering* 82(5). 871–879. doi:10.1002/cjce.5450820502.
- Renardy, Yuriko & Michael Renardy. 2002. PROST: A parabolic reconstruction of surface tension for the volume-of-fluid method. *Journal of Computational Physics* 183(2). 400–421. doi:10.1006/jcph.2002.7190.
- Rider, William J. & Douglas B. Kothe. 1998. Reconstructing Volume Tracking. *Journal of Computational Physics* 141(2). 112–152. doi:10.1006/jcph.1998.5906.
- Robbins, David J., M. Samir El-Bachir, Lynn F. Gladden, R. Stewart Cant & Erik von Harbou. 2012. PVAm–PIP/PS composite membrane with high performance for CO₂/N₂ separation. *AIChE Journal* 59(4). 215–228. doi:10.1002/aic.
- Roberts, David A., Emma L. Johnston & Nathan A. Knott. 2010. Impacts of desalination plant discharges on the marine environment: A critical review of published studies. *Water Research* 44(18). 5117–5128. doi:10.1016/j.watres.2010.04.036.
- Russo, Giovanni & Peter Smereka. 2000. A Remark on Computing Distance Functions. *Journal of Computational Physics* 163(1). 51–67. doi:10.1006/jcph.2000.6553.
- Saha, Bidyut Baran, Ibrahim I. El-Sharkawy, Muhammad Wakil Shahzad, Kyaw Thu, Li Ang & Kim Choon Ng. 2016. Fundamental and application aspects of adsorption cooling and desalination. *Applied Thermal Engineering* 97. 68–76. doi:10.1016/j.applthermaleng.2015.09.113.
- Saleh, A., J. A. Qudeiri & M. A. Al-Nimr. 2011. Performance investigation of a salt gradient solar pond coupled with desalination facility near the Dead Sea. *Energy* 36(2). 922–931. doi:10.1016/j.energy.2010.12.018.
- Sato, Yohei & Bojan Ničeno. 2012. A conservative local interface sharpening scheme for the constrained interpolation profile method. *International Journal for Numerical Methods in Fluids* doi:10.1002/flid.2695.
- Sato, Yuji, Tsutomu Hirose, Futoshi Takahashi & Mikio Toda. 1973. Pressure Loss and Liquid Holdup in Packed Bed Reactor With Cocurrent Gas-Liquid Down Flow. *Journal of Chemical Engineering of Japan* 6(2). 147–152. doi:10.1252/jcej.6.147.

- Schneider, Philip J. & David H. Eberly. 2003. *Geometric Tools for Computer Graphics*. doi: 10.1016/B978-1-55860-594-7.X5000-0.
- Schrage, Robert. 1953. *A theoretical study on interphase mass transfer*: Columbia University dissertation.
- Sebastia-Saez, Daniel, Sai Gu & Marco Ramaioli. 2018. Effect of the contact angle on the morphology, residence time distribution and mass transfer into liquid rivulets: A CFD study. *Chemical Engineering Science* 176. 356–366. doi:10.1016/j.ces.2017.09.046.
- Sebastia-Saez, Daniel, Sai Gu, Panneerselvam Ranganathan & Konstantinos Papadikis. 2013. 3D modeling of hydrodynamics and physical mass transfer characteristics of liquid film flows in structured packing elements. *International Journal of Greenhouse Gas Control* 19. 492–502. doi:10.1016/j.ijggc.2013.10.013.
- Setoodeh, Narjes, Rahbar Rahimi & Abolhasan Ameri. 2011. Modeling and determination of heat transfer coefficient in a basin solar still using CFD. *Desalination* 268(1-3). 103–110. doi:10.1016/j.desal.2010.10.004.
- Sharaf, M. A., A. S. Nafey & Lourdes García-Rodríguez. 2011. Thermo-economic analysis of solar thermal power cycles assisted MED-VC (multi effect distillation-vapor compression) desalination processes. *Energy* 36(5). 2753–2764. doi:10.1016/j.energy.2011.02.015.
- Sharon, H. & K. S. Reddy. 2015. A review of solar energy driven desalination technologies. *Renewable and Sustainable Energy Reviews* 41. 1080–1118. doi:10.1016/j.rser.2014.09.002.
- Sherwood, T. K., G. H. Shipley & F. A.L. Holloway. 1938. Flooding Velocities in Packed Columns. *Industrial and Engineering Chemistry* 30(7). 765–769. doi:10.1021/ie50343a008.
- Sidi-Boumedine, Réda & Ludovic Raynal. 2005. Influence of the viscosity on the liquid hold-up in trickle-bed reactors with structured packings. *Catalysis Today* 105(3-4). 673–679. doi: 10.1016/j.cattod.2005.06.040.
- So, K. K., X. Y. Hu & N. A. Adams. 2012. Anti-diffusion interface sharpening technique for two-phase compressible flow simulations. *Journal of Computational Physics* 231(11). 4304–4323. doi:10.1016/j.jcp.2012.02.013.
- Soh, Gim Yau, Guan Heng Yeoh & Victoria Timchenko. 2016. An algorithm to calculate interfacial area for multiphase mass transfer through the volume-of-fluid method. *International Journal of Heat and Mass Transfer* 100. 573–581. doi:10.1016/j.ijheatmasstransfer.2016.05.006.
- Spiegler, K.S. & O. Kedem. 1966. THERMODYNAMICS OF HYPERFILTRATION (REVERSE OSMOSIS): CRITERIA FOR EFFICIENT MEMBRANES K. S. SPIEGLER Sea Water Conversion Laboratory, University of California, Berkeley, Calif. (U.S.A.). *Desalination* 1. 311–326.
- Srithar, K. & T. Rajaseenivasan. 2018. Recent fresh water augmentation techniques in solar still and HDH desalination – A review. *Renewable and Sustainable Energy Reviews* 82(April 2017). 629–644. doi:10.1016/j.rser.2017.09.056.

- Srivastava, Pankaj K. & S. K. Agrawal. 2013. Experimental and theoretical analysis of single sloped basin type solar still consisting of multiple low thermal inertia floating porous absorbers. *Desalination* 311. 198–205. doi:10.1016/j.desal.2012.11.035.
- Stichlmair, J., J.L. Bravo & J.R. Fair. 1989. General model for prediction of pressure drop and capacity of countercurrent gas/liquids packed columns. *Gas Separation & Purification* 3(1). 29–28. doi:10.1021/ja01267a009.
- Stockfleth, Ron & Gerd Brunner. 2001. Holdup, pressure drop, and flooding in packed countercurrent columns for the gas extraction. *Industrial and Engineering Chemistry Research* 40(1). 347–356. doi:10.1021/ie000466q.
- Suárez, Francisco, Scott W. Tyler & Amy E. Childress. 2010. A fully coupled, transient double-diffusive convective model for salt-gradient solar ponds. *International Journal of Heat and Mass Transfer* 53(9-10). 1718–1730. doi:10.1016/j.ijheatmasstransfer.2010.01.017.
- Suess, P. & L. Spiegel. 1992. Hold-up of Mellapak structured packings. *Chemical Engineering and Processing* 31(2). 119–124. doi:10.1016/0255-2701(92)85005-M.
- Sussman, Mark. 1994. *A Level Set Approach for Computing Solutions to Incompressible Two-Phase Flow*: University of California, Los Angeles dissertation.
- Sussman, Mark & Elbridge Gerry Puckett. 2000. A Coupled Level Set and Volume-of-Fluid Method for Computing 3D and Axisymmetric Incompressible Two-Phase Flows. *Journal of Computational Physics* 162(2). 301–337. doi:10.1006/jcph.2000.6537.
- Tanaka, Hiroshi & Yasuhito Nakatake. 2005. Factors influencing the productivity of a multiple-effect diffusion-type solar still coupled with a flat plate reflector. *Desalination* 186(1-3). 299–310. doi:10.1016/j.desal.2005.07.005.
- Tanguy, Sébastien, Thibaut Ménard & Alain Berlemont. 2007. A Level Set Method for vaporizing two-phase flows. *Journal of Computational Physics* 221(2). 837–853. doi:10.1016/j.jcp.2006.07.003.
- Tay, J. H., S. C. Low & S. Jeyaseelan. 1996. Vacuum desalination for water purification using waste heat. *Desalination* 106(1-3). 131–135. doi:10.1016/S0011-9164(96)00104-X.
- Thu, Kyaw, Young Deuk Kim, Gary Amy, Won Gee Chun & Kim Choon Ng. 2013. A hybrid multi-effect distillation and adsorption cycle. *Applied Energy* 104. 810–821. doi:10.1016/j.apenergy.2012.12.007.
- Tryggvason, G., B. Bunner, A. Esmaeeli, D. Juric, N. Al-Rawahi, W. Tauber, J. Han, S. Nas & Y. J. Jan. 2001. A Front-Tracking Method for the Computations of Multiphase Flow. *Journal of Computational Physics* 169(2). 708–759. doi:10.1006/jcph.2001.6726.
- Unverdi, Salih Ozen & Grétar Tryggvason. 1992. A front-tracking method for viscous, incompressible, multi-fluid flows. *Journal of Computational Physics* 100(1). 25–37. doi:10.1016/0021-9991(92)90307-K.

- Van Der Leeden, P., Liem Djan Nio & P. C. Suratman. 1955. The velocity of free falling droplets. *Applied Scientific Research* 5(5). 338–348. doi:10.1007/BF03184597.
- Veza, JoséM M. 1995. Mechanical vapour compression desalination plants - A case study. *Desalination* 101(1). 1–10. doi:10.1016/0011-9164(95)00002-J.
- Wang, G. Q., X. G. Yuan & K. T. Yu. 2005. Review of mass-transfer correlations for packed columns. *Industrial and Engineering Chemistry Research* 44(23). 8715–8729. doi:10.1021/ie050017w.
- Wang, Jinwen, Derrick S. Dlamini, Ajay K. Mishra, Mary Theresa M. Pendergast, Mavis C.Y. Wong, Bhekhe B. Mamba, Viatcheslav Freger, Arne R.D. Verliefdde & Eric M.V. Hoek. 2014. A critical review of transport through osmotic membranes. *Journal of Membrane Science* 454. 516–537. doi:10.1016/j.memsci.2013.12.034.
- Wang, Peng & Tai Shung Chung. 2012. A conceptual demonstration of freeze desalination-membrane distillation (FD-MD) hybrid desalination process utilizing liquefied natural gas (LNG) cold energy. *Water Research* 46(13). 4037–4052. doi:10.1016/j.watres.2012.04.042.
- Wang, Xiaolin, Alexander Christ, Klaus Regenauer-Lieb, Kamel Hooman & Hui Tong Chua. 2011. Low grade heat driven multi-effect distillation technology. *International Journal of Heat and Mass Transfer* 54(25-26). 5497–5503. doi:10.1016/j.ijheatmasstransfer.2011.07.041.
- Wang, Xiaolin & Kim Choon Ng. 2005. Experimental investigation of an adsorption desalination plant using low-temperature waste heat. *Applied Thermal Engineering* 25(17-18). 2780–2789. doi:10.1016/j.applthermaleng.2005.02.011.
- Wang, Zhihong, Tao Yang, Zhixi Liu, Shicheng Wang, Yang Gao & Mingou Wu. 2019. Mass Transfer in a Rotating Packed Bed: A Critical Review. *Chemical Engineering and Processing - Process Intensification* 139(March). 78–94. doi:10.1016/j.cep.2019.03.020.
- Wen, Tao, Lin Lu, Weifeng He & Yunran Min. 2020a. Fundamentals and applications of CFD technology on analyzing falling film heat and mass exchangers: A comprehensive review. *Applied Energy* 261(August 2019). 114473. doi:10.1016/j.apenergy.2019.114473.
- Wen, Tao, Yimo Luo, Lin Lu & Weifeng He. 2020b. Enhancing the falling film dehumidification performance from the prospective of CFD simulation. *International Journal of Heat and Mass Transfer* 151. doi:10.1016/j.ijheatmasstransfer.2020.119459.
- Williams, Matthew W., Doug Kothe, Deniece Korzekwa & Phil Tubesing. 2002. Numerical methods for tracking interfaces with surface tension in 3-D mold filling processes. *American Society of Mechanical Engineers, Fluids Engineering Division (Publication) FED* 257(1 B). 751–759. doi:10.1115/FEDSM2002-31131.
- Wolf-Zöllner, V., F. Seibert & M. Lehner. 2019. Extended performance comparison of different pressure drop, hold-up and flooding point correlations for packed columns. *Chemical Engineering Research and Design* 147. 699–708. doi:10.1016/j.cherd.2019.05.028.

- Wu, Hao, Bill Buschle, Yunjie Yang, Chao Tan, Feng Dong, Jiabin Jia & Mathieu Lucquiaud. 2018. Liquid distribution and hold-up measurement in counter current flow packed column by electrical capacitance tomography. *Chemical Engineering Journal* 353(February). 519–532. doi:10.1016/j.cej.2018.07.016.
- Wu, Jun W., Mark J. Biggs & Eric J. Hu. 2010. Thermodynamic analysis of an adsorption-based desalination cycle. *Chemical Engineering Research and Design* 88(12). 1541–1547. doi:10.1016/j.cherd.2010.04.004.
- Wu, Jun W., Mark J. Biggs, Philip Pendleton, Alexander Badalyan & Eric J. Hu. 2012. Experimental implementation and validation of thermodynamic cycles of adsorption-based desalination. *Applied Energy* 98. 190–197. doi:10.1016/j.apenergy.2012.03.022.
- Xie, Xiaocui, Hua Liu, Chang He, Bingjian Zhang, Qinglin Chen & Ming Pan. 2019. Deciphering the heat and mass transfer behaviors of staggered tube bundles in a closed wet cooling tower using a 3-D VOF model. *Applied Thermal Engineering* 161(July). 114202. doi:10.1016/j.applthermaleng.2019.114202.
- Xu, Z. P., A. Afacan & K. T. Chuang. 2000. Predicting mass transfer in packed columns containing structured packings. *Chemical Engineering Research and Design* 78(1). 91–98. doi:10.1205/026387600526924.
- Yang, Li, Fang Liu, Zhengchang Song, Kunlei Liu & Kozo Saito. 2018. 3D numerical study of multiphase counter-current flow within a packed bed for post combustion carbon dioxide capture. *Energies* 11(6). doi:10.3390/en11061441.
- Yeoh, Guan Heng & Jiyuan Tu. 2010. *Computational Techniques for Multiphase Flows*. Elsevier. doi:10.1016/C2009-0-16604-7.
- Youngs, D. L. 1982. Time-dependent multi-material flow with large fluid distortion. .
- Youssef, P. G., R. K. Al-Dadah & S. M. Mahmoud. 2014. Comparative analysis of desalination technologies. *Energy Procedia* 61. 2604–2607. doi:10.1016/j.egypro.2014.12.258.
- Zahed, A. H. & M. D. Bashir. 1990. A case study of a solar energy transfer and storage system in a freeze desalination project in Yanbu, Saudi Arabia. *Solar and Wind Technology* 7(4). 441–446. doi:10.1016/0741-983X(90)90028-Z.
- Zejli, D., R. Benchrifa, A. Bennouna & O. K. Bouhelal. 2004. A solar adsorption desalination device: First simulation results. *Desalination* 168(1-3). 127–135. doi:10.1016/j.desal.2004.06.178.
- Zejli, Driss, Ahmed Ouammi, Roberto Sacile, Hanane Dagdougui & Azzeddine Elmidaoui. 2011. An optimization model for a mechanical vapor compression desalination plant driven by a wind/PV hybrid system. *Applied Energy* 88(11). 4042–4054. doi:10.1016/j.apenergy.2011.04.031.

- Zhao, Chuang Yao, Wen Tao Ji, Pu Hang Jin, Ying Jie Zhong & Wen Quan Tao. 2018. Hydrodynamic behaviors of the falling film flow on a horizontal tube and construction of new film thickness correlation. *International Journal of Heat and Mass Transfer* 119. 564–576. doi:10.1016/j.ijheatmasstransfer.2017.11.086.
- Zhao, Dongfeng, Jianliang Xue, Shi Li, Hui Sun & Qing dong Zhang. 2011. Theoretical analyses of thermal and economical aspects of multi-effect distillation desalination dealing with high-salinity wastewater. *Desalination* 273(2-3). 292–298. doi:10.1016/j.desal.2011.01.048.
- Zhao, Yucheng & Hamn Ching Chen. 2017. A new coupled level set and volume-of-fluid method to capture free surface on an overset grid system. *International Journal of Multiphase Flow* 90. 144–155. doi:10.1016/j.ijmultiphaseflow.2017.01.002.
- Zimmerman, Z. 1994. Development of large capacity high efficiency mechanical vapor compression (MVC) units. *Desalination* 96(1-3). 51–58. doi:10.1016/0011-9164(94)85156-5.